# Thermodynamic studies of metal-insulator transitions in organic charge-transfer salts

**Dissertation**

zur Erlangung des Doktorgrades
der Naturwissenschaften

vorgelegt beim Fachbereich Physik
der Johann Wolfgang Goethe-Universität
in Frankfurt am Main

von
**Elena Aurelia Gati**
aus Frankfurt am Main

Frankfurt am Main (2017)
D(30)

vom Fachbereich Physik der Johann Wolfgang Goethe-Universität als Dissertation angenommen.

Dekan: Prof. Dr. Owe Philipsen

**Gutachter:**
Prof. Dr. Michael Lang
Prof. Dr. Jens Müller
Prof. Dr. Takahiko Sasaki

Tag der Einreichung: 17.01.2017
Tag der Disputation: 01.06.2017

# Kurzfassung

Die vorliegende Arbeit „Thermodynamic studies of metal-insulator transitions in organic charge-transfer salts “ beschäftigt sich mit thermodynamischen Untersuchungen von Metall-Isolator-Übergängen in organischen Ladungstransfersalzen. Diese Materialen gehören der Gruppe der stark korrelierten Elektronensysteme an, deren Eigenschaften seit Jahrzehnten ein zentrales Forschungsgebiet in der Festkörperphysik darstellen, da sie sich durch eine Vielfalt interessanter physikalischer Phänomene auszeichnen. Als Beispiele für solch exotisches Verhalten sind hier die Hochtemperatursupraleitung [1–3] oder Multiferroizität [4,5] zu nennen, die nicht nur für die Grundlagenforschung hochinteressant sind, sondern auch ein enormes Potential für technische Anwendungen bieten. Grundlage für die Erklärung und Beschreibung dieser Phänomene ist ein Verständnis des sogenannten Mott Metall-Isolator-Übergangs, der einen Phasenübergang von einem elektrisch leitenden zu einem isolierenden Zustand als Folge von starken Coulomb-Abstoßungen der für den Stromtransport verantwortlichen Elektronen untereinander darstellt. Obwohl dieser Phasenübergang bereits im Jahr 1937 von Sir Nevill F. Mott theoretisch vorhergesagt wurde [6,7] und auch zu diesem Zeitpunkt Systeme, wie die als gute Kandidaten für die Realisierung eines solchen Mott isolierenden Zustands geltenden Übergangsmetalloxide [8,9], bekannt waren, so sind einige wichtige Eigenschaften dieses Phasenübergangs bis heute ungeklärt. Dazu gehört unter anderem das universelle kritische Verhalten in der Nähe eines solchen Phasenübergangs.

Im Allgemeinen sind Phasenübergänge, die uns häufig im Alltag begegnen, durch die kollektive Änderung eines Vielteilchensystems von einem Zustand in einen anderen gekennzeichnet. Hierbei unterscheidet man zwischen Phasenübergängen erster Ordnung, die sich durch Diskontinuitäten in einigen physikalischen Größen auszeichnen, und Phasenübergängen zweiter Ordnung, die kontinuierlich ablaufen. Diese Phasenübergänge zweiter Ordnung sind besonders interessant, denn, obwohl auf den ersten Blick in der Natur viele verschiedene solcher Phasenübergänge in den unterschiedlichsten Systemen zu finden sind, so verhalten sich viele Systeme in der Nähe solcher Übergänge sehr ähnlich. Das Verhalten ist dabei sogar universell und erlaubt es, die vielen verschiedenen Phasenübergänge in wenige, bekannte sogenannte Universalitätsklassen einzuordnen. Dieses Konzept der Universalität wurde in den 1950er-Jahren vorgeschlagen und später durch experimentelle und theoretische Arbeiten verifiziert [10,11]. Die diesem Konzept zugrundeliegende Idee ist, dass in der Nähe solcher Phasenübergänge die Korrelationslänge, also der Abstand, über den zwei

Teilchen aus dem Ensemble miteinander wechselwirken, divergiert und somit alle Teilchen miteinander in Wechselwirkung stehen. Dadurch spielen nur übergeordnete Parameter, wie beispielsweise die Symmetrie eines Systems, die entscheidende Rolle am Phasenübergang und nicht die Einzelheiten des jeweiligen Systems. Die Identifizierung der Universalitätsklasse stellt daher den Schlüssel zum Verständnis des Phasenübergangs dar.

Zentrales Thema dieser Arbeit ist die experimentelle Bestimmung der Universalitätsklasse des Mott Metall-Isolator-Übergangs in einem Festkörper. Er findet statt, sobald in einem Material mit ungefähr halbgefüllten Leitungsband die Stärke der Elektronenabstoßung $U$ zwischen zwei Elektronen auf demselben Gitterplatz größer als die kinetische Energie $W$ der Ladungsträger ist. Neben den Übergangsmetalloxiden sind auch quasi-zweidimensionale organische Ladungstransfersalze, wie das hier im Detail untersuchte Ladungstransfersalz $\kappa$-(BEDT-TTF)$_2$Cu[N(CN)$_2$]Cl, ganz nah am Mott Übergang gelegen [12]. In diesen Materialien werden durch den Ladungstransferprozess vom Elektronendonor BEDT-TTF ($C_{10}H_8S_8$) zum Elektronenakzeptor $X$ = Cu[N(CN)$_2$]Cl im Verhältnis 2:1 freie Ladungsträger generiert, deren Konzentration im Leitungsband durch eine sehr starke strukturelle Dimerisierung auf ein Loch pro Gitterplatz im Durchschnitt festgelegt wird [13]. Die Delokalisierung dieser Ladungsträger wird durch den Überlapp der $\pi$-Molekülorbitale des organischen Moleküls BEDT-TTF gewährleistet. Jedoch ist die Bandbreite $W$, die ein Maß für den Überlapp darstellt, in diesen Materialen im Vergleich zu einem normalen Metall relativ gering. Zudem ist die gegenseitige Coulomb-Abstoßung $U$ in diesen Materialien ungefähr genauso groß wie die Bandbreite $W$ [13]. Daher reicht in diesen Materialen das Verhältnis von $U/W$ bereits sehr nahe an das kritische Verhältnis heran. Um den Mott Übergang in diesen Materialien zu erreichen, kann zum Beispiel hydrostatischer Druck $P$ auf den Mott Isolator angelegt werden. Dabei bewirkt der Druck, dass die Molekülorbitale sich stärker überlappen und somit die Korrelationsstärke $U/W$ abnimmt, bis der Mott Übergang in den leitenden Zustand bei einem kritischen Druck $P_c$ stattfindet [12]. Experimente haben gezeigt, dass dieser Übergang bei tiefen Temperaturen ein Phasenübergang erster Ordnung ist. Die Phasengrenzlinie endet in einem kritischen Endpunkt, der einen Übergang zweiter Ordnung darstellt. Somit sollte das Verhalten in der Nähe des kritischen Endpunkts universelle Eigenschaften zeigen.

Werden in der Beschreibung des Mott Übergangs nur die elektronischen Freiheitsgrade zur Vereinfachung des komplexen Vielteilchenproblems betrachtet, so wie es beispielsweise in Experimenten mit ultrakalten Quantengasen simuliert werden kann [14], so unterstützen viele Theoretiker die Ansicht, dass der Mott Übergang sich ähnlich dem Phasenübergang zwischen einer Flüssigkeit und einem Gas verhält, also der Ising Universalitätsklasse angehört [15, 16]. Alle bisher durchgeführten Experimente an Festkörpern [17–20] wurden im Rahmen dieser Vereinfachung analysiert. Es wurde allerdings noch nicht experimentell überprüft, inwieweit diese Vereinfachung die Eigenschaften eines realen Festkörper-Systems, in dem kritische elektronische Freiheitsgrade an ein Atomgitter gekoppelt sind, beschreibt.

Die Gültigkeit dieser vereinfachenden Annahme ist in der Tat in Frage zu stellen, da dieser Phasenübergang sehr sensitiv auf äußeren Druck reagiert, der in erster Linie den Abstand zwischen einzelnen Atomen im Gitter variiert. Der Einfluss einer solchen Kopplung auf das kritische Verhalten des Mott Übergangs wurde erst vor kurzem in theoretischen Arbeiten diskutiert [21, 22]: Weit weg vom kritischen Endpunkt, wo elektronische Fluktuationen gering sind und demnach die Störung *perturbativ* behandelt werden kann, offenbart das Gitter nur eine ganz schwache Antwort auf die Fluktuationen. Das Material zeigt dann ein normales elastisches Verhalten gemäß dem bekannten Hooke'schen Gesetz, demzufolge die Länge linear auf eine äußere Spannung reagiert. Wenn man sich jedoch dem kritischen Punkt annähert und die kritischen Fluktuationen anwachsen, so bricht irgendwann die *perturbative* Näherung zusammen und das Gitter sollte in einer nicht-*perturbativen* Weise auf die äußere Spannung reagieren. Die Konsequenz hieraus wäre, dass das Gitter weich wird [21,23,24], also einer der elastischen Moduli verschwindet. Experimentell würde sich dieses Szenario in einer Verletzung des Hooke'schen Gesetzes widerspiegeln, also einer stark nicht-linearen Längenänderung als Folge des äußeren Drucks. Da das Gitter langreichweitige Scherkräfte vermittelt, wurde vorhergesagt, dass die nicht-*perturbative* Kopplung an das Kristallgitter einen Übergang zu einem Landau-kritischen Verhalten mit den kritischen Exponenten der *mean-field*-Universalitätsklasse verursacht [21].

Um die Rolle der Gitterfreiheitsgrade in der Nähe des druckinduzierten Mott Übergangs im Detail zu untersuchen, wurden in dieser Arbeit Messungen der relativen Längenänderungen $\Delta L/L$ unter äußerem Helium-Gasdruck um den kritischen Endpunkt an dem organischen Ladungstransfersalz $\kappa$-(BEDT-TTF)$_2$Cu[N(CN)$_2$]Cl durchgeführt. Die hierfür eingesetzte Apparatur, die dadurch besticht, dass Längenänderungen mit einer sehr hohen Auflösung von $\Delta L/L \approx 5 \cdot 10^{-10}$ als Funktion eines äußeren Druckes bis zu 250 MPa bestimmt werden können, wurden in den letzten Jahren in der Arbeitsgruppe von Prof. Dr. Michael Lang entwickelt und aufgebaut [25,26]. Das Herzstück dabei ist ein miniaturisiertes kapazitives Dilatometer [27], dessen Arbeitsprinzip sehr einfach ist. Das Dilatometer besteht im Wesentlichen aus einem Plattenkondensator, dessen untere Platte fest an einen Rahmen fixiert ist, wohingegen die obere Platte frei beweglich und lediglich über flexible Federn mit dem Rahmen verbunden ist. Die Probe, deren relative Längenänderung bestimmt werden soll, wird auf die obere Platte gestellt und über einen Stempel in seiner Position fixiert [28]. Sobald nun die Probe ihre Länge ändert, sich also beispielsweise ausdehnt, so drückt sie die beiden Kapazitätsplatten näher aneinander. Die Änderung des Plattenabstands, der über die Messung der Kapazität des Kondensators bestimmt werden kann, erlaubt nun, Rückschlüsse auf die Längenänderung der Probe zu ziehen. Die hohe Auflösung liegt darin begründet, dass Kapazitäten sehr präzise gemessen werden können, und der hier verwendete Plattenkondensator sich durch eine hohe Planparallelität auszeichnet. Die Einbettung eines solchen Dilatometers in eine Gas-Druckzelle erlaubt es nun, solche Messungen auch

unter Druck durchzuführen. Die Druckzelle ist dabei über eine Kapillare mit einem Kompressor, der sich auf Raumtemperatur befindet, verbunden. Im Allgemeinen ermöglicht das große Kompressorvolumen, die temperaturinduzierten Druckänderungen in der deutlich kleineren Druckzelle auszugleichen. Die besondere Herausforderung in dem vorliegenden Fall ist es, dass die Druckzelle, die speziell für diese Anwendung entwickelt wurde, ein relativ großes Volumen von 80 $\mathrm{cm}^3$ hat und dadurch unter Umständen das Kompressorvolumen von 800 $\mathrm{cm}^3$ nicht ausreicht, um einen Druckausgleich über große Temperaturbereiche zu garantieren. Da der Mott Übergang in dem hier untersuchten Ladungstransfersalz bei ca. 25 MPa liegt, wurden in dieser Arbeit Gasflaschen mit Maximaldruck von 30 MPa an den Kompressor angeschlossen, die ein sehr großes Volumen von $5 \cdot 10^4\,\mathrm{cm}^3$ im Vergleich zur Druckzelle haben. Weiterhin wurde ein hochpräzises Druckmanometer mit einer Auflösung von $\Delta P = 0.03\,\mathrm{MPa}$ installiert, wodurch es möglich ist, Messungen als Funktion der Temperatur bei konstanten äußeren Druck wie auch als Funktion eines variablen Druckes bei konstanter Temperatur durchzuführen.

Mit Hilfe dieser einzigartigen Technik war es möglich, die Längenänderungen von $\kappa$-(BEDT-TTF)$_2$Cu[N(CN)$_2$]Cl entlang aller drei kristallographischen Achsen um den kritischen Mott Endpunkt, der bei $(P_c, T_c) \approx (23{,}4\,\mathrm{MPa},\ 36{,}5\,\mathrm{K})$ liegt, zu vermessen. Dabei zeigte sich unterhalb von $T_c$ ein leicht verbreiteter Sprung der Länge als Funktion des Druckes. Diese Beobachtung ist im Einklang mit der Tatsache, dass es sich hier um einen Phasenübergang erster Ordnung handelt. Interessanterweise konnten von $T_c \approx 36.5\,\mathrm{K}$ bis hin zu Temperaturen von 43 K, also ca. 20% oberhalb des kritischen Endpunktes, ein stark nicht-lineares Verhalten der Länge als Funktion des äußeren Drucks beobachtet werden. Diese Verletzung des Hooke'schen Gesetzes, bei dem die nicht-linearen Gittereffekte umso stärker werden, je näher man sich dem elektronisch getriebenen kritischen Punkt nähert, zeigt eindeutig, dass der Mott Übergang in einem realen Festkörper sich durch eine sogenannte *kritische Elastizität* als Folge der Kopplung der Elektronen- und Gitterfreiheitsgrade auszeichnet. Um nun die beobachteten Längenänderungen in Bezug auf das kritische Verhalten zu analysieren, bietet es sich an, die Daten im Rahmen des theoretisch vorhergesagten isostrukturellen kritischen Endpunkt als Konsequenz aus der nicht-*perturbativen* Kopplung zu behandeln. Dabei kann die relative Längenänderung direkt mit dem Ordnungsparameter in Verbindung gebracht werden. So ist es möglich, die relative Längenänderung als Summe eines kritischen und eines nicht-kritischen Beitrags zu modellieren. Der kritische Beitrag kann bei einem isostrukturellen Endpunkt durch eine *mean-field*-Theorie beschrieben werden, wohingegen der nicht-kritische Beitrag durch das Hooke'sche Gesetz gegeben ist. Die hier gewonnenen Daten lassen sich in einem sehr großen Temperatur- und Druckbereich mit ausgezeichneter Übereinstimmung durch ein solches Modell beschreiben. Dies belegt im Falle des hier untersuchten organischen Ladungstransfersalzes eindeutig die entscheidende Rolle der Gitterfreiheitsgrade beim Phasenübergang: Durch die Ankopplung der

Elektronen- an die Gitterfreiheitsgrade ist der kritische Endpunkt des Mott Übergangs durch die kritischen Exponenten der *mean-field*-Universalitätsklasse dominiert.

Aus dem in dieser Arbeit untersuchten Fallbeispiel lassen sich wichtige Erkenntnisse über die Eigenschaften des Mott Übergangs im Allgemeinen gewinnen. Ist das kritische elektronische System in ein kompressibles Gitter eingebunden, wie in jedem realen Festkörpersystem, so spielen nicht nur elektronische Freiheitsgrade, sondern insbesondere deren Kopplung zum Gitter eine wesentliche Rolle am Phasenübergang. Ein Anzeichen für die Relevanz einer solchen Kopplung ist, dass der Phasenübergang durch externen Druck kontrolliert werden kann. Dies ist der Fall in diversen Übergangsmetalloxiden [17, 29–31] sowie organischen Ladungstransfersalzen [12, 32, 33]. Die Konsequenz ist, dass unabhängig von der Stärke einer solchen Kopplung jedes reale System in einem ausreichend kleinen Abstand zu dem Mott kritischen Endpunkt die universellen Eigenschaften eines isostrukturellen Festkörper-Festkörper Endpunkts zeigt, obwohl der Phasenübergang von starken Elektronenkorrelationen getrieben ist. Die Entschlüsselung der Universalitätsklasse und der damit einhergehenden Identifizierung der Wechselwirkung von Elektronen und Atomen als treibende Kraft werfen nun einen ganz neuen Blick auf die theoretische Modellierung des Mott Übergangs sowie der in der Nähe auftretenden exotischen Phänomene.

Weiterhin wurde in dieser Arbeit das organische Ladungstransfersalz $\kappa$-(BEDT-TTF)$_2$Hg(SCN)$_2$Cl mit Hilfe von thermodynamischer Methoden wie der Messung der thermischen Ausdehnung untersucht. Das besondere an diesem Material ist, dass es nicht wie das oben diskutierte $\kappa$-(BEDT-TTF)$_2$Cu[N(CN)$_2$]Cl, das sich durch eine starke Dimerisierung auszeichnet, einen Mott Übergang in einem halb gefüllten Leitungsband zeigt. Stattdessen weist dieses Material als Folge einer schwächeren Dimerisierung einen Ladungsordnungsübergang [34] auf, der typischerweise in zu einem viertel gefüllten Leitungsbändern in der Anwesenheit von starken elektronischen Korrelationen stattfindet. Es konnte gezeigt werden, dass dieser Ladungsordnungsübergang mit signifikanten Änderungen der Gitterparameter verbunden ist, die auf die Ladungsverschiebung durch Coulombkräfte zurückzuführen sind. Dieses Material stellt somit ein geeignetes Referenzmaterial dar, um die Wechselwirkung von Ladungs-, Spin- und Gitterfreiheitsgraden bei unterschiedlicher Bandfüllung in den organischen Ladungstransfersalzen in Zukunft genauer zu erforschen.

# Contents

# 1. Introduction

This thesis is dedicated to the thermodynamic study of metal-insulator transitions in organic charge-transfer salts. These materials belong to the group of strongly correlated electron systems [13], which have been in the focus of condensed matter research in the past decades. The interest in these materials arises from the variety of ground state properties including high-temperature superconductivity [2,3], unusual metallic and insulating phases [9], multiferroicity [4,5] and exotic magnetic phenomena, such as spin-liquid phases [35,36]. These exotic states emerge from the interplay between charge, spin and lattice degrees of freedom within the solid.

In order to address the effects of lattice degrees of freedom in strongly correlated electron systems, measurements of the thermal expansion proved to be particularly suited. The thermal expansion describes macroscopic changes of the length $L$ of a crystal as a function of the temperature $T$, which result from the change of interatomic distances due to the anharmonicity of the underlying crystal lattice. Employing the method of capacitive dilatometry [28] allows one to resolve relative length changes of $\Delta L/L \approx 10^{-10}$, i.e., length changes of about 0.01 Å of a crystal of 10 mm length. As a result, this technique is well-suited to detect even the tiniest modifications of the crystal lattice. As a matter of fact, the combination of thermal expansion measurements with pressure [25] provides an even more powerful tool in this regard, as pressure allows one to continuously tune the lattice constant in a particularly clean manner. The lattice potential, in turn, is a fundamental parameter for the quantum states of the electrons, signaling the importance of the coupling of the charge and lattice degrees of freedom in solids. Pressure experiments thus allow one to directly influence electronic degrees of freedom while thermal expansion measurements can directly probe the response of the underlying crystal lattice.

A central theme within the field of strongly correlated electron systems is the Mott metal-insulator transition [7], which is a prime example of the manifestation of strong electron correlations in solids. The transition itself is believed to be the key in understanding the emergent phenomena on either side of the transition. It occurs in materials with an approximately half-filled conduction band, as soon as the Coulomb repulsion between two electrons sitting on the same lattice site $U$ exceeds their kinetic energy or band width $W$. Even though the transition can be described in a simplified picture, which takes only electronic degrees of freedom into account, a detailed quantitative explanation of this phenomenon

is still lacking due to the complexity of the many-body problem. Especially, the universal properties of the phase transition itself remain illusive up to today.

Prime examples to study the physics of strong electron correlations are organic charge-transfer salts, as they show narrow bands with small $W$, comparable in size to $U$ [12, 13]. The quasi two-dimensional salts of the $\kappa$-(BEDT-TTF)$_2X$ family, where BEDT-TTF stands for bisethylenedithio-tetrathiafulvalene and $X$ is a monovalent anion, are situated close to a pressure-induced Mott transition. In case of $\kappa$-(BEDT-TTF)$_2$Cu[N(CN)$_2$]Cl, a pressure of only $P \approx 25\,\mathrm{MPa}$ is needed to access the Mott transition, making this material particularly suited to investigate the universal properties of the Mott transition. The main focus of this work lies on the investigation of the role of electron-lattice coupling at the Mott transition by measuring the thermal expansion of this particular organic conductor under pressure.

## 1.1. Outline of this thesis

This thesis is, in total, divided into 8 chapters, starting with an introduction.

Chapter 2 introduces basic thermodynamic aspects, such as the definition of thermodynamic quantities and phase transitions. The focus here will be an illustration of the concept of universality to highlight its importance in understanding phase transitions. The behavior around phase transitions will be contrasted to glass-like behavior. Following that, different types of metal-insulator transitions will be reviewed with focus on those arising from electronic correlations. At the end, a few basic definitions for the descriptions of lattice effects in solids within elasticity theory are given.

Chapter 3 provides a detailed explanation of the measurement techniques used in this work. This will include mainly a description of thermal expansion measurements at ambient pressure and, importantly, also under $^4$He-gas pressure. The central topic in this chapter will be the methods used for converting the capacitance data into relative length changes by taking into account the influence of the dielectric constant of the pressure medium. At the end of this chapter, a short overview of magnetization measurements and other measurement techniques, the results of which are presented in this work, will be given.

Chapter 4 presents an overview of the properties of organic charge-transfer salts with focus on the family of quasi-two-dimensional $\kappa$-(BEDT-TTF)$_2X$ salts. Structural properties as well as physical properties, such as the generalized temperature-pressure phase diagram, will be discussed to underline their role as model systems for the study of strongly correlated electron systems.

Chapter 5 represents the main chapter of this work, in which the universal behavior of the Mott critical endpoint will be discussed in great detail. The chapter starts with a review on existing literature results on the Mott critical behavior. After that, the result of

thermal expansion measurements, obtained in the present work, aiming at the investigation of electron lattice coupling at the Mott transition, are presented. The chapter closes with two preliminary data sets on two future research directions, which arose during this work, namely a comparison between thermodynamic and transport studies of the metal-insulator transition and the effects of disorder on the Mott transition.

Chapter 6 gives a very short introduction to the controversially discussed topic of ferroelectricity in these $\kappa$-phase organic charge-transfer salts. In addition, an experimental study of the dielectric and magnetic properties of various single crystals of $\kappa$-(BEDT-TTF)$_2$Cu[N(CN)$_2$]Cl is presented.

Chapter 7 discusses the thermodynamic properties of another salt of the $\kappa$-(BEDT-TTF)$_2X$ family, namely $\kappa$-(BEDT-TTF)$_2$Hg(SCN)$_2$Cl. Interestingly, this material shows a charge-order metal-insulator transition [34] instead of a Mott transition, as it is situated closer to the case of a quarter-filled conduction band. Thus, it shows the prerequisite to reveal a ferroelectric polarization making it an interesting material for gaining more insight into this property in the $\kappa$-phase salts. To this end, transport, i.e., resistance and dielectric, properties, as well as thermodynamic properties, i.e., thermal expansion and specific heat, will be discussed which aim at understanding the intriguing interplay of charge, spin and lattice degrees of freedom at this charge-order transition.

Chapter 8 concludes the thesis and points out directions for further research aspects that came to light during this work.

# 2. Basic Theory

In this chapter, a definition of the basic thermodynamic properties that are studied in the present work, namely the thermal expansion and the magnetization, as well as an introduction to phase transitions are given. The main focus here lies on the concept of universality, which will play a major role throughout the thesis. Afterwards, a special phase transition, namely the metal-insulator transition, and the basic mechanisms to drive these phase transitions will be discussed. This explication will be complemented by a short introduction of magnetic properties of systems close to such a metal-insulator transition. In the end, a short introduction to the basics of elasticity theory will be given to demonstrate how lattice degrees of freedom in a solid are treated.

## 2.1. Thermodynamic quantities and relations

### 2.1.1. Thermal expansion coefficient

The thermal expansion coefficient $\alpha$ describes the change of the length $L$ of a material upon changing the temperature $T$ at constant pressure $P$. These length changes originate in the anharmonicity of the underlying crystal potential [37]. In principle, the thermal expansion coefficient can be determined along all three crystallographic axes of the system. It is defined by

$$\alpha_i(T) = \frac{1}{L_i(T)} \left( \frac{\partial L_i(T)}{\partial T} \right)_P , \tag{2.1}$$

with $i = a, b, c$ being one of the crystallographic directions of a crystal. Similarly, one can define the volumetric expansion coefficient $\beta$ which describes changes of the volume $V$ as a function of temperature at constant pressure,

$$\beta(T) = \frac{1}{V(T)} \left( \frac{\partial V(T)}{\partial T} \right)_P . \tag{2.2}$$

In case of a crystal system with three orthogonal crystal axes, this gives $\beta(T) = \alpha_a(T) + \alpha_b(T) + \alpha_c(T)$.

The length of a material can also vary upon applying pressure on the material. This effect is accounted for by the isothermal compressibility $\kappa_T$

$$\kappa_T = -\frac{1}{V}\left(\frac{\partial V}{\partial P}\right)_T. \tag{2.3}$$

All of these quantities are thermodynamic quantities and can therefore be derived from thermodynamic potentials, e.g., the free energy $\mathcal{F}$,

$$\mathrm{d}\mathcal{F} = -S\mathrm{d}T - P\mathrm{d}V \tag{2.4}$$

with $S$ being the entropy. The volumetric expansion coefficient $\beta$ can be rewritten in terms of the free energy as follows

$$\begin{aligned}
\beta(T) &= -\kappa_T \frac{\partial^2 \mathcal{F}}{\partial V \partial T} && (2.5)\\
&= \kappa_T \left(\frac{\partial S}{\partial V}\right)_T && (2.6)\\
&= -\frac{1}{V}\left(\frac{\partial S}{\partial P}\right)_T. && (2.7)
\end{aligned}$$

The volumetric expansion coefficient therefore depends on the pressure derivative of the entropy. In contrast, the specific heat $C_P$ describes the temperature derivative of the entropy,

$$C_P(T) = T\left(\frac{\partial S}{\partial T}\right)_P. \tag{2.8}$$

In order to compare the temperature dependencies of the volumetric expansion coefficient and the specific heat, it is useful to evaluate their ratio

$$\begin{aligned}
\frac{\beta(T)}{C(T)} &= -\frac{1}{V\cdot T}\frac{\left(\frac{\partial S}{\partial P}\right)_T}{\left(\frac{\partial S}{\partial T}\right)_P} && (2.9)\\
&= \frac{1}{V\cdot T}\left(\frac{\partial T}{\partial P}\right)_S && (2.10)\\
&= \frac{-\kappa_T}{V}\left(\frac{\partial \ln T}{\partial \ln V}\right)_S. && (2.11)
\end{aligned}$$

It turns out that the ratio is governed by the compressibility and by the so-called Grüneisen parameter $\Gamma$ which is defined as

$$\Gamma := -\left(\frac{\partial \ln T}{\partial \ln V}\right)_S . \tag{2.12}$$

$\Gamma$ measures the volume dependence of a characteristic temperature or frequency in a system, be it of phononic, magnetic or electronic origin[1]. As the volume dependence of the characteristic frequencies arises from the anharmonicity of the crystal potential, i.e., higher-order terms in the potential beyond the harmonic approximation, the Grüneisen ratio is often used as a measure of the anharmonicity of the lattice [37]. It is worth noting that in many cases the compressibility as well as the Grüneisen ratio show only a weak temperature dependence, so that each contribution to the thermal expansion (phononic, magnetic etc.) shows the same temperature dependence as the respective contribution to the specific heat. This correspondence can be used, e.g., for the determination of the phononic background to the thermal expansion, as there are several theoretical approaches available to model the phononic specific heat (Debye and Einstein models; see Sec. 7.2 for an application of these models) or even an experimental determination of the phonon contribution to specific heat may be available. A breakdown of this scaling can be found at critical endpoints, e.g., at quantum critical points [38] as well as finite-temperature critical endpoints [20][2]. The latter case will be the main topic of chapter 5 and will be discussed there in detail.

### 2.1.2. Magnetization and susceptibility

The magnetization $\vec{M}$ specifies the amount of magnetic dipole moments $\vec{m}$ per volume:

$$\vec{M} = \frac{\mathrm{d}\vec{m}}{\mathrm{d}V}. \tag{2.13}$$

The magnetic susceptibility $\chi$ describes the derivative of the magnetization with respect to the field[3] $\vec{H}$,

$$\chi = \left(\frac{\mathrm{d}\vec{M}}{\mathrm{d}\vec{H}}\right)_T . \tag{2.14}$$

[1] In general, the Grüneisen parameter has to be defined independently for every characteristic temperature.

[2] This becomes evident when looking at eq. 2.9 into which the derivatives of the entropy with respect to $P$ as well as to $T$ enter. At a line of second-order transitions, $T$ and $P$ are related to each other and thus, the derivatives of the entropy contribute similarly to $\Gamma$ and cancel each other out. However, at a critical end point, $T$ and $P$ are independent variables so that the derivative with respect to $P$ is unequal to the one with respect to $T$ [20].

[3] In literature, the magnetic field $\vec{H}$ and the magnetic induction $\vec{B}$ are often used synonymously, even if they are not equal to each other.

## 2.2. Thermodynamics of phase transitions

Thermodynamics describes the macroscopic properties of large assemblies of interacting particles resulting from their collective behavior in thermal equilibrium. By variation of external parameters, such as the pressure $P$, the temperature $T$, magnetic field $\vec{B}$, a change from one stable phase A to another stable phase B can occur, a so-called *phase transition* [39, 40]. Phase transitions are phenomena known from everyday life: The evaporation of water represents one well-known example of phase transitions. To understand the underlying collective behavior and the principles, which lead to various kinds of ordered phases, is a fundamental task in solid state research.

The classification of phase transitions was established by Paul Ehrenfest in 1933 and relies on derivatives of the Gibbs free energy $\mathcal{G}$, which corresponds to one of the thermodynamic potentials. The total differential of the Gibbs free energy is given by

$$\mathrm{d}\mathcal{G} = -S\mathrm{d}T + V\mathrm{d}P - m\mathrm{d}B. \tag{2.15}$$

Within this classification, a phase transition is of $n^{th}$ order, when the $n^{th}$ derivative of $\mathcal{G}$ with respect to $T$, $P$ or $B$ is discontinuous but the $(n-1)^{th}$ is still continuous[4] [39,40]. When discussing phase diagrams of real systems (see, e.g., Fig. 2.1), predominantly phase transitions of first- and second-order are observed. A first-order transition shows a discontinuity in the first derivative of the Gibbs free energy, e.g., in the entropy and the volume, and are therefore sometimes referred to as *discontinuous transitions*. Hysteretic behavior is characteristic for such kind of a transition, as it involves a finite latent heat $\Delta Q \propto \Delta S$. Within phase diagrams, first-order phase transition lines represent coexistence lines, indicating that there is a macroscopic coexistence of the two phases at the transition point. In contrast, second-order phase transitions (or *continuous phase transitions*) show a divergence of the second derivative of $\mathcal{G}$, such as the specific heat $C$, at the transition point, the so-called critical point, without any hysteresis. Distinct points in a phase diagram are the second-order critical endpoints of first-order transition lines, above which the two phases become indistinguishable [39, 40]. The existence of such points allows, in turn, the transformation of a substance from one phase to another in a smooth manner without undergoing a phase transition.

With the help of thermodynamic potentials and distinct properties of first- and second-order phase transitions, pressure dependencies of the phase transition line $T_0(P)$ can be

[4] The Ehrenfest classification is widely used nowadays even though it was criticized as the specific heat at a second-order phase transition does not necessarily show a discontinuity, but in many cases a divergence. A superconductor, e.g., shows a discontinuity in specific heat, as described by classical theories as the mean-field theory, whereas, e.g., the susceptibility in a magnetic system diverges at the transition temperature. In literature, therefore, the terms *continuous* and *discontinuous* phase transitions are more frequently used, which describe whether a latent heat accompanies the transition or not.

derived. In case of a first-order transition, the Clausius-Clapeyron equation relates the pressure dependency of the transition temperature to the change of volume and entropy across the phase transition [39, 40],

$$\frac{\mathrm{d}T_0}{\mathrm{d}P} = \frac{\Delta V}{\Delta S}. \tag{2.16}$$

For second-order phase transitions the pressure dependence is given by the Ehrenfest equation and reads as follows,

$$\frac{\mathrm{d}T_0}{\mathrm{d}P} = V_{mol} T_0 \frac{\Delta \beta}{\Delta C_P}. \tag{2.17}$$

In general, a phase transition is governed by two competing contributions to the system's free energy $\mathcal{F} = \mathcal{U} - TS$: Whereas the tendency to order is driven by the minimization of the internal energy $\mathcal{U}$, thermal fluctuations[5] favor a high entropy $S$, i.e., a high degree of disorder. Many phase transition are thus described as a spontaneous symmetry breaking of the underlying symmetry of the system in the ordered state, as, e.g., translational or rotational symmetries. For the description of the behavior of physical quantities close to a phase transition, it is reasonable to introduce a so-called order parameter $\langle \phi \rangle$[6] which measures the degree of order in a system. It is zero in the high-temperature disordered state, but finite in the low-temperature ordered state. In most of the cases, the order parameter can be associated with a measurable physical quantity related to the phase transition. In the following, a few examples for phase transitions and their respective order parameter are given [41–43]:

- Liquid gas-transition: Density $\rho - \rho_c$
- Ferromagnet: Magnetization $\vec{M}$
- Superconductor: Superconducting gap $\Delta$

However, it is not always easy to identify the order parameter of a phase transition, i.e., a parameter that is zero in the high-temperature disordered phase and finite in the low-temperature ordered phase. This is indeed the case for the Mott metal-insulator transition [43] which will be discussed in great detail in chapter 5.

[5] In the case of quantum phase transitions, i.e., transitions which take place at $T = 0\,\mathrm{K}$, quantum fluctuations instead of thermal fluctuations are of importance. However, these types of transitions are not in the focus of the present work and will therefore not be considered in the following paragraphs about critical behavior.

[6] $\langle . \rangle$ refers to the thermodynamic average over space and time.

### 2.2.1. Critical phenomena and universality

In the following, the discussion will be restricted to the behavior of continuous phase transitions, as experimental as well as theoretical works showed that they obey universal behavior, i.e., a generic behavior independent of microscopic details of the system [40,41,44]. They are therefore prime examples to study collective properties arising from interacting particles. This is in contrast to first-order phase transitions, the properties of which usually depend on microscopic details of the system.

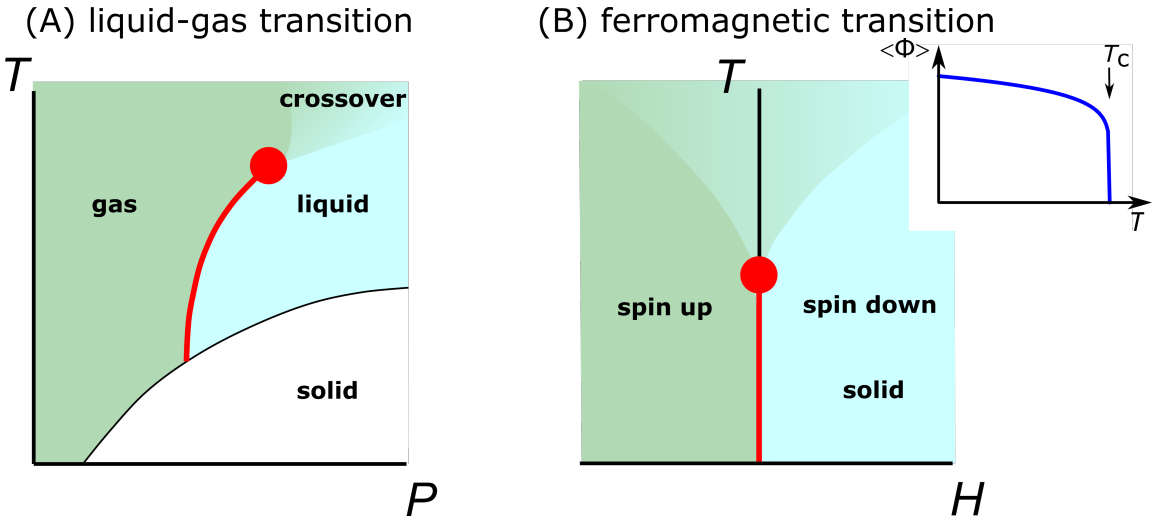


Figure 2.1.: Phase diagram of the liquid-gas transition as a function of pressure $P$ (A) and the ferromagnetic transition in the Ising model as a function of the magnetic field $H$ (B). The thick red line corresponds to a line of first-order transitions which ends in a second-order (continuous) critical endpoint, indicated by the red circle at $(T_c, P_c)$ (A) and at $(T_c, H_c = 0)$ (B) . Above the critical endpoint the two phases are indistinguishable, i.e., only a crossover behavior can be observed. Around the critical endpoint, fluctuations dominate the physical properties. As an example, in the inset, the temperature dependence of the order parameter $\langle\phi\rangle$, which is the density difference (A) and the magnetization (B), below the critical endpoint is shown which follows a power-law dependence, $\langle\phi\rangle \propto (-t)^\beta = ((T_c - T)/T_c)^\beta$, as a function of the reduced temperature $t$ with the same exponent $\beta$.

The idea of universal behavior of physical quantities close to a second-order critical point was stimulated by the observation of similarities of phase diagrams for different systems. Famous examples are the similarities between the liquid-gas transition (see Fig. 2.1 (A)) and the ferromagnetic transition in the Ising model (see Fig. 2.1 (B)) around the continuous critical endpoint of first-order transitions located at $T = T_c$. Here, the liquid and the gaseous phase can be related to the spin-up and spin-down phase in the ferromagnet. Not only are the phase diagrams strikingly similar, but also the systems were found to behave similarly close to the phase transition, i.e., physical quantities depend in the same way on external parameters. In general, a physical quantity $F$ close to a second-order phase tran-

sition shows power-law behavior with the reduced temperature $t = \frac{T-T_c}{T_c}$ and an exponent $\lambda$ [40, 41],

$$F(t) \sim |t|^{\lambda} \text{ with } t = \frac{T - T_c}{T_c}. \tag{2.18}$$

The exponent $\lambda$ is called the critical exponent which characterizes the critical behavior.

$$\lambda = \lim_{t \to 0} \frac{\ln |F(t)|}{\ln |t|}. \tag{2.19}$$

The central question is why different systems with different microscopic interactions behave so similarly upon approaching the critical point. Upon approaching the critical point, even if the average of the order parameter $\langle \phi \rangle$ is zero, fluctuations are no longer negligible and spatial correlations of the order parameter on the length scale $\xi$ are present, i.e., $\langle \phi(\vec{r})\phi(\vec{r'}) \rangle - \langle \phi(\vec{r}) \rangle \langle \phi(\vec{r'}) \rangle \propto \exp\left(\frac{-|\vec{r}-\vec{r'}|}{\xi}\right)$. This correlation length $\xi$ diverges upon approaching the critical point and becomes the only relevant length scale in the system. It therefore dominates over microscopic details of the system, as, e.g., the lattice structure or the microscopic interaction, and only general characteristics, such as the dimension or the symmetry, are important. This allows for a categorization of different phase transitions according to their critical behavior into a few known *universality classes* [40, 41, 44]. The identification of the universality class is thus an important tool to classify the collective behavior of any many-body system close to a phase transition.

In order to fully characterize the critical behavior and to assign it to a certain universality class, four different critical exponents are important, which are denoted as $\alpha$, $\beta$, $\gamma$ and $\delta$. They can be extracted experimentally from the behavior of different physical quantities close to the critical point, such as the specific heat, measurements of the order parameter as a function of temperature $t$, or isothermal measurements of the order parameter as a function of the respective field[7] $h$. In Table 2.1 the definition of the different critical exponents, the respective physical quantity, and the corresponding power-law are given [40, 41, 44]. The power-law dependence for the magnetization is exemplarily shown in the inset of Fig. 2.1.

As all of these quantities are related to thermodynamic potentials, these exponents are not fully independent from each other, but related by *scaling relations*[8],

[7] For magnetic transitions, the field $h$ corresponds to the reduced magnetic field $h = \frac{H-H_c}{H_c}$. In the case of the liquid-gas transition, the field can be associated with the reduced pressure $h = \frac{P-P_c}{P_c}$. As will be discussed in detail later, in case of the Mott critical endpoint the pressure (*strain*) acts as the symmetry-breaking field.

[8] These relations can be understood following the scaling hypothesis of the free energy, which will be introduced later.

| Exponent | Description | Definition |
|---|---|---|
| $\alpha$ | specific heat exponent | $C(t) \sim \lvert t\rvert^{-\alpha}$ |
| $\beta$ | order parameter exponent | $\langle\phi\rangle(t) \sim M(t) \sim \lvert -t\rvert^{\beta}, t < 0$ |
| $\gamma$ | susceptibility exponent | $\chi(t) \sim \lvert t\rvert^{-\gamma}, t > 0$ |
| $\delta$ | isothermal field exponent | $M(h) \sim \lvert h\rvert^{1/\delta}$ |
| $\nu$ | correlation length exponent | $\xi(t) \sim \lvert t\rvert^{-\nu}$ |

Table 2.1.: Definition of the most important critical exponents $\alpha$, $\beta$, $\gamma$, $\delta$ and $\nu$: $C$ refers to the specific heat, $\langle\phi\rangle$ to the order parameter, $\chi$ to the susceptibility (in a magnetic system; in case of the liquid-gas transition an analogous definition of the compressibility is applicable), $M$ to the magnetization (or analogously to the density difference), $\xi$ to the correlation length. $t$ represents the reduced temperature and $h$ the reduced field (or pressure). Note that not all of these exponents are independent from each other.

$$\gamma = \beta(\delta - 1) \tag{2.20}$$

$$\text{and } \alpha + 2\beta + \gamma = 2. \tag{2.21}$$

It follows that the knowledge of two exponents, such as $\beta$ and $\delta$, is sufficient to extract the other critical exponents [40, 41, 44].

In table 2.2 theoretical values for these exponents are listed for various universality classes [40, 41, 44]. The universality classes correspond to critical points that differ with respect to the symmetry of the order parameter, the dimensionality of the system (1D, 2D or 3D) or the interaction range (short- or long-ranged). The mean-field model is a comparably simple model to describe phase transitions, as it assumes that every particle is exposed to an average field created by the other particles, thereby reducing a many-body-problem to an effective one-particle-problem. This model describes well the thermodynamic behavior far away from the critical point, where fluctuations are naturally small. It is often referred to as *trivial* behavior. In contrast, the other universality classes feature *non-trivial* critical behavior depending on the dimensionality of the order parameter: The Ising model describes critical points the order parameter of which is one-dimensional, i.e., a scalar. The applicability of the mean-field and Ising universality classes to the Mott critical endpoint will be in the focus of this thesis and therefore will be introduced in more detail below. The XY and Heisenberg universality classes represent models with two-dimensional and three-dimensional order parameters. All of these universality classes are known for a long time and were studied intensively [40, 41, 44]. Surprisingly, a new universality class, not known before, was claimed recently based on the analysis of conductance data around the Mott endpoint [18]. The exponents derived there were found to fulfill the scaling relations. These exponents are included in the table in 2.2 as *unconventional criticality* and will be introduced later in chapter 5 in great detail.

| **Model** | $\alpha$ | $\beta$ | $\gamma$ | $\delta$ |
|---|---|---|---|---|
| Mean field (MF) | $0_{dis}$ | 0.5 | 1 | 3 |
| 2D-Ising | $0_{log}$ | 0.125 | 1.75 | 15 |
| 3D-Ising | 0.11 | 0.325 | 1.24 | 4.82 |
| 3D-XY | -0.015 | 0.35 | 1.3 | 4.8 |
| 3D-Heisenberg | -0.115 | 0.365 | 1.24 | 4.82 |
| *unconcentional criticality* [18] | -1 | 1 | 1 | 2 |

Table 2.2.: Critical exponents $\alpha$, $\beta$, $\gamma$, $\delta$ for different universality classes [45]. $0_{dis}$ refers to a discontinuity in the specific heat, whereas $0_{log}$ describes a logarithmic divergence of the specific heat. 2D and 3D refer to the dimensionality of the system.

Before continuing to discuss different models quantitatively, the concept of scaling and scale invariance will be reviewed in more detail with focus on the scale-invariant form of the free energy. At the phase transition not only the correlation length diverges, but also the correlation time, implying that fluctuations occur on all length and time scales. As proposed by L. Kadanoff [10] and B. Widom [11] and later on treated by renormalization group theory, the singular part of the free energy is as a consequence scale invariant[9] close to the critical point [40, 41, 44], i.e., the system's properties look similar independent of the length scale one looks at (*scaling hypothesis*) [43]. The free energy $\mathcal{F}$ can therefore be rewritten as a function of only one parameter, which rescales the external parameters $t$ and $h$ into a single parameter $\frac{h}{|t|^{\delta\beta}}$, and follows a homogeneous function,

$$\mathcal{F}(t,h) = |t|^{\beta}\mathcal{F}_{\pm}\left(\frac{h}{|t|^{\delta\beta}}\right), \tag{2.22}$$

where $\mathcal{F}_{\pm}(x)$ represent unique scaling functions. Correspondingly, all the derivatives of the free energy show scaling behavior. It follows that by a proper rescaling of any experimental data, such as the volume, i.e., by the choice of the right critical exponents, the data set over a wide $t$-$h$-range should fall onto these two functions. This concept is called the *scaling collapse* and is important for the unambiguous determination of the critical exponents and the universality class. Conversely, given that these functions are known, all thermodynamic properties in a wide $t$-$h$-range around the critical endpoint can be calculated by the respective derivative of the free energy. Unfortunately, this function is not analytically determinable for all universality classes. However, these scaling functions are known numerically for the mean-field universality class, as well as for the 2D-Ising model and allow for a calculation of the thermal expansion coefficient, which is the quantity of interest in the present thesis.

[9] It is worthwhile to note that power laws are the only scale-invariant dependencies known. Therefore the physical properties are characterized by the power laws close to the critical endpoint, as defined in eq. 2.18 and Tab. 2.1 [43].

A first phenomenological approach to describe thermodynamic properties quantitatively close to a continuous phase transition, was developed by L. Landau [46]. He proposed that the free energy is non-singular and can be expanded in a power series in the order parameter, as the latter is small close to the critical point. Here, the equilibrium order parameter $\langle\phi\rangle_{eq}$ minimizes the free energy with respect to the order parameter. As this approach relies on a spatially homogeneous order parameter, $\phi(\vec{r}) = \phi$, Landau theory is actually a *mean-field theory* which is exact only in a regime where fluctuations are small. The limitation of this approach, known as the *Ginzburg-criterion*, will be discussed later on.

In the absence of an external field, the expansion of the free energy up to $4^{th}$ order in the order parameter[10] $\phi$ with three free parameters $F_0$, $r$ and $u$ is given by

$$\mathcal{F}(r,\phi) = \mathcal{F}_0 + \frac{r}{2}\phi^2 + u\phi^4. \tag{2.23}$$

This expansion includes only even powers in $\phi$ to retain the symmetry of the problem, i.e., that the high-temperature phase is invariant under the transformation $\phi \leftrightarrow -\phi$. Minimization of this potential leads to two different solutions, separated at $r = 0$,

$$\langle\phi\rangle_{eq} = \begin{cases} 0, r \geq 0, & \text{disordered state} \\ \pm\sqrt{-r/u}, r < 0, & \text{ordered state.} \end{cases} \tag{2.24}$$

The parameter $r$ is therefore related to the thermal tuning parameter $t = (T - T_c)/T_c$ and can be rewritten up to the lowest non-vanishing order as $r = at = a(T - T_c)/T_c$. For stability reasons, a positive $u > 0$ is required. The equilibrium solution for $T < T_c$ shows a square-root dependence $\langle\phi\rangle_{eq} \propto (-t)^{1/2}$, yielding the critical exponent $\beta = 1/2$, which represents the $\beta$-exponent for the mean-field universality class. A field $h$ couples linearly to the order parameter and therefore enters as an odd power of the order parameter,

$$\mathcal{F}(r,h,\phi) = \mathcal{F}_0 + \frac{r}{2}\phi^2 + u\phi^4 - \phi h. \tag{2.25}$$

Minimization of this potential leads to the following solution, which is presented here in the scale-invariant form, and reflects all the critical exponents of the mean-field universality class:

$$\langle\phi\rangle_{eq} = -\frac{\text{sign}(h)|h|^{1/3}}{u^{1/3}}\Psi\left(\frac{r}{u^{1/3}|h|^{2/3}}\right) \tag{2.26}$$

$$\text{with } -1 + x\Psi(x) + \Psi^3(x) = 0. \tag{2.27}$$

[10] The following equations present a mean-field theory of a scalar order parameter.

This potential is capable of describing all relevant aspects of the phase diagram (Fig. 2.1): A line of first-order transitions can be found at $h = 0$ for $T \leq T_c$, corresponding to the two (metastable) solutions in equation 2.24 for $r < 0$. In case of a finite, but small, symmetry breaking field $h$, one stable and one metastable minimum can be found, which is characteristic of the coexistence region. For large $h$, there is only one minimal solution left, as the metastable solution disappears. Correspondingly, as the symmetry is broken by the external field, no thermal phase transition occurs at finite $h$ [43].

However, spatial correlations, which are not included in Landau's original approach, are of relevance close to the phase transitions, since thermodynamic quantities diverge upon approaching the critical point. Surprisingly, the Landau theory can predict diverging thermodynamic quantities even though it neglects fluctuations. Thus it can predict its own failure [43]. The validity of this approach can be tested in the framework of an extended Landau-theory (called *Ginzburg-Landau-theory*), in which the homogeneous order parameter is replaced by a spatially varying order parameter $\phi \rightarrow \phi(\vec{r})$ [40]. The power-series expansion then reads as follows, including a gradient term of the order parameter with respect to the spatial coordinate $\vec{r}$ and prefactor $\xi_0$:

$$\mathcal{F}(r, h, \phi(\vec{r})) = \mathcal{F}_0 + \frac{r}{2}\phi(\vec{r})^2 + \frac{u}{4}\phi(\vec{r})^4 + \xi_0^2(\vec{\nabla}_{\vec{r}}\phi(\vec{r}))^2 - \phi(\vec{r})h. \tag{2.28}$$

Landau theory is only valid if the deviations of the order parameter from its average value are much smaller than the order parameter itself,

$$\langle(\phi(\vec{r}) - \langle\phi\rangle_{eq})^2\rangle \ll \langle\phi\rangle_{eq}^2. \tag{2.29}$$

Evaluating these equations leads to the so-called *Ginzburg criterion*

$$\frac{2u}{\xi_0^{d/2}} k_B T_c |2r|^{d/2-2}\big|_{r\rightarrow 0} \ll 1. \tag{2.30}$$

This criterion is strictly fulfilled only for dimensions $d > 4$ , the so-called upper critical dimension, making Landau theory in those cases exact. In contrast, it necessarily breaks down in lower dimensions very close to the critical point giving rise to non-trivial critical exponents in the immediate vicinity of the critical point [40]. Details of the breakdown depend on the non-universal prefactors in the free energy and thus depend on the investigated system. It turns out that, for example at the superfluid transition, the critical regime should be experimentally accessible, whereas at the superconducting transition[11] the system obeys

[11] Here, mainly conventional superconductors with a large correlation length $\xi$ are considered.

mean-field critical behavior within the complete experimentally accessible regime due to the large correlation length of the electrons forming a Cooper pair[12].

Mean-field models were successfully applied in the description of paramagnets or van-der-Waals gases [40]. A model that attracted enormous interest, as it is analytically solvable in one and two dimensions and features non-trivial critical behavior, is the Ising model. The critical properties around the critical endpoint for the ferromagnetic transition, as well as the liquid-gas transition, belong to the Ising universality class. The Ising model is a spin-model, in which the spin $S_i$ on position $i$ on a periodic lattice can point either up or down, giving rise to a scalar order parameter. These spins interact only with their nearest neighbors via an isotropic interaction energy $J$. The resulting Hamiltonian $\mathcal{H}$ then reads as follows,

$$\mathcal{H} = -J \sum_{i,j} S_i S_j - H \sum_{i=1}^{N} S_i. \tag{2.31}$$

Even if the interaction is short-ranged in this model, the model can account for a long-range magnetic-ordering transition in two and three dimensions, with a continuous critical point. Notably, the specific heat in this model does not show a power-law divergence, but rather a logarithmic divergence. This results in corrections to the formulation of the scale-invariant form of the free energy, which is denoted in the following for the 2D-Ising universality class [20, 47]:

$$\mathcal{F}(t,h) = \frac{t^2}{8\pi} \ln t^2 + |h|^{2/y_h} \mathcal{F}_{\pm}(t/|h|^{y_t/y_h}) \tag{2.32}$$

with $y_t = 1$ and $y_h = 15/8$.

In summary, the remarks above outline why the determination of the critical behavior is such a powerful tool in understanding a phase transition. In chapter 5, the investigation of the universal properties around the Mott transition (see Sec. 2.4) will be discussed in order to identify and understand the relevant parameters governing the phase transition.

## 2.3. Glass-like behavior

The previous considerations on phase transitions were all based by assuming thermodynamic equilibrium. To study such equilibrium properties by an experiment, the observation time $t$ must be much larger than the system's relaxation time $\tau$, $t \gg \tau$. The situation is different

[12] An estimation of the Ginzburg radius, i.e., the distance to the critical point in which non-trivial fluctuations dominate, is often desired. However, its estimation from the experimental side is generally a difficult task, as usually not all parameters from the free energy are known.

for *glass transitions* in which the relaxation of a system, e.g., via its structural degrees of freedom, slows down dramatically, implying a rising $\tau$. Eventually, the relaxation time $\tau$ may reach a value of the same order of magnitude as the observation time $t$. Hence, the thermodynamic equilibrium cannot be reached and a metastable state with short-range order is frozen around the glass transition at $T_g$.

Thermodynamic probes, such as measurements of the thermal expansion coefficient $\alpha$ [13,48], are suitable tools to discriminate glass transitions from thermodynamic transitions. The characteristic properties of a glass transition are an increase of $\alpha(T)$ above $T_g$, a cooling-rate dependency and a pronounced hysteresis upon warming and cooling through $T_g$. In a simple model, glass transitions can be described qualitatively by a two-level process [48,49] with energies $E_1$ and $E_2 = E_1 + 2\Delta E$ which are separated by an activation barrier of energy $E_A$. The relaxation time of the system is expected to be governed by a thermally-activated process in the following manner

$$\tau(T) = \nu_0^{-1} \exp\left(\frac{E_A}{k_B T}\right), \tag{2.33}$$

with $\nu_0$ being a characteristic frequency. The definition of the glass-transition temperature itself relies on the criterion $-|q| \cdot \frac{\mathrm{d}\tau}{\mathrm{d}T}|_{T_g} \approx 1$ with the cooling-rate $q = \frac{\mathrm{d}T}{\mathrm{d}t}$. It corresponds to the temperature at which $t$ and $\tau$ become comparable in size. Therefore an investigation of the cooling-rate dependency of $T_g$ allows for an estimation of the activation energy $E_A$ of such a relaxation process,

$$\ln|q| = -\frac{E_A}{k_B} \cdot T_g^{-1} + \text{const.} \tag{2.34}$$

In organic-charge transfer salts, glass-like freezing of structural entities is often observed, if those entities can adopt two different configurations [13] (see chapter 4 for more details). As these motions are frozen in below $T_g$ and experimental observation times are limited, a residual disorder at low temperatures is always present. In Sec. 7.3, the glass transition of the organic charge-transfer salt $\kappa$-(BEDT-TTF)$_2$Hg(SCN)$_2$Cl will be investigated to extract the activation energy. This, in turn, can be compared with recent calculations [50] on the energies of the various structural configurations, and can provide further insight into this field.

## 2.4. Ground states in strongly correlated electron systems

Strongly correlated electron systems, in general, offer a wide range of different ground states, which are dominated by the interplay of charge, spin and lattice degrees of freedom. Prime examples of such systems are organic charge-transfer salts [12, 13]. Of particular interest

is the Mott metal-insulator transition [7] in which, by increasing the strength of electronic interactions, a transition from a conducting to an insulating state can be observed. The Mott transition is the key for understanding the various intriguing states including unconventional high-temperature superconductivity [1–3], spin-liquid phases [35,36] or multiferroic phases [4,5]. In the following, various aspects of metallic and insulating behavior in solids will be introduced. Especially, an overview of the physics of the correlation-driven Mott transition will be given, the properties of which are in the focus of the present work. These properties will be contrasted with other types of insulators, namely the band insulator, the Peierls insulator and the Anderson insulator.

### 2.4.1. Metallic and insulating behavior of solids

The electronic properties of solids are, in general, determined by the Coulomb interactions between all constituents, i.e., electrons and atoms. The systems are described by a quantum-mechanical Hamiltonian containing kinetic energy terms, for each the electrons and the nuclei, as well as Coulomb interaction terms that account for electron-nuclei interactions, nuclei-nuclei interactions and electron-electron interactions. The Schrödinger equation for this problem is commonly not solvable due to the large number of interacting particles ($N \approx 10^{23}$). A first approach for solving the problem is to map the many-body problem onto an effective one-particle problem by considering one electron in a periodic potential created by the lattice sites [51].

This simplified model, which neglects the interaction among the electrons and ignores the motion of the crystal atoms, is able to answer the question why materials are insulating, while others are conducting [52, 53]. In contrast to free electrons, for which all energy levels are allowed, there are constraints in the presence of a periodic lattice, giving rise to the formation of bands. Due to the periodic boundary conditions, each band contains a discrete number of states, namely $2N$ with $N$ being the number of unit cells in the crystal. As electrons are fermions, it follows, that only one electron can occupy a given state which is characterized by the momentum $\vec{k}$, the band index and the spin number. For the electrical properties, the highest occupied band and the respective Fermi energy is of importance [37]. In case of a partially filled highest band, electrons can easily scatter into different states upon the application of an external field, thereby causing an electrical current. In contrast, if the highest occupied band is completely filled, there are no empty states available and therefore no electrical current can pass through the crystal. However, as we will discuss in the case of the Mott insulator [7], in which electron-electron interactions are of fundamental importance, a partially filled conduction band is not sufficient to obtain a metallic ground state.

Approaches to calculate the band structure in solid-state physics are particularly well understood in the following two limits [37]. The first approach treats delocalized, nearly free electrons, in which the lattice potential acts only as a small perturbation. In this limit, the electrons are well described by their wave-like character. In contrast, the second approach deals with the opposite case of strongly localized electrons residing in their atomic orbitals, i.e., a description which emphasizes the particle character. This ansatz is called the *tight binding*-approach and provides a starting point which is well suited for the description of the band structure of the organic charge-transfer salts due to the relatively large size of the organic molecules and weak overlaps of wave functions between neighboring sites. Within this framework, the band structure is gained by a linear superposition of the wave functions of the isolated atoms or molecules in which the corrections to the atomic potentials in forming the lattice potential are assumed to be small. As a result, an energy $\propto W$ can be gained while forming the crystal. This results in a larger bandwidth $W$ as larger the overlap is.

However, the theoretical description becomes distinctly more difficult for strongly correlated electron systems, where the dominating electron-electron interactions are of the order of the kinetic energy itself. This situation is often found in systems with narrow bandwidth and small charge carrier density. These systems do not necessarily fall into one of the above-mentioned limits and the challenge from a theoretical viewpoint is an accurate, simultaneous description of the itinerant as well as the localized character of the electrons [54]. The prime example for studying such effects arising from strong correlations is the Mott transition [9]. In the following, the Mott insulator, which goes beyond the conventional single-particle band picture, will be introduced.

#### Mott insulator

In the 1930's, transport studies on many transition-metal oxides showed that these materials are bad metals or insulators even though they have partially filled $d$ bands [8]. This observation was in conflict with the simplified single-particle picture, presented above. In subsequent theoretical works, following ideas from R. Peierls, N.F. Mott argued that strong electron-electron correlations would be responsible for the insulating ground state [6, 7, 55–57]. He considered a lattice model with a single electronic orbital on each site, in which electrons, which sit on the same site, would feel a strong Coulomb repulsion $U$. As a consequence, the conduction band would split into two bands, a lower one formed by electrons that occupy an empty site and an upper one by electrons that occupy a site which is already taken by another electron. In half-filled systems, the lower band would be fully occupied and the upper band empty. Since for a large enough $U$ a gap opens between these two bands of the order of $U$, the material is an insulator, the so-called *Mott insulator*. The

underlying idea is based on the screening of charge carriers: Whereas in an ordinary metal with high electron densities the quasi-free electron cloud screens the atomic potential very efficiently, giving rise to rather loosely bound valence electrons, such screening effects are less pronounced in materials with low electron density favoring a localization of the charge carriers to minimize their energy.

The discovery of the Mott transition initiated a long and intensive research on strongly correlated electron systems from both experimental as well as theoretical points of view (see, e.g., [9, 58–60] for reviews). Points of particular interest include how to control and model the properties of such a system, i.e., by means of which control parameters a *metal-insulator transition* (MIT) can be induced, and what are the properties on either side of the transition. A seemingly simple theoretical model accounting for this problem is the *Hubbard model* [61–65], which takes into account electrons only from a single orbital. Its Hamiltonian reads in the notation of second quantization, as follows,

$$\begin{aligned} \mathcal{H} &= \mathcal{H}_t + \mathcal{H}_U && (2.35)\\ &= t \sum_{\langle i,j\rangle,\sigma} (c^\dagger_{i,\sigma} c_{j,\sigma} + \text{h.c.}) + \sum_i U n_{i,\uparrow} n_{i,\downarrow} && (2.36)\\ \text{with } n_{i,\sigma} &= c^\dagger_{i,\sigma} c_{i,\sigma}, && (2.37) \end{aligned}$$

where $i, j$ are the lattice site indices, $\langle ij\rangle$ is the summation over nearest neighbors and $\sigma = (\uparrow, \downarrow)$ the spin of the electron. The kinetic term $\mathcal{H}_t$ is given by the hopping energy $t$ and describes hopping processes from lattice site $j$ to lattice site $i$ (see Fig. 2.2 (b)) by the creation (annihilation) operator $c^\dagger_{i,\sigma}$ ($c_{i,\sigma}$). The hopping parameter $t$ can be extracted from a tight-binding approach and is directly related to the bandwidth $W$. The long-ranged Coulomb interaction is reduced in this model to a local interaction $\mathcal{H}_U$, which only acts with an energy $U$ on electrons on the same lattice site within the same orbital (see Fig. 2.2 (B)), but with different spins due to the Pauli exclusion principle. Even though this model contains drastic simplifications of the full many-body Hamiltonian, it was successful in predicting some of the low-energy and low-temperature properties, as usually only a few bands cross the Fermi energy [9].

The crucial tuning parameters in this model are the hopping energy $t \sim W$, the Coulomb repulsion $U$ (see Fig. 2.2 (B) for a scheme of these energy scales) and the band filling $n$. This in turn allows for two different routes to access a Mott insulator-to-metal transition (MIT), a *bandwidth-controlled* MIT or a *bandfilling-controlled* MIT [9]. In the former case, the MIT occurs at fixed, approximately half-filling as a function of varying correlation strength $U/t$, which is accessible in real systems by tuning the bandwidth $W$. This is in contrast to the bandfilling-controlled MIT where the carrier number is changed away from half-filling.

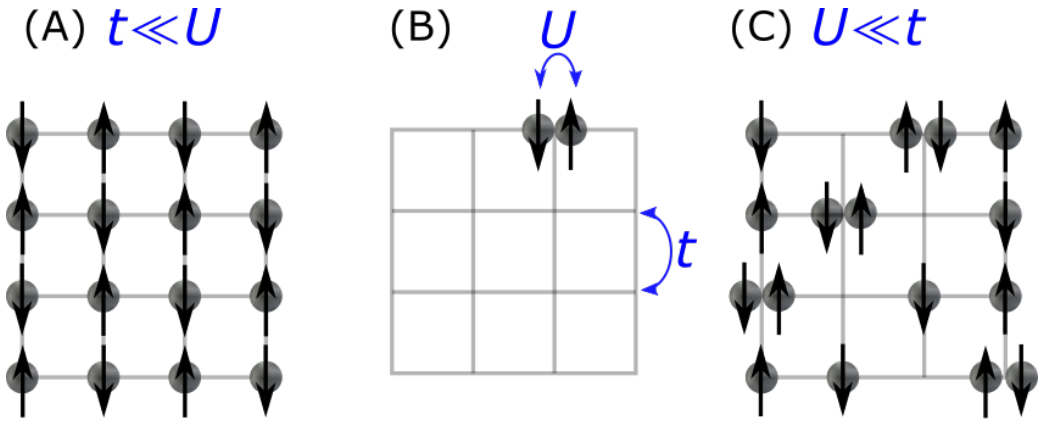


Figure 2.2.: Schematic illustration of a bandwidth-controlled Mott insulator at half filling on a square lattice: Picture (B) indicates the energy scales involved in the Hubbard model. $t$ refers to the hopping energy between two lattice sites, whereas $U$ describes the mutual repulsion of two electrons occupying the same lattice site. The limits of $t \ll U$ (A) and $U \ll t$ (C) are illustrated, causing an insulating and metallic state, respectively.

In case of the organic charge-transfer salts, as depicted in detail in chapter 4, the carrier number is usually fixed by their stochiometry [13]. A few of these materials show a half-filled conduction band and are therefore ideal candidates for the investigations of bandwidth-controlled MITs [12]. In figure 2.2 (A) and (C) the extreme cases for a bandwidth-controlled Mott transition at half-filling are shown in a real-space lattice picture: In the limit $t \ll U$ (see Fig. 2.2 (A)), double occupancies are suppressed and electrons are localized. In the opposite limit $U \ll t$ (see Fig. 2.2 (C)), the kinetic energy dominates, which favors electron hopping, giving rise to metallic behavior. Consequently, at some critical value $(U/t)_c$ a phase transition between these insulting and metallic phases is expected. Experiments, in which the external pressure $P$ is varied to control $U/t$, often find this transition to be of first order at low temperatures [17, 66]. This first-order line ends in a second-order critical endpoint, around which universal critical behavior should be detectable (see chapter 5 for the experimental investigation of Mott phase diagrams and the universal behavior).

A theoretical ansatz for solving the Hubbard Hamiltonian, which features the experimentally observed first-order transition, is provided by dynamical mean-field theory (DMFT) (see Fig. 2.3 (A)). It allows for a non-perturbative treatment of interactions and is exact in the limit of infinite dimensions [54, 59, 67–69]. By investigating the evolution of the density of states, the Mott transition was identified to be of the mass-diverging type instead of the vanishing carrier-number type: Starting on the metallic side at zero temperature in the absence of correlations $U = 0$, the density of states spectrum consists of a quasiparticle peak centered at the Fermi energy (see Fig. 2.3 (B),1), responsible for a Fermi-liquid type of behavior. Upon approaching the MIT at $(U/W)_c \approx 1$ the quasiparticle peak and thereby the mass become strongly renormalized, i.e., the quasiparticle peak becomes dis-

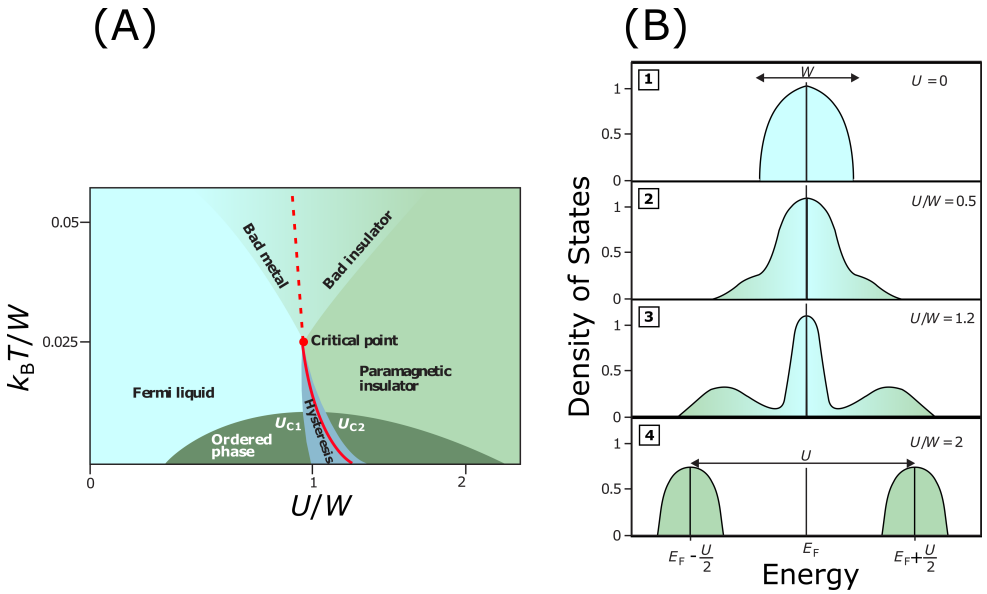


Figure 2.3.: DMFT results for the phase diagram of the Mott transition within the Hubbard model: (A) Phase diagram of the Mott transition as a function of correlation strength $U/W$, which shows a first-order transition at low temperatures accompanied by a hysteresis between $U_{c1}/W$ and $U_{c2}/W$. The first-order transition line ends in a second-order critical endpoint around $U/W \approx 1$. (B) Evolution of the density of states from a coherent quasiparticle peak centered at the Fermi energy in the absence of correlation (1) to the incoherent gap formation in the presence of strong correlations (4) demonstrating the shift of spectral weight upon crossing the MIT transition (after Ref. [54]).

tinctly narrower, with a shift of spectral weight to the lower and upper Hubbard bands (see Fig. 2.3 (B), 2-3). The Hubbard bands are separated in the spectrum by a gap of the order of $U - W$. When $U$ is much larger than $W$, the quasiparticle peak disappears and a fully-gapped system can be observed (see Fig. 2.3 (B),4) [54,59].

According to the DMFT calculations, the quasiparticle peak vanishes upon increasing the temperature on the metallic side close to the MIT to a temperature $T^*$ and all charge carriers become nearly localized [54,59]. This supports the experimental notion that above a certain temperature, the metal and the insulator are indistinguishable, and that the phase diagram shows a critical endpoint (see Fig. 2.3 (A)) [54,59] with universal behavior.

Within DMFT, the parameters $t$ and $U$ are fitting parameters and cannot be determined independently. To determine these parameters and the respective electronic band structure in real materials, common practice is to apply *density functional theory* (DFT) calculations. This is a first principle technique to calculate the ground state energy which only relies on the crystal structure, i.e., the positions of the atoms and their charges. It maps the interacting system on a non-interacting system in an effective potential of the same density [51]. However, the effective potential is usually unknown. The most common approximation for the effective potential, which has to be determined self-consistently, is the *local density*

*approximation* (LDA). It assumes that the exchange interaction acts only locally [51], which is a rather severe simplification and failed in various systems with strong correlations. In order to overcome this obstacle and to achieve an *ab initio* determination of the interactions in strongly correlated electron systems, strong efforts were made to combine DFT and DMFT [70].

Despite the great success of DMFT and DFT for purely electronic models to describe essential features of the phase diagram, important aspects, such as the universal behavior around the Mott transition, still remain illusive up to date. A more detailed review of the existing theoretical and experimental literature on this topic will be given in chapter 5. As will be demonstrated in that chapter, the major result of the present work is that not only the electronic degrees of freedom are important at the phase transition, but also their interaction with the underlying crystal lattice.

### Charge ordering insulators

The Hubbard model in the form presented above with only one local Coulomb interaction has to be extended for providing an appropriate description of other ground-state properties, such as charge density waves (CDW). This so-called *extended Hubbard-model* in addition takes into account a Coulomb interaction $\tilde{V}$ between neighboring sites (see Fig. 2.4).

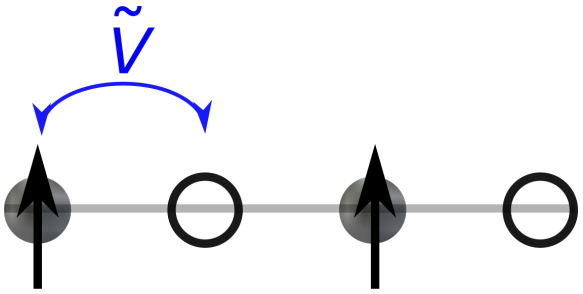


Figure 2.4.: Intersite interaction $\tilde{V}$ in a quarter-filled lattice which can favor a charge-ordered ground state. Grey balls correspond to one electron with a spin (arrow). Empty circle represent empty lattice sites.

The Hamiltonian of the extended Hubbard-model reads as follows:

$$\mathcal{H} = \sum_{\langle i,j\rangle,\sigma} (t c^{\dagger}_{i,\sigma} c_{j,\sigma} + \text{h.c.} + \tilde{V} n_{i,\sigma} n_{j,\sigma}) + \sum_{i} U n_{i,\uparrow} n_{i,\downarrow}. \tag{2.38}$$

This model is especially suitable for describing one- and two-dimensional organic charge-transfer salts with quarter-filled conduction bands, as it features charge-ordered states arising from a strong intersite coupling $\tilde{V}$ (see [71, 72] for reviews on the experimental and theoretical description of these states). Within the charge-ordered phase, charges arrange

themselves in a superstructure (see Fig. 2.4), which breaks the translational invariance of the crystal lattice. As this phenomenon is associated with a localization of the electrons, a charge-ordered phase would be insulating. In case the system is metallic above the charge-ordering transition, the charge order would be accompanied by a metal-insulator transition. The strong interest in these phases is not only due to the strong electron-electron correlations driving it, but also as it is the prerequisite for ferroelectricity, representing a polar charge-ordered state. However, the charge-ordered state itself is non-polar and therefore a breaking of the inversion symmetry is necessary to create an overall polar behavior [73]. Ferroelectricity as a result of dimerization and displacement of atoms, which breaks the inversion symmetry, was found in various one-dimensional charge-transfer salts [74, 75]. In recent years, experiments on dimerized two-dimensional organic charge-transfer salts [5, 75–77] have been in the focus of research, which point to ferroelectricity in these materials as well. The experimental evidence and the coupling of these charge degrees of freedom to other degrees of freedom, such as magnetic degrees of freedom, will be discussed in this thesis in chapter 6.

### Peierls insulators

In contrast to the above-mentioned insulators caused by electron-electron correlations, the Peierls transition describes a metal-insulator transition due to the interaction of the electrons with the lattice giving rise to static lattice deformations. It can be explained by considering an one-dimensional chain: Such a chain with half-filled conduction band is very susceptible to a lattice dimerization (see Fig. 2.5). The reason is that as a consequence of the doubling of the unit cell, an energy reduction due to opening of gaps at the Fermi energy prevails, despite the cost of elastic energy. In two and three dimension this transition is in general suppressed [78].

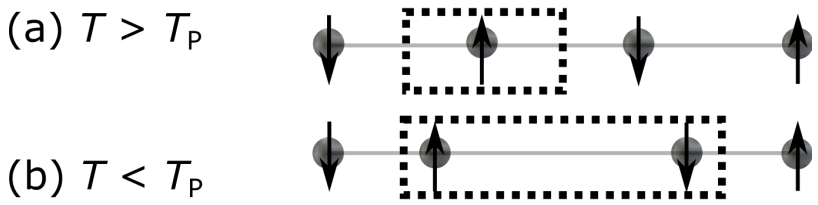


Figure 2.5.: Lattice deformation at a Peierls-transition of a one-dimensional uniform chain above $T_P$ (a) to a dimerized chain below $T_P$ (b), responsible for a metal-insulator transition in one-dimensional systems. The broken rectangle indicates the size of the unit cell which doubles after cooling through the Peierls transition.

#### Anderson insulator

The Anderson insulator can be understood in a single-particle picture in the presence of disorder, i.e., a random variation of the lattice potential, as proposed by P. Anderson in 1958 [79]. The disordered sites act as a scattering center for the electronic waves and the incoming and back-scattered waves interfere. In case of strong disorder this interference can lead to a full suppression of the diffusion of waves and is responsible for the *Anderson insulator* at $T = 0\,\mathrm{K}$ [78,80]. Such type of an insulator is therefore not a result of a gap opening at the Fermi energy, implying a vanishing carrier number, but has a finite density of states at the Fermi edge [9].

The above-presented diverse categories of insulators are caused by different types of interactions: electron-electron interactions in case of the Mott and the charge-order insulators, electron-phonon interactions in case of the Peierls insulator and electron-disorder interaction in case of the Anderson insulator. In real materials, however, the distinction between these different types of insulators and the respective mechanism at work is not conclusive, as in general, all interactions matter. Even if the above-mentioned insulating behaviors themselves are often not fully understood from theoretical and experimental point of view, the interaction of different mechanisms can be of interest in order to gain a better understanding of the properties of real systems. An example is the *Mott-Anderson insulator* which addresses the interplay of strong electronic correlations and disorder, see, e.g., Ref. [81]. In the present work, the effect of disorder will be studied by considering a charge-transfer salt close to the Mott critical endpoint which was exposed to x-ray irradiation, see Sec. 5.4.

### 2.4.2. Magnetism and frustration in strongly correlated electron systems

Until now, the discussion was restricted on charge degrees of freedom in strongly correlated electron systems close to the Mott transition. However, in many cases it is found that Mott insulators order antiferromagnetically at low temperatures, demonstrating that spin degrees of freedom are active in the charge-localized state. Theoretically, the ordering can be inferred from treating the hopping term in the Hubbard Hamiltonian in eq. 2.37 perturbatively in the limit $t/U \rightarrow 0$, i.e., in the strongly localized limit. The result of such a treatment is that the Hubbard Hamiltonian can be transformed into a Heisenberg Hamiltonian, which describes the interaction of three-dimensional spins $\vec{S}_i$ via an exchange energy $J$ that favors antiferromagnetic ordering [82],

$$\mathcal{H} = J \sum_{i,j} \vec{S}_i \cdot \vec{S}_j, \tag{2.39}$$

$$\text{with } J = \frac{4t^2}{U}. \tag{2.40}$$

In a more intuitive picture, the antiferromagnetic order is favored over the ferromagnetic one due to so-called *virtual hopping*. In the latter case, any hopping is forbidden due to the Pauli exclusion principle. In contrast, if the interaction is antiferromagnetic, hopping is in general possible, even though the probability amplitude for such a process is low due to the high cost of the Coulomb repulsion energy. Nevertheless, the energy is lower in the antiferromagnetic case due to the finite probability for the electron to spread out.

The Heisenberg model can account for well-known types of magnetic order as antiferromagnetism and ferromagnetism, depending on the sign of the exchange coupling $J$, in the limit of strong localization. In general, the details of the Hamiltonian and the magnetic properties depend on the dimensionality and the geometry of the lattice. In systems with reduced dimensions strong quantum fluctuations can prevent long-range order to form. Another route to increase quantum fluctuations is to increase the degree of *magnetic frustration* in a system (see, e.g., [36] for a recent review). It describes systems in which all interactions cannot be minimized simultaneously. To this end, at least one interaction has to be antiferromagnetic. A magnetically frustrated system provides the playground for studying the emergence of exotic phases, such as the spin-liquid phase. This state is characterized by strong spin correlations, but lacks long-range magnetic order and thus breaking of spatial symmetry [83]. Frustration can be provided either by geometry, as is the case for an isotropic triangular lattice with antiferromagnetic Ising exchange interactions, or by competing interactions of ferromagnetic and antiferromagnetic nature. The former case is a prime example to understand the principle of frustration: All the spins would like to align antiparallel to each other. However, this requirement can be satisfied only along one bond. The result is a highly degenerate ground state with various allowed spin configurations with a high residual entropy and low-lying excitations which are of particular interest in this research field.

In order to quantify the degree of frustration in real systems with an triangular lattice, the ratio $J'/J$ or $t'/t$ is considered which compares the competing exchange energies $J$ and $J'$. As closer this ratio is to 1, the more frustrated the system is. Experimentally, the degree of frustration can be explored by comparing the antiferromagnetic ordering temperature $T_N$ with the Curie-Weiss temperature $T_{CW}$. The latter is a measure of the dominant-exchange coupling $J$ and is roughly coinciding with $T_N$ in non-frustrated systems [84]. Thus, whenever $T_N$ is much smaller than $T_{CW}$, the system is said to be highly frustrated.

Organic charge-transfer salts of the $\kappa$-(BEDT-TTF)$_2X$ family, as will be introduced in chapter 4, have a triangular lattice with frustrating interactions [13]. Depending on the particular choice of the anion $X$, the degree of frustration can vary from moderately high values of $t'/t \approx 0.4$ to very high values close to 1. This reflects the great variability of these systems with respect to their magnetic properties.

## 2.5. Basic definitions of elasticity theory of crystals

In the previous section, different models were introduced to describe strong electronic correlations. These models have in common that they consider only electronic degrees of freedom. However, the coupling of electrons to the lattice is often not negligible and manifests itself in, e.g., anomalies in the thermal expansion, which is a quantity that directly measures lattice effects. In what follows, a short introduction of the elasticity theory of crystals is given. This may help to better understand the analysis of the thermal expansion results in Sec. 5.2. The basic definitions and concepts outlined here can be found in various textbooks, see, e.g., [37,85,86].

A crystal lattice is defined by a periodic arrangement of atoms with a lattice spacing $a$. The motion of the atoms is coupled and, through the ansatz of plane waves, every atom oscillates around its equilibrium position with an amplitude $u_n$. This situation is mathematically encountered by coupled differential equations of motions. In the following, we will concentrate mainly on low-energy excitations and thereby discuss the elastic properties of the solid in the long-wavelength limit. In this border case, the difference in the amplitude $u_{n+1} - u_n$ is small in comparison to the wavelength. Consequently, the elastic behavior can be effectively treated in the framework of a continuum theory.

The displacement vector $\vec{u}(\vec{r}) = \vec{r'} - \vec{r}$ describes the difference between the initial position $\vec{r}$ and the final position $\vec{r'}$. Within continuum theory, the displacement between two constituents can be linearized $\vec{u}(\vec{r_1}) - \vec{u}(\vec{r_2}) = \sum_i \frac{\partial \vec{u}(\vec{r_1})}{\partial x_i}(\vec{r_1} - \vec{r_2})_i$ with $i = 1, 2, 3$, so that the overall deformations from the initial length $l$ to the final length $l'$ [87] are given by

$$\begin{aligned} \mathrm{d}l'^2 &= (\vec{r_1'} - \vec{r_2'})^2 && (2.41)\\ &= (\vec{r_1} + \vec{u}(\vec{r_1}) - \vec{r_2} - \vec{u}(\vec{r_2}))^2 && (2.42)\\ &= \mathrm{d}l^2 + \sum_{i,k} 2\varepsilon_{ik}(\vec{r_1})\,\mathrm{d}x_i \mathrm{d}x_k && (2.43) \end{aligned}$$

with the strain tensor $\varepsilon_{ij}$

$$\varepsilon_{ij} = \frac{1}{2}\left(\frac{\partial u_i}{\partial x_j} + \frac{\partial u_j}{\partial x_i} + \frac{\partial u_l}{\partial x_i}\frac{\partial u_l}{\partial x_j}\right). \tag{2.44}$$

As the displacements in a rigid body are in general comparatively small, the last term in eq. 2.44, which is $\propto \mathcal{O}(\Delta u^2)$, is often ignored. The strain tensor is a symmetric second rank tensor and can therefore be diagonalized, so that the volume change $\Delta V/V$ is given by the trace of this tensor

$$\frac{\Delta V}{V} = \frac{\Delta L_a}{L_a} + \frac{\Delta L_b}{L_b} + \frac{\Delta L_c}{L_c} = \sum_i \varepsilon_{ii}. \tag{2.45}$$

The diagonal elements of the strain tensor with $i = j$ therefore describe changes of the volume, whereas the non-diagonal terms with $i \neq j$ describe shear deformations.

Without external forces, the solid resides in its equilibrium position and the internal forces cancel each other out. Deformations occur upon the application of external forces $F$, which lead to internal forces $F_i$, and they can be expressed in terms of the stress tensor $\sigma_{ik}$,

$$F_i = \frac{\partial \sigma_{ik}}{\partial x_k} \tag{2.46}$$

$$\int F \mathrm{d}V = \oint \sigma_{ik} \mathrm{d}f_k. \tag{2.47}$$

The stress tensor depicts the $i$-th component of the force which acts on the surface element $\mathrm{d}f_k$. This tensor is also symmetric. In the experiments, presented in this thesis, hydrostatic pressure $P$ is applied, i.e., a compressive stress along all directions. The force then reads as $F_i = -P\mathrm{d}f_i$ and the stress tensor is in this case given by

$$\sigma_{ik} = -P\delta_{ik}. \tag{2.48}$$

Since deformations and displacements are usually very small, the respective free energy $\mathcal{F}$ can be expanded in a power series

$$\mathcal{F} = \mathcal{F}_0 + \sum_{i,j,k,l} \frac{1}{2} C_{ijkl}\varepsilon_{ij}\varepsilon_{kl}. \tag{2.49}$$

The linear term in the expansion vanishes as it corresponds to the equilibrium condition. The rank four tensor $C_{ijkl}$ is called the elastic modulus tensor, which has in general 81 components. However, various of the components are identical for symmetry reasons,

$$C_{ijkl} = C_{jikl} = C_{ijlk} = C_{klij}, \tag{2.50}$$

leaving behind 21 independent components. The strain-stress relation can be derived from differentiating the potential. In first approximation for small deformations, the relation between the stress and the strain is linear. This law is known as *Hooke's law of elasticity* and reads in its generalized form as

$$\sigma_{kl} = \sum_{i,j} C_{klij}\epsilon_{ij}. \tag{2.51}$$

For convenience, the elastic modulus tensor, the strain tensor and the stress tensor are written in Voigt notation, making use of the symmetries. Thus, the elastic constant matrix is written in a $6 \times 6$ matrix using the following transformation of the indices $11 \to 1, 22 \to 2, 33 \to 3, 23 \to 4, 13 \to 5, 12 \to 6$. Exemplarily, the elastic matrix is given here for the orthorhombic crystal group [88], as most of the organic charge-transfer salts discussed here, possess an orthorhombic crystal structure:

$$C = \begin{pmatrix} C_{11} & C_{12} & C_{13} & 0 & 0 & 0 \\ C_{12} & C_{22} & C_{23} & 0 & 0 & 0 \\ C_{13} & C_{23} & C_{33} & 0 & 0 & 0 \\ 0 & 0 & 0 & C_{44} & 0 & 0 \\ 0 & 0 & 0 & 0 & C_{55} & 0 \\ 0 & 0 & 0 & 0 & 0 & C_{66} \end{pmatrix}. \tag{2.52}$$

Whereas the upper $3 \times 3$ matrix describes the response under compressive strain, the lower part accounts for shear strain. In general, for a crystal to be stable, the matrix has to be positive definite, i.e., it possesses six non-degenerate positive eigenvalues in case of the orthorhombic elastic matrix [88].

In the long-wavelength limit, the dispersion of the acoustic phonons $\omega(\vec{q})$ can be linearized with the sound velocity being the proportionality constant. The dispersion is in general determined by the dynamical matrix $D_{il}$, which solves the equations of motions with the mass density $\rho$,

$$\sum_l D_{il}(\vec{q})\vec{u_l}(\vec{q},\omega) = \rho\omega^2\vec{u_i}(\vec{q},\omega) \tag{2.53}$$

$$D_{il}(\vec{q}) = \sum_{j,k} C_{ijkl}q_j q_k. \tag{2.54}$$

It follows, that the sound velocities in a crystal are determined by the elastic constant matrix, which depend on the compressive as well as shear properties of the solid. This fact will be especially important at the isostructural solid-solid transition, predicted for the Mott transition in a real material [21]. At such a transition, as discussed in detail in Sec. 5.2, one of the elastic moduli vanishes. However, according to eq. 2.54, the acoustic phonon velocities remain finite due to the shear properties of a solid.

# 3. Experimental techniques

In this chapter a detailed description of the experimental techniques, which were used in this work, is given. The main focus of this chapter lies on the method of capacitive dilatometry in order to perform high-resolution measurements of the thermal expansion of a solid. The kind of dilatometer used here was developed in the 1980's [28]. It represents a well-established technique for measuring length changes as a function of temperature $T$ at constant magnetic field $B$ or as a function of $B$ at $T$ = const. A new development was made in the group of Prof. Dr. M. Lang over the last couple of years in order to perform such measurements also as a function of pressure $P$ [25, 26]. This represents a unique possibility to tune a material to distinct points in the pressure-temperature phase diagram and measure lattice effects at the same time. Measurements in this work were performed at ambient pressure as well as under pressure. Additionally, some organic charge-transfer salts were characterized concerning their magnetic properties with a commercial SQUID magnetometer.

## 3.1. Thermal expansion measurements

The changes of length and volume of a solid as a function of an external parameter are fundamental quantities in solid state research. In contrast to specific heat measurements, the length change can be determined in every crystallographic direction (see eq. 2.1) thereby providing information about the system's anisotropies. In principle, there are several different experimental techniques available with which length changes can be explored (e.g. x-ray diffraction, optical measurements, etc.). Among these techniques, capacitive dilatometry has proven to be one of the most sensitive ones in measuring length changes[1]. It reaches a maximum resolution of $\Delta L/L \approx 10^{-10}$, which corresponds to detectable length changes of $0.01\,\text{Å}$ for a crystal of 1 cm length.

The working principle of a capacitive dilatometer [28] (see figure 3.1) will be explained in the following: The dilatometer cell consists of a frame which houses a plate capacitor. The lower plate of this capacitor is fixed to the frame, whereas the upper plate is movable

[1] At this point it's worthwhile to note that capacitive dilatometry can only provide measurements of length changes corresponding to relative length changes of lattice parameters, but not absolute measurements of lattice parameters. For the latter, x-ray diffraction measurements are clearly preferred.

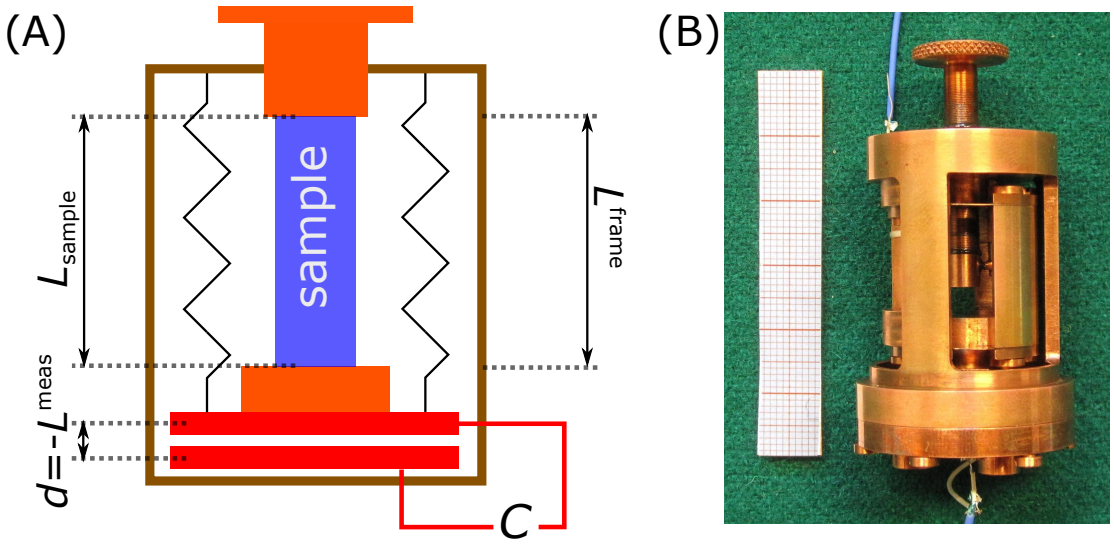


Figure 3.1.: (A) Scheme of the capacitive dilatometer: capacitor plates (red), frame (brown), springs (black), piston (orange) and sample (blue); Grey lines and arrows indicate the quantities which contribute to the analysis of the capacitance data, i.e., $L_{sample}$, $L^{frame}$ and $d = -L^{meas}$, for details see text. (B) Picture of the thermal expansion cell used in the ambient pressure setup before gold-plating [89].

and only fixed to the frame by springs. The sample is placed on top of the upper plate and is fixed by a piston. The springs allow the capacitor to follow changes of the sample, i.e., to change the distance between the plates, once the sample changes its length. The distance of the plates $d$ is related to the capacitance $C$ of a plate capacitor by equation 3.1. The measurement of changes in the capacitance then allows a direct measure of the length changes of the crystal.

$$C = \frac{\varepsilon_0 \varepsilon_r A}{d}. \tag{3.1}$$

Only three proportionality constants, namely the vacuum permittivity $\varepsilon_0 = 8.85 \cdot 10^{-12} \frac{\mathrm{As}}{\mathrm{Vm}}$, the dielectric constant of the medium $\varepsilon_r$ and the area of the capacitor plates $A$, have to be taken into account for the calculation. The high resolution of this technique is based on the hiqh quality of the plate capacitor, i.e., a very high degree of parallelism of the plates, as well as the high resolution of the used capacitance bridges.

Before performing a measurement of a crystal, it must be ensured that the springs are prestressed, so that the upper plate can follow any length change, be it a contraction or an elongation. This prestressing is realized by screwing down the piston, which in turn also slightly changes the plate distance prior to the measurement. This procedure defines a *starting capacitance*, as the capacitance is enlarged in comparison to the empty cell capacitance during this process. In general, a higher starting capacitance is helpful, since, according to equation 3.1, the change in the capacitance $\Delta C$ for a given change $\Delta d$ grows

as $\Delta C \propto C^2$. Thus, a higher resolution is obtained with increasing $C$. On the other hand, by the application of the starting capacitance, a uniaxial pressure is exerted to the crystal, which also grows with the starting capacitance. Especially for the organic charge-transfer salts, this is a crucial parameter since these crystals can easily break under uniaxial pressure. In addition, uniaxial pressure can affect the physical properties, as phase transitions are highly pressure sensitive in this material class due to the soft organic molecular entities. The determination of the uniaxial pressure and the corresponding choice of the starting capacitance is discussed in Appendix section A.3 for the two dilatometer cells, which were used during this work. The potential influence of the uniaxial pressure exerted by the dilatometer on the results will be discussed for every system independently.

For a detailed analysis of the data, i.e., for a conversion of $\Delta C$ into length changes $\Delta L$, it has to be considered that not only the crystal's length is changing as a function of temperature, but also the cell is exposed to temperature changes. This leads to an expansion of the frame and pistons and to changes of the radius of the capacitor plates [28][2]. The cells are manufactured out of high-purity copper (Cu), thus the expansion of the cell parts is known from literature [90]. Following equation 3.1, the relative length change of the combined system, consisting of sample and Cu-cell, $\Delta L^{meas} = -\Delta d$ (see Fig. 3.1 (A)), with $\Delta d$ corresponding to the change of plate distance of the capacitor, between two temperatures $T$ and $T_0$, can be calculated by equation 3.2.

$$\Delta L^{meas}(T) = L(T) - L(T_0) \tag{3.2}$$

$$= \pi \varepsilon_0 r^2 (1+\delta) \cdot \left( \frac{C(T) - C(T_0)}{C(T_0) \cdot C(T)} - 2\frac{\Delta r}{r}\frac{1}{C(T)} \right). \tag{3.3}$$

This equation takes into account the following two aspects:

- The factor $\delta$ was introduced to account for inhomogeneities of the electric field of the plate capacitor at the edges of the plates. This factor can be calculated for a given cell geometry, see [28] for details. However, since $\delta \ll 1$, it represents only a small correction.
- The second term in the brackets considers thermally-induced relative length changes of the radius $r$ of the capacitor plates, which influence the capacitance via $A = \pi r^2$, see eq. 3.1. As the plates are manufactured from high purity Cu, $\Delta r/r$ of Cu can be used, which is well known from literature [90].

[2] All the following explanations are based on the assumption that the dielectric constant $\varepsilon_r$ of helium, which surrounds the dilatometer cell, is $\approx 1$. This approximation is sufficient at ambient pressure. Under pressure this approximation breaks down. The effect of pressure on the analysis of the data will be discussed in detail in section 3.1.2.

In addition, the so-derived $\Delta L^{meas}$ needs to be corrected for the expansion of the Cu frame [91,92]. The only part of the frame that contributes to the measured length changes is a piece of the frame $L_{Cu}^{frame}$, which has exactly the same length as the crystal (see Fig. 3.1 (A)). The rest of the frame does not contribute to the measured thermal expansion, because the frame and the pistons all are manufactured out of Cu, thus showing identical length changes as a function of $T$. The contribution $\Delta L_{Cu}^{frame} = L_{sample} \cdot (\Delta L/L)_{Cu}$ can be easily calculated by using literature results for the expansion of Cu, $(\Delta L/L)_{Cu}$ [90]. This contribution is cell-independent, but dependent on the length of the sample measured. In addition, a cell-dependent factor $\Delta L^{cell}$ is introduced, which takes into account deviations from the expansion of copper, e.g., by the expansion of the springs which are manufactured out of copper beryllium. This factor is determined experimentally by measuring the expansion of a Cu block in the Cu cell. Since $\Delta L_{sample}$ and $\Delta L_{Cu}^{frame}$ are identical in this case, the measured changes of the capacitance in such an experiment directly reflect the additional cell effect. In summary, the length change of the crystal can be calculated using equation 3.4 taking into account the various contributions described above,

$$\Delta L_{sample}(T) = \Delta L^{meas}(T) + \Delta L_{Cu}^{frame}(T) - \Delta L^{cell}(T). \tag{3.4}$$

The thermal expansion coefficient, which is proportional to the derivative of the sample length with respect to temperature, can now be calculated numerically by using the differential quotient between two data points (see equation 3.5),

$$\alpha = \frac{1}{L_{sample}} \frac{\partial L_{sample}}{\partial T} \tag{3.5}$$

$$\approx \frac{1}{L_{sample}(300\ \mathrm{K})} \frac{\Delta L_{sample}(T_2) - \Delta L_{sample}(T_1)}{T_2 - T_1}, \tag{3.6}$$

$$\text{and } T = (T_1 + T_2)/2, \tag{3.7}$$

$$\text{and } \Delta L(T) = L(T) - L(T_0), \tag{3.8}$$

with $T_0$ being a reference temperature. In order to reduce the noise level, the derivative of the $\Delta L_{sample}$ data was determined using the following procedure. The $\Delta L(T)/L$ data were divided into equidistant intervals of typically 0.2 K. The width of the intervals depends on the temperature range and is thus mentioned specifically, whenever data of the thermal expansion coefficient are shown. In each of these intervals the mean slope was determined from a linear regression. The mean slope together with the mean temperature in this interval corresponds to one data point in the $\alpha$ vs. $T$ representation.

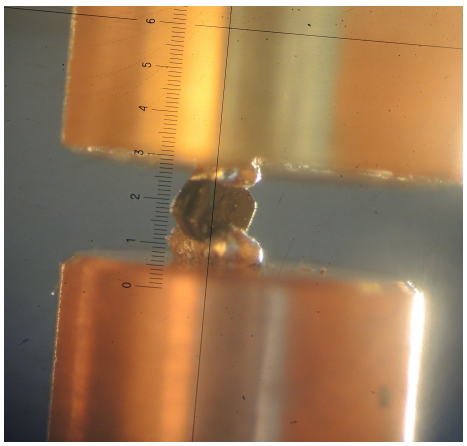

Figure 3.2.: A crystal of $\kappa$-($d_8$-BEDT-TTF)$_2$Cu[N(CN)$_2$]Br (black color; batch no. kd8Br-5-3) mounted from edge to edge in the thermal expansion cell (gold-plated copper piston above the sample and copper block below the sample) with two gallium spheres (silver color). The scale indicates the length of the crystal as well as the size of the gallium spheres (2 units $\equiv$ 1 mm).

### Mounting of fragile crystals of organic charge-transfer salts

The mounting of crystals of organic charge-transfer salts is a challenging task for various reasons. First of all, the crystals are very small and brittle. They easily break into several pieces if only a tiny force is applied. Second, thermal expansion measurement usually require crystals with plane-parallel surfaces perpendicular to the crystallographic direction of interest. This is necessary in order to fix the crystals between the pistons in a mechanically stable way. In case of the organic-charge transfer salts, the desired crystal direction often points from one edge of the crystal to the other. At the same time cutting or polishing is not feasible as it would damage or break the crystal. In order to get around these problems, the edges of the crystal are embedded into two gallium spheres which distribute the applied force through the dilatometer on large areas of the crystal, as shown in figure 3.2. Gallium is a well-suited material for this purpose, as it has quite a low melting point of 29.76 °C [93]. It allows to place and orientate the sample in the liquid state of gallium by heating slightly above room temperature and to stabilize the conditions by solidifying the gallium with the help of cold nitrogen vapor. With this technique, it is possible to measure even very thin crystals in every crystallographic direction. Of course, the expansion of gallium also contributes to the results. However, the expansion of gallium is small in comparison to the expansion of the measured organic crystals, which are distinct by a comparatively strong expansion. Furthermore, the absolute length of the gallium, which contributes to the results, is small (typically 0.1 mm), since the crystal is pushed into the gallium spheres. Thus, there is often only a thin layer of gallium between the piston and the sample, which contributes

to the $\Delta L_{meas}$ results, so that in total the contribution of the gallium is considered to be negligible.

### 3.1.1. Thermal expansion at ambient pressure

#### Description of the setup

Thermal expansion at ambient pressure was measured within a $^4$He bath cryostat, the temperature of which can be lowered from 4.2 K to 1.2 K upon pumping the bath. The cryostat is equipped with a magnet with a maximum field of 12 T. The home-built expansion cell [89,94] is surrounded by two vacuum chambers, which can be filled with $^3$He exchange gas depending on how much thermal coupling of the insert to the bath is desired. The amount of exchange gas is usually fixed to a value in the range of a few mbar pressure, thus ensuring that the approximation of the dielectric constant of the medium $\varepsilon_r \approx 1$ is valid. A heater is placed on the inner can, which allows a precise temperature control. In order to measure the temperature, three Cernox thermometers are installed in the setup. Thermometer A is placed on the cell and calibrated from 1.2 K up to 320 K. Thermometer B is at the same position and calibrated from 20 K to 320 K. This sensor has a higher sensitivity in the intermediate temperature range above 20 K. The third thermometer C is placed in the compensated zone of the magnet in order to avoid magnetoresistive effects in the temperature measurement. A LakeShore 340 controller enables one to perform a continuous temperature control between 1.5 K and 200 K.[3] In the most cases, a temperature sweep rate of $\pm 1.5$ K/h was used to ensure thermal equilibrium. The capacitance is measured in a three-terminal-configuration. For this purpose, either a "Ultra Precision" Capacitance Bridge from the Company Andeen Hagerling (AH 2550 A), which works at a constant frequency of 1 kHz, or a 1616 Precision Capacitance Bridge from the Company General Radio, which can be operated with a variable frequency, was used. In the latter case, the voltage across the bridge is balanced to zero at constant temperature by a variation of the settings of the inductive divider in the bridge prior to the measurements. Once the capacitance changes as a function of temperature, voltage changes across the bridge occur. As these changes are small, the measured voltage can be linearized and converted into a capacitance change. The voltages are measured by a Lock-In amplifier (Company EG & G, Model 7260), the frequency of which was in most of the cases fixed to 997 Hz. The high resolution of the Lock-In amplifier is giving rise to an order of magnitude higher sensitivity than the capacitance bridge AH 2550 A. However, the former one is not suited if higher

[3] In general also a temperature control up to 300 K would be possible. Unfortunately, over the years the Cu cell oxidized, which causes an anomaly at around 220 K [95] and avoids taking reliable data above 200 K. This problem could also not be solved by building a new dilatometer cell [94]. Furthermore, tests showed that also the pressure in the outer can increases significantly above 215 K, making a precise temperature control difficult [94].

capacitance changes are expected, as the linear relation of voltage and capacitance could break down. Thus, commonly the AH2550 A bridge is used for measurements of the organic charge-transfer salts. The data is recorded by a TestPoint computer program written by Dr. Ulrich Tutsch.

### 3.1.2. Thermal expansion under $^4$He-gas pressure

Thermal expansion measurements provide an important information on the thermodynamics of a system. The combination of this technique with a new parameter, namely pressure $P$ is promising, as it allows to tune the lattice and with it the electronic properties continuously. The latter can be important for studying phase transitions as well as the interplay with other phases at higher $P$. This technique was developed in the last years in the group of Prof. Dr. M. Lang. The design of the setup was already described in Refs. [25, 26]. As a pressure-transmitting medium $^4$He is used. $^4$He has remarkable advantages compared to other pressure media: It provides truly hydrostatic pressure conditions[4], as it shows a large range in temperature and pressure compared to other pressure media, in which it is either in its liquid or its gaseous phase. It does not solidify at all at ambient pressure up to 2.5 MPa down to lowest temperatures [97]. If the pressure is higher than 2.5 MPa, helium solidifies only at very low temperatures. This is particulary important, as the technique of capacitive dilatometry requires that the capacitor plates can move freely, which is impossible in a solid pressure medium. Thus, only helium as a pressure-transmitting medium guarantees an operation of the present setup down to low-enough temperatures. The operation range of the setup, within the liquid or the gaseous phase of $^4$He, can be inferred from the $P$-$T$-solidification line of helium. It can be described by the following empirical formula [98]

$$P\,[\mathrm{MPa}] = 1.6325 \cdot \left[ \left( \frac{T\,[\mathrm{K}]}{0.992} \right)^{1.5544} - 1 \right]. \tag{3.9}$$

Even if the operation under pressure is somehow limited with regard to the accessible temperature range, the maximum pressure of 250 MPa of the setup, corresponding to a solidification temperature of about 25 K, enables the investigation of various low-temperature phase transitions at $T > 25\,\mathrm{K}$.

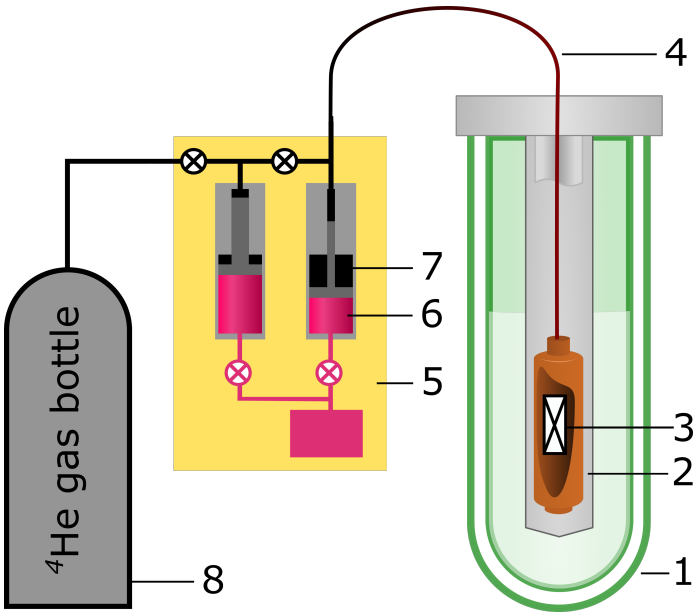


Figure 3.3.: Scheme of a low-temperature experiment performed under $^4$He-gas pressure: (1) cryostat, (2) pressure cell, (3) experimental probe, (4) capillary, (5) compressor, (6) oil reservoir, (7) gas reservoir, (8) helium gas bottle [99].

### Description of the setup

The dilatometer cell, which is installed in the present setup, was made out of high-purity Cu. It was designed and manufactured by Dr. Robert Küchler (MPI CPFS[5], Dresden) [27]. It is smaller in radius and size than the homemade dilatometer cell, which results in a slightly lower resolution of $\Delta L/L \approx 5 \cdot 10^{-10}$. The dilatometer cell is placed in a pressure cell [100] out of CuBe (see Fig. 3.3), which was designed in collaboration with Unipress company[6]. It has a large inner volume of $V = 81.4\,\mathrm{cm}^3$ in order to house the thermal expansion cell. Within the pressure cell, an InSb-pressure sensor[7] is mounted for an *in situ* pressure determination. The pressure cell is connected via a capillary (also out of CuBe) to a gas compressor (U11/MP5 from Unipress) [101]. The gas compressor itself is equipped with two manometers. The gas is supplied to the compressor from a $^4$He-gas bottle, which is connected to the compressor by stainless-steel tubes from the Companies Air Liquide and Swagelok. At the compressor outlet to the bottle, i.e., within the stainless-steel tube line, a high-precision manometer ($\Delta P \leq 0.03\,\mathrm{MPa}$) from the Company Keller was installed. It can be read out by the computer software *Logger 5*, provided by the company.

[4] Especially the organic charge-transfer salts studied in this work are extremely sensitive to non-hydrostatic pressure components due to their strongly anisotropic pressure coefficients [96].
[5] Max-Planck-Institut für Chemische Physik fester Stoffe.
[6] Institute of High Pressure Physics, Polish Academy of Science, Unipress Equipment Division.
[7] Installed and calibrated by Unipress.

Such kind of a gas-pressure setup has remarkable advantages, as it allows to compensate for temperature-induced pressure changes on the low-temperature side, thus enabling measurements at $P \simeq$ const. This is achieved by keeping the pressure cell, which is subject to temperature changes, connected to the room-temperature reservoir of the compressor at all times. However, this guarantees $P \simeq$ const. conditions only as long as the volume of the pressure cell is much smaller than the volume of the room-temperature reservoir. This condition is not satisfied in the present setup due to the large volume of the pressure cell, thereby causing significant pressure changes upon varying the temperature. In the present work, in which $P \leq 30\,\mathrm{MPa}$ was sufficient to explore the physical properties of interest, this problem was circumvented by using a gas bottle as the pressure reservoir with much larger volume ($V \approx 5 \cdot 10^4\,\mathrm{cm}^3$). Such helium-gas (99,99999% purity) bottles can be purchased with a maximum pressure of 30 MPa. The use of gas bottles as a pressure reservoir in the present case allows two operation modes of the system:

- The pressure can be held constant and the temperature of the sample can be varied. For temperature changes within the regime $20\,\mathrm{K} \leq T \leq 60\,\mathrm{K}$, pressure changes less than $|\Delta P| \leq 0.05\,\mathrm{MPa}$ can be expected. The standard sweep rate for $T$-dependent measurements was $\pm 1.5\,\mathrm{K/h}$.
- The temperature can be held constant ($|\Delta T| = \pm 0.1\,\mathrm{mK}$ on short term (30 min) and $|\Delta T| < 15\,\mathrm{mK}$ on long term (24 h)) and the pressure can be slowly released by a valve on the compressor side. The pressure-time relation follows to a good approximation an exponential decay, which is recorded by the manometer at the compressor. On average, the pressure decrease was about $-1.5\,\mathrm{MPa/h}$. Here, the huge volume of the gas bottle ensures that the pressure in the cell does not decrease too fast after opening the valve and thus guarantees that the measurements are performed under conditions close to equilibrium.

The pressure cell is surrounded by two vacuum chambers, whereas on the inner chamber the heater is installed. The insert is placed in a $^4$He-bath cryostat with a minimum temperature of 1.4 K. In this cryostat, a magnet with a maximum field of 14 T is installed. Temperature control is performed with a LakeShore temperature controller (LS 340). A Cernox thermometer ($1.4\,\mathrm{K} \leq T \leq 300\,\mathrm{K}$) is placed outside the pressure cell, i.e., directly on top of the pressure cell. In order to ensure thermal equilibrium between the sample inside the cell and the thermometer outside, very slow sweep rates of $\pm 1.5\,\mathrm{K/h}$ were used. An additional thermometer ($20\,\mathrm{K} \leq T \leq 300\,\mathrm{K}$) is placed on Cu blocks around the capillary in the compensated zone of the magnet. Resistances are mounted on the Cu blocks as well which can be used as a capillary heater in case of a blockage by frozen gases, either nitrogen or oxygen. The data from the capacitance Bridge, the InSb-sensor and the temperature sensors are recorded by a TestPoint program written by Dr. Ulrich Tutsch.

### Dielectric constant of helium under pressure

As the capacitor is immersed in the pressure medium $^4$He, the assumption that the dielectric constant of the medium $\varepsilon_r \approx 1$ is no longer valid. In general, $\varepsilon_r$ depends on the temperature $T$ as well as the pressure $P$, keeping in mind that the volume is kept constant. Importantly, the particle number in the pressure cell is subject to changes, as the pressure cell is connected to the compressor, acting as a huge particle reservoir. On a qualitative level, the dielectric constant $\varepsilon_r$ grows with pressure and/or decreasing temperature. This general trend can be easily explained in a qualitative picture by considering the dipole moment of each particle: With increasing density of dipole moments the dielectric constant increases. This is the case when pressure is increased. Moreover, the number of particles is also increasing if the temperature is lowered, since particles out of the reservoir are then added to the pressure cell in order to compensate the temperature-induced pressure effects. In the following, experiments to determine the dielectric constant quantitatively will be discussed. The precise knowledge of $\epsilon_r = \epsilon_r(T, P)$ is of crucial importance for the analysis of the capacitance data in terms of the length change of the sample. These results will be compared to theoretical approaches to calculate $\epsilon_r(T, P)$ with a thermodynamic ansatz.

### Experimental determination of the dielectric constant

The dielectric constant of $^4$He was determined experimentally by using a reference sample, such as aluminum (Al) or Cu, and measuring the capacitance as a function of $T$ and $P$. In order to evaluate the data, it was assumed that the contributions of the Cu cell and the reference sample, in this case annealed Al, as a function of pressure are negligibly small in comparison to the effects of the dielectric constant. This assumption can be verified by considering the rather small uniaxial compressibilities of Cu and Al of $\kappa_{Cu} = 1/3\,\kappa_{V,Cu} \approx 2 \cdot 10^{-6}/\mathrm{MPa}$ and $\kappa_{Al} = 1/3\,\kappa_{V,Al} \approx 4 \cdot 10^{-6}/\mathrm{MPa}$ (see e.g. [102]), respectively. The associated length changes typically correspond to capacitance changes of $\mathcal{O}(10^{-3}\,\mathrm{pF})$, whereas changes of the capacitance induced by the dielectric constant in the temperature and pressure range of interest, are typically in the order of $\mathcal{O}(10^{-1}\,\mathrm{pF})$, see below. Based on these assumptions, the pressure-induced capacitance changes result only from the change of the dielectric constant of the medium under pressure. Consequently, the dielectric constant can be calculated by $\varepsilon_r(P, T) = C(P, T)/C(P = 0\,\mathrm{MPa}, T)$. This procedure was checked experimentally by measuring Al as well as Cu individually at the same pressure (see Appendix A.2 for details). Errors are mainly resulting from sudden jumps of the capacitance value $\Delta C_i$, which happen from time to time as a result of mechanical shocks. In general, a total change of the capacitance of $\sum_i |\Delta C_i| \approx 2 \cdot 10^{-3}\,\mathrm{pF}$ at maximum at a capacitance of 12 pF after several temperature or pressure runs was observed. This results

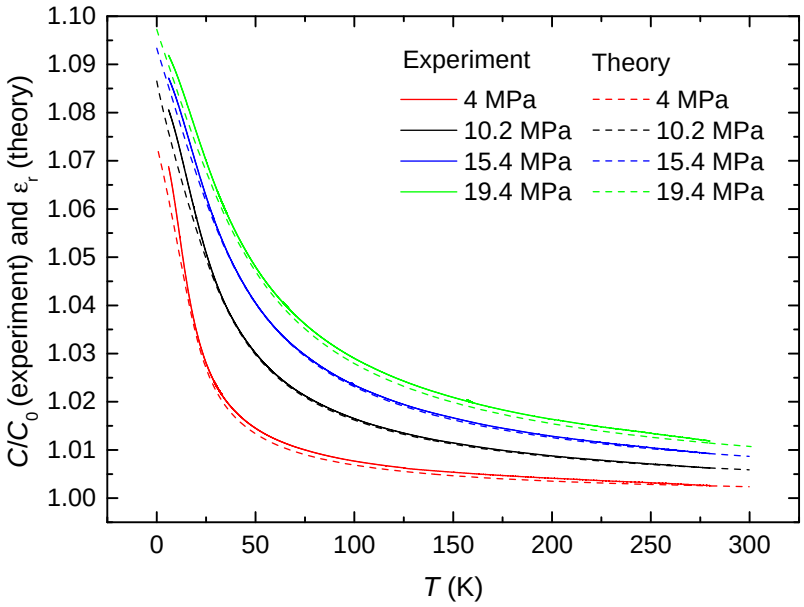


Figure 3.4.: The dielectric constant of $^4$He measured as a function of temperature from low temperatures ($T = 6\,\mathrm{K}$) up to room temperature for selected pressure of 4, 10.2, 15.4 and 19.4 MPa (solid lines). $C/C_0$ stands for $C(T, P = \text{const.})/C(T, P = 0\,\mathrm{MPa})$. For comparison the calculated curves of $\epsilon(P, T)$ from a van-der-Waals model with pressure-dependent volume of the molecules are shown by broken lines for the same pressure values (see Sec. A.1 for details of the calculation).

in an upper limit for the systematic error of the dielectric constant of $\Delta\varepsilon_r/\varepsilon_r \approx 2 \cdot 10^{-4}$ due to capacitance jumps.

### Comparison of experimental and theoretical results for the dielectric constant

Figure 3.4 shows the experimentally determined dielectric constant of helium $\varepsilon_r(P, T) = C(P, T)/C(P = 0\,\mathrm{MPa}, T)$ (solid lines) for four selected constant pressures of $P = 4\,\mathrm{MPa}$, $10.2\,\mathrm{MPa}$, $15.4\,\mathrm{MPa}$ and $19.4\,\mathrm{MPa}$ from $T = 6\,\mathrm{K}$ up to $280\,\mathrm{K}$. In general, the data set reveals the already described trend that the dielectric constant grows with increasing $P$ as well as with decreasing $T$ up to values of $\varepsilon_r \approx 1.093$ at $P = 19.4\,\mathrm{MPa}$ and $T = 6\,\mathrm{K}$. At high temperatures, the dielectric constant shows a weak temperature dependence, whereas it has a very strong temperature dependence at low temperatures, i.e., in the region of interest for the performed measurements. Apparently, the dielectric constant $\epsilon_r(P, T)$ shows a weak temperature dependence down to about $50\,\mathrm{K}$ for lower pressure. At the same time, the increase at low temperatures is much steeper for the low-$P$ data, see, e.g., the data at $4\,\mathrm{MPa}$. Moreover, the strong increase at low temperatures is characterized by an inflection point at low temperatures ($T \approx 20\,\mathrm{K}$).

These experimental results can be compared to theoretical calculations that consider helium as a van-der-Waals gas with pressure-dependent volume of the molecules (for details of the calculations see Sec. A.1.). The results of the calculations are shown by broken lines for exactly the same pressures, at which measurements were performed. They confirm the general tendency of the curves, namely a strong increase of $\varepsilon_r$ to low temperatures. Especially at high temperatures they describe the measured data quite well[8], whereas below $T \approx 40\,\mathrm{K}$ strong deviations to the experimentally obtained data can be observed. In all cases, the theoretical approach underestimates the absolute value of the dielectric constant at low temperatures. In addition, the theoretical approach is also not able to capture the inflection point in the experimental data of $\epsilon_r(T, P)$. As the increase at low temperatures is steeper for lower pressures, the theoretical description seems to become more appropriate at higher pressures, at which the increase is weaker. All in all, the deviations from the van-der-Waals description are becoming apparent as lower the temperature and pressure are. It can be speculated that the discrepancies can be explained by the presence of the critical endpoint of the liquid-gas transition line in $^4$He at a low temperature of 5.2 K and low pressure of 0.22 MPa [97], which involves strong fluctuations of the particle density, and/or quantum effects. However, in order to substantiate this speculation, clearly more measurements in the low-pressure regime are necessary.

Unfortunately, until now, the model calculations do not describe the experimental data with high-enough accuracy. Thus, a detailed understanding of the dielectric constant as a function of $P$ and $T$ is missing. For this reason, an accurate experimental determination of $\varepsilon_r(T, P)$ in the range $20\,\mathrm{K} \leq T \leq 57\,\mathrm{K}$ and $10\,\mathrm{MPa} \leq P \leq 30\,\mathrm{MPa}$ was performed, which is used as an input for the analysis of the data shown in chapter 5, which were taken in this temperature and pressure range. In order to get a comprehensive set of data, measurements were performed as a function of $T$ at constant $P$ as well as as a function of $P$ at constant $T$ (see figure 3.5 (A) and (B), respectively). To this end, pressure steps of about 1 MPa and temperature steps of about 1 K were used. The step width was chosen close enough so that an interpolation between two data sets gives results of high-enough accuracy (see Appendix A.2 for a test of the interpolation procedure). Both data sets lie on top of each other within the error margin of $\Delta\varepsilon_r \approx \pm 1 \cdot 10^{-4}$. Within the investigated $T$-$P$-range, $\varepsilon_r(P, T)$ varies up to 3%, thus representing a rather large $T$- and $P$-dependent background contribution. This in turn illustrates that the dielectric constant has to be determined with a very high precision. The reproducibility of these measurements is indicated in figure 3.5 (A) by two measurements taken at nearly identical pressures, i.e., at $P = 26.25\,\mathrm{MPa}$ and 26.35 MPa, which show an almost identical behavior. The small offset results only from the small pressure difference of $\Delta P = 0.1\,\mathrm{MPa}$, which is just slightly larger than the range, in

[8] At this point, it is worthwhile to mention that small offsets can results from the previously-mentioned capacitance jumps. Since the coefficient of thermal expansion $\alpha \propto \frac{\mathrm{d}C}{\mathrm{d}T}$ with $C \propto \epsilon_r$, a precise knowledge of $\frac{\mathrm{d}\epsilon_r}{\mathrm{d}T}$ is required.

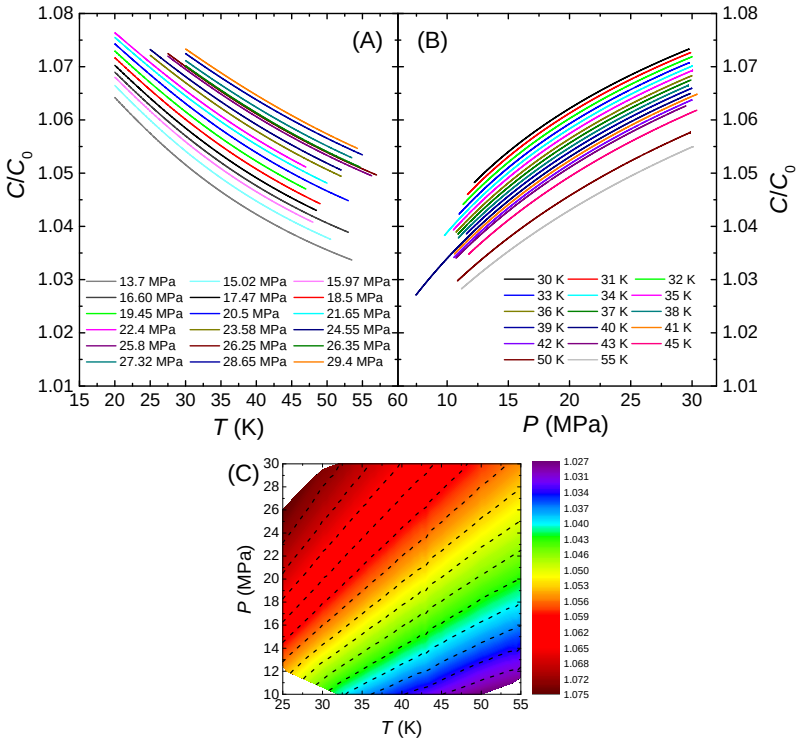


Figure 3.5.: (A) Experimentally determined dielectric constant of $^4$He $\epsilon_r(P,T) = \frac{C(P,T)}{C(P=0,T)} = \frac{C}{C_0}$ at constant pressures between 13.7 MPa and 29.4 MPa; (B) Experimentally determined dielectric constant $\epsilon_r(P,T) = C/C_0$ at constant temperatures between 30 K and 55 K; (C) Contour plot of the interpolated dielectric constant in the above mentioned $T$-$P$-range which is used to analyze thermal expansion under pressure data. Broken lines show constant-$\varepsilon_r$ lines in the investigated $T$-$P$-range with $\Delta\varepsilon_r = 0.003$ between two lines.

which the pressure can be kept constant $|\Delta P| < 0.05$ MPa. In order to obtain the dielectric constant for every $T$ and $P$ value within the investigated $T$-$P$-range, the data set $\varepsilon_r(P,T)$ was interpolated, the result of which is shown in figure 3.5 (C). It was used for the analysis of all the experimental data, shown in chapter 5.

### Correction of background contributions

In order to calculate length changes from capacitance data, which were taken under pressure, the raw capacitance data are first divided by the corresponding value of the experimentally determined dielectric constant $\varepsilon_r(T,P)$ at the given $T$ and $P$ values. This procedure yields capacitance values $C_0$, which are corrected for the dielectric constant of $^4$He.

$$C_0(T, P = \text{const.}) = C(T, P = \text{const.})/\varepsilon_r(T, P = \text{const.}) \quad (3.10)$$

$$C_0(T = \text{const.}, P) = C(T = \text{const.}, P)/\varepsilon_r(T = \text{const.}, P) \quad (3.11)$$

These $C_0(T, P)$ data now reflect only length changes of the sample and the cell, at fixed pressure as a function of $T$ or at fixed temperature as a function of $P$. Therefore the data can be processed similarly as in the ambient pressure case, as illustrated above, in order to obtain the relative length change $\Delta L/L$[9] and the thermal expansion coefficient $\alpha$.

## 3.2. Magnetization measurements with a SQUID magnetometer

Magnetization measurements in a temperature range $2\,\text{K} \leq T \leq 300\,\text{K}$ and in a field range of $0\,\text{T} \leq B \leq 5\,\text{T}$ were performed by using a commercial SQUID magnetometer MPMS-XL5 from Quantum Design. SQUID magnetometry provides the most precise determination of flux changes (for more details, see [104]).

In addition, we were able to combine the SQUID measurements with an available He-gas pressure cell (GC10/3, Unipress) which can be operated up to a maximum pressure of 500 MPa.

## 3.3. Other techniques

Within this thesis, some results of complementary transport and thermodynamic measurements are discussed. As these data were not obtained by the author of this thesis, here only a short summary of these techniques will be given.

### 3.3.1. Transport measurements under $^4$He-gas pressure

In this thesis, some results of resistance measurements under $^4$He-gas pressure and dielectric measurements will be presented. The former measurements were performed by Sebastian

[9] We note that the volume compressibility of Cu of $\kappa_V \approx 6 \cdot 10^{-6}$/MPa [102] is distinctly smaller than the compressibility determined for an organic charge-transfer salt of $\kappa_V = 80 \cdot 10^{-6}$/MPa [103]. As a consequence, due to the lack of a precise determination of the compressibility of Cu at low temperatures and low pressures, the contribution of the Cu cell was neglected in the analysis of the expansion data as a function of $P$. Consequently, $\Delta L_{sample}(P, T = \text{const.}) = \Delta L_{meas}(P, T = \text{const.})$ was used. This neglects a very small linear background contribution to the relative length change data as a function of $P$ due to the neglected expansion of Cu.

Köhler and David Zielke in the group of Prof. Dr. M. Lang, whereas the latter ones were performed by Jonas Fischer and Dr. Peter Lunkenheimer at the University in Augsburg.

For both of these measurements, the samples were contacted in a four-terminal configuration. The resistance is measured with a DC current of $1\,\mu$A with the current applied within the plane. Dielectric measurements were performed in an out-of-plane configuration with a small AC current with varying frequency.

### 3.3.2. Specific heat measurements

Measurements of the specific heat were performed by David Zielke in the group of Prof. Dr. M. Lang by using a home-built *ac* calorimeter [105] which allows for a precise determination of the specific heat of small single crystals in the temperature range $1.8\,\mathrm{K} \leq T \leq 35\,\mathrm{K}$.

## 3.4. Sample preparation

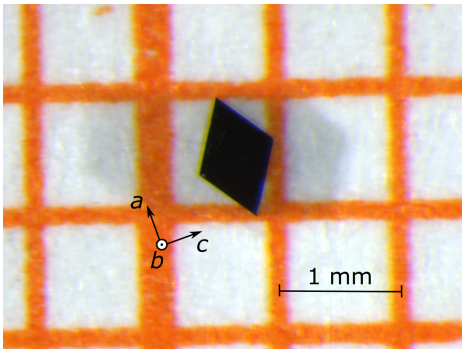


Figure 3.6.: Representative picture of a crystal of an organic-charge transfer salt. Shown here is a crystal of $\kappa$-(BEDT-TTF)$_2$Cu[N(CN)$_2$]Cl from Batch #AF063, with view on the in-plane $a$ and $c$ axis. The $b$ axis is oriented perpendicular to the image plane.

Crystals of the organic charge-transfer salts $\kappa$-(ET)$_2X$ were prepared by Dr. H. Schubert in the group of Prof. Dr. M. Lang. Furthermore, some crystals were also provided by collaborators (Dr. J. A. Schlueter, Argonne National Laboratory/National Science Foundation, USA and Prof. Dr. T. Sasaki, Institute for Material Research, Sendai, Japan). The preferred growth technique for these crystals, consisting of a donor and an acceptor molecule, is the method of electrochemical crystallization. Here, the organic neutral donor molecules are oxidized at the anode surface by a controlled current rate between the cathode and the anode. These radical cations can then recombine with the charge-compensating anions that are dissolved in the solution. Crystals of either block- or needle-like shape start to grow at the anode surface [13].

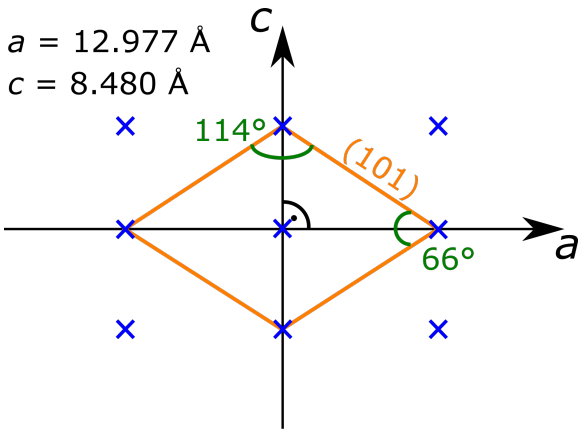


Figure 3.7.: Scheme for the determination of the angles between (101) surfaces of the organic charge-transfer salt $\kappa$-(BEDT-TTF)$_2$Cu[N(CN)$_2$]Cl. This system has an orthorhombic crystal structure with three perpendicular axes. The scheme shows a view on the $ac$ plane. Blue crosses indicate lattice points within this plane the positions of which are determined by the lattice parameters ($a = 12.977$ Å and $c = 8.480$ Å). Orange lines correspond to (101) surfaces. These surfaces cut in angle of 66° and 114° at the $a$ axis and $c$ axis.

The crystals typically have in-plane dimensions of about $0.7 \times 1\,\mathrm{mm}^2$ and out-of-plane dimensions of about 0.5 mm (see Fig. 3.6). The orientation of each crystal was determined by an analysis of the crystal angles by using the knowledge of the crystal structure parameters. Exemplarily, the characteristic angles for $\kappa$-(BEDT-TTF)$_2$Cu[N(CN)$_2$]Cl, an in-depth investigated material in this work, will be given. As confirmed by x-ray investigations [106], this material has the tendency to grow with (101) surfaces. These planes cut in an angle of 66° and 114° at the $a$ axis and $c$ axis, respectively (see Fig. 3.7).

# 4. Properties of organic charge-transfer salts

The search for conducting materials based on organic molecules has been a long-standing and intensive research field at the common interface between chemistry and physics. The discovery of the first conducting organic charge-transfer salt TTF-TCNQ in 1973 [107] and the subsequent discovery of superconductivity in $(TMTSF)_2PF_6$ [108], opened the new and diverse research field of low-dimensional molecular conductors. These materials are outstanding by the variety of accessible physical ground state properties, including superconductivity, unusual metallic and insulating states, charge- and spin-density-waves, exotic magnetic properties, such as spin-liquid states, as well as ferroelectricity. This diversity is complemented by a great variety of organic donor and acceptor molecules as a starting point for the synthesis of new materials. The so-designed materials are characterized by a high tuneability of dimensionality and interaction strengths. The focus of the present work lies on the study of physical properties at the boundary of the metallic and insulating phases of quasi-two-dimensional (quasi-2D) organic charge-transfer salts, which are based on the organic donor molecule BEDT-TTF. In the following, the properties of these salts from structural and physical points of view will be introduced. The content of this chapter is mainly based on Ref. [13].

## 4.1. Charge transfer

In order to realize metallic behavior, free charge carriers have to be created, the wave functions of which are delocalized throughout the crystal.

Free charge carriers are generated by a charge-transfer process between two initially neutral molecules, namely one electron-rich donor molecule $D$ with low ionization energy and an acceptor molecule $A$ with high electron affinity, which are combined in a ratio of $m : n$. In the resulting system $D_mA_n$, the donor molecule carriers a positive charge $\delta$ and the acceptor molecule a negative charge $-\delta$, whereas $\delta$ is denoted as the charge-transfer ratio.

$$[D_m] + [A_n] \rightarrow [D_m]^{+\delta} + [A_n]^{-\delta}. \tag{4.1}$$

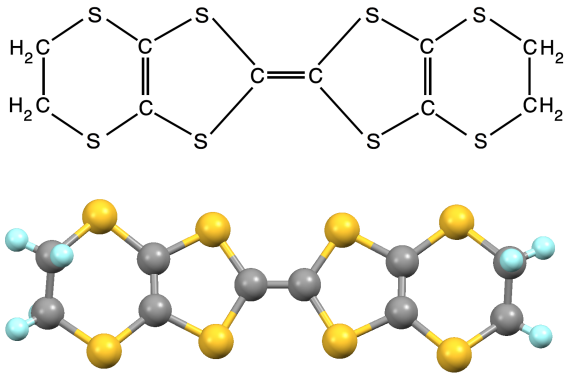


Figure 4.1.: BEDT-TTF-molecule (abbreviated as ET) consisting of 10 carbon atoms (grey), 8 sulfur atoms (yellow) and 8 hydrogen atoms (cyan) (after [109]).

The amount of free charge carriers and thereby the band filling is fixed by the charge-transfer process. In most of the organic charge-transfer salts, donor and acceptor molecules are combined in a ratio 2:1 with a charge-transfer ratio of $\delta = 1$, i.e., a charge transfer of one electron from two donor molecules to one acceptor molecule. As the acceptor molecules adopt a closed-shell configuration after the charge-transfer process, they do not contribute free charge carriers anymore and the remaining free charge carriers are the hole carriers on the donor molecules. As a result, the conduction band is quarter-filled in terms of hole carriers. The charge-transfer process is distinctly different from a doping process in various aspects. In particular, the charge-transfer process allows to control the band-filling in a particularly clean manner, as no doping atoms are involved which act as impurities.

These charge carriers (holes) are delocalized over the crystal as the molecular orbitals overlap due to the rather dense packing of the molecules, i.e., by *inter*molecular processes. The molecular orbitals here are $\sigma$ and $\pi$ orbitals, which are formed of overlapping $s$ and $p$ orbitals of the single atoms of the donor molecule. Whereas the $\sigma$ orbitals are rather localized, the $\pi$ orbitals are extended perpendicular to the molecular axis allowing for a sizable overlap with the neighboring molecules. As the hole carriers on the $\pi$ orbitals have a comparably low binding energy, they can be easily excited. Often the consideration of either the highest occupied molecular orbital (HOMO) or the lowest unoccupied molecular orbital (LUMO) is sufficient to describe the material's physical properties. They are used as an input for tight-binding calculations of the band structure.

The most widely used organic donor molecules are derivatives of tetrachalcogenafulvalene (TCF), such as BEDT-TTF, which is used as a donor for the synthesis of quasi-2D charge-transfer salts. BEDT-TTF ($C_6S_8[(CH_2)_2]_2$) stands for *bis(ethylenedithio)tetrathiafulvalene* and is often abbreviated as ET (see Fig. 4.1).

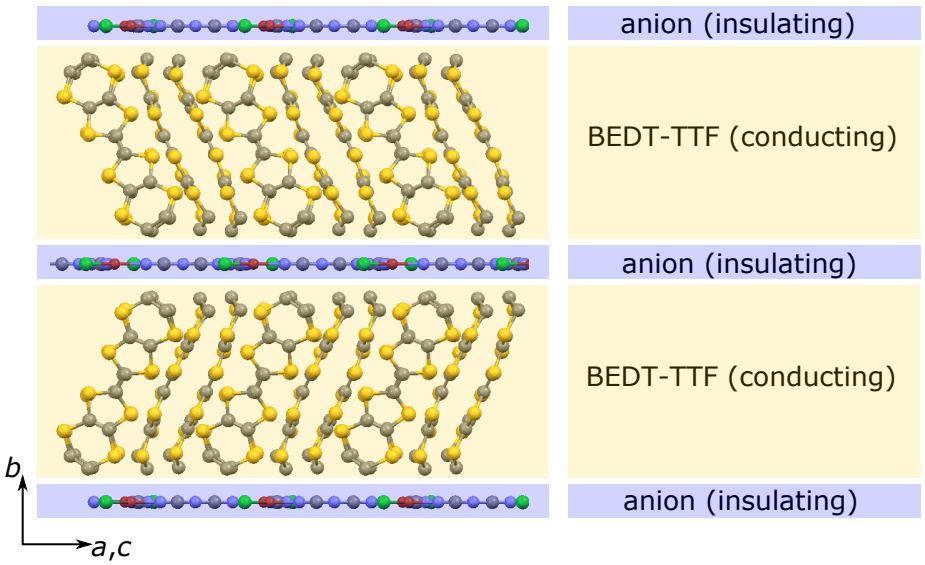


Figure 4.2.: Structure of an BEDT-TTF(ET)-based organic charge-transfer salt with alternating $(ET)_2^+$-layers (conducting) and $X^-$ anion layers (insulating) along the $b$ axis, reflecting the quasi-2D character of these systems within the $ac$ plane. Hydrogen atoms are omitted for clarity.

## 4.2. Structure of (BEDT-TTF)-based charge-transfer salts

As mentioned above, the $\pi$ orbitals are extended perpendicular to the molecular planes and lead to a delocalization due to the $\pi$-orbital overlap of neighboring molecules. This in turn enables a control of dimensionality in these systems by adjusting the $\pi$-orbital overlap in the various crystallographic directions. Typically, systems with organic donors like TMTTF favor a quasi-1D behavior, whereas systems with donors such as BEDT-TTF yield a more quasi-2D behavior. In the following, the focus will lie on the quasi-2D organic charge-transfer salts and their peculiar structural motifs. They are characterized by a layered structure (see Fig. 4.2), which is characteristic for a low-dimensional system, with alternating $(ET)_2^+$-layers and $X^-$ layers with $X$ being the acceptor molecule. The insulating anion layers thereby prevent an overlap of the $\pi$ orbitals along the out-of-plane direction. Thus, the dominant $\pi$-orbital overlap is found within the $(ET)_2^+$-layer, featuring an only weakly anisotropic overlap of the $\pi$ orbitals. The materials follow a rational design principle, which is based on the properties of the ET molecule. One key aspect is that upon formation of the crystal the neutral, distorted ET molecule becomes planar (except for the ethylene end groups, as discussed later), which allows for a closer packing of the ET molecules. The ET molecule itself has enlarged $\pi$ orbitals in comparison to TMTTF, which is a typical donor for the formation of quasi-1D salts, as the ET molecule contains more carbon rings. In addition, the ET molecules cannot form infinite face-to-face stacks. Consequently, in contrast to the quasi-1D salts, the interactions within the plane are of the same order of

magnitude, thus forming a 2D conduction plane. Experimentally, the directional-dependent conductance was found to reflect this strong structural anisotropy: Whereas the in-plane conductance displays only a weak anisotropy, the out-of-plane conductance is orders of magnitude lower owing to the insulating anion layers (see Fig. 4.2).

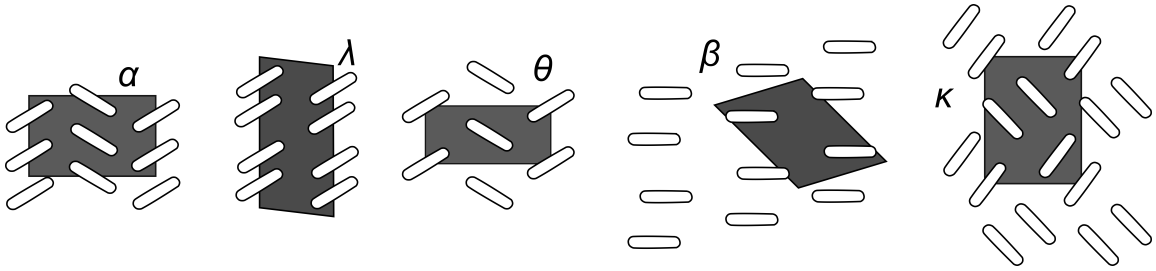


Figure 4.3.: Scheme of the spatial arrangement of the ET-molecules (white ellipses) for the different polymorphic phases that are labeled with Greek letters ($\alpha$, $\lambda$, $\theta$, $\beta$ and $\kappa$) together with their unit cells (grey ares) (Figure reprinted from Ref. [13] with permission of Springer).

A peculiar structural motif of the ET-salts, relevant for their physical properties, is that the loose intra-stack coupling leads to various polymorphic phases (see Fig. 4.3). These are distinguished by different packing schemes of the ET molecules and labeled by the Greek letters $\alpha, \beta, \lambda, \kappa$ and $\theta$. Herein, the $\kappa$-phase, in focus of this work, is outstanding, as it does not form interacting stacks, but interacting dimers, which consist out of two face-to-face-aligned ET molecules. Neighboring dimers are oriented nearly perpendicular to each other, resulting in a weak in-plane anisotropy.

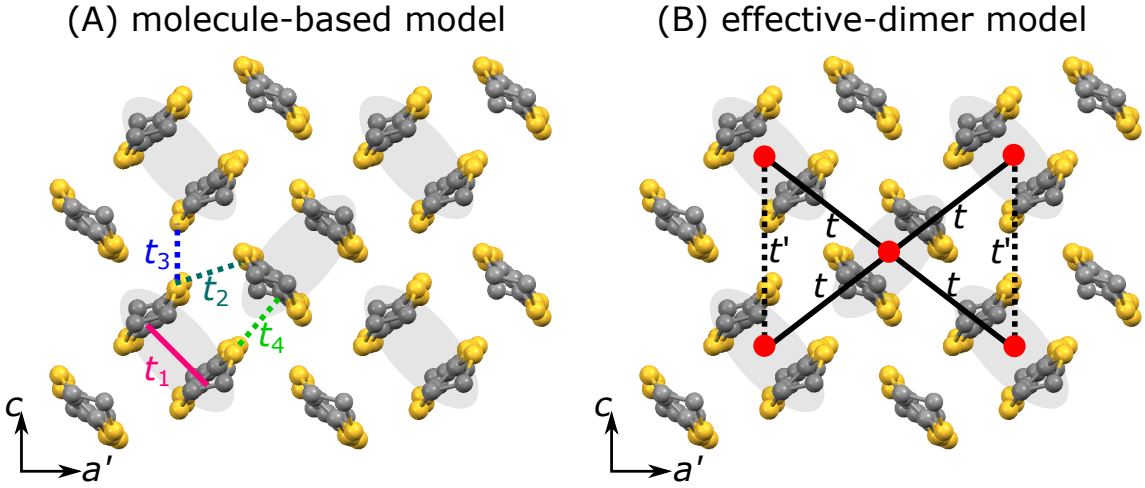


Figure 4.4.: (A) View on the conduction plane of $\kappa$-$(ET)_2X$ salts, which demonstrates the typical $\kappa$-type arrangement of ET molecules. Grey ellipses indicate the two ET molecules, which form one dimer. The solid and broken lines denote the four important hopping parameters $t_1$ to $t_4$ in a molecule-based model. (B) Within the effective-dimer model, each dimer corresponds to one lattice site (red circle). These lattice points form a triangular lattice, which is a frustrated lattice with interactions $t$ and $t'$. Hydrogen atoms are omitted for clarity.

| Anion $X$ | $Cu[N(CN)_2]Cl$ [112] | $Cu[N(CN)_2]Br$ [113] | $Hg(SCN)_2Cl$ [34] |
|---|---|---|---|
| Structure | orthorhombic *Pmna* | orthorhombic *Pmna* | monoclinic *C2/C* |
| $a$ (Å) | 12.977 | 12.948 | 36.596 |
| $b$ (Å) | 29.979 | 29.961 | 8.289 |
| $c$ (Å) | 8.480 | 8.535 | 11.750 |
| $\alpha$ (°) | 90 | 90 | 90 |
| $\beta$ (°) | 90 | 90 | 90.067 |
| $\gamma$ (°) | 90 | 90 | 90 |

Table 4.1.: Room-temperature crystallographic data for three different organic charge-transfer salts of the $\kappa$-$(BEDT\text{-}TTF)_2X$ family investigated in this thesis: $a, b, c$ are the lattice parameters, $\alpha, \beta, \gamma$ the angles. Note that for $\kappa$-$(BEDT\text{-}TTF)_2Cu[N(CN)_2]Cl$ and $\kappa$-$(BEDT\text{-}TTF)_2Cu[N(CN)_2]Br$ the $b$ axis is the out-of-plane axis, but for $\kappa$-$(BEDT\text{-}TTF)_2Hg(SCN)_2Cl$ the $a$ axis corresponds to the out-of-plane axis.

As implied by the arrangement of the ET molecules in the $\kappa$ phase, the hopping interaction between the two ET molecules forming the dimer $t_1$ (see Fig. 4.4 (A)) is much larger than the hopping to the ET molecules of neighboring dimers $t_2, t_3$ and $t_4$ due to the larger overlap of the molecular orbitals. This was confirmed by theoretical calculations, which claim that $t_1$ is at least twice as large as $t_2$, $t_3$ and $t_4$ (e.g. [110]). These materials are therefore usually treated in an *effective-dimer model* [111], in which one dimer corresponds to one lattice site (see Fig. 4.4 (B)). This ansatz is justified, as the strong dimerization leads to a splitting of the conduction band into two bands, the bonding and anti-bonding bands, separated by a dimerization gap. The size of the gap is determined by $t_1$ and hence large enough that intra-dimer effects can be treated as a small perturbation. As in this approximation, one lattice site carries one hole on average, the conduction band, which is composed of the anti-bonding dimer orbital, is effectively half-filled. The interactions between the dimers can be reduced to two main contributions, namely $t$ and $t'$, which are determined by the hopping terms to the individual molecules of neighboring dimers. They are related to $t_2$, $t_3$ and $t_4$ by $t = (|t_2| + |t_4|)/2$ and $t' = |t_3|/2$ [111]. As the lattice is in this case a triangular lattice, the interactions $t$ and $t'$ promote magnetic frustration in these systems.

The systems with $X$ = $Cu[N(CN)_2]Cl$, $Cu[N(CN)_2]Br$ or $Cu_2(CN)_3$ represent the most intensively studied materials of the $\kappa$-$(ET)_2X$ family. The former two anions form polymeric chain-like structures, whereas the latter one forms a planar network of Cu ions. Depending on the choice of the anion, these materials are at low temperatures either antiferromagnetic Mott insulators, superconductors or spin-liquid candidate materials. This high sensitivity to small modifications in the crystal structures or packing motifs (see Tab. 4.1 for crystallographic data for selected $\kappa$-$(ET)_2X$ salts) reflects that small changes of the $\pi$-orbital overlap have significant consequences.

So far, mainly inter-molecular degrees of freedom were discussed. Nevertheless, these organic charge-transfer salts are built of extended and complex molecules instead of single-

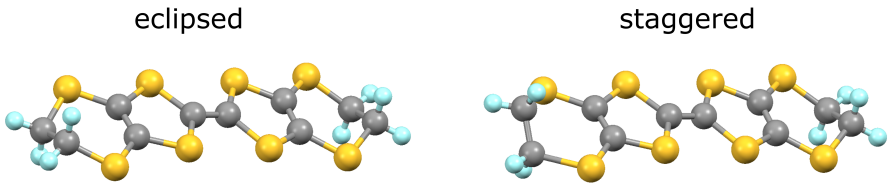


Figure 4.5.: Eclipsed (left) and staggered (right) confirmation of the ethylene end groups in the BEDT-TTF molecule (after [114]).

point like atoms, making the considerations of intra-molecular degrees of freedom inevitable. Importantly, the ethylene end groups of the ET molecule can adopt two different configurations, an eclipsed and a staggered conformation (see Fig. 4.5), referring to an either parallel or canted orientation of the outer C-C bonds with respect to each other. As the switching between the two orientations is a thermally-activated process, the ethylene end groups are disordered at high temperatures and freeze in many materials into one of these configurations at low temperatures in a glassy manner. The low-temperature configuration depends on the anion and the crystal structure. Although the differences in these conformations are small, they can cause subtle changes in the overlap of the $\pi$ orbitals and thereby influence the electronic structure, see, e.g., Ref. [115]. In addition, due to the glassy-freezing a certain amount of intrinsic structural disorder [49] is unavoidable. The amount of disorder can be controlled by the cooling speed through $T_g$ (see Sec. 4.3).

## 4.3. Physical properties and phase diagrams of the $\kappa$-(BEDT-TTF)$_2X$ family

Despite their complexity in real space, the $\kappa$-(ET)$_2X$ systems are considered as model systems to investigate the physics of strong electron correlations, as the effective-dimer model is a relative simple model to account for the various ground state properties. The electronic correlations are in this material class particularly strong, in some cases even exceeding the electron's kinetic energy. As these systems are effectively half-filled, they are often situated close to an experimentally accessible interaction-induced Mott transition.

The correlations are particularly enhanced in these materials for various reasons: First, the carrier density is quite small ($\approx 10^{-21}\,\mathrm{cm}^{-3}$) due to the large-sized organic molecules, which house only one free charge carrier. Taking also the low dimensionality of these systems into account, screening of Coulomb interactions is less effective in contrast to normal metals, resulting in a comparably large effective $U$ value of the order of $U \approx 0.5\,\mathrm{eV}$. Second, the bandwidth, which measures the kinetic energy, is relatively small owing to the small overlap of $\pi$ orbitals, so that these system have narrow bands with $U \sim W \sim 0.5\,\mathrm{eV}$.

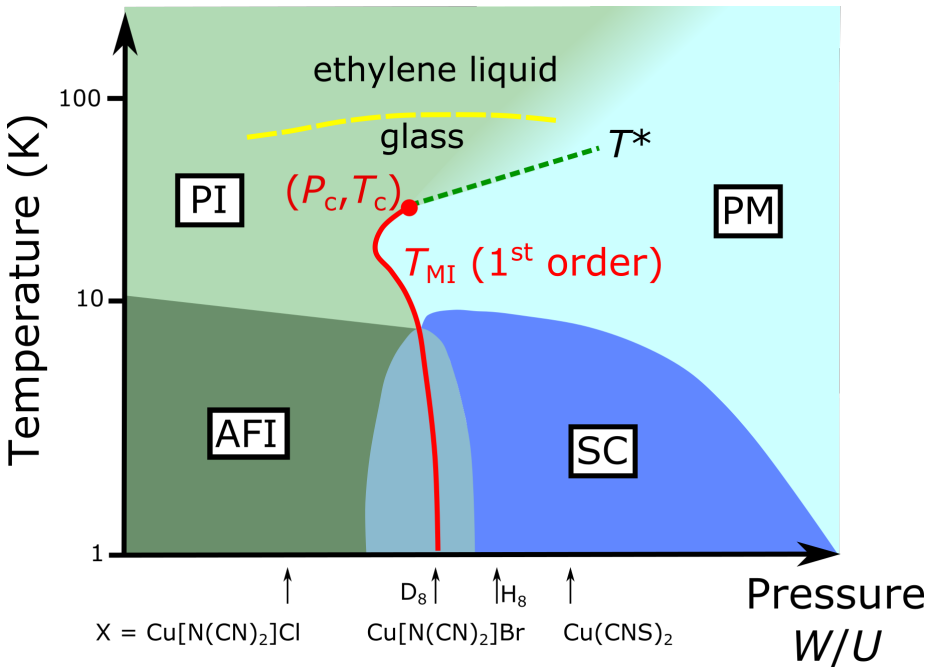


Figure 4.6.: Schematic phase diagram of the κ-(ET)$_2X$ family as a function of pressure, the correlation strength $W/U$, or for different anions $X$. PI (AFI) refers to the paramagnetic (antiferromagnetic) insulating state, PM to the paramagnetic metallic state, SC to the superconducting state. The red line corresponds to the first-order transition line between the Mott insulating and the metallic state, which ends in a second-order critical endpoint located at $(P_c, T_c)$ (red circle). The green line indicates the position of the $T^*$ anomaly, for detail see text. The yellow line indicates the position of the glassy freezing of the ethylene end groups at $T_g \approx 70\,\mathrm{K}$. The arrows indicate the position of the materials with different anions $X$ in this generalized phase diagram (Data from [66,116–119], picture after [12,114]).

The concept of considering these systems as model systems [12] is that the application of pressure on these materials is equivalent to tuning the ratio $U/W$. The latter parameter is the key parameter in the Hubbard model, the simplest model for describing strongly correlated electron systems (see Sec. 2.4). Therefore, pressure studies on these systems provide a good test ground for exploring fundamental aspects of correlated electron systems, since pressure provides a very fine-tuneable and clean working environment. The analogy between $P$ and $U/W$ is motivated by the fact that various κ-phase materials with different $X$, in which the choice of the anion $X$ corresponds to different chemically-induced pressure values, on either side of the Mott transition all have a half-filled conduction band. Hence, the Mott transition for the present case of the organic charge-transfer salts is a bandwidth-controlled MIT. The effect of pressure is to change the spacing between the ET molecules, which changes the overlap of the $\pi$ orbitals and, consequently, the bandwidth $W$ increases and the correlation strength $U/W$ decreases.

The unified phase diagram, combining the effects of correlation strength $U/W$, physical pressure $P$ or chemical pressure, is shown in Fig. 4.6 [12]. It was mapped out by various transport [18, 66, 118], magnetic (NMR and ac-susceptibility [116]) and lattice (ultrasound [117] and thermal expansion [119]) probes, either as a function of applied hydrostatic pressure or by changing the anion $X$. The prominent feature in the phase diagram is the first-order transition line (red line), which separates the Mott insulating state from the metallic state. The line ends in a second-order critical endpoint. The universal behavior around the Mott critical endpoint is a long-lasting issue of great importance for the community of strongly correlated electron systems, as it is believed to hold the clue for a better understanding of the Mott transition itself. These fundamental properties will be in the focus of chapter 5, in which the existing literature of theoretical and experimental work will be reviewed before the new results from the present study on the organic conductors will be presented. In particular, it will be demonstrated that the electron-lattice coupling is of importance here, which sheds light on the controversially discussed topic of the Mott transition.

Even if the Mott transition itself is of high interest, the phases in its near proximity are not less exciting. Systems on the insulating side of the transition, as e.g. $\kappa$-$(ET)_2Cu[N(CN)_2]Cl$, show antiferromagnetic order, whereas the systems on the metallic side often turn superconducting at low temperatures with transition temperatures as high as $T_c \approx 12\,\mathrm{K}$, the highest $T_c$ among all organic charge-transfer salts (see the phase diagram in Fig. 4.6). The competition of magnetic ordering and superconductivity close to the Mott transition is reminiscent of the phase diagram of the high-temperature cuprate superconductors [120] which undergo a bandfilling-controlled MIT. These similarities, including the quasi-2D character, make the organic charge-transfer salts suited reference systems to explore possible superconducting pairing mechanisms, which are often speculated to be of magnetic origin. The key for unraveling the pairing mechanism is often sought after in the determination of the superconducting gap symmetry. This is, however, difficult to be determined unambiguously by experiments, as discussed in various reviews on that topic, see, e.g., Refs. [121, 122], with ongoing efforts [123].

In regard to the similarities to the cuprates, the unusual metallic behavior in the normal state should also be mentioned. Various measurements of transport, magnetic, as well as elastic properties indicated an anomalous behavior around $T^* \approx 40\,\mathrm{K}$ (see green dashed line in fig. 4.6). Around this temperature there is a crossover from a Fermi-liquid metallic behavior at low temperatures to a bad-metal behavior at high temperatures. Various interpretations of these observations were proposed over the years, stemming from the analysis of different probes. The opening of a pseudo-gap in the spin-excitation spectrum [12, 124], a reduction of the density of states at the Fermi level [125–128], the formation of a density-wave-instability [119, 129] or a purely correlation-driven mechanism, as proposed by DMFT

calculations [116, 130], including a divergence of the compressibility of electronic degrees of freedom close to the Mott endpoint [117, 131], were suggested to explain the observed anomalies at $T^*$. More recent thermodynamic considerations on the behavior close to a second-order critical endpoint suggested that this crossover is closely linked to the critical endpoint [132] and can be understood in the framework of the scale invariance of the critical properties around the Mott endpoint [20]. The identification of these crossover features served as an important criterion for the determination of the critical endpoint and was indispensable for discussing the critical behavior in the present work, as will be discussed in detail in chapter 5.

Exciting materials on the Mott insulating side of the transition are κ-$(ET)_2Cu[N(CN)_2]Cl$ (abbreviated as κ-Cl hereafter) and κ-$(ET)_2Cu_2(CN)_3$ (abbreviated as κ-CuCN hereafter). NMR measurements identified the former material to undergo a transition into a commensurate antiferromagnetic state at $T_N \approx 27\,\mathrm{K}$ with an ordered moment of $(0.4\text{-}1)\,\mu_B$ [133]. The magnetic ordering is accompanied by a spontaneous canting of the spins at $T \approx 23\,\mathrm{K}$, implying a weak ferromagnetic moment, which was attributed to interlayer ordering along with an intralayer antiferromagnetic ordering. It was argued that the canting of the spins can be inferred from the presence of a Dzyaloshinskii-Moriya interaction [134]. In contrast, in κ-CuCN no magnetic order down to 32 mK was found [35] which is about 4 orders of magnitude smaller than the dominant exchange coupling of $J \approx 250$ K, identifying this system as a very promising candidate for a spin-liquid ground state. One particularly puzzling effect here is that various quantities (e.g., Ref. [135]) reveal anomalous behavior around 6 K, the origin of which is still unresolved.

| Anion $X$ | $t'/t$ | ground state |
|---|---|---|
| $Cu[N(CN)_2]Br$ | 0.42 | sc |
| $Cu[N(CN)_2]Cl$ | 0.44 | afm |
| $Cu(NCS)_2$ | 0.58 | sc |
| $Cu_2(CN)_3$ | 0.83 | spin-liquid? |

Table 4.2.: Calculated frustration ratios $t'/t$ for different κ-$(ET)_2X$ salts, together with their (proposed) ground state. sc stands for the superconducting state, afm for the antiferromagnetic state. Values taken from [136, 137].

To understand how these different magnetic ground states can evolve, a good estimate of the degree of frustration in these systems with triangular lattices is advantageous, which can be gained from various theoretical approaches. Table 4.2 summarizes results for $t'/t$ [136, 137]. These values, however, can vary slightly depending on details of the theoretical method used. There is consensus that the systems κ-$(ET)_2Cu[N(CN)_2]X$ with $X$ = Cl and Br show only a rather weak frustration, whereas κ-CuCN reveals a more isotropic lattice with a frustration ratio close to 1. This tendency is in agreement with the absence of magnetic ordering in this compound.

Nevertheless, these materials were in the focus of research not only because of their magnetic properties, but also lately due to their anomalous dielectric response [5, 76]. In both of these Mott insulating materials, the dielectric effects were attributed to intra-dimer charge degrees of freedom, i.e., effects beyond the effective-dimer model. However, this issue was controversially discussed in literature [138, 139]. In this respect, $\kappa$-Cl attracted special attention, as the dielectric response was attributed to a ferroelectric order, which coincides with magnetic order, making this material the first multiferroic charge-transfer salt [5]. This simultaneous occurrence of different types of ferroic order is indicative of a strong coupling of charge and spin degrees of freedom and led to the proposal of a new mechanism for multiferroicity, which is driven by charge order [5]. The experimental evidence for this scenario will be reviewed in more detail in chapter 6. In addition, a detailed study of $\kappa$-$(ET)_2Hg(SCN)_2Cl$ will be presented in chapter 7, which turned out to be a good reference system to study the coupling of charge and spin degrees of freedom in more detail.

After the discussion of the various low-temperature properties of these materials, the glassy freezing of the ethylene end groups at higher temperatures (see yellow dotted line in Fig. 4.6) and its implications on the electronic properties should be introduced. It was already mentioned that the ethylene end groups of the ET molecule can in principle adopt two conformations, the dynamics of which slows down rapidly at $T_g \approx 70\,\mathrm{K}$, preventing the system to order into one of these conformations. Instead, the system shows a glass-like freezing, in which the relative occupancy of the two different conformations depends on the cooling speed. The existence of such a glassy behavior was confirmed in many materials by various experiments [119, 140]. However, not all of these materials show a glassy freezing. Lately, a prediction for the occurrence of glassy behavior was made, based on *ab initio* calculations, which emphasize the importance of the coupling between the ET molecules and the anion layer in forming the glassy state [50]. The impact of this glassy freezing on the ground-state properties is twofold. On the one hand, the slightly different overlap of the $\pi$ orbitals of the ET molecules upon different cooling protocols, and correspondingly different occupancies of their ethylene end group conformations, can lead to significant changes of $W$ and thereby of the correlation strength $U/W$ [115]. This effect led to the idea of fine-tuning the systems by different cooling procedures, as the properties of such a system are completely reversible after heating the sample above $T_g$. This technique was applied to tune materials which are situated on the verge of the Mott transition across the critical $U/W$ ratio corresponding to that of the critical endpoint [49, 141]. On the other hand, the various cooling procedures are not only causing a change of $U/W$, but also a change of the amount of frozen disorder, which creates different random potentials. The importance of disorder is investigated by the Mott-Anderson model. Recently, an estimate of the amount of frozen disorder was presented in Ref. [49], claiming a disorder level in the range of a few percent for very high cooling speeds of more than 10 K/h. Within the

present work, the existence of a glassy freezing of the ethylene end groups in the material $\kappa$-(ET)$_2$Hg(SCN)$_2$Cl was detected by thermal expansion measurements. These results will be discussed in the context of newly proposed theoretical predictions of Ref. [50] in chapter 7.

Experimental access to the effects of disorder on the low-temperature properties of strongly correlated electron systems is highly desired to gain a deeper understanding of the behavior in real systems. The organic charge-transfer salts provide an ideal playground for such studies, as (i) they are in general very clean crystals, as demonstrated by quantum oscillation experiments [142] and (ii) as they offer various possibilities to introduce disorder in a well-defined manner. Besides employing different cooling speeds through the glass transition, which, as mentioned, is reversible, but nevertheless accompanied by a second effect, namely a change of $U/W$, an irradiation of the crystals with x-rays is used as another method to introduce disorder [143]. It was demonstrated that x-ray irradiation mainly creates molecular defects in the anion layer and leaves the conducting ET layer intact. The defects in the anion layer thereby create a random potential for the hole carriers in the ET layers. This process is in contrast to a charge-carrier doping, which was originally assumed to be the main mechanism induced by x-ray irradiation.

Typical irradiation times used in experiments range from 0 h up to 600 h, however, a quantitative estimate of the corresponding degree of disorder is difficult. The most pronounced effect of irradiation was observed on $\kappa$-(ET)$_2$Cu[N(CN)$_2$]Br, which showed to undergo a transition from a metallic phase with superconductivity at low temperatures to a disorder-induced Anderson-type insulating state [143]. Recently, the suppression of magnetic order in the Mott insulating $\kappa$-Cl by irradiation for 500 h [144] raised enormous interest in disorder-related phenomena. In this material, irradiation causes a decrease of the resistivity, which was assigned to a formation of a soft Coulomb gapped insulator [143]. However, the influence of disorder in these systems is still not well understood and asks for further work from experimental and theoretical side. In the present work, a short paragraph (Sec. 5.4) will be devoted to some preliminary studies on the influence of disorder on the behavior close to the Mott critical endpoint. In particular, the results are used to estimate the effect of disorder on the location of the first-order transition line of the Mott transition and the critical endpoint.

# 5. Mott criticality in the organic charge-transfer salts $\kappa$-(BEDT-TTF)$_2X$

The following chapter is devoted to the discussion of the universal properties of the Mott critical endpoint, which is experimentally accessible by applying external pressure on selected strongly correlated electron systems. As investigated in this work in detail by performing thermal expansion measurements around the critical endpoint[1], the fact that the transition is tuneable by pressure already indicates the decisive role of the lattice in this transition, which is driven by electron-electron interactions. By studying the organic charge-transfer salt $\kappa$-(ET)$_2$Cu[N(CN)$_2$]Cl, a prime example for examining the Mott transition in a particularly clean manner, it will be demonstrated that the coupling of electronic and lattice degrees of freedom drastically alters the critical properties. This study therefore goes beyond previous investigations, the considerations of which are solely based on electronic degrees of freedom. The chapter starts with an overview of related literature results. This will be followed by a detailed discussion of the results of thermal expansion providing new insights on how the coupling of electrons to a compressible lattice alters the critical properties.

## 5.1. Literature results

As outlined before in Sec. 2.2, the analysis of the critical behavior can provide insight into the collective behavior of an interacting many-body system. In turn, in order to fully understand the principles governing the transition, microscopic insight into its critical behavior is required.

General ideas on the critical behavior of the Mott transition are based on the similarities of the phase diagram to that of the liquid-gas transition. In the latter case, the order parameter is well known, namely the density difference between the liquid and the gaseous phase, which is a scalar quantity. Consequently, the critical behavior can be described by Ising critical exponents, meaning that the transition belongs to the Ising universality class.

[1] This work is a collaborative work between experimental physics, theoretical physics and material design, i.e., crystal growth. It was published as "*Breakdown of Hooke's law of elasticity at the Mott critical endpoint in an organic conductor*, E. Gati *et al.*, Science Advances **2**, e1601646 (2016) [145]". In particular, theoretical concepts and analyses presented in this chapter were developed by PD Dr. Markus Garst, Universität zu Köln and TU Dresden.

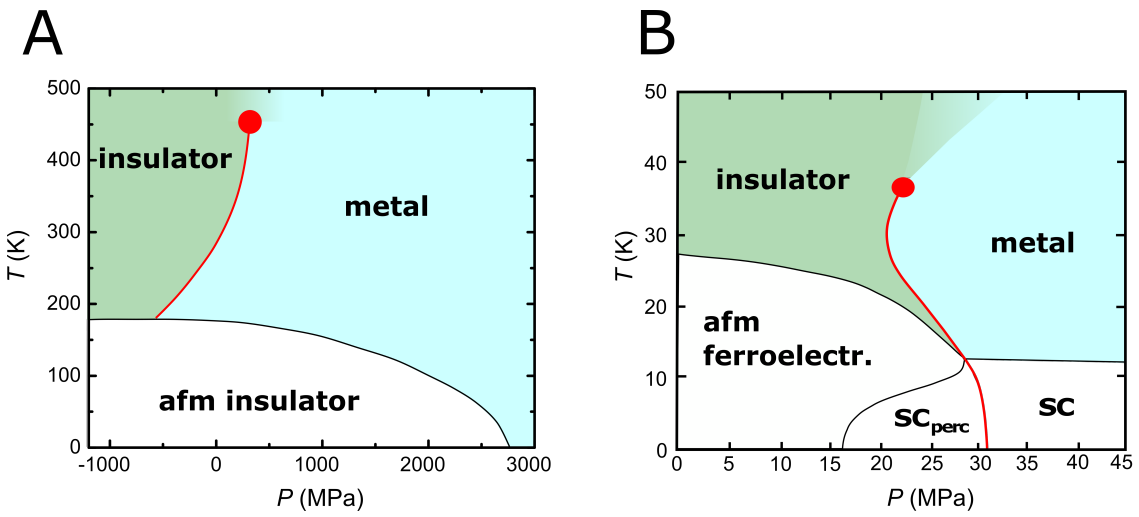


Figure 5.1.: Phase diagrams of $(V_{1-x}Cr_x)_2O_3$ [17,146] (A) and $\kappa$-(BEDT-TTF)$_2$Cu[N(CN)$_2$]Cl [66, 116–118] (B) under pressure. Red line corresponds to the first-order transition line, which ends in the second-order critical endpoint (red circle). The low-pressure side of the transition (green area) marks the insulating region, whereas the high-pressure side (blue area) marks the metallic region. At low temperatures, far below the critical endpoint, antiferromagnetic (afm) order or superconductivity (sc) can be observed.

However, the order parameter of the Mott transition is a matter of debate. This in turn drastically hampers the analysis of any experimentally determined quantity the relationship of which to the order parameter is unknown. Starting from the Hubbard model, which is a purely electronic model, it was argued [15, 16] that the number of double occupancies of lattice sites, i.e., the number of so-called doublons, could adopt the role of the order parameter. As this quantity is also a scalar, this ansatz led to the widely-accepted view that the Mott transition in a purely electronic system is governed by the same universal properties as the liquid-gas transition, corresponding to Ising criticality. Following this idea, the insulating phase with a low number and low density of doublons can be identified with the gaseous phase, whereas the metallic phase with a high density of doublons corresponds to the liquid phase.

Despite great efforts devoted to resolve the critical behavior around the Mott critical endpoint experimentally, no consensus has been achieved yet. Prime candidates to study a pressure-induced Mott critical endpoint include transition-metal oxides and the organic charge-transfer salts. Most of the efforts were concentrated on investigations of Cr-doped $V_2O_3$ and $\kappa$-(ET)$_2$Cu[N(CN)$_2$]Cl, the phase diagrams of which are shown in Fig. 5.1. Whereas the latter material is distinct by its quasi-2D electronic structure, the former one is 3D in character. Besides the structural differences, the phase diagrams are rather similar, despite the differences in the energy scales. The critical endpoint in these systems (red circle in Fig. 5.1) lies at $(P_c, T_c) \approx (373\,\mathrm{MPa}, 457\,\mathrm{K})$ [17, 146] and $(P_c, T_c) \approx (24\,\mathrm{MPa}, 36\,\mathrm{K})$

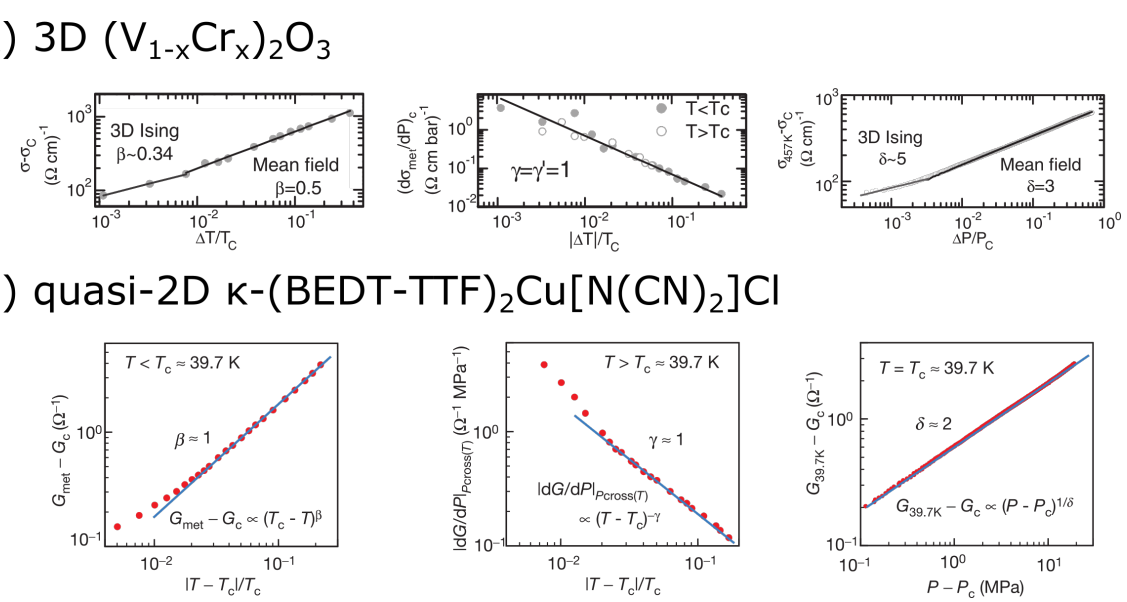


Figure 5.2.: Analysis of the conductance around the pressure-induced Mott critical endpoint in terms of the critical exponents $\beta, \gamma$ and $\delta$ in $(V_{1-x}Cr_x)_2O_3$ [17] (A) and the quasi-2D $\kappa$-(BEDT-TTF)$_2$Cu[N(CN)$_2$]Cl (B) [18], by examining the slope of various straight lines in double-logarithmic representations. Content reprinted from Ref. [17] with permission of the American Association for the Advancement of Science and from Ref. [18] with permission of the Nature Publishing Group.

[66, 116–118] for $(V_{1-x}Cr_x)_2O_3$ and $\kappa$-Cl, respectively. Noteworthy is the extraordinarily low pressure that is necessary to reach the critical endpoint in $\kappa$-Cl, which points towards a strong sensitivity of the electronic degrees of freedom to slight modifications in the lattice.

In order to evaluate the critical behavior in these materials, the order parameter has to be linked to an experimental observable. Following the suggestions provided by DMFT calculations, the double occupancy as the order parameter is supposed to be associated with the quasiparticle weight of the metallic phase at the Fermi level. It was argued that the quasiparticle weight is measurable by analyzing the metallic conductance close to the Mott transition [16, 59]. As this approach is based on calculations of the Hubbard model, it is only taking electronic degrees of freedom into account. In order to identify the universality class, the measured conductance was analyzed in double-logarithmic plots of the critical conductance with respect to either the reduced temperature or the reduced pressure for both of the above mentioned compounds (see Fig. 5.2). The results on Cr-doped $V_2O_3$ were interpreted to be consistent with the Ising universality class [17] (see Fig. 5.2 (A)), as the behavior seems to deviate from the mean-field critical exponents within a radius given by the Ginzburg criterion. In contrast, the set of critical exponents ($\beta = 1$, $\gamma = 1$, $\delta = 2$) proposed for $\kappa$-Cl [18] is neither fitting to the Ising universality class nor the mean-field universality class (see Tab. 2.2). Even though this set cannot be attributed to any known universality class, the exponents fulfill the scaling relations. Thus, it was claimed that

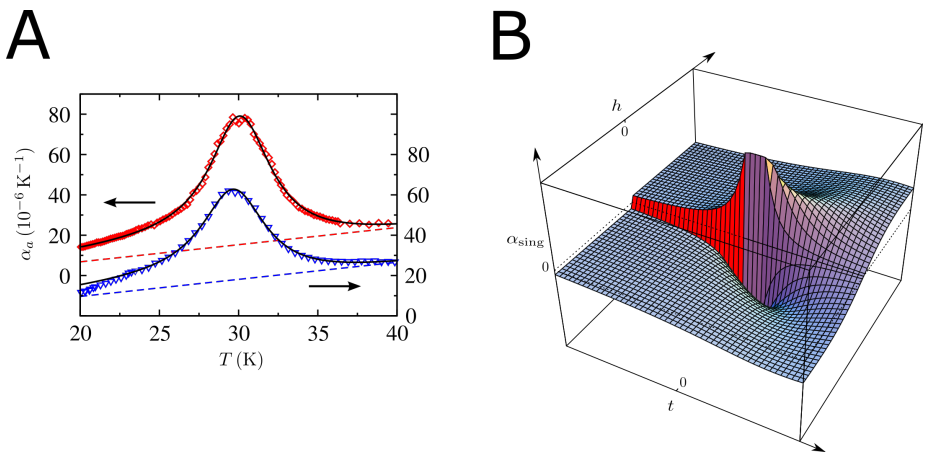


Figure 5.3.: (A) Study of the critical behavior by measurements of the thermal expansion coefficient $\alpha$ on deuterated $\kappa$-(BEDT-TTF)$_2$Cu[N(CN)$_2$]Br on two different samples (red and blue symbols). The black lines show fits of the thermal expansion data to the calculated expansivity for the 2D Ising universality class. (B) Theoretical prediction for the singular part of the thermal expansion coefficient $\alpha_{sing}$ around the pressure-induced Mott transition, based on the 2D Ising universality class. Content reprinted from [20] with permission of The American Physical Society.

the Mott transition in $\kappa$-Cl belongs to a new, *unconventional* type of universality class, which was proposed to be inherent to the system's quasi-2D structure implying pronounced quantum effects [147, 148]. The exponent $\delta$ was confirmed by NMR measurements [149], which assumed that antiferromagnetic correlations are reflecting the order parameter.

The analysis of the conductance, i.e., a transport quantity, for extracting the critical behavior and the resulting unconventional universality class, has been controversially discussed in literature. A main aspect in the discussion was the relation of the order parameter and the measured conductivity. It was argued that, in contrast to previous considerations by DMFT calculations, the global conductivity can in general depend on all singular observables, in particular also the energy density [150]. It follows that the critical conductance scales to the order parameter by the exponents $\alpha$ and $\beta$, $\Delta G \propto \phi^{(1-\alpha)/\beta}$ . A reanalysis of the conductance data on $\kappa$-Cl by Ref. [18] with this new scaling ansatz provided consistency with the 2D Ising universality class [150]. In addition, the authors associated the rather small critical region in $V_2O_3$ in comparison to $\kappa$-Cl with effects of quenched disorder in a random-field Ising model, which acts differently in three and two dimensions.

A different approach to the critical phenomena was provided by thermal expansion measurements. These experiments do not only offer a firm thermodynamic access to the critical phenomena, but are also capable to study the effects of the coupling of electronic to lattice degrees of freedom, an aspect, which was not included in the previous analyses of the critical exponents. The feasibility of thermal expansion measurements to investigate critical phenomena was nicely demonstrated by measurements on $\kappa$-(d8-ET)$_2$Cu[N(CN)$_2$]Br, in

which all eight hydrogen atoms in the ET molecule were replaced by deuterium [20, 132] (see Fig. 5.3 (A)). This material is situated right on the verge of the Mott transition (see Fig. 4.6) and can therefore be studied at ambient pressure to follow the signatures of criticality. The study revealed strong and pronounced lattice effects [132]. The analysis of the critical contribution to the thermal expansion coefficient $\alpha$ was initially performed on the basis of a scaling theory for the 2D Ising model, i.e., a simplified purely electronic model. The data set, taken at a chemical pressure equivalent to a physical pressure distance to the critical point of $P - P_c \approx 5\,\mathrm{MPa}$, was found to be fully compatible with the 2D Ising universality class (solid lines in Fig. 5.3 (A)). Even though the analysis of the experimental data does not provide an experimental proof of the universality class, as data is available only comparably far away from the endpoint, the results of the scaling theory derived in Ref. [20] allow to predict the behavior of $\alpha$ around the critical endpoint (see Fig. 5.3 (B)). Most importantly, a breakdown of the Grüneisen scaling ($\alpha \propto C$) was predicted for a finite-temperature critical endpoint, which until then was only established for a quantum-critical point [38]. Remarkable features predicted for the thermal expansion coefficient include a sign-change of $\alpha$ upon tuning the system across the transition and crossover lines, emanating from the critical endpoint (see Fig. 5.6 for the sketch of the location of the crossover lines in the phase diagram). These crossover lines were identified with the maximum response of the thermal expansion coefficient $\alpha_{max}(T)$ [20]. Indeed, indications in various physical quantities for such a crossover at $T^*$ were observed and reviewed in Sec. 4.3.

Even though several authors pointed out the existence of sizable lattice effects around the Mott transition (see e.g. [29, 132, 146]), indicating that lattice degrees of freedom are involved in the transition, the influence of the compressible crystal lattice on the Mott critical behavior has not been explored experimentally yet. This is surprising, as the tuning variable of the Mott transition is pressure, which directly points towards the importance of electron-lattice coupling. The effect of pressure is to change the overlap between neighboring orbitals and by this to promote metallicity. Conversely, the critical electronic subsystem also exerts an internal pressure on the lattice, the response of which can ideally be studied by dilatometric measurements. Recently, it was proposed theoretically by evaluating the thermodynamics of the free energy that electron-lattice-coupling can drastically alter the critical properties close to the finite-temperature Mott endpoint [21]. Far away from the endpoint, when fluctuations are small, the lattice response is expected to be weak and the coupling acts only as a small perturbation. As a consequence, the system displays either the non-trivial critical behavior of the Mott transition or mean-field critical behavior, depending on the size of the Ginzburg regime in the material under investigation (see white and blue areas in Fig. 5.4 (A)). The system's elastic response in this regime is characterized by a normal elastic behavior, i.e., a linear variation of the sample length with changing the pressure. This is known as *Hooke's law of elasticity* (see Fig. 5.4 (B), top). However,

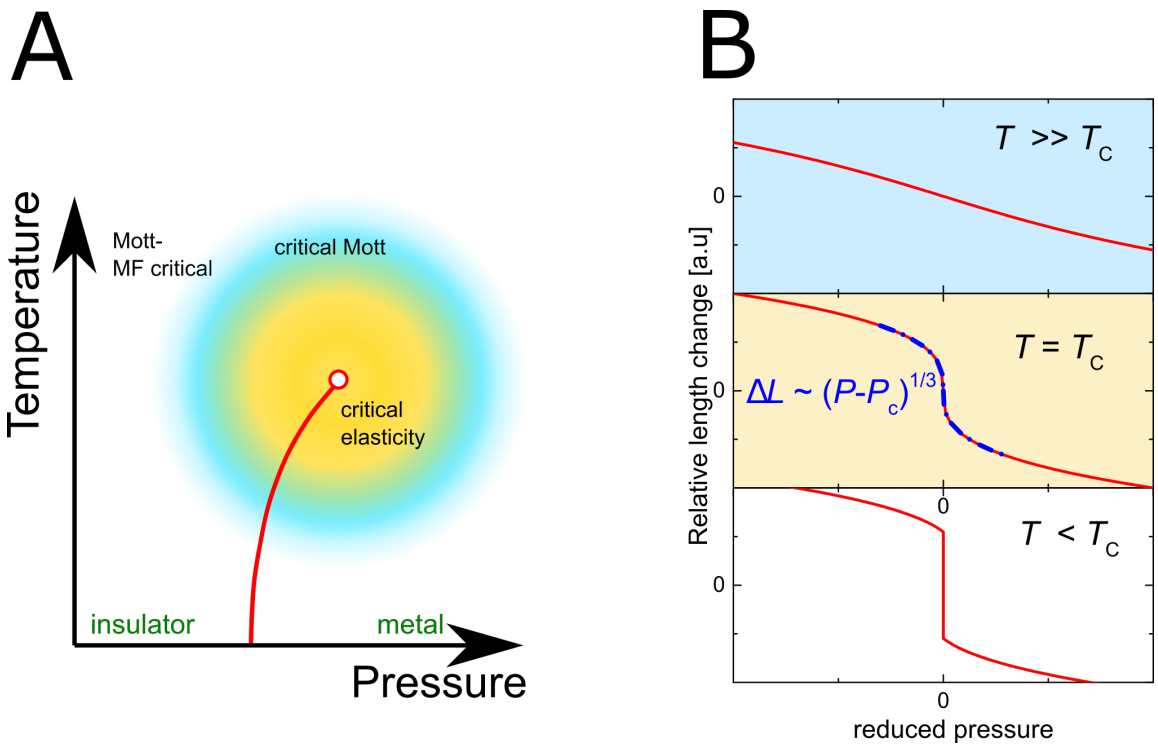


Figure 5.4.: (A) Generic temperature-pressure phase diagram, as predicted by Refs. [21, 22], for a pressure-tuned Mott transition in a real material with a finite shear modulus. The red solid line represents the first-order transition line, which ends in a second-order critical endpoint (red open circle). Far away from the endpoint, fluctuations are small and a description of the critical properties in terms of a mean-field model (MF) is applicable (white area). Closer to the endpoint, within a radius determined by the Ginzburg criterion, fluctuations dominate and non-trivial critical exponents prevail (light blue circle). Nevertheless, these strong fluctuations are coupled to lattice degrees of freedom which eventually causes a crossover to critical elasticity governed by mean-field critical exponents (yellow circle), for details see text. (B) Prediction of the relative length change as a function of reduced pressure $\frac{P-P_c}{P_c}$, with $P_c$ the critical pressure, for various temperatures, i.e., $T \gg T_c$, within the blue-shaded critical Mott regime, $T = T_c$, within the yellow-shaded critical elasticity regime, and $T < T_c$ [151]. The blue dotted line indicates the predicted mean-field type critical behavior very close to $T_c$ with the mean-field critical exponent $\delta = 3$.

upon approaching the endpoint, when fluctuations increase, the coupling necessarily causes a non-perturbative reaction of the crystal lattice. As a consequence, an elastic modulus vanishes [21,23,24] and the lattice gets soft. Such kind of a softening was already observed in critical piezoelectric ferroelectrics [152]. The smoking-gun experiment to detect such a non-perturbative response is provided by the observation of a *breakdown of Hooke's law*, i.e., by a strongly non-linear variation of the length as a function of pressure, as illustrated in Fig. 5.4 (B), middle. Importantly, this breakdown of Hooke's law is expected to be accompanied by a crossover to mean-field criticality (Fig. 5.4 (A), yellow area) sufficiently close to the critical endpoint [21,22], as the long-ranged shear forces of the crystal lattice suppress the

long-wavelength fluctuations and the acoustic phonon modes remain non-critical due to the finite shear modulus of the solid. It is therefore expected that the driving electronic fluctuations induce a macroscopic instability of the crystal lattice at a temperature higher than the bare electronic critical temperature. Consequently, the critical properties around the endpoint would be described in terms of a solid-solid endpoint rather than a liquid-gas endpoint. The order parameter for the former endpoint is the strain field $\varepsilon \propto \Delta L/L$, and thus measurements of the relative length change are the ideal tool to test the critical properties around the Mott endpoint in real materials with a compressible lattice.

The organic charge-transfer salt $\kappa$-Cl represents a promising system to check for the proposed isostructural solid-solid endpoint for the following reasons: First, the electron-lattice coupling in this material class is naturally strong due to the rather soft lattice of this molecule-based material. It ensures that already a very small pressure of $P \lesssim 30\,\mathrm{MPa}$ is sufficient to cover a wide-enough range around the critical endpoint. In addition, based on the thermodynamic analysis of Ref. [21] the width of the critical elasticity regime in this system is expected to be wide enough to be detectable, stretching out over a range of several degrees Kelvin around the critical endpoint. Second, as a matter of fact, the system on both sides of the transition has the same crystallographic structure and space group, which implies that no symmetry breaking structural changes accompany the transition. This is confirmed by comparing $\kappa$-Cl with its metallic counterpart $\kappa$-(BEDT-TTF)$_2$Cu[N(CN)$_2$]Br, both of which are known to be isostructural at room temperature, see Tab. 4.1 for the room-temperature lattice parameters. In addition, there are indications from neither x-ray [113,153] nor thermal expansion measurements [119] for a structural transition in both compounds down to lowest temperature, i.e., 2 K.

## 5.2. Study of the thermal expansion around the Mott critical endpoint

In the following, the results of relative length changes $\Delta L/L$ of $\kappa$-Cl around its pressure-induced Mott endpoint will be presented. To this end, several crystals were studied to check for reproducibility and to rule out non-intrinsic sample-dependent effects. A list of the investigated samples is presented in Tab. 5.1, in which it is indicated in detail along which crystallographic axes measurements were performed. It is also noted, whether the measurements were performed as a function of $T$ at $P = \mathrm{const.}$ or as a function of $P$ at $T = \mathrm{const.}$ All of these crystals were cooled down slowly through the glass transition at $T_g \approx 67\,\mathrm{K}$ with a rate of $-3\,\mathrm{K/h}$ in order to minimize the degree of disorder in the ethylene end groups of the ET molecules. The main results of this study will be discussed by using the data taken on $\kappa$-Cl #AF063, for which a complete data set along all crystallographic

| | $\Delta L(T)/L$ | | | $\Delta L(P)/L$ | | |
|---|---|---|---|---|---|---|
| | $a$ | $b$ | $c$ | $a$ | $b$ | $c$ |
| $\kappa$-Cl #AF063 | x | x | x | x | x | x |
| $\kappa$-Cl #AF063 - II | x | | | x | x | x |
| $\kappa$-Cl #5-7-FRA1 | x | | | | | |
| $\kappa$-Cl #kmm1034 | x | | | | | |
| $\kappa$-d8-Br #5-3 | x | | | | | |

Table 5.1.: Overview of investigated single crystals in the study of Mott criticality by measurements of the relative length change. $\Delta L(T)/L$ and $\Delta L(P)/L$ correspond to measurements that were performed as a function of temperature or pressure along the respective axis $a$, $b$ or $c$. x marks for which crystals the respective crystallographic axis were measured. $\kappa$-Cl refers to a crystal of the compound $\kappa$-(BEDT-TTF)$_2$Cu[N(CN)$_2$]Cl, $\kappa$-d8-Br refers to a crystal of the compound $\kappa$-(d8-BEDT-TTF)$_2$Cu[N(CN)$_2$]Br.

directions is available. At the end of the discussion, the reproducibility of these results will be demonstrated by discussing corresponding data for the other crystals. In addition, it will be demonstrated that the small uniaxial pressure exerted by the dilatometer cell has no effect on the interpretation of the data.

### Relative length changes across the Mott transition

Figure 5.5 shows results of the relative length change $\Delta L_i/L_i$ as a function of $P$ at various $T$ =const. for the in-plane $i = a$ axis (A) and the out-of-plane $b$ axis (B). The reason for choosing these axes is that they show the strongest uniaxial effects at the Mott transition. In contrast, the expansion along the $c$ axis is negligibly small at the transition, as will be discussed later in this section (see Fig. 5.10), so that the volume change across the Mott transition can be approximated by $(\Delta V/V)_{Mott} \approx (\Delta L_a/L_a)_{Mott} + (\Delta L_b/L_b)_{Mott}$. The temperature range studied here ranges from 30 K, which is well below the critical temperature of $T_c \approx 36.5$ K, up to 55 K. The precise determination of the critical endpoint will be illustrated later in this section.

In order to identify the signatures of the Mott transition, we start by discussing the data at lowest temperature, i.e., at 30 K (black lines in Fig. 5.5). Along both axes, an abrupt change of the length as a function of pressure around $P \approx 22$ MPa can be observed. These slightly broadened jumps are consistent with the first-order character of the transition well below $T_c$. More precisely, the length along both axes, and consequently also the volume, are decreasing by about $(\Delta V/V)_{Mott} \approx -5 \cdot 10^{-4}$ while tuning the system from the insulating state at lower pressures to the metallic state at higher pressures. Such a response is expected at the Mott transition, as the delocalization of the charge carriers contributes to the cohesion of a solid. This observation presents a first hint that $(\Delta V/V)_{Mott}$ is indeed

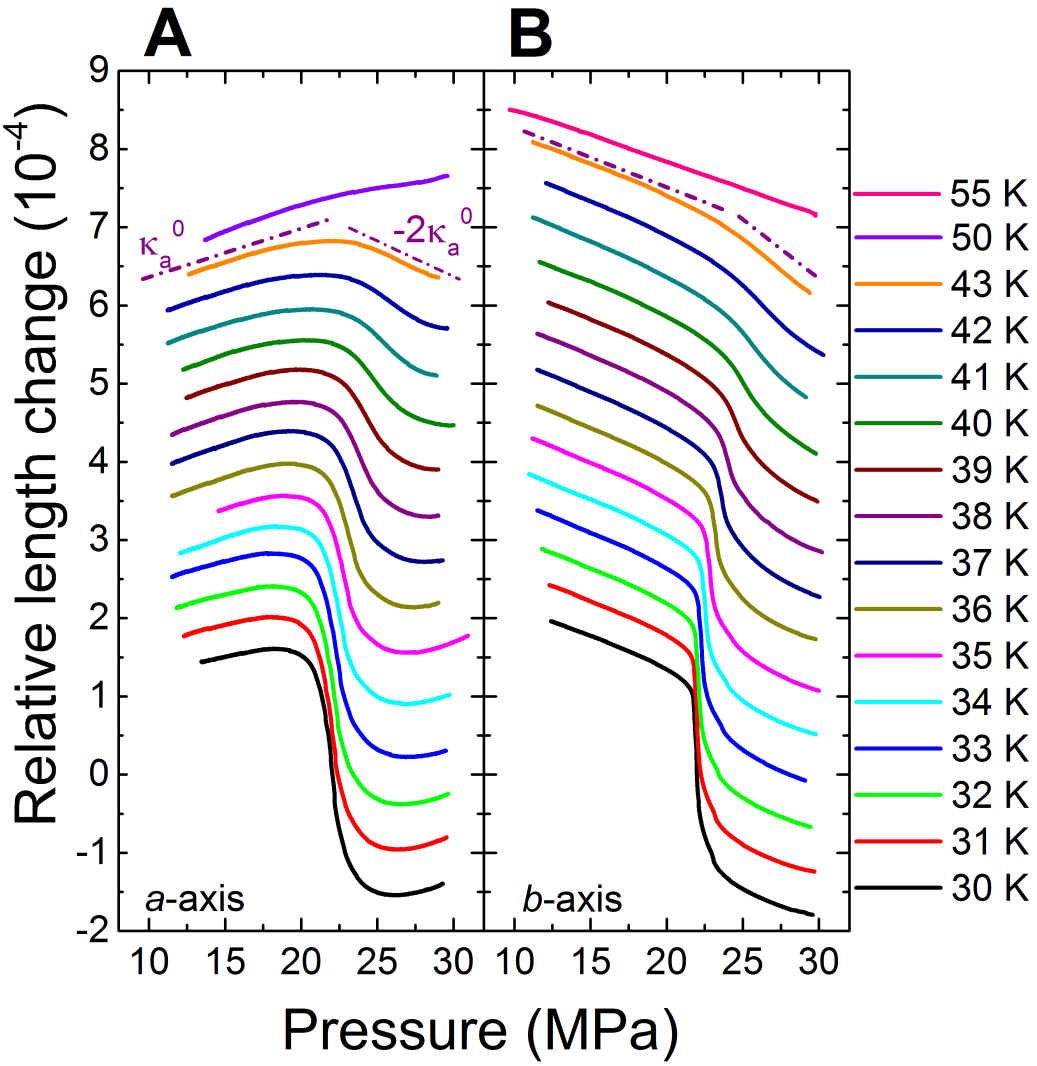


Figure 5.5.: Relative length changes $\Delta L_i/L_i$ of $\kappa$-(BEDT-TTF)$_2$Cu[N(CN)$_2$]Cl as a function of pressure around the Mott critical endpoint for various temperatures between 30 K and 55 K around $T_c \approx 36.5$ K. The data in (A) correspond to $\Delta L_i/L_i$ measured along the in-plane $i = a$ axis and in (B) to $\Delta L_i/L_i$ measured along the out-of-plane $b$ axis. Broken lines are guides to the eyes and represent the pressure-induced compressibility changes at 43 K with $\kappa_a^0$ being the normal elastic compressibility. The data set highlights the observed breakdown of Hooke's law of elasticity by displaying a strong non-linear behavior in wide ranges of temperature and pressure. The data were offset for clarity.

proportional to the order parameter. Far away from the transition, the length changes in an approximately linear manner as a function of pressure with similar slopes on the low- and high-pressure flank. This normal elastic behavior is described by Hooke's law of elasticity. For stability reasons, it is expected that the volume shrinks upon application of external, hydrostatic pressure, so that often the length of all crystallographic axes decrease under pressure. Nevertheless, also a highly anisotropic behavior, as observed here, is allowed as

long as the total volume shrinks with increasing pressure. In the present case, the $b$ axis shows the usual elastic behavior, i.e., a negative slope as a function of $P$, whereas the $a$ axis is expanding at the same time. A plausible explanation for this anisotropy is known as the Poisson effect and can be inferred from the arrangement of the ET molecules (see Fig. 4.2): For $\kappa$-Cl, the long axis of the ET molecules is slightly inclined with respect to the $b$ axis. Upon application of hydrostatic pressure, it seems likely that the loose interlayer-coupling favors a progression of the inclination, and thereby an elongation of the sample along the $a$ axis. Upon increasing the temperature above $T = 30\,\mathrm{K}$, the jump size decreases continuously until $T \approx 36\,\mathrm{K}$. Above this temperature, the discontinuity is vanished and is instead redeemed by a continuous crossover behavior, the signatures of which become progressively less and less pronounced with increasing temperature up to about $T = 43\,\mathrm{K}$.

Of particular interest is the behavior of $\Delta L_i(P)/L_i$ at temperatures above the critical endpoint. For temperatures from $T_c \approx 36.5\,\mathrm{K}$ up to $43\,\mathrm{K}$, a highly non-linear change of $\Delta L_i(P)/L_i$ with pressure in a wide pressure range can be observed. These non-linearities can be quantified by considering the uniaxial compressibilities $\kappa_i = -\mathrm{d}(\Delta L_i/L_i)/\mathrm{d}P$, i.e., the slope of the $\Delta L_i(P)/L_i$ curves. Here, we focus on the curve taken at $43\,\mathrm{K}$, which is $\Delta T \approx 6.5\,\mathrm{K}$ above the critical endpoint at $T_c$. Even though this temperature strongly exceeds $T_c$, pressure-induced changes of the compressibility can be clearly resolved. The $\Delta L_i(P)/L_i$ curve at this temperature can be divided in two regimes, both following an approximately linear behavior with distinctly different slopes (see broken lines in Fig. 5.5). Remarkable is that the uniaxial compressibility along the $a$ axis is even changing its sign as a function of pressure resulting in an overall pressure-induced change $|\Delta\kappa_a^0|/\kappa_a^0 \approx 3$. Not less dramatic are the changes of the compressibility along the $b$ axis, namely $|\Delta\kappa_b^0|/\kappa_b^0 \approx 1$. It should be noted that these changes of the compressibilities along both axes are of the order of the background compressibilities themselves, thus marking an eminently strong response of the lattice. In contrast to these drastic variations, observed in the present case up to $43\,\mathrm{K}$, at higher temperatures, as, e.g., $55\,\mathrm{K}$, an approximately linear change of the length as a function of $P$ is revealed along the $b$ axis over the whole investigated pressure range. This is characteristic for an usual elastic behavior, which is captured by the well-known Hooke's law of elasticity. The full data set shows that upon approaching the endpoint, when the critical electronic fluctuations become enhanced, a strongly non-linear response of the strain to external stress sets in. This highlights a breakdown of Hooke's law of elasticity in wide ranges of temperature and pressure around the Mott transition. It reflects an intimate coupling of the critical electronic system to lattice degrees of freedom giving rise to a critical elasticity. Further evidence for this conclusion, namely the strong changes in the compressibility upon approaching the endpoint, can be found in previous

ultrasonic investigations on this particular compound [117].

### Phase diagram of $\kappa$-Cl

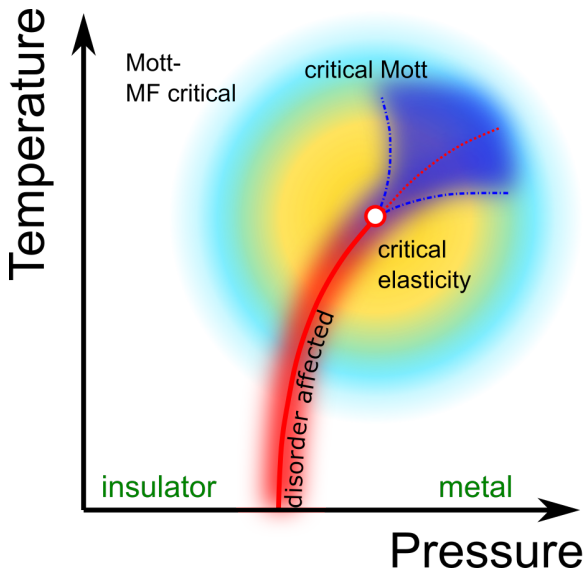


Figure 5.6.: Schematic phase diagram of the pressure-tuned Mott transition in a real material with finite shear moduli. The critical regions, i.e., the Mott-mean field (MF) critical region, the critical Mott region as well as the region of critical elasticity, were already introduced in Fig. 5.4. The red solid line represents the first-order transition line. Due to the presence of some disorder, the first-order transition features are not infinitely sharp, but obey a finite width, which is indicated by the pink shaded area. The red open circle marks the critical endpoint. The smooth extrapolation of the first-order transition line to higher temperatures, represented by the red dashed line, is called the *Widom* line. The blue dotted line (blue shaded regime) represent the predicted crossover lines (crossover regime).

Before discussing the critical behavior, which can be extracted from the above-presented $\Delta L_i/L_i$ data, we will focus on the determination of the phase diagram. It includes characteristic features, such as the first-order transition line, the *Widom* line, i.e., the smooth extrapolation of the first-order transition line to higher temperatures, the crossover lines and the critical endpoint located at $(P_c, T_c)$ (see Fig. 5.6). As a matter of fact, a precise determination of $(P_c, T_c)$ is of crucial importance for the proper determination of the critical properties, as the analysis of the power-law behavior is particularly sensitive to the choice of $(P_c, T_c)$. As literature results suggest different positions of the critical endpoint in the phase diagram, which might be related to different sample qualities (see Sec. 5.4), it is essential to determine $(P_c, T_c)$ independently for the present sample. In the following, two different approaches will be presented in order to identify the critical endpoint with a sufficiently

high accuracy. Both procedures are based on the proper discrimination of crossover features from anomalies at the first-order transition.

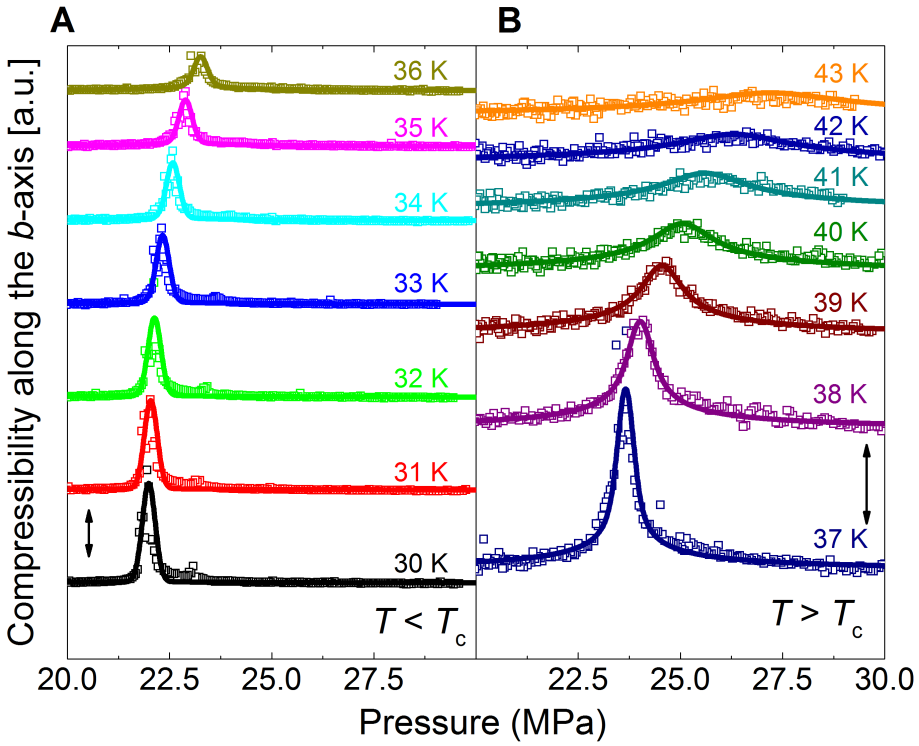


Figure 5.7.: Uniaxial compressibilities of κ-(BEDT-TTF)$_2$Cu[N(CN)$_2$]Cl, measured along the $b$ axis, which were determined by numerical differentiation of the $\Delta L_b(P)/L_b$ data (for details, see text), for various temperatures below $T_c \approx 36.5\,\mathrm{K}$ (A) and above $T_c$ (B). Note the different scales used for the data at $T \leq 36\,\mathrm{K}$ (A) and $T \geq 37\,\mathrm{K}$ (B). The length of the arrow in each plot indicates the scale which is $2.5 \cdot 10^{-4}$/MPa (A) and $1 \cdot 10^{-4}$/MPa (B). For clarity, the data were offset. The solid lines represent the uniaxial compressibilities derived from a fit to the experimental data with a mean-field model, for details see text.

In a first step, we determine the inflection point of each $\Delta L_i(P)/L_i$ curve and assign these points to the first-order transition line below $T_c$ and the *Widom* line above $T_c$, respectively. For this purpose, the $\Delta L_i(P)/L_i$ data were differentiated numerically with respect to pressure according to the following procedure: The data set was divided into equidistant intervals of 20 points corresponding to an average width of $\Delta P = 0.05\,\mathrm{MPa}$. In each interval the mean slope was determined from a linear regression. The result of this procedure is exemplarily shown for the data taken along the $b$ axis in Fig. 5.7 for $T \leq 36\,\mathrm{K}$ (A) and $T \geq 36\,\mathrm{K}$ (B). The inflection point, i.e., the maximum of the compressibility, is shifting to higher pressures with increasing temperature. These inflection points define a characteristic line $P_c(T)$. This line can be separated at $P_c(T_c)$ into the first-order transition line and the *Widom* line, shown in Fig. 5.8 by red closed and open symbols, respectively. In this figure, the so-derived characteristic lines, based on the present thermodynamic results, are compared with the corresponding lines determined from transport, i.e., conductivity,

measurements [18], shown in green. We find a very good overall agreement of the Mott transition lines obtained from these different measurements on different crystals. Within this thesis, preliminary measurements on the effect of disorder on the Mott transition line were performed on crystals, which had been exposed to x-ray irradiation. These measurements indicated a shift of the Mott transition line to lower pressures upon increasing degree of disorder (see Sec. 5.4 for a detailed discussion of these results). Based on this observation, the good agreement of the transition line for the pristine crystals, studied here and in Ref. [18], can be considered as an indication for a similar, high quality of those crystals.

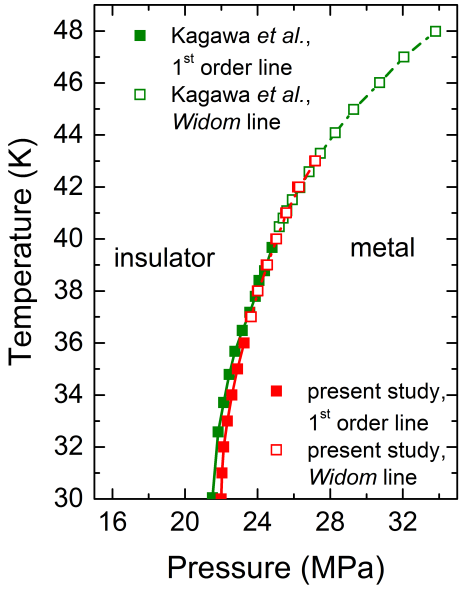


Figure 5.8.: Comparison of phase transition line (closed symbols) and *Widom* line (open symbols) determined from thermodynamic (red symbols) vs. transport measurements (green symbols), reported by Kagawa *et al.* [18], on $\kappa$-(BEDT-TTF)$_2$Cu[N(CN)$_2$]Cl.

For the determination of ($P_c$, $T_c$) we come back to the properties of the compressibility, shown in Fig. 5.7. For an idealized system, an infinitely sharp jump of the length as a function of $P$ at the first-order transition below $T_c$ is expected reflecting a diverging compressibility at the transition. However, in every real system due to the presence of some amount of disorder, the transition is slightly broadened, which corresponds to a finite width of the peak in the compressibility even below $T_c$. For a first estimate of $T_c$, a closer inspection of the compressibility peak structure at lower and higher temperatures is useful: Below $T \leq 36\,\mathrm{K}$ sharp spikes occur in the compressibility, which indicate that some discontinuities are involved in the length change which can be assigned to the first-order character of the transition. In contrast, these spikes are absent for $T \geq 37\,\mathrm{K}$, in accordance with a smooth crossover behavior as a function of $P$. These observations yield an estimate of $36\,\mathrm{K} \lesssim T_c \lesssim 37\,\mathrm{K}$.

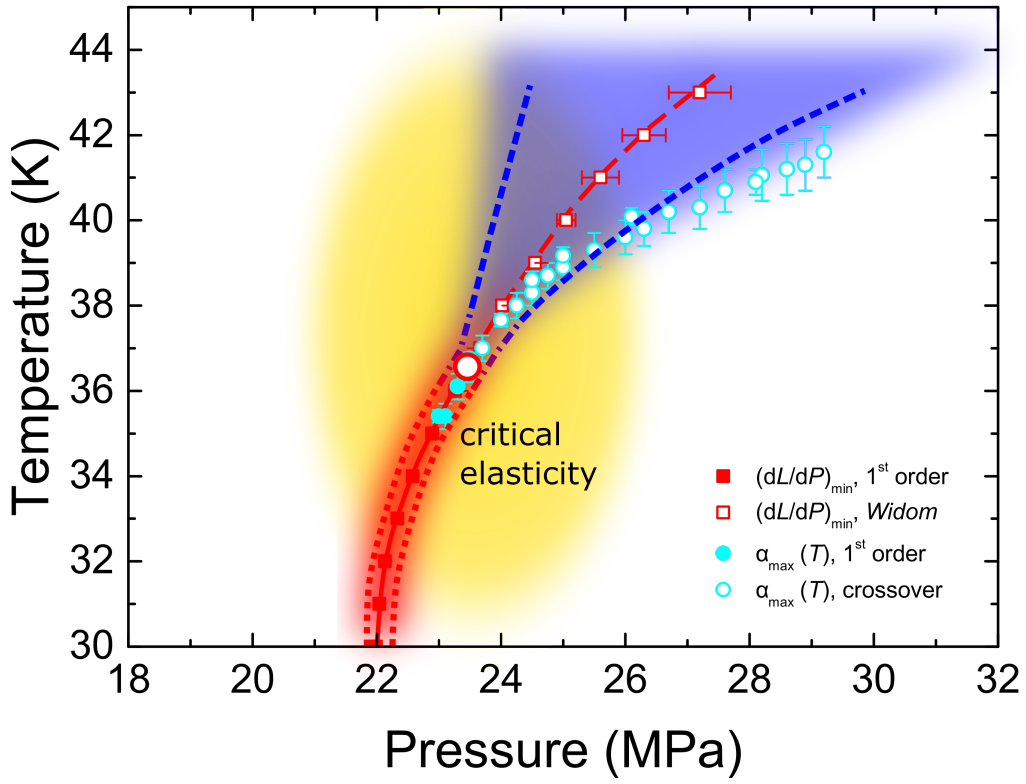


Figure 5.9.: Experimentally determined temperature-pressure phase diagram for $\kappa$-(BEDT-TTF)$_2$Cu[N(CN)$_2$]Cl. Full (open) red squares represent the first-order transition line (*Widom* line) determined from the inflection points of $\Delta L_i(P)/L_i$. The red open circle indicates the critical endpoint, the determination of which is discussed in detail in the main text. Cyan full (open) symbols correspond to the position of maximum response, $\alpha_{max}$, of the thermal expansion coefficient, $\alpha(T) = 1/L\,\mathrm{d}L/\mathrm{d}T$, that is assigned to the first-order transition line (crossover line). Red and blue shaded areas are indicating the experimentally determined width of the features in $\Delta L_b/L_b$ and can, as explained in the main text, be attributed to the disorder-affected (red) and the criticality-related (blue) regime, respectively. These areas are delimited by the broken lines in the same color code, which were determined by the full width at half maximum in $\kappa_i(P)$ within the given error bars. The yellow ellipse represents the estimate of the range in temperature and pressure, in which critical elasticity with mean-field critical exponents dominates.

In order to analyze the character of the observed features in the compressibility in more detail, we consider the width of the anomalies in $\Delta L_i(P)/L_i$ (see Fig. 5.7). The inclusion of a finite width for all $T$, including $T < T_c$, is important, as it helps to handle the additional scale, which is relevant in every real systems due to the presence of disorder. Such an additional scale besides the correlation length is also of high relevance for the analysis of the critical properties. Below $T_c$ the width of the peak in $\kappa_i(P)$ is dominated by these disorder effects, which we assign to spatial variations of internal stress induced by impurities and/or other crystal defects. Thus, we expect the width of the features to be practically temperature independent below $T_c$. In contrast, upon increasing the temperature sufficiently

above $T_c$, the width is increasing rapidly with temperature and hence can be assigned to criticality. In the following, we estimate the width of the features in $\Delta L_i(P)/L_i$ by determining the full width at half maximum of the peak in $\kappa_i$. This information is included in the phase diagram in Fig. 5.9 by the red and blue shaded areas, delimited by the broken lines in the same color code, for $T \leq 36\,\mathrm{K}$ and $T \geq 37\,\mathrm{K}$, respectively. For temperatures below 36 K, the width is nearly temperature independent, so that we assign the red-shaded regime to the disorder-affected regime. In contrast, for $T \geq 38\,\mathrm{K}$ the width rapidly grows with increasing the temperature. We therefore assign the temperature-dependent width of these feature to a measure of the crossover lines. As these crossover lines emanate from the critical endpoint, an extrapolation of these lines towards lower temperatures provides a highly accurate method to estimate the critical endpoint. Extrapolating these lines, which are highlighted in blue in the phase diagram in Fig. 5.9, from high temperatures above $T \approx 38\,\mathrm{K}$, above which disorder affects are expected to play a minor role, to lower temperatures yields an intersection point of $T_c = (36.7 \pm 0.5)\,\mathrm{K}$. This value is in full accordance with the rough estimate of $T_c$, presented above.

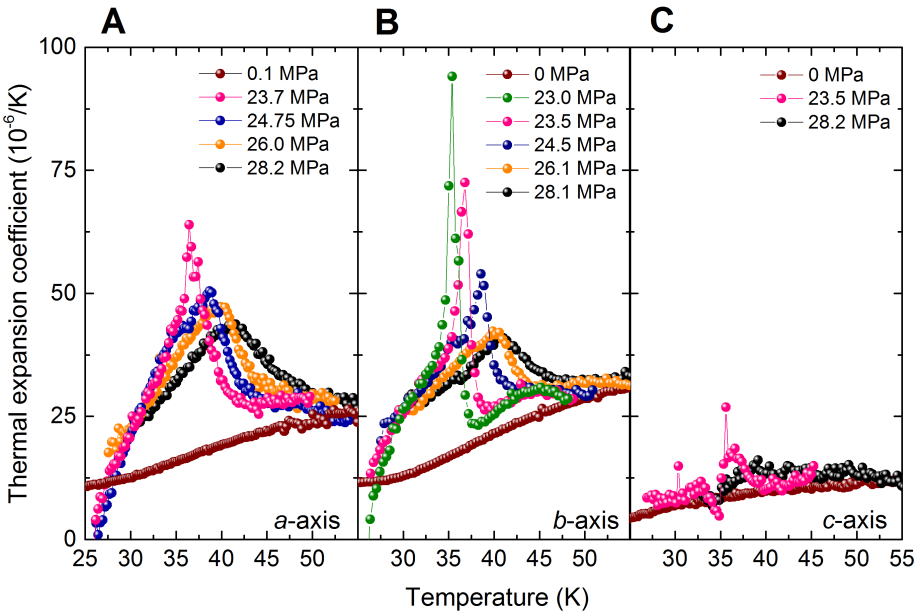


Figure 5.10.: Uniaxial coefficients of thermal expansion, $\alpha_i = L^{-1}\mathrm{d}L/\mathrm{d}T$, along all three crystallographic axes, i.e., along the in-plane $a$ (A) and $c$ axis (C) as well as the out-of-plane $b$ axis (B), around the pressure-induced Mott transition in $\kappa$-(BEDT-TTF)$_2$Cu[N(CN)$_2$]Cl. The data were taken at varying constant pressure as a function of temperature $T$ upon warming. The data set obtained at ambient pressure, included in all subfigures, is given as an estimate for the non-critical background contribution to the thermal expansion coefficient.

An alternative approach to estimate ($P_c$, $T_c$) is to first determine the crossover line corresponding to the maximum response of the thermal expansion coefficient, $\alpha(T) = L^{-1}\mathrm{d}L/\mathrm{d}T$, as proposed in Ref. [20]. Then, in a second step, the intersection point of this

line with the first-order transition line can be determined to obtain ($P_c$, $T_c$). To begin with, we discuss the salient features of the temperature-dependent thermal expansion data, and will afterwards focus on the determination of ($P_c$, $T_c$). Figure 5.10 shows the results of the uniaxial coefficients $\alpha_i(T)$ measured along all crystallographic axes, i.e., along the in-plane $a$ (A) and $c$ axis (C) as well as the out-of-plane $b$ axis (B). These data were determined from the measured $\Delta L_i(T)/L_i$ data, taken at varying constant pressures as a function of temperature, by numerical differentiation. Here, $\Delta L_i(T)/L_i$ corresponds to $(L_i(T) - L_i(T_0))/L_i$, with $T_0$ being a reference temperature and $L_i$ the room-temperature crystal length. For the numerical differentiation, the data set was divided into equidistant intervals of width $\Delta T = 0.2\,\mathrm{K}$, in each of which the mean slope was determined from a linear regression. As previously mentioned and observed in a similar way in the thermal expansion measurements on $\kappa$-(d8-ET)$_2$Cu[N(CN)$_2$]Br [132], mainly the expansion along the in-plane $a$ and the out-of-plane $b$ axis are affected by the Mott transition, yielding pronounced anomalies. In contrast, the expansion along the $c$ axis barely shows any effect beyond the non-critical background, the estimate of which is given by the ambient pressure thermal expansion curves included in Fig. 5.10. It was already pointed out in Ref. [132], that this result is rather surprising as the inter-dimer interaction $t'$ is directed along the $c$ axis.

As the first-order transition line has a finite slope at the critical endpoint, temperature-dependent measurements not only provide insight into the crossover scale, but also allow to discriminate between rounded crossover anomalies in $\alpha(T,\, P = \text{const.})$, expected for $P > P_c$, from diverging anomalies resulting from jump-like discontinuous length changes, expected for $P < P_c$. The positive contribution to the thermal expansion coefficient represents a lattice expansion upon warming, which is expected while going from the low-temperature metallic state to the high-temperature insulating state. Nevertheless, sharp spikes in $\alpha$ with the tendency to diverge are visible only for $P < 23.7\,\mathrm{MPa}$ and can, thus, be attributed to the first-order character of the transition. The position of the maximum response of $\alpha(T,\, P = \text{const.})$ at $T_{max}(P)$ for $P < 23.7\,\mathrm{MPa}$ is included as the temperature of the first-order transition in the phase diagram in Fig. 5.9 by full cyan symbols. For $P \geq 23.7\,\mathrm{MPa}$, the singular character (spikes) of the feature is absent, and instead a smooth and continuous crossover behavior is observed. The maximum in $\alpha$ for $P > P_c$ marks the position of a crossover line emerging from the critical endpoint (see Ref. [20] for a precise prediction of this line for the 2D-Ising universality class) and is depicted in the phase diagram (Fig. 5.9) by open cyan symbols. The intersection of this crossover line with the first-order transition line, determined from $P$-dependent measurements, now enables a determination of $T_c$ and $P_c$. Applying this technique, yields a critical endpoint of $T_c = (36.5 \pm 0.5)\,\mathrm{K}$ and $P_c = (23.4 \pm 0.2)\,\mathrm{MPa}$. In summary, the two different approaches to determine the critical endpoint provide consistent results indicating the high reliability

of the $(P_c, T_c)$ data. In the following discussion of the analysis of the critical behavior, we will use $T_c = (36.5 \pm 0.5)\,\mathrm{K}$ and $P_c = (23.4 \pm 0.2)\,\mathrm{MPa}$.

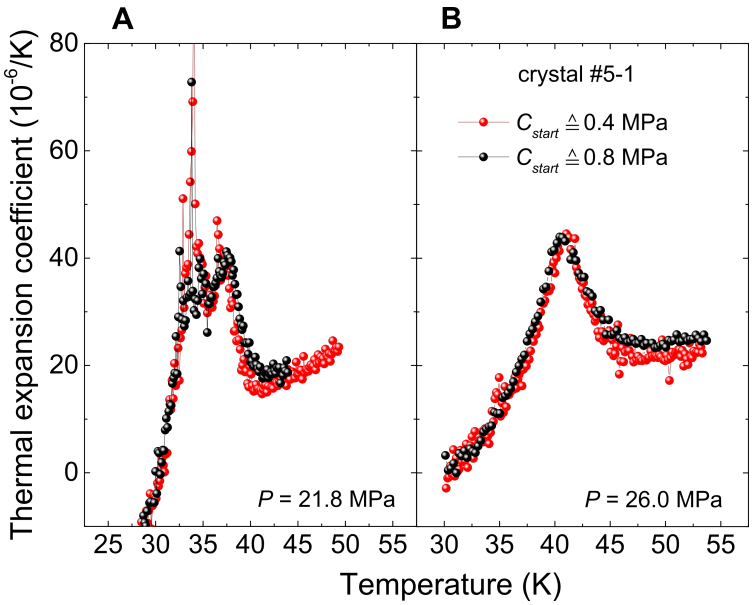


Figure 5.11.: Effect of a small uniaxial pressure exerted by the dilatometer cell. Measurements of the thermal expansion coefficient $\alpha(T) = L^{-1}\mathrm{d}L/\mathrm{d}T$ upon warming on a $\kappa$-(BEDT-TTF)$_2$Cu[N(CN)$_2$]Cl crystal (#5-1) are shown along the $a$ axis at $P = 21.8\,\mathrm{MPa}$, i.e., $P < P_c$, (A) and $P = 26\,\mathrm{MPa}$, i.e., $P > P_c$, (B). These measurements were performed with two different starting capacitances, which correspond to a very small ($\approx 0.4\,\mathrm{MPa}$, red symbols) and a slightly higher ($\approx 0.8\,\mathrm{MPa}$, black symbols) uniaxial pressure. The multiple peak structure, as observed at $P = 21.8\,\mathrm{MPa}$, i.e., at $P < P_c$, is a result of the domain formation accompanying the first-order transition, caused by extrinsic disorder, as discussed in the text below.

Before continuing with a discussion of the critical properties, it is necessary to ensure that the uniaxial pressure, exerted by the dilatometer (see Appendix A.3 for more details), has a negligible effect on the observed anomalies and, as a consequence, on the critical properties. The force exerted by the dilatometer on the sample is typically between 0.2 and 0.8 N, which can be adjusted by screwing down the piston. It can be quantified by the value of the starting capacitance in comparison to the capacitance of the empty cell. The uniaxial pressure is correspondingly given by the applied force divided by the cross-section of the sample (see Sec. 3.4 for the typical sample dimensions). In order to demonstrate the effect of the uniaxial pressure component on the experimental results, we performed measurements of the thermal expansion coefficient $\alpha_a(T)$ on a different $\kappa$-Cl crystal (#5-1) for two different starting capacitances under otherwise identical conditions. This crystal had a cross-section of about $0.7\,\mathrm{mm}^2$ perpendicular to the measured $a$ direction. The chosen starting capacitances correspond to a small uniaxial pressure of about 0.4 MPa and a slightly higher uniaxial pressure of 0.8 MPa. In Fig. 5.11 we present results of $\alpha(T)$ for two different hydrostatic pressures, namely $P = 21.8\,\mathrm{MPa}$ (A) and $P = 26\,\mathrm{MPa}$ (B). The for-

mer pressure corresponds to a pressure on the insulating side of the transition, i.e., $P < P_c$, whereas the latter one to a pressure on the metallic side, i.e., $P > P_c$. The obtained data sets indicate no significant changes of the thermal expansion coefficient on either side of the transition upon increasing the uniaxial pressure slightly, so that we can safely neglect the uniaxial pressure component.

### Modeling of the relative length changes

After having pinpointed $(P_c, T_c)$, we can now proceed with analyzing the critical behavior. For this purpose, a representation of the experimental data in terms of a scaling collapse was favored by several researches, as, e.g., in Refs. [17, 18]. Such a conventional one-parameter scaling collapse relies on the existence of one relevant length scale in the system, i.e., the (diverging) correlation length of fluctuations, in order to establish scale invariance. However, in every real system, the presence of disorder, which causes a broadening of the critical signatures, implies an additional length scale and, thus, precludes the possibility to perform such an one-parameter scaling collapse.

Instead, motivated by the strong lattice effects, resulting in a breakdown of Hooke's law, we employ an effective elasticity theory and compare the theoretical results with our experimental data. The elasticity theory is renormalized by electronic degrees of freedom, which drive the system to an isostructural solid-solid endpoint, as theoretically proposed in Ref. [21]. The starting point for this theory is the eigenvalue equation of the elastic constant matrix in Voigt notation. $\kappa$-Cl possesses an orthorhombic crystal structure, the elastic constant matrix of which was given in eq. 2.52 (see Sec. 2.5 for the definitions of quantities used in the present paragraph). Stability of the system requires that the matrix has six positive, non-degenerate eigenvalues $\lambda_\alpha$ with $\alpha = 1, ..., 6$. The eigenvectors associated with the first three eigenvalues describe the response under compressive strain, whereas the last three eigenvalues are associated with shear strain. In the following, as our data were taken under hydrostatic pressure, i.e., under compressive strain, we focus on the eigenvalue equation for the first three eigenvalues $\lambda_\alpha$ with $\alpha = 1, 2, 3$,

$$\begin{pmatrix} C_{11} & C_{12} & C_{13} \\ C_{12} & C_{22} & C_{23} \\ C_{13} & C_{23} & C_{33} \end{pmatrix} \vec{v}_\alpha = \lambda_\alpha \vec{v}_\alpha. \tag{5.1}$$

Following the classification of Cowley *et al.* [154], at an isostructural lattice instability, one of these eigenvalues vanishes, which we denote in the following by $\lambda_1$ with eigenvector $\vec{v_1}$. It is important to note that even though one eigenvalue vanishes, the long-wavelength acoustic

phonon velocities soften, but remain finite at the instability. These long-wavelength acoustic phonons represent the fluctuations of the order parameter of the structural transition, which corresponds to nothing else than the strain field $\varepsilon$ [154]. Their velocities remain finite due to the presence of finite shear moduli (see eq. 2.54) in a solid, and thus remain non-critical. This behavior is in contrast to e.g. a liquid with no shear moduli. The consequence is that at the solid-solid endpoint the behavior is described by mean-field criticality without critical fluctuations, i.e., without the presence of a diverging correlation length [21].

The diagonal components of the strain tensor $(\varepsilon_{11}, \varepsilon_{22}, \varepsilon_{33})$, which are directly proportional to the measured relative length changes, can accordingly be expanded in the same eigenvector basis, given by $\vec{v_1}, \vec{v_2}, \vec{v_3}$ with expansion coefficients $\epsilon_\alpha$ with $\alpha = 1, 2, 3$,

$$\begin{pmatrix} \varepsilon_{11} \\ \varepsilon_{22} \\ \varepsilon_{33} \end{pmatrix} = \varepsilon_1 \vec{v}_1 + \varepsilon_2 \vec{v}_2 + \varepsilon_3 \vec{v}_3. \tag{5.2}$$

We can now identify the order parameter of the isostructural transition with the strain singlet $\varepsilon_1$, as it is associated with the vanishing eigenvalue of the elastic constant matrix $\lambda_1$. The relative length changes along the three crystallographic axes, are correspondingly given by

$$\frac{\Delta L_a}{L_a} = -\varepsilon_{11} = -\Big(\varepsilon_1 v_{1,1} + \varepsilon_2 v_{2,1} + \varepsilon_3 v_{3,1}\Big) \tag{5.3}$$

$$\frac{\Delta L_b}{L_b} = -\varepsilon_{22} = -\Big(\varepsilon_1 v_{1,2} + \varepsilon_2 v_{2,2} + \varepsilon_3 v_{3,2}\Big) \tag{5.4}$$

$$\frac{\Delta L_c}{L_c} = -\varepsilon_{33} = -\Big(\varepsilon_1 v_{1,3} + \varepsilon_2 v_{2,3} + \varepsilon_3 v_{3,3}\Big). \tag{5.5}$$

The relative length changes along the individual crystallographic axes are thus all given by the contribution of the critical singlet $\epsilon_1$, i.e., the critical non-degenerate eigenvalue of the strain tensor, as well as two non-critical singlets $\epsilon_2$ and $\epsilon_3$,

$$\Delta L_i/L_i \;=\; (\Delta L_i/L_i)_{critical} + (\Delta L_i/L_i)_{non-critical} \text{ with } i = a, b, c. \tag{5.6}$$

The response of the relative length change along a particular crystallographic direction to the presence of one critical singlet is governed by the respective components of the eigenvector $\vec{v_1}$, namely $(v_{1,1}, v_{1,2}, v_{1,3})$, which are the proportionality constants between $\varepsilon_1$ and $\Delta L_i/L_i$. We assume that $v_{1,3}$ is by far the smallest of all three components and even

very close to zero, as the expansion along the $c$ axis is barely affected by the Mott transition (see Fig. 5.10).

Similarly, the stress tensor $\sigma_{ij}$ can be expanded in the same basis:

$$\begin{pmatrix} \sigma_{11} \\ \sigma_{22} \\ \sigma_{33} \end{pmatrix} = \sigma_1\vec{v}_1 + \sigma_2\vec{v}_2 + \sigma_3\vec{v}_3. \tag{5.7}$$

However, the stress tensor is very well known, as it is determined by the applied hydrostatic pressure, i.e., $\sigma_{ij} = -(P - P_c(T))\delta_{ij}$ in its dimensionful form. Thereby, we consider $P_c(T)$ to be temperature dependent, as the first-order transition line has a finite slope at $T_c$. These so-called mixing of variables and its importance for a proper description of the critical behavior will be discussed later in this section. Rewriting eq. 5.7 leads to the definition of the expansion coefficients $\sigma_\alpha = -(P - P_c(T))(1,1,1) \cdot \vec{v_\alpha}$ with $\alpha = 1,2,3$ by making use of the orthogonality of the eigenvectors $\vec{v_\alpha}$.

First, we treat the behavior of the non-critical singlets $\varepsilon_2$ and $\varepsilon_3$ under compressive stress. We assume that these non-critical singlets obey normal elastic behavior, i.e., follow Hooke's law of elasticity, which can be written in the above-defined basis set as follows:

$$\varepsilon_\alpha = -\frac{\sigma_\alpha}{\lambda_\alpha} \tag{5.8}$$

with $\alpha = 2,3$.

Thus, the non-critical contribution to the relative length change along a crystallographic axis $i$ with $i = a,b,c$ can be expressed by $\kappa_i^0 \cdot (P - P_c(T))$ (see eq. 5.5) with $\kappa_i^0$ being the non-critical background compressibilities, as defined in the beginning of this section,

$$\kappa_i^0 = \frac{v_{2,i}}{\lambda_2}(1,1,1) \cdot \vec{v}_2 + \frac{v_{3,i}}{\lambda_3}(1,1,1) \cdot \vec{v}_3. \tag{5.9}$$

However, following the suggestions of Ref. [21], the critical singlet $\varepsilon_1$, representing the order parameter of this solid-solid transition, is governed by the critical mean-field Landau potential $\tilde{\mathcal{V}}$, which was already introduced in Sec. 2.2,

$$\tilde{\mathcal{V}}(\varepsilon_1) = \frac{\lambda_1}{2}\varepsilon_1^2 + \frac{\tilde{u}}{4}\varepsilon_1^4 + \varepsilon_1\sigma_1, \tag{5.10}$$

with the eigenvalue $\lambda_1 = c(T - T_c)$ and $c$ a proportionality constant. As $\lambda_1$ vanishes at the critical endpoint, it can be identified with the temperature-dependent tuning variable (see Sec. 2.2 for more details). The constant $\tilde{u}$ is giving rise to a non-linear term in the strain-stress relation. The latter relation can be obtained by minimizing the potential with respect to $\varepsilon_1$, which yields the expectation value of $\varepsilon_1$. This expectation value $\varepsilon_1$ is the one, which is measured by the critical contribution to the relative length change.

$$\lambda_1 \varepsilon_1 + \tilde{u}\varepsilon_1^3 = -\sigma_1. \tag{5.11}$$

In the following discussion about the modeling of the experimental data, we will make use of the scale invariance of the solution of this equation. Thus, we introduce the dimensionless rigidity $r$, which is proportional to the respective eigenvalue $\lambda_1$, and the dimensionless stress $\sigma$,

$$r = \frac{1}{cT_c}\lambda_1 = \frac{T - T_c}{T_c}, \quad \sigma = \frac{\sigma_1}{aP_c(T_c)} = -\frac{P - P_c(T)}{P_c(T_c)},$$

and rescale the strain and the non-linearity correspondingly

$$\varepsilon = \frac{cT_c}{aP_c(T_c)}\varepsilon_1, \quad u = \frac{a^2 P_c^2(T_c)}{c^3 T_c^3}\tilde{u}, \tag{5.12}$$

with the abbreviation $a = (1,1,1) \cdot \vec{v_1}$. The mean-field equation in the rescaled form reads as $r\varepsilon + u\varepsilon^3 = -\sigma$. The solution to this equation was already introduced in eq. 2.27. As apparent, the rigidity vanishes $r = 0$ at $T_c$, and the strain responds in a non-linear manner to the applied stress, $\varepsilon \sim (-\sigma)^{1/\delta}$ with the mean-field critical exponent $\delta = 3$. This strongly non-linear response corresponds to a breakdown of Hooke's law.

In summary, within this elasticity theory, the relative length change can be written as a sum of the non-critical background and the critical contribution. The total relative length change is then given as follows

$$\Delta L_i/L_i = -\kappa_i^0 \left(P - P_c(T)\right) - \mathrm{A}_i\, \varepsilon((T - T_c)/T_c, -(P - P_c(T))/P_c(T_c), u) \tag{5.13}$$

with $A_i = v_{1,i} a P_c(T_c)/(cT_c)$ being the proportionality constant in the rescaled representation between the mean-field critical singlet $\epsilon_1$ and the relative length change. The non-critical background, as derived above in detail, results from the non-critical singlets $\varepsilon_2$ and $\varepsilon_3$. Their contribution is a consequence of the low symmetry of the orthorhombic

crystal structure, which implies that the elastic constant matrix has six non-degenerate eigenvalues. The mean-field critical contribution, i.e., the contribution of $\varepsilon_1$, is responsible for the strong non-linearities close to the endpoint. Nevertheless, far away from the endpoint it also provides an, in first approximation, linear contribution over a distinct pressure window to the strain-stress-relation.

However, in order to describe our experimental data, we have to employ a phenomenological description of the effects of disorder to account for the experimentally observed broadening of the first-order transition. We ascribe this broadening to disorder due to extrinsic effects of the crystal structure. For this purpose, we assume the presence of a multi-domain state, where for simplicity each domain with strain $\varepsilon(r, \sigma + s, u)$ contributes independently to the mean strain. Thus, the mean strain $\langle \varepsilon(r, \sigma, u) \rangle_w$ is given by the average of the several domains,

$$\langle \varepsilon(r, \sigma, u) \rangle_w = \int_{-\infty}^{\infty} ds P_w(s) \varepsilon(r, \sigma + s, u) \tag{5.14}$$

with $P_w(s)$ being the distribution function. It turned out that a Gaussian stress distribution with variance $w$ and zero mean is able to capture the broadening reasonably well, as it ensures that the mean stress is zero at $\sigma = 0$.

$$P_w(s) = \frac{1}{\sqrt{2\pi w}} e^{-\frac{s^2}{2w}}. \tag{5.15}$$

However, it is important to stress that this is a phenomenological approach which does not allow to draw any conclusion about microscopic processes. Especially, the influence of intrinsically-generated disorder, i.e., dislocation effects and grain boundaries as a result of simultaneous expansion and contractions of the crystal, on the stress distribution [155,156] are beyond the scope of the present work. Nevertheless, a proper theoretical study to account for these effects in the presence of an underlying isostructural transition are highly desired in future.

The variance of the Gaussian stress distribution can be nicely determined for $T \ll T_c$, i.e., for very large rigidity $r$, where the mean-field strain $\varepsilon$, i.e., without taking broadening effects into account, obeys in first approximation a step function,

$$\varepsilon(r, \sigma, u) \approx -\text{sign}(\sigma) \sqrt{-r/u}. \tag{5.16}$$

In this limit, the derivative of the averaged strain with respect to the stress reflects nothing else than the stress distribution itself,

$$\frac{\partial}{\partial\sigma}\langle\varepsilon(r,\sigma,u)\rangle_w \approx -2\sqrt{-\frac{r}{u}}P_w(\sigma). \tag{5.17}$$

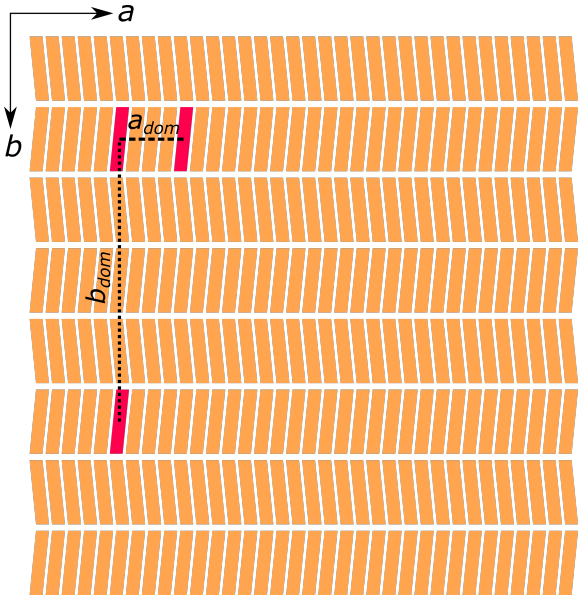


Figure 5.12.: Schematic representation of the domain formation in $\kappa$-(BEDT-TTF)$_2$Cu[N(CN)$_2$]Cl. Orange trapezoids represent BEDT-TTF molecules and their respective arrangement along the in-plane $a$ axis and the out-of-plane $b$ axis. BEDT-TTF molecules marked in red correspond to defects on every $n$-$th$ lattice site. The size of the domain is estimated to be the distance between two defect sites. These domain sizes $a_{dom}$ and $b_{dom}$ along the $a$ and $b$ axis, respectively, are indicated by the dotted lines.

Thus, the variance $w$ of the distribution function $P_w(s)$ can then be conveniently determined by fitting the distribution function to the derivative of the experimental data. Here, we determined the variance $w$ at the lowest temperature measured, i.e., at 30 K, which is much lower than $T_c \approx 36.5$ K. Figure 5.7 (A) shows the comparison between the derivative of the experimental relative length data along the $b$ axis (open black symbols) and a Gaussian fit (solid line) to this data at 30 K. The good agreement of the experimental data and the fit shows that a Gaussian stress distribution is accounting well for the disorder broadening. The analysis of the variance was independently performed for the $a$ and the $b$ axis, as it is already apparent from the bare data in Fig. 5.5 that the disorder-affected broadening regime is larger along the $a$ axis than along the $b$ axis. Therefore the evaluation of the variance yields two different values of $w_a = 1.3 \cdot 10^{-3}$ and $w_b = 4.6 \cdot 10^{-5}$ for the $a$ and the $b$ axis, respectively. Note that we defined the Gaussian distribution function (see eq. 5.15) in such a way that $w^{1/2}$ measures the size of the disorder-affected broadening

regime. Thus, the observed difference in the variance corresponds to an anisotropy ratio of the affected pressure regimes of $(w_a/w_b)^{1/2} \approx 5$. This rather large anisotropy implies that more different domains contribute to the measurements along the $a$ axis than along the $b$ axis resulting in a strongly anisotropic domain shape with the $b$ axis being the long axis. Importantly, this anisotropy is already inherent to the arrangement of the ET molecules. In order to relate the anisotropy of the ET molecules (orange trapezoids in Fig. 5.12) with the anisotropy of the domain size, we first consider a small number of defect sites (red trapezoids in Fig. 5.12), which are randomly distributed over the whole crystal. However, on average every *n-th* lattice site will be affected. The size of one domain is then given by the distance between two defect sites (broken lines), noted as $a_{dom}$ and $b_{dom}$ for the $a$ and $b$ axis. Since the ET molecule is the longest along the $b$ axis, the domain size $b_{dom}$ is clearly much larger than $a_{dom}$ and is thereby reflecting the spatial anisotropy of the structure in $\kappa$-Cl. Indeed, the ratio $a_{dom}/b_{dom} \approx 4.5$ and is, thus, in well agreement with the observed anisotropy of the variance of $(w_a/w_b)^{1/2} \approx 5$, i.e., the disorder-affected broadening regime. These observations on the anisotropic domain formation and the suggestion that this specific formation is already inherent to the crystal structure regime provide the basis for a firm description of the experimental data with respect to the disorder broadening.

After employing elasticity theory and making assumptions to model the disorder-related broadening, the full model to describe the experimentally observed relative length changes reads as follows:

$$\Delta L_i/L_i = -\kappa_i^0 \left(P - P_c(T)\right) - \mathrm{A}_i \left\langle \varepsilon((T-T_c)/T_c, -(P-P_c(T))/P_c(T_c), u)\right\rangle_w. \qquad (5.18)$$

For this purpose, all data sets were normalized to their inflection points $P_c(T)$ to eliminate offset contributions arising from the temperature-dependent non-critical background expansion. In this equation, we considered only mixing terms in the pressure or stress variable, i.e., a temperature-dependent critical pressure $P_c(T)$, and neglect a possible pressure dependence of the tuning parameter $r = \frac{T-T_c}{T_c}$. Such a possible pressure dependence can be effectively absorbed in the non-linear term of the potential $u$ by rescaling the mean-field equation $r\varepsilon + u\varepsilon^3 = -\sigma$, and shows up as only a subleading correction in the non-linearity after a Taylor expansion. Importantly, this equation for the relative length change contains only three free parameters, namely $\kappa_i^0$, $\mathrm{A}_i$ and $u$, as $P_c(T)$, $P_c(T_c)$, $T_c$ and $w$ were already determined experimentally. We will now apply this model to the experimental data, i.e., to the data set taken along the $a$ as well as to the $b$ axis, covering a pressure range $15\,\mathrm{MPa} \lesssim P \lesssim 30\,\mathrm{MPa}$ and in total 14 different temperatures $30\,\mathrm{K} \leq T \leq 43\,\mathrm{K}$. The wide range in temperature and pressure, investigated here, guarantees that the three independent fit parameters can be determined uniquely.

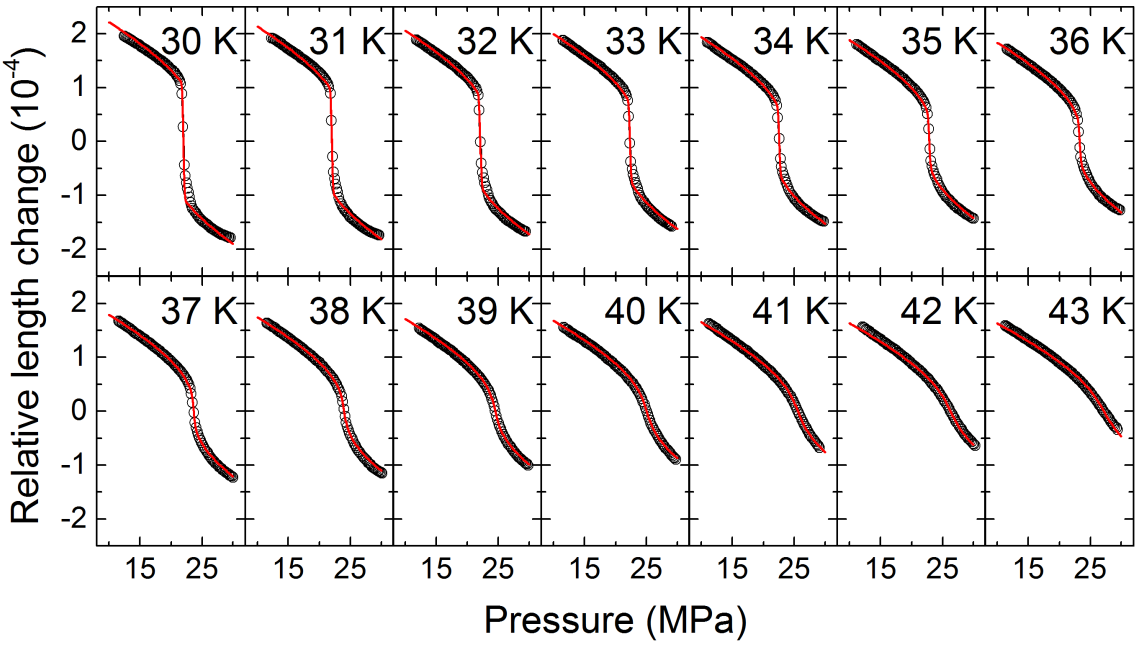


Figure 5.13.: Data of the relative length change of $\kappa$-(BEDT-TTF)$_2$Cu[N(CN)$_2$]Cl along the $b$ axis (black open circles) for various temperatures ranging from $T = 30\,\mathrm{K}$ to $43\,\mathrm{K}$ around $T_c \approx 36.5\,\mathrm{K}$, together with the fit to the mean-field model, introduced in eq. 5.18 (red solid line).

Figure 5.13 shows the experimentally determined relative length change data along the $b$ axis $\Delta L_b/L_b$ (black open symbols) and the corresponding fit with the mean-field model (solid red line), introduced in detail above in eq. 5.18. We find that the fit with only three free parameters $\kappa_b^0$, A$_b$ and $u$ provides an excellent description of the experimental data over the complete investigated temperature and pressure range. For the non-critical background contribution, we find $\kappa_b^0 = 4 \cdot 10^{-6}/\mathrm{MPa}$. This value is of the same order of magnitude as the normal elastic compressibility determined for a related $\kappa$-phase organic charge-transfer salt [103], and thus represents a reasonable value for the background contribution. The non-linearity of the potential, characterized by $u$, is found to be $u = 0.18$. Since we performed the fits individually to each $T = \mathrm{const.}$ data set, even though we obtain the same values for $\kappa_b^0$ and $u$, the proportionality constant $A_b$ obeys slightly different values for each data set. Nevertheless, these values, indicated by the symbols in Fig. 5.14, appear to be not independent from each other, as they follow to a good approximation a $T$-linear variation $A_b = (0.86 - 1.01(T - T_c)/T_c) \cdot 10^{-4}$ (solid line in Fig. 5.14). Such a temperature dependence of the proportionality constant could e.g. arise from a smooth $T$-dependence of the elastic tensor which, in turn, influences its eigenvalues and -vectors. As derived above in detail, the components of the eigenvector determine how strongly the lattice change responds to the presence of a critical singlet. We used this $T$-linear parametrization of $A_b$ for the model curves shown in Fig. 5.13.

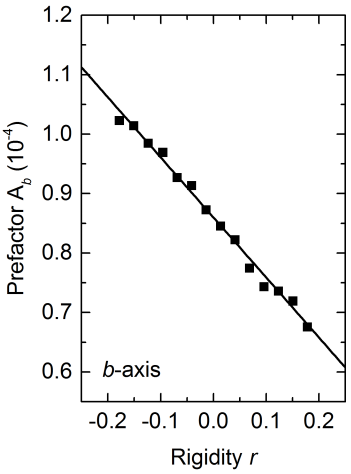


Figure 5.14.: Variation of the fit parameter $A_b$ as a function of the rigidity $r = \frac{T-T_c}{T_c}$ derived from individual fits of the experimental $\Delta L_b(P)/L_b$ data with the mean-field model, displayed in eq. 5.18, in the regime $30\,\mathrm{K} \leq T \leq 43\,\mathrm{K}$. The solid line represents a $T$-linear parametrization of the $A_b$ data, which was used for the modeling, shown in Fig. 5.13.

We stress that fits of equal quality can be obtained upon changing the fixed parameter $T_c = (36.5 \pm 0.5)\,\mathrm{K}$ within its error bars. Thereby, the $A_b$ values change by about 5% at maximum. However, upon changing $T_c$ beyond the error bars results in fits, which deviate significantly from the experimental data around $T_c$. In addition, treating $T_c$ as an additional free parameter in the fitting procedure, the optimal fit is obtained with $T_c = 36.2\,\mathrm{K}$, which is in very good agreement with the previously independently determined value of $T_c = (36.5 \pm 0.5)\,\mathrm{K}$. Overall, the excellent agreement of our data set and the mean-field model is apparent not only by looking on the bare data, but also by considering the compressibility, i.e., the derivative of the experimental data (symbols) and the model fits (solid lines), shown in Fig. 5.7.

Furthermore, not only the $b$ axis data can be well described, but also the $a$ axis data can be modeled with equally high quality by the mean-field model, as demonstrated in Fig. 5.15. It is important to note that the fit obtained here yields the same non-universal constant $u = 0.18$, as previously determined for the $b$ axis data. This lends further credibility to our modeling, as both axes are measuring the same critical singlet $\varepsilon_1$. The latter one is governed by the critical mean-field potential with non-linearity $u$. Thus, the measurements on different crystallographic axes represent an independent approach to the same critical properties. The good agreement of both data sets with the fit, based on the same non-linearity $u$, strengthens the applicability of this model to the Mott critical endpoint in this material $\kappa$-Cl. In contrast to the critical properties, the background compressibility $\kappa_a^0$ and the proportionality constant $A_a$ have to be determined independently. We obtain $\kappa_a^0 = -10.5 \cdot 10^{-6}/\mathrm{MPa}$. The unusual negative sign of the compressibility, corresponding

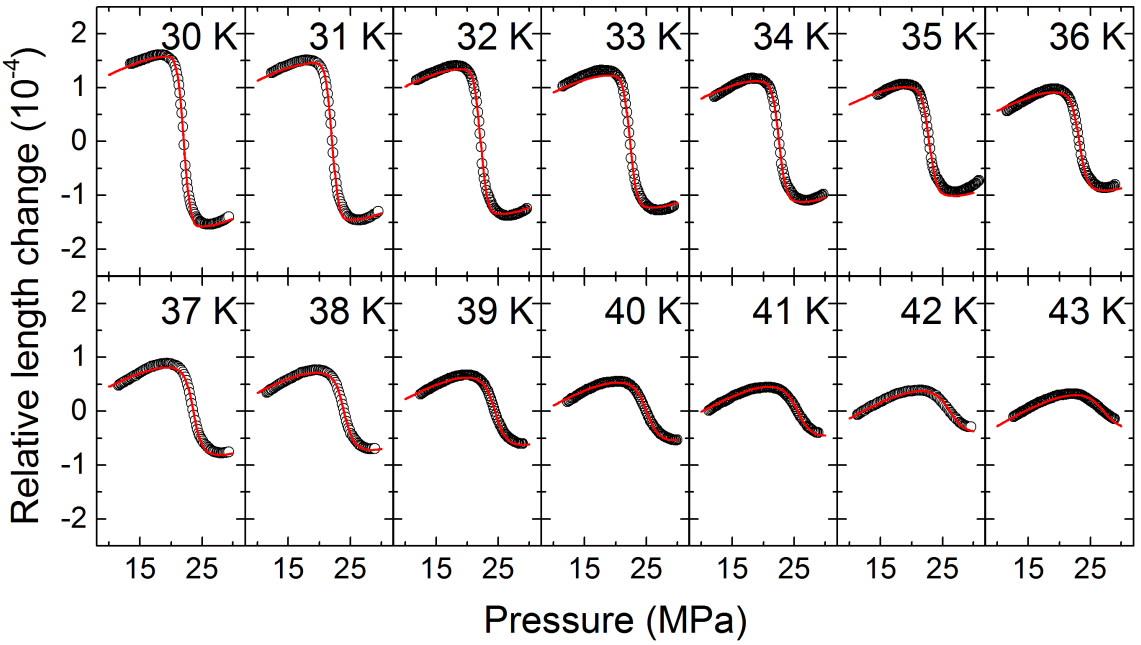


Figure 5.15.: Data of the relative length change of $\kappa$-(BEDT-TTF)$_2$Cu[N(CN)$_2$]Cl along the $a$ axis (black open circles) for various temperatures ranging from $T = 30\,\mathrm{K}$ to $43\,\mathrm{K}$ around $T_c \approx 36.5\,\mathrm{K}$, together with the fit to the mean-field model, introduced in eq. 5.18 (red solid line).

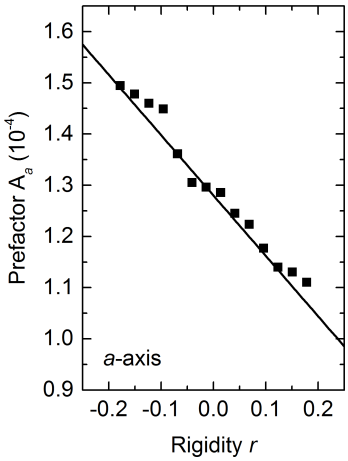


Figure 5.16.: Variation of the fit parameter $A_a$ as a function of the rigidity $r = \frac{T-T_c}{T_c}$ derived from individual fits of the experimental $\Delta L_a(P)/L_a$ data with the mean-field model, displayed in eq. 5.18, in the regime $30\,\mathrm{K} \leq T \leq 43\,\mathrm{K}$. The solid line represents a $T$-linear parametrization of the $A_a$ data, which was used for the modeling, shown in Fig. 5.15.

to an expansion of the $a$ axis upon pressurizing the system, can be assigned to the pressure-induced progressive inclination of the ET molecules with respect to the $b$ axis, as discussed above in detail. As similarly observed for the $b$ axis fit, the proportionality constant $A_a$ reveals different values as a function of the rigidity $r$ (symbols in Fig. 5.16), which never-

theless follow to a good approximation a $T$-linear variation. The following parametrization $A_a = (1.28 - 1.18(T - T_c)/T_c) \cdot 10^{-4}$ (solid line in Fig. 5.16) was used for the fits in Fig. 5.15.

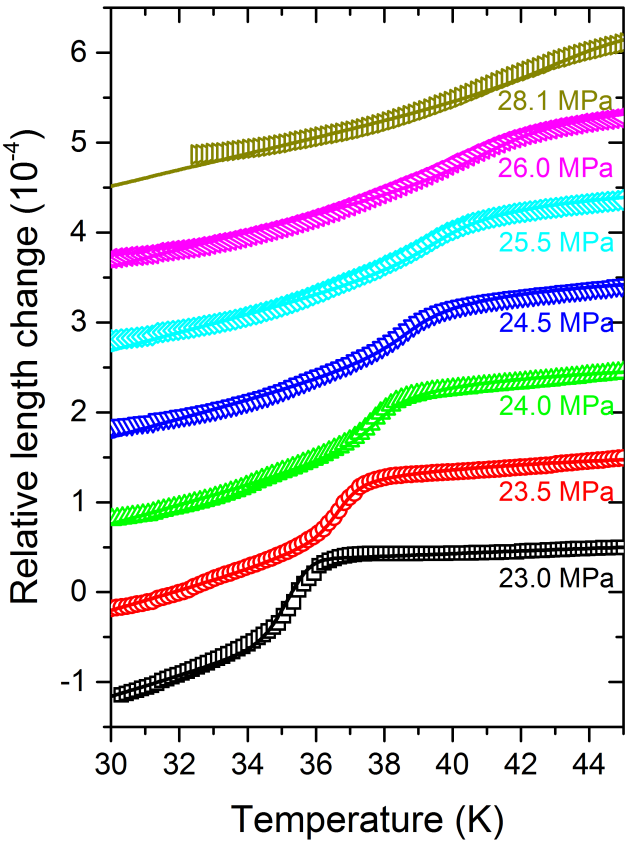


Figure 5.17.: Data of the relative length change of $\kappa$-(BEDT-TTF)$_2$Cu[N(CN)$_2$]Cl, taken along the $b$ axis, as a function of temperature $\Delta L_b(T)/L_b$ at various constant pressures (open symbols), together with a modeling of the data with the mean-field equation 5.18 (solid lines). The parameters of the mean-field equation $u$ and $A_i$ were taken from the fit to the pressure-dependent data at constant $T$. The non-critical background expansion was approximated with a polynomial of $\mathcal{O}(T^2)$. Data were offset for clarity.

All in all, we have convincingly shown that the pressure-dependent measurements of the relative length change $\Delta L_i(P)/L_i$ along $i = a, b$ can be described on a quantitative level by the above-mentioned mean-field model, which implies mean-field criticality of the Mott critical endpoint in $\kappa$-Cl. The fit also provides a scale-invariant description of the critical relative length change $(\Delta L_i/L_i)(T,P)_{critical}$ over the complete $T$-$P$-range, investigated here. Accordingly, $(\Delta L_i/L_i)(T,P)_{critical}$ must also provide a description of the experimentally determined relative length change as a function of $T$, $\Delta L_i(T)/L_i$, the derivative of which was already shown in Fig. 5.10. Even though the three free parameters, $\kappa_i^0$, $A_i$ and $u$, are known from the analysis of the pressure-dependent data, the non-critical background to the temperature-dependent relative length change is unknown. Unfortunately,

there is neither an experimental nor a theoretical access to get hold of the non-critical background. We therefore assumed that close to $T(\alpha_{max})$, corresponding to the inflection point of $\Delta L_i(T)/L_i$, the background can be approximated by a polynomial of $\mathcal{O}(T^2)$, and fitted the experimental data by a sum of this polynomial with in total three free parameters and the known scale-invariant $(\Delta L_i/L_i)(T,P)_{critical}$. Figure 5.17 shows the result of this fit (solid lines), together with the experimental data, taken along the $b$ axis, for various constant pressures ranging from $P = 23.0\,\mathrm{MPa}$ up to $28.1\,\mathrm{MPa}$, i.e., over a wide range of pressure across the Mott transition. As demonstrated in the figure, the fit describes well the anomalous behavior of the relative length change around $T(\alpha_{max})$. Deviations of the fit at temperatures away from $T(\alpha_{max})$ can be assigned to the comparatively simple background approximation. The good agreement of this fit, based on parameters from pressure-dependent studies, with the temperature-dependent data provides a significant crosscheck for the applicability of this mean-field model.

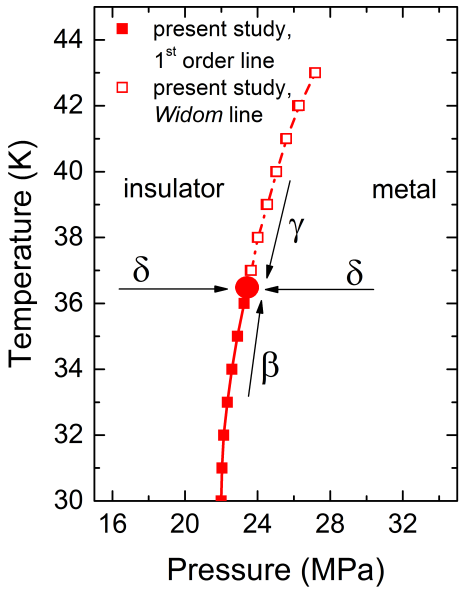


Figure 5.18.: Scheme of the scans (arrows) in the phase diagram, each of which allows for a determination of one of the critical exponents $\beta$, $\gamma$ or $\delta$. Red solid line, which is a guide to the eye line to the determined transition pressures (red closed squares), represents the first-order transition line. Red full circle corresponds to the critical endpoint. Dotted line, which is a guide to the eye line to the *Widom* pressures (red open symbols), represents the *Widom* line.

### Independent estimate of the critical exponents

Despite the excellent agreement of our full data set with mean-field criticality, the applied model, for sure, does not provide an independent approach to determine the critical prop-

erties, as we assume initially that the critical singlet $\epsilon_1$ is governed by a mean-field critical potential. As introduced in Sec. 2.2, an independent approach to the critical properties is provided by the analysis of the power-law dependency of different physical quantities with respect to either temperature or pressure close to the critical endpoint. The quantity of interest, namely the critical exponent (see Tab. 2.2 for the critical exponents of the various universality classes), is then obtained from the slope of the straight line in a double-logarithmic representation of the physical quantity with respect to either temperature or pressure. We can, in general, access the critical exponents $\beta$, $\gamma$ and $\delta$ from our experiment (see Fig. 5.18). To this end, we have to assume that the order parameter is proportional to $\Delta L/L$. It was already suggested by other researchers that the relative length change could act as an order parameter at the Mott transition, as the volume/length is the thermodynamic conjugate variable to the tuning parameter, namely the pressure (see, e.g., Ref. [20])[2]. Thus, the relative length change is related to the critical exponents in the following manner:

$$(\Delta L/L)\,|_{P=P_c(T)} \propto (T_c - T)^{\beta} \tag{5.19}$$

$$\kappa|_{P=P_c(T)} \propto (T - T_c)^{-\gamma} \tag{5.20}$$

$$(\Delta L/L)\,|_{T=T_c} \propto (P - P_c(T_c))^{1/\delta}. \tag{5.21}$$

However, a small amount of disorder, which is present in every real system, introducing an additional length scale in the system, can drastically complicate the analysis of such plots. Despite these complications, we will show in the following that we can identify ranges in temperature and pressure, in which disorder effects play a minor role, and thus enable an independent estimate of the critical exponents. We will demonstrate that this independent approach to the critical properties provides a set of critical exponents which are fully consistent with the mean-field universality class. This, in turn, verifies the applicability of the mean-field model, which is able to simultaneously describe the full two-dimensional $(T, P)$ data set with underlying mean-field criticality and the effects of disorder.

First, we discuss the estimation of the critical exponent $\delta$ from a double-logarithmic plot of the relative length change as a function of the reduced pressure very close to the critical endpoint $T = T_c$, in the presence of a small amount of disorder. To this end, let us first have a look on the critical contribution to the relative length change determined from the mean-field fit, based on eq. 5.18. This model includes a phenomenological approach to describe disorder effects. Thus, it helps to identify and understand the influence of the additional length scale and possible deviations from a simple power-law behavior. Figure 5.19 (A)

[2]Note that the assumption that the relative length change could act as an order parameter already implies a crucial role of the lattice for the critical behavior. The aim here is to show independently in an unbiased approach that this influence of lattice degrees of freedom is accompanied by a crossover to mean-field criticality.

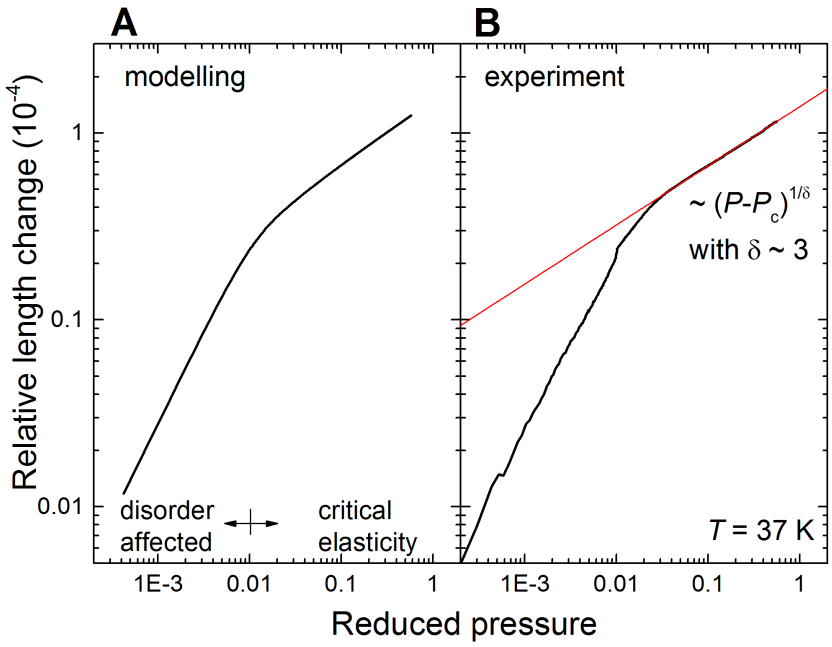


Figure 5.19.: Estimate of the critical exponent $\delta$ in a double-logarithmic plot of the singular contribution to the relative length change as a function of the reduced pressure $|(P-P_c(T_c))/P_c(T_c)|$. (A) Singular contribution to $\Delta L/L$, determined from the mean-field fit, based on eq. 5.18. Two regimes with two approximately straight lines in the double-logarithmic representation can be identified which are associated to the disorder-affected regime close to $P_c$ and the critical elasticity regime slightly off $P_c$. (B) Singular contribution to $\Delta L/L$, determined from the experimentally measured $\Delta L_b/L_b$ along the $b$ axis. The red line corresponds to a linear fit of $\log(\Delta L_b/L_b)$ vs. $\log(|(P-P_c(T_c))/P_c(T_c)|)$ with a slope $\delta = 3.2$.

shows the critical contribution of the mean-field fit, based on eq. 5.18 $(\Delta L/L)_{critical}$, i.e., after subtracting the non-critical background, in a double-logarithmic presentation as a function of the reduced pressure $|(P-P_c(T_c))/P_c(T_c)|$. Two different ranges, in both of which the logarithmic representation of $(\Delta L/L)_{critical}$ follows approximately a straight line, can be identified. These ranges are separated at $|(P-P_c(T_c))/P_c(T_c)| \approx 0.02$. We interpret the occurrence of two different regimes as an indication for the presence of two different length scales, which dominate the behavior at different distances from the critical endpoint. At small distances to the critical endpoint, we attribute the behavior to a disorder-affected deviation from the simple-power law. The latter can be observed at distances somewhat further away from the endpoint and is characterized by the mean-field critical exponent $\delta = 3$, as naturally implied in the model.

Figure 5.19 (B) shows the experimentally determined relative length change along the $b$ axis $\Delta L_b/L_b$ at $T = 37\,\mathrm{K}$ in the corresponding double-logarithmic representation. As the possibility of performing pressure sweeps is currently limited to pressures $P \leq 30\,\mathrm{MPa}$, much more data points are available for $P < P_c$ than for $P > P_c$. We therefore restrict

the analysis to this low-$P$ regime, nevertheless, a similar analysis is in principle possible for $P > P_c$. The non-critical background contribution was subtracted to obtain the singular part of the relative length change. Similarly to the theoretical model curve, the experimental data can also be divided into two different regimes with two different slopes. Our data analysis is, as identified for the theoretical model curve, restricted to the pressure range slightly off the critical pressure, where disorder effects play a minor role. The slope of a linear fit to the $\log(\Delta L_b/L_b)$ vs. $\log(|(P - P_c(T_c))/P_c(T_c)|)$ (red line in Fig. 5.19) corresponds to a critical exponent $\delta = (3.2 \pm 0.2)$, which is fully consistent with the critical exponent $\delta$ of the mean-field universality class. However, it is incompatible with the values for any other universality class, listed in Tab. 2.2.

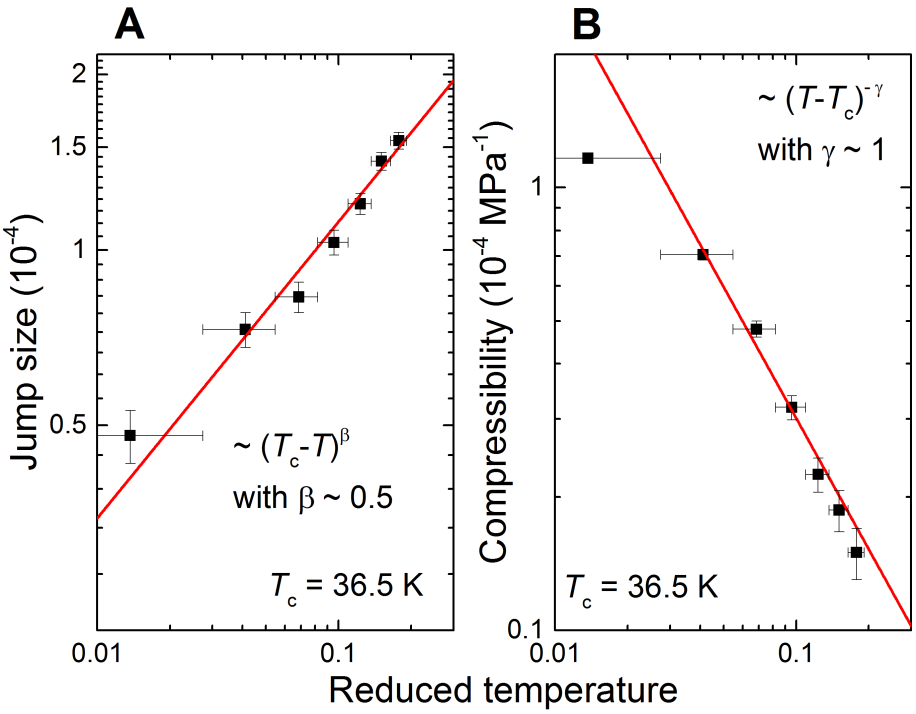


Figure 5.20.: Estimate of the critical exponents $\beta$ and $\gamma$. (A) Double-logarithmic plot of the size of the jump in the relative length change along the $b$ axis at the first-order transition, i.e., for $T < T_c$, as a function of the reduced temperature $(T_c - T)/T$. The red line corresponds to a linear fit of $\log((\Delta L_b/L_b)_{P=P_c(T)})$ vs. $\log((T_c - T)/T)$ with slope $\beta = 0.52$. (B) Double-logarithmic plot of the singular part of the compressibility $\kappa_b$ for $T > T_c$ as a function of the reduced temperature $(T - T_c)/T_c$. The red line corresponds to a linear fit of $\log(\kappa_{b,P=P_c(T)})$ vs. $\log((T - T_c)/T_c)$ with a slope $\gamma = 1$.

Analogously, we can proceed with estimating the critical exponents $\beta$ and $\gamma$ by analyzing temperature-dependent scans below and above $T_c$ (see Fig. 5.18), respectively. The exponent $\beta$ describes how the first-order jump of the length vanishes upon approaching the critical endpoint. Due to the finite width of the jumps below $T_c$, we apply the following procedure to determine the jump size with only a small experimental uncertainty: In a

hypothetically clean system, the compressibility, i.e., the derivative of $\Delta L/L$, at the critical endpoint should be infinitely large. In any real system, however, it is finite due to broadening effects. The same holds true for the first-order length jumps below $T_c$. Thus, we assume that we can map the critical compressibility in a system with disorder onto that for the ideal clean system. Following this idea, we identify the jump in the relative length by considering the $\Delta L_b/L_b$ between those two pressure points where the compressibility is at least as high as the critical compressibility. The so-derived jump sizes $(\Delta L_b/L_b)_{P=P_c(T)}$ are plotted in the double-logarithmic representation in Fig. 5.20 (A), which follow to a good approximation a straight line. A linear fit to $\log((\Delta L_b/L_b)_{P=P_c(T)})$ vs. $\log((T_c - T)/T)$ yields a slope of $\beta = (0.52 \pm 0.07)$. The error bar of this fit is mainly affected by the error bar in the determination of $T_c$. This value is also in good agreement with the critical exponent $\beta$ of the mean-field universality class, but far away from the values for other universality classes.

The exponent $\gamma$ can be estimated by a consideration of the maximum critical compressibility above the critical endpoint in the crossover regime, i.e., the critical compressibility along the *Widom* line. For this purpose, the maximum critical compressibility values at different $T$, displayed in Fig. 5.7, have to be corrected for the non-critical elastic background. All these values, obtained in this study for various different $T$ ranging from $T = 37\,\mathrm{K}$ up to 43 K, are plotted in a double-logarithmic fashion in Fig. 5.20 (B). However, we restrict the analysis of the critical exponent to the region $(T - T_c)/T_c > 0.15$. In this region, corresponding to $T > 38\,\mathrm{K}$, disorder effects are expected to play a minor role and do therefore not strongly affect the estimation of the critical exponent. The analogous analysis performed here, i.e., a linear fit, reveals a critical exponent $\gamma = (1.0 \pm 0.1)$. As listed in Tab. 2.2, this value is in accordance with the value obtained for mean-field criticality.

Our independent estimate of the critical exponents $\beta, \gamma$ and $\delta$ demonstrates that the observed relative length changes indeed reveal mean-field criticality. This analysis verifies the ansatz for the description of the critical properties, namely a description within the mean-field model, based on eq. 5.18.

### Comparison with measurements on other crystals

Before proceeding with discussing the impact of the present experimental result, we will show that the results obtained on other crystals of $\kappa$-Cl are fully consistent with those obtained on crystal #AF063, which were presented above. This discussion will also help to estimate sample-to-sample variations. We will prove that these effects play only a minor role and that the strong coupling of electronic and lattice degrees of freedom at the Mott critical endpoint is indeed an universal feature.

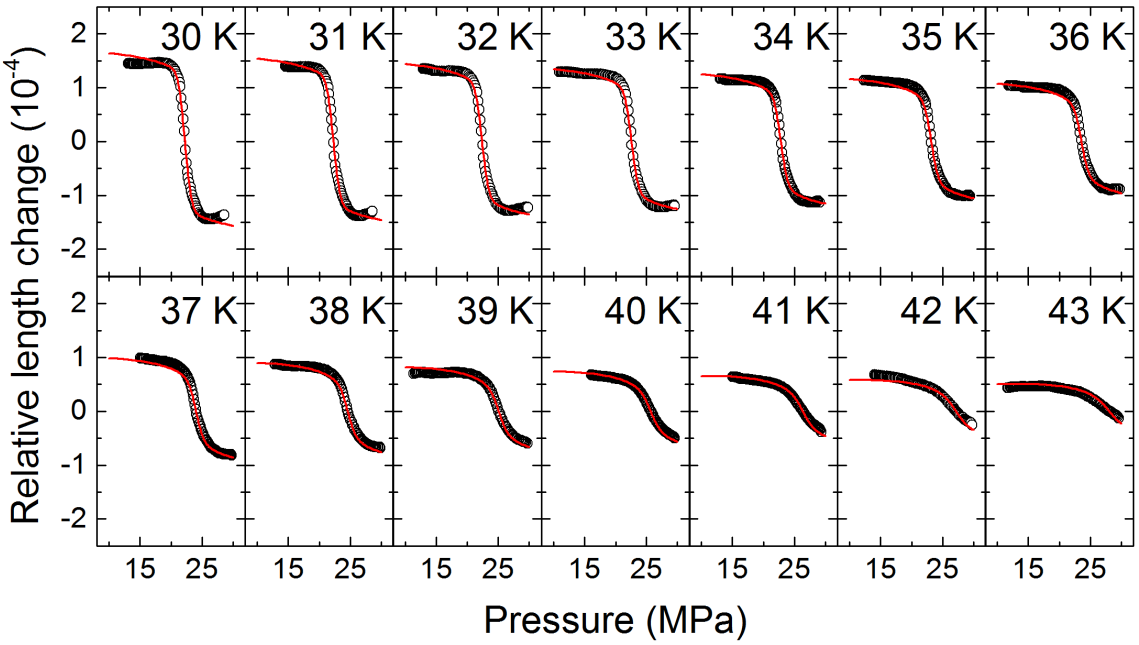


Figure 5.21.: Data of the relative length change $\Delta L_a/L_a$, taken on crystal κ-(BEDT-TTF)$_2$Cu[N(CN)$_2$]Cl #AF063-II (black open symbols), as a function of pressure at various different constant temperatures $30\,\mathrm{K} \leq T \leq 43\,\mathrm{K}$ and modeling with the mean-field fit, based on eq. 5.18 (red solid line).

To this end, we will focus on the pressure-dependent measurements of the relative length change $\Delta L_a/L_a$ performed along the $a$ axis of crystal #AF063-II (see Tab. 5.1 for a full list of investigated samples), which are shown in Fig. 5.21 by black open symbols in the same temperature range as investigated above, i.e., $30\,\mathrm{K} \leq T \leq 43\,\mathrm{K}$. The behavior of the length as a function of pressure and the evolution with temperature is very similar to the previous observations for #AF063: We observe a broadened jump of the length from the insulating to the metallic side below $T_c \approx 37.5\,\mathrm{K}$ (see below for the determination of the critical endpoint for this particular sample), which results in a decrease of the length and the respective volume at the Mott transition. The jump size along the $a$ axis, revealed here, of $\Delta L_a/L_a|_{P=P_c(T=30\,\mathrm{K})} \approx -3 \cdot 10^{-4}$ at 30 K is comparable in size with the jump size determined along the same crystallographic axis for #AF063. This jump evolves into a continuous crossover behavior for $T > T_c$. Importantly, we again find that the length changes reveal the same strongly non-linear variation as a function of pressure over a wide temperature and pressure range from $T_c \approx 37.5\,\mathrm{K}$ to higher temperatures $T \approx 43\,\mathrm{K}$. However, besides the striking similarities, one remarkable difference between the two data sets on two different crystals can be observed: Whereas the $a$ axis data for crystal #AF063 shows the unusual positive slope far away from the endpoint, corresponding to a lattice expansion upon pressurizing, the $a$ axis measurements shown here, reveal a more or less flat

behavior of the length as a function of pressure far away from the endpoint. The reasons for these deviations are unclear at present.

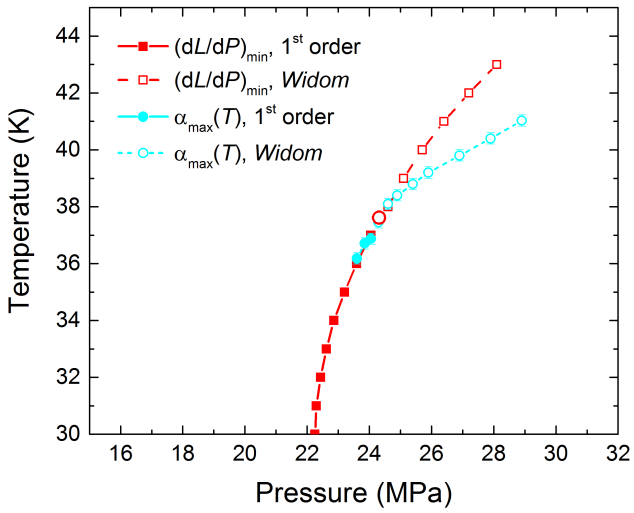


Figure 5.22.: Phase diagram for $\kappa$-(BEDT-TTF)$_2$Cu[N(CN)$_2$]Cl determined from measurements of relative length changes along the $a$ axis on crystal #AF063-II. Full red symbols, connected by the red solid line, correspond to first-order transition pressures. Red open circle corresponds to the critical endpoint. Open red symbols, connected by the red dashed line, correspond to *Widom* pressures. Full (open) cyan circles represent the transition points (crossover points) determined by the maximum response of the thermal expansion coefficient $\alpha(T) = L^{-1}\mathrm{d}L/\mathrm{d}T$ from temperature-dependent measurements.

Nevertheless, this data set can be analyzed in a similar manner, as presented in detail above, to extract the phase diagram (see Fig. 5.22), including the critical endpoint. The first-order transition line and the *Widom* line are slightly shifted to higher pressures compared to the previous results for #AF063. For fixing the critical endpoint, we focus here on the determination of the crossover line corresponding to the maximum in the thermal expansion coefficient. We find that the critical pressure $P_c(T_c) \approx 24.1\,\mathrm{MPa}$ is also shifted to slightly higher pressures. The temperature of the critical endpoint, determined from the crossing point of the crossover line and the first-order line, is for this particular sample located at $T_c \approx 37.5\,\mathrm{K}$, which is about 1 K higher than for the previous sample. This indicates sample-to-sample variations in the details of the phase diagram, which in turn emphasize the need to determine the phase diagram for every sample individually, especially when the critical properties are in the focus of the investigations.

In order to model this data with the introduced mean-field model, the variance of the Gaussian distribution function for the description of the broadening effects has to be determined from a Gaussian fit to the derivative of the experimental data well below $T_c$, i.e., at 30 K. The analysis yields a value of $w_a = 1.2 \cdot 10^{-3}$ which deviates by less than 10% from the variance determined for the other sample along the same crystallographic axis.

The fit was performed with the individually determined variance and with an identical non-linearity $u = 0.18$ as in the former description of the measurement results along the $a$ and the $b$ axis of crystal #AF063. By using a distinctly smaller background compressibility $\kappa_a^0 = 2.5 \cdot 10^{-6}$/MPa, as already apparent from the bare data, and a $T$-linear proportionality constant $A_a = (0.86 - 1.41(T - T_c)/T_c) \cdot 10^{-4}$, we obtain a very good description of the experimental data set with this mean-field model (see Fig. 5.21).

From the above-presented data and analysis of a second crystal, we can infer the following robust statements about the critical behavior around the second-order critical endpoint of the Mott transition in $\kappa$-Cl: In a wide range in temperature and pressure around critical endpoint, the length changes respond in a strongly non-linear fashion to the externally-applied stress. This breakdown of Hooke's law reflects an intimate non-perturbative coupling of the critical electronic degrees of freedom to the lattice, evoking a softening of the crystal lattice. The relative length changes, as demonstrated by various approaches, can be well described on a quantitative level by mean-field criticality, as theoretically predicted for such a coupled system [21].

### Discussion

The obtained data set with focus on the intensively investigated crystal #AF063 allows us to identify different regimes close to the critical endpoint, in each of which a different scale is of importance. This, in turn, will help us to relate our results to literature results. We identified strongly renormalized compressibilities $\kappa_i$ around $(P_c, T_c) \approx (23.4\,\mathrm{MPa}, 36.5\,\mathrm{K})$ up to a temperature of at least 43 K, and up to 25 MPa in pressure. This range in temperature and pressure, corresponding to a width of $\Delta T/T_c \approx 20\%$ and $\Delta P/P_c \approx 10\%$ (yellow regime in Fig. 5.9), is expected to be governed by the critical elasticity, i.e., the non-perturbative coupling of critical electronic fluctuations and the lattice. As a consequence, we conclude that the immediate region around the critical endpoint is governed by mean-field criticality. The presence of critical elasticity can also be inferred [22] for the archetype Mott system $V_2O_3$, which is located somewhat off the critical endpoint on the metallic side of the transition. The experimental evidence in this particular transition-metal oxide is provided by a detailed investigation of the elastic tensor by ultrasonic measurements [157] which showed a substantial softening of one of the elastic constants.

In addition, we identified a region very close to the endpoint, in which disorder effects play a crucial role. However, this region is about a factor of 10 smaller than the critical elasticity regime and can therefore be effectively treated within the framework of critical elasticity with disorder effects playing only a minor role.

However, further away from the endpoint and away from the critical elasticity regime, the lattice response to the critical electronic fluctuations is much weaker. Thus, in this regime the coupling between the electrons and the lattice can be treated as a small perturbation and electronic criticality should prevail. This regime is expected to be characterized by either non-trivial critical (Ising) exponents or mean-field exponents, which depends on the size of the Ginzburg regime [22] (light blue region in Fig. 5.6), determined by the Ginzburg criterion (see Sec. 2.2 for the explanation of the Ginzburg criterion). In case the Ginzburg region is larger than the critical elasticity regime, a crossover from critical elasticity to non-trivial Ising exponents is expected, as depicted in Fig. 5.6. However, if the Ginzburg region is smaller than the critical elasticity regime, a direct crossover from an elastic mean-field behavior to an electronic mean-field behavior would be expected. The present data unfortunately do not allow for an analysis of the critical exponents far away from the critical elastic regime due to its large extension and the limited $T$-$P$-range accessible by our experiment. The thermal expansion measurements on $\kappa$-(d8-ET)$_2$Cu[N(CN)$_2$]Br [132], presented in Sec. 5.1, which is located $(P - P_c)/P_c \approx 20\%$ off the critical endpoint on the metallic side, i.e., right at the border of the investigated $P$-range here, showed consistency with the 2D Ising universality class [20]. This observation might indicate that the Ginzburg regime is larger than the elastic mean-field regime in the present material.

The results, obtained here, on the organic-charge transfer salt $\kappa$-Cl clearly demonstrate, that measurements of the strain of the crystal lattice are of fundamental importance in probing and understanding the criticality of the finite-temperature Mott endpoint. They also indicate that elastic degrees of freedom have to be considered in further theoretical work in order to understand the analysis of the conductance data [18]. A detailed understanding of the transport properties close to the critical endpoint might be particularly interesting, as the present material was recently discussed to obey quantum critical signatures in the conductance data [148,158,159] in an intermediate temperature range $T_c < T \leq U/k_B, W/k_B$ owing to the rather low $T_c \approx 36\,\mathrm{K}$ compared to the rather strong competing interactions of $U/k_B, W/k_B \approx \mathcal{O}(10^4\,\mathrm{K})$. This quantum-critical background might, in turn, influence the analysis of the conductance close to $T_c$.

Recently, by applying the method of fluctuation spectroscopy, an analysis of the resistance fluctuations close to the finite-temperature critical endpoint in this family of organic charge-transfer salts showed a divergent increase of fluctuations, which is accompanied by a drastic shift of spectral weight to lower frequency [141]. This scenario was associated with the well-known critical slowing down of the fluctuations close to a second-order critical endpoint. However, the scenario discussed here, in which we identified the critical endpoint as an isostructural critical endpoint, implies the absence of a diverging correlation length [22,154] and thus, a saturation of the critical slowing down would be expected. The critical slowing down, observed in experiments, could alternatively arise from slow dynamics of the domain

formation due to the presence of disorder. A conclusive statement about the origin of the slowing down cannot be made at this point, so that further studies that include elastic degrees of freedom and disorder effects are needed to identify the origin of the slowing down close to the Mott transition.

In summary, the thermal expansion measurements around the Mott critical endpoint for $\kappa$-Cl showed that lattice degrees of freedom are of high importance in the description of the critical properties and the universal behavior in real materials, in which the critical electronic system is embedded into a compressible lattice. The strong influence of elastic degrees of freedom at the Mott transition can be inferred from the fact that the transition itself can be tuned by pressure, as it is the case for many Mott systems, such as various $\kappa$-(ET)$_2X$ [32, 66, 116] or Et$_x$Me$_{4-x}Z$[Pd(dmit)$_2$]$_2$ [33] organic charge-transfer salts and transition metal-oxides, such as $(V_{1-x}M_x)_2O_3$ [17, 29, 160], NiO [30] or $PbCrO_3$ [31]. In all of these systems, the universal behavior will be eventually governed by critical elasticity sufficiently close to the Mott endpoint. In contrast, in $VO_2$ doping experiments suggest that the transition is insensitive to pressure, so that the elastic coupling in this system is expected to be rather weak. Indeed, in this system an extended regime was found in which the critical behavior is encountered for by the random-field Ising model [161]. All in all, the strength of elastic coupling close to the Mott critical endpoint and thereby the size of the critical elasticity regime should be larger the steeper the first-order transition line in the $T$-$P$ phase diagram is. In other words, the steepness of the first-order transition line measures how susceptible the system to pressure-tuning is. It is determined, according to the Clausius-Clapeyron equation 2.16, by the ratio of volume change to the change of entropy, $\Delta V/\Delta S$, across the first-order-transition. According to the third law of thermodynamics, $\Delta S$ has to vanish for $T_c \to 0$. Correspondingly, $\mathrm{d}T_c/\mathrm{d}P$ has to increase and the critical elastic regime is expected to grow for materials with lower $T_c$. Nevertheless, irrespective of the size of the critical elasticity regime, our results clearly demonstrate that the Mott transition in every real material, which is amenable to pressure tuning, shows the universal properties of an isostructural solid-solid endpoint, obeying mean-field critical behavior, rather a liquid-gas endpoint with Ising criticality.

Following this detailed discussion about the critical behavior around the Mott transition in real materials, we want to present preliminary studies addressing open issues which arose in the course of the present work: First, we compare measurements of the relative length change to the conductance obtained on the same single crystal to address the controversy of transport vs. thermodynamic measurements in the presence of a compressible lattice. Secondly, we will study the influence of disorder on the Mott transition by a systematic control of the amount of disorder by x-ray irradiation (see Sec. 4.3 for an introduction on the effects of x-ray irradiation on the organic charge-transfer salts).

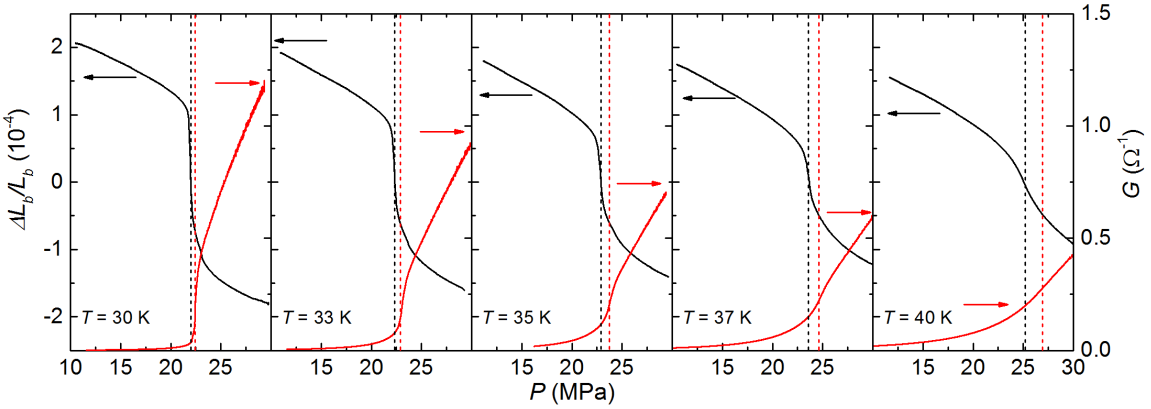


Figure 5.23.: Comparison between results of the relative length change $\Delta L_b/L_b$ and of the conductance $G$ as a function of pressure on the same single crystal of $\kappa$-(BEDT-TTF)$_2$Cu[N(CN)$_2$]Cl #AF063 around its pressure-induced Mott transition for various selected constant temperatures between $T = 30\,\mathrm{K}$ and $T = 40\,\mathrm{K}$. The left scale corresponds to the scale of the relative length change data, shown by black solid lines, the right scale corresponds to the scale of the conductance data, shown by red solid lines. The black (red) dashed lines indicate the pressure at which the slope of the relative length change (conductance) is the largest.

## 5.3. Comparison with conductance experiments

In the following, we will discuss preliminary results of the conductance[3] and the relative length change, measured along the $b$ axis, around the Mott transition in $\kappa$-Cl. This comparison aims to shed light on the controversial results on the Mott critical behavior obtained from thermodynamic vs. transport probes. To this end, we measured the relative length change (see Sec. 5.2) and the conductance on the same single crystal $\kappa$-Cl #AF063 as a function of pressure at various different temperatures across $T_c$ (see Fig. 5.23). In both cases, the data sets were recorded in decreasing pressure runs. First, we focus on the data set taken at lowest temperature, i.e., 30 K. The behavior of the relative length change as a function of pressure was discussed intensively above. The conductance $G$ exhibits a sharp jump at the Mott transition from the poorly conducting insulating state $G \approx \mathcal{O}(0.01\,\Omega^{-1})$ to a (bad) metallic state with $G \approx \mathcal{O}(1\,\Omega^{-1})$. In the metallic state, the conductance changes rather quickly with pressure, whereas in the insulating state the pressure dependence of the conductance is rather weak. The conductance hence shows an asymmetric behavior on either side of the transition. Such a behavior is rather untypical for a quantity, which is directly related to the order parameter, as the order parameter has to fulfill certain symmetry operations. Consequently, only the conductance in the metallic region was suggested to capture the universal behavior [17]. This observation is in contrast with the measurements of the relative length changes, which obey to a good approximation symmet-

[3] The results of resistance/conductance measurements, presented in this section, were obtained together with David Zielke (AG Lang).

ric behavior around the transition. Another remarkable aspect, which becomes evident by comparing the transport and the thermodynamic data set, relates to the inflection point of each of these curves. The inflection point of $\Delta L_b/L_b$ (dashed black line), which we identified above as the first-order transition pressure, is located distinctly lower in pressure than the pressure of maximal conductance change (dashed red line), which was associated with the first-order transition in previous works [18,118]. This implies that the first-order transition line and the *Widom* line in the phase diagram determined from a thermodynamic and a transport probe are different. This result might not be surprising, as a percolative current path can dominate the conductance measurements. This discrepancy becomes more apparent while following the signatures up to higher temperatures: Whereas at low temperatures the pressure difference between these two criteria amounts to only $\approx 1\,\mathrm{MPa}$ at $T = 30\,\mathrm{K}$, it increases up to $\approx 2.5\,\mathrm{MPa}$ at $T = 40\,\mathrm{K}$. Especially, the deviations are distinctly larger in the crossover regime above $T_c \approx 36.5\,\mathrm{K}$.

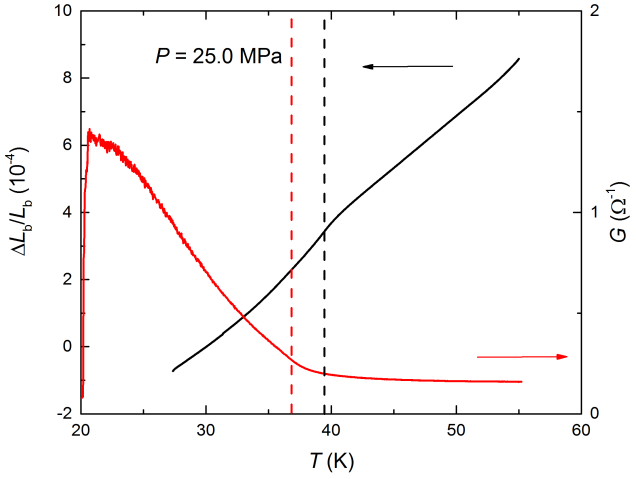


Figure 5.24.: Comparison of the relative length change $\Delta L_b/L_b$ (black solid line) and conductance $G$ (red solid line) measured on the same single crystal of $\kappa$-(BEDT-TTF)$_2$Cu[N(CN)$_2$]Cl as a function of temperature upon warming at $P = 25\,\mathrm{MPa}$. The black (red) dashed line indicates the position of the maximum of the thermal expansion coefficient, $\alpha = L^{-1}\mathrm{d}L/\mathrm{d}T$ (position of the rapid change of conductance, identified with the entrance into the crossover regime).

Similarly, in order to access the crossover features in both quantities, a comparison of temperature-dependent measurements is useful (see Fig. 5.24). As outlined in detail above, the maximum $\alpha_{max}$ in the thermal expansion coefficient $\alpha = L^{-1}\mathrm{d}L/\mathrm{d}T$ was suggested as a measure of the crossover scale [20]. The position of this maximum, i.e., the inflection point of $\Delta L_b/L_b$, at this specific pressure of $P = 25\,\mathrm{MPa}$ is located at $T \approx 39\,\mathrm{K}$, marked by the black dashed line. At this specific pressure, even though $P > P_c \approx 23.4\,\mathrm{MPa}$, the material is insulating at very low temperatures due to the S-shaped first-order transition line (see Fig. 4.6). It undergoes a first-order transition, characterized by a sharp jump of

the conductance, at around 20 K from the insulating to a metallic phase. Upon increasing the temperature, the conductance decreases continuously. At around $T \approx 37$ K (red dashed line), the conductance decreases with temperature in a more rapid manner, before it starts to flatten at even higher temperatures. We consider this temperature, at which the conductance changes quickly, as the temperature at which the entrance into the crossover regime takes place. Clearly, not only the first-order transition line and the *Widom* line, but also the crossover line, identified from the different probes with features located at 39 K (thermodynamic) and 37 K (transport) at $P = 25$ MPa, respectively, are rather different.

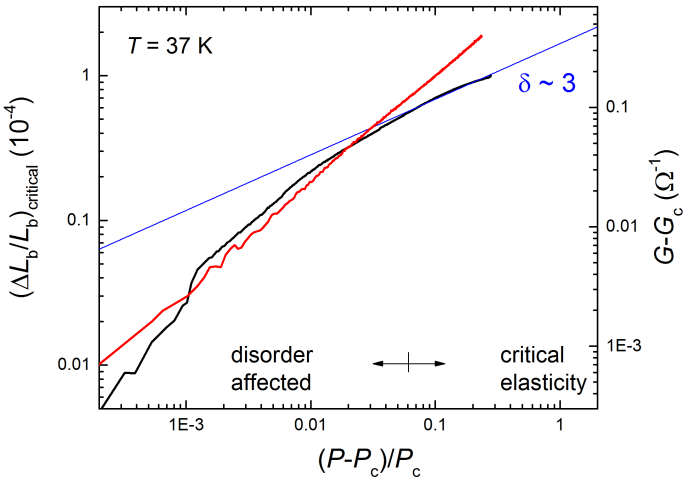


Figure 5.25.: Comparison between the critical contribution on the metallic side to the relative length change $(\Delta L_b/L_b)_{critical}$ (black solid line) and to the conductance $G - G_c$ (red solid line) as a function of the reduced pressure $(P - P_c)/P_c$ on the same single crystal of $\kappa$-(BEDT-TTF)$_2$Cu[N(CN)$_2$]Cl at $T = 37$ K. The pressure range can be divided into two regions in both of which different effects dominate, namely into the disorder-affected regime and the critical elasticity regime, as discussed in detail in the main text. The blue line indicates the fit of the relative length change data obeying the mean-field critical exponent $\delta = 3$.

Last, we would like to explicitly compare the functional dependence of the critical relative length change and the critical conductance as a function of the reduced external parameters $T$ or $P$. This comparison should help to solve the controversial estimates of critical exponents, as determined from transport and thermodynamic quantities. To this end, we exemplarily compare the determination of the critical exponent $\delta$ at 37 K, which can be estimated from the pressure-dependent analysis of the behavior very close to $T_c$. This example is particularly suited, as many data points are available for both data sets and as a very good understanding of the observed features in the relative length change (see Fig. 5.19) was gained previously. Note that we focus on the relative length change and the conductance on the metallic side of the phase transition (see Fig. 5.25). In Fig. 5.19, we showed the estimate of the exponent $\delta$ on the insulating side of the transition, as more data points are available on the insulating side due to the restriction in the maximum pressure of the current setups

for performing pressure sweeps of 30 MPa. Following the notation from Papanikolaou *et al.* [150], we assign $\delta$ to the exponent determined from the relative length change $\Delta L_b/L_b$ (black solid line) and $\delta_\sigma$ to the exponent determined from conductance measurements $G$ (red solid line). We argued above in Sec. 5.2 that we can identify a range in pressure slightly off the critical pressure in which disorder effects play a minor role, and thus, enables one to estimate the critical exponents. In this regime, we can identify the mean-field critical exponent $\delta = 3$ (blue solid line) after subtracting the non-critical background from the experimental data. To estimate $\delta_\sigma$, we plotted the critical conductance $G - G_c$ in the same manner as in previous reports [18], with $G_c = G_c(P_{c,G}, T_c)$. Note that we used the turning point of $G$ at $P_{c,G}$ as a reference point, similarly to previous investigations, irrespective of the above-mentioned deviations between the transition pressures determined from thermodynamic and transport measurements. The critical conductance is clearly following a linear behavior in this doube-logarithmic representation, nevertheless with a distinctly different slope than the relative length change. The estimate of the exponent yields $\delta_\sigma \approx 1.2$, a value which deviates significantly from the value reported in literature of $\delta_\sigma \approx 2$ [18]. The reason for this deviation is unclear at present and calls for an estimate of $\delta_\sigma$ on other single crystals to exclude sample-to-sample variations. As suggested by Papanikolaou *et al.* [150] by analyzing a resistor network on the basis of the 2D-Ising model, the exponent determined from conductance measurements $\delta_\sigma = \frac{\delta\beta}{1-\alpha}$ is connected to all the three critical exponents. It would thus follow that $\delta_\sigma = 1.5$ for the mean-field universality class and $\delta_\sigma = 15/8$ for the 2D Ising universality class. The value, found here, of $\delta_\sigma \approx 1.2$ is close to the mean-field value. However, as the relation between $\delta_\sigma$ and the critical exponents was only derived for the 2D Ising universality class and importantly, elastic degrees of freedom were not included in this approach, we cannot assign $\delta_\sigma$ unequivocally to a universality class. The analysis rather demonstrates that the conductance and the relative length change are not proportional to each other. Thus, it supports the notion that the conductance cannot play the role of the order parameter close to the Mott critical endpoint in $\kappa$-Cl. Taken all together, these preliminary data sets emphasize the need to model transport quantities, as the conductance, in the presence of an elastic crystal lattice. This will help not only to solve the controversy on the critical exponents, but also to provide an understanding of the salient features of the phase diagram from the various probes.

## 5.4. Study of the influence of disorder on the Mott transition by x-ray irradiation

The study of the critical properties of the Mott transition demonstrated that disorder effects, as present in every real material, can play a crucial role in the immediate vicinity around the critical endpoint. The interplay of disorder and strong electronic correlations

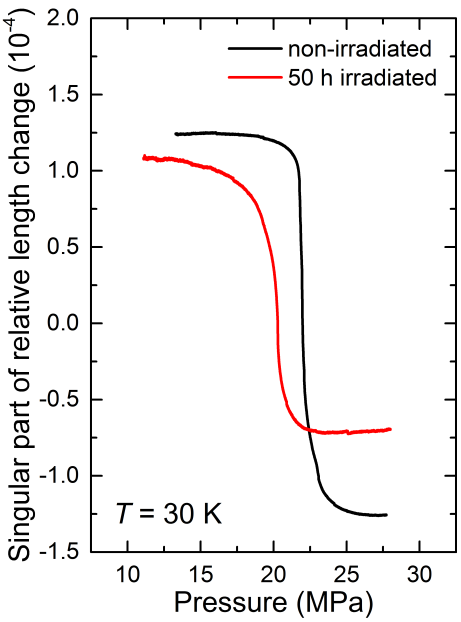


Figure 5.26.: Effect of disorder induced by x-ray irradiation on the first-order Mott transition of $\kappa$-(BEDT-TTF)$_2$Cu[N(CN)$_2$]Cl. Singular part of the relative length change, measured along the $b$ axis, at $T = 30\,\mathrm{K}$ on the pristine crystal #AF063, studied in great detail in this work (black solid line), and crystal #AF063-3, which was exposed to x-ray irradiation for a time of 50 h (red solid line).

is currently intensively investigated from theoretical and experimental side. As introduced in Sec. 4.3, x-ray irradiation of the pristine crystals provides a suitable experimental tool to study systematically the influence of disorder on the Mott transition. To this end, we studied the lattice effects around the Mott transition on two $\kappa$-Cl crystals #AF063-3 and #AF063-4, both of which were exposed to x-ray irradiation for 50 h (see Ref. [143] for details of the irradiation procedure)[4]. These crystals are out of the same batch as the previously investigated crystals #AF063 and #AF063-2, so that sample-to-sample variations in the pristine form are expected to be sufficiently small.

Figure 5.26 shows the singular part of the relative length change along the $b$ axis $\Delta L_b/L_b$, taken at $T = 30\,\mathrm{K}$, for the irradiated crystal $\kappa$-Cl #AF063-3 (red solid line). For comparison, the critical relative length changes of the non-irradiated crystal #AF063, studied in great detail in Sec. 5.2, are shown. We observe a discontinuity at distinctly lower pressures for the irradiated sample. This jump of the length, which is also reduced in size, is slightly more broadened compared to that of the pristine sample. The broadening can be quantified by determining the variance of a Gaussian distribution function by a fit to the derivative of this data (see Sec. 5.2). We obtain a variance $w_{b,irr} \approx 2.6 \cdot 10^{-4}$ which is about a factor of 5 larger than the variance $w_b \approx 4.6 \cdot 10^{-5}$ determined for the non-irradiated crystal. This

[4]X-ray irradiation of the crystals was performed by Prof. Dr. Takahiko Sasaki, Sendai, Japan.

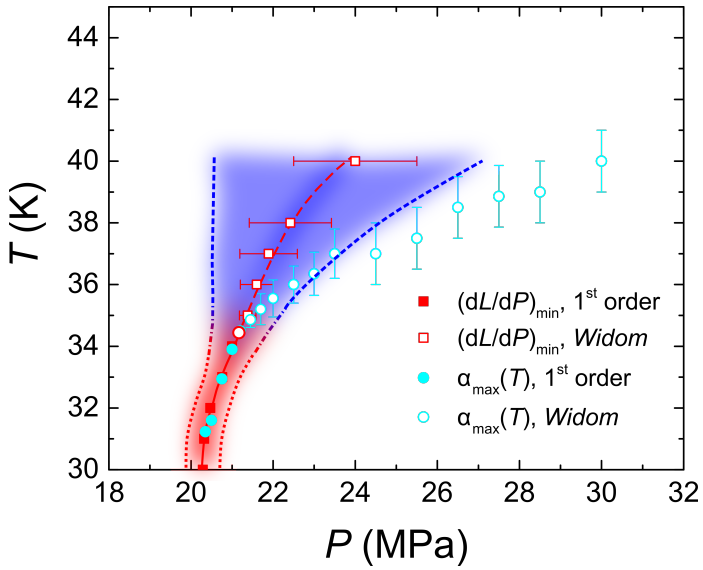


Figure 5.27.: Phase diagram for crystal κ-(BEDT-TTF)$_2$Cu[N(CN)$_2$]Cl #AF063-3, which was exposed to x-ray irradiation for 50 h. Red full (red open) symbols correspond to the first-order transition line (*Widom* line) determined from the inflection point of the relative length change $\Delta L_b/L_b$. Cyan full (open) symbols correspond to the position of maximum response, $\alpha_{max}$, of the thermal expansion coefficient, $\alpha(T) = L^{-1}\mathrm{d}L/\mathrm{d}T$, assigned to the first-order transition line (crossover line). Red and blue shaded areas indicate the experimentally determined width of the features in $\Delta L_b/L_b$ and can be attributed to the disorder-affected (red) and criticality-related (blue) regime, respectively.

difference in the variance corresponds to a ratio in size of the disorder-affected regimes of $\sqrt{5} \approx 2.2$ (see red shaded area in the phase diagram in Fig. 5.27).

Figure 5.27 shows the phase diagram determined from the full data set, consisting of pressure sweeps at various different temperatures and temperature sweeps at various different pressures (both not shown). These measurements revealed similar features as discussed above for the non-irradiated samples, so that the same criterions can be applied to determine the phase diagram and the critical endpoint. Remarkably, the Mott first-order transition line and the *Widom* line are shifted to lower pressures upon introducing disorder into the system. A similar shift to lower pressures upon irradiation was also observed in measurements of the relative length change on crystal #AF063-4, the results of which are not shown here, as well as in resistance measurements on a different sample [162]. Correspondingly, also its critical endpoint is shifted to lower pressures. The precise location of the critical endpoint can, e.g., be determined by the crossing point of the crossover line, determined from the maximum response, $\alpha_{max}$, of the thermal expansion coefficient [20], $\alpha(T) = L^{-1}\mathrm{d}L/\mathrm{d}T$, and the first-order transition line. We find a critical endpoint of $(P_c, T_c) \approx (21\,\mathrm{MPa},\ 34.5\,\mathrm{K})$, i.e., a shift of $P_c$ and $T_c$ to lower values. The shift to lower pressure upon increasing the disorder strength is consistent with results from DMFT cal-

culations on the Mott-Anderson Hamiltonian [163]. We thus interpret the position of the first-order transition line with respect to the pressure axis as a measure of the amount of disorder present in a system. It follows that the good agreement of the phase transition lines in Fig. 5.8 is an indication for the same high quality of crystal used in this work and in Ref. [18].

Nevertheless, the analysis of the critical behavior becomes more difficult upon increasing the disorder. To explore the criticality in more detail, a better understanding of critical electronic fluctuations in the presence of elastic degrees of freedom and disorder effects is clearly inevitable.

## 5.5. Summary

In this chapter, we presented a detailed study of the universal critical behavior around the second-order Mott critical endpoint, the knowledge of which is the key to an understanding of the phase transition itself. The Mott critical endpoint in purely electronic systems is believed to be governed by Ising criticality. By employing measurements of the relative length change on the organic charge-transfer salt $\kappa$-Cl, a breakdown of Hooke's law of elasticity was found which demonstrates the importance of considering lattice degrees of freedom in the analysis of the critical behavior. Due to the long-ranged shear forces of the crystal lattice, this breakdown of Hooke's law is accompanied by a crossover to mean-field criticality. Thus, even though the Mott transition is driven by strong electronic correlations, its critical endpoint for any pressure-tuneable system corresponds to that of an isostructural solid-solid endpoint with mean-field critical exponents. This fundamental result demonstrates the necessity to include lattice degrees of freedom into models that aim at an understanding of the various emergent features around the Mott transition.

# 6. Ferroelectricity in $\kappa$-(BEDT-TTF)$_2X$ organic charge-transfer salts

Ferroelectric materials, in which a spontaneously occurring electric polarization can be switched by an external electrical field, represent an exciting class of materials. Thereby, not only the mechanisms, which are responsible for the emergence of the ferroelectric state itself, are of high interest, but also the potential for technical applications motivates the research in this field. The quasi-1D organic charge-transfer salts are prime examples of the so-called electronic ferroelectrics (see e.g. [164]), in which the polarization is induced by an off-center displacement of the electronic charge carriers [73]. In recent years, also the quasi-2D organic charge-transfer salts were investigated for their dielectric properties. Dielectric spectroscopy itself presents one fundamental tool to investigate ferroelectricity [75]. The first discovery of multiferroicity, i.e., a spontaneous magnetic and electric order, in an organic charge-transfer salt [5], namely $\kappa$-Cl, caught special attention. However, the dielectric response of $\kappa$-Cl is controversially discussed in literature. In the following, a short review of the literature results on the dielectric properties of the $\kappa$-(ET)$_2X$ organic charge-transfer salts will be given. Afterwards, a study of the dielectric properties and the magnetic properties on the same single crystals of $\kappa$-Cl will be presented to investigate the coupling between spin and charge degrees of freedom in more detail. In addition, possible sample-to-sample variations will be identified.

## 6.1. Literature results on the dielectric properties of the $\kappa$-(ET)$_2X$ salts

The $\kappa$-(ET)$_2X$ organic charge-transfer salts obey a strongly dimerized structure with one hole carrier per dimer on average. They were consequently described as dimer-Mott insulators with an effective half-filled conduction band, as pointed out in detail in chapters 4 and 5. Nevertheless, a dielectric investigation on two Mott insulating $\kappa$-(ET)$_2X$ salts, namely $\kappa$-Cl [5] and $\kappa$-CuCN [76], revealed a dielectric response, i.e., a peak in the dielectric constant $\varepsilon'(T)$, at low temperatures (see Fig. 6.1). As the dielectric constant couples to the electric field, a dielectric anomaly is in general caused by a motion of charges [75]. In both of these experimental works on $\kappa$-Cl and $\kappa$-CuCN, the dielectric behavior was assigned to

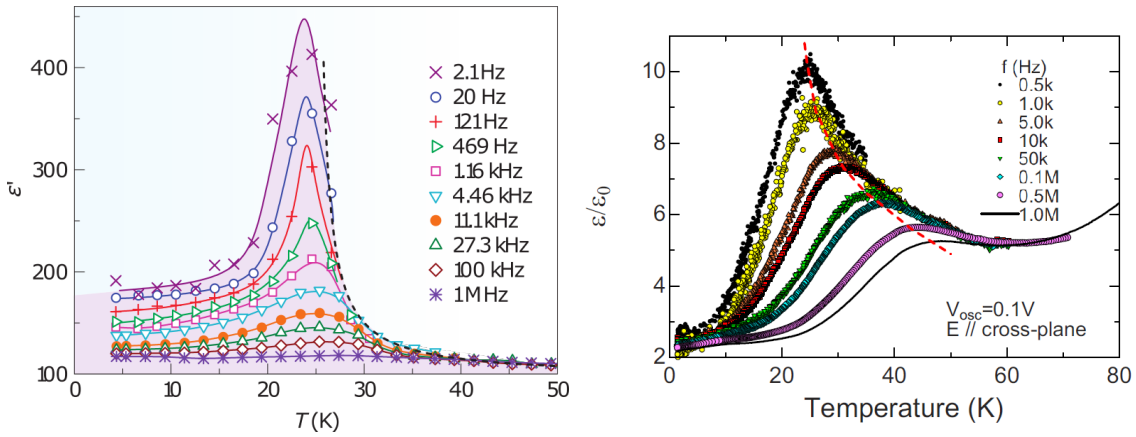


Figure 6.1.: Temperature dependence of the dielectric constant of the κ-phase organic charge-transfer salts κ-(BEDT-TTF)$_2$Cu[N(CN)$_2$]Cl (left) [5] and κ-(BEDT-TTF)$_2$Cu$_2$(CN)$_3$ (right) [76], taken at different frequencies ranging from low frequencies in the Hz-regime to high frequencies in the MHz-regime. The peak of the dielectric constant is frequency-independent for κ-(BEDT-TTF)$_2$Cu[N(CN)$_2$]Cl, characteristic for an order-disorder type ferroelectric. In contrast, the peak observed for κ-(BEDT-TTF)$_2$Cu$_2$(CN)$_3$ shows a distinct frequency dependence, indicative for a relaxor type of ferroelectric. Content reprinted from Ref. [5] with permission of the Nature Publishing Group and from Ref. [76] with permission of the American Physical Society.

intra-dimer charge degrees of freedom deep in the Mott insulating state. The importance of such intra-dimer charge degrees of freedom in these inherently quarter-filled systems was pointed out by theoretical works earlier (see e.g. [165]), in which an additional intersite Coulomb repulsion term $\tilde{V}$ is considered in the Hubbard Hamiltonian (see Sec. 2.4).

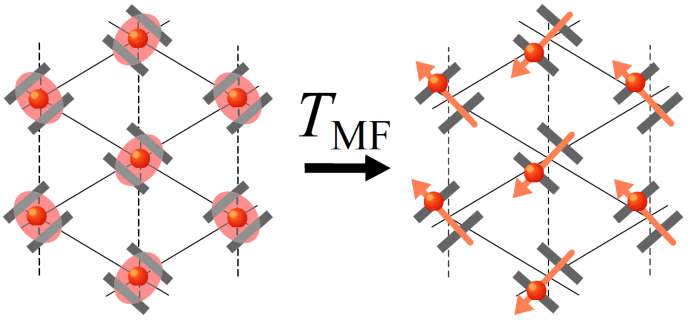


Figure 6.2.: Schematic picture of the charge order within the ET dimer upon cooling through the multiferroic transition temperature $T_{MF}$. The grey rectangles correspond to the ET molecules, which form dimers on a triangular lattice. Red circle corresponds to the hole charge carrier. Above $T_{MF}$ (left), the charge is delocalized on the dimer, as indicated by the red sphere. Below $T_{MF}$ (right), the charge locks into one of the ET molecules and creates thereby a dipole moment (orange arrow). Taken from Ref. [166], after Ref. [5].

Despite this common explanation for the occurrence of a dielectric anomaly, the dielectric response in these two materials is slightly different. Whereas in κ-Cl the peak position is almost independent of frequency (see Fig. 6.1, left), the peak position in κ-CuCN shows

a distinct frequency dependence (see Fig. 6.1, right). The latter behavior is characteristic for so-called relaxor type of ferroelectricity, in which short-range correlations cause cluster-like ferroelectric order [167]. In contrast, the frequency-independent peak in $\kappa$-Cl is the signature of an order-disorder type ferroelectricity with long-range order. In this type of ferroelectrics, dipoles are disordered at high temperatures and order below the transition temperature $T_{FE}$ with an overall net polarization $\vec{P}$. In general, in order to create an overall polarization a breaking of the underlying inversion symmetry is necessary. Indeed, a purely electronic mechanism, which breaks the inversion symmetry by a combination of bond- and site-centered charge order [73], similar to the quasi-1D charge-transfer salts, provides a plausible scenario for the occurrence of ferroelectricity in the $\kappa$-phase organic charge-transfer salts (see Fig. 6.2) [5]. The dipoles arise from the hole carriers which fluctuate within the dimer. At high temperatures the holes are delocalized, thereby only establishing bond-centered charge order. Once the charge locks into one of the ET molecules below $T_{FE}$, site-centered charge order is established as well, breaking the inversion symmetry and thus creating an overall net polarization. Such an electronic mechanism is in contrast to the off-center displacement of ions in conventional ferroelectrics [75]. Signatures of the additional localization of charge carriers were revealed in the temperature-dependent behavior of the resistance of $\kappa$-Cl in the same study. In addition, ferroelectricity was demonstrated by so-called PUND measurements, in which a current is observed upon reversal of the electric field, indicative of a macroscopic switching of polarization, and by field-dependent polarization measurements $P(E)$.

The surprising result of the study on $\kappa$-Cl [5] was not only that charge degrees of freedom are still active in the Mott insulating phase, but also that the ferroelectric order coincides with the magnetic order of this system at $T_{MF} \approx 27\,\mathrm{K}$ [133], making this material the first multiferroic organic charge-transfer salt. This implies a strong coupling between spin and charge degrees of freedom in this material. Further, experiments on the magnetic-field dependence of the dielectric properties suggested that here a new mechanism for multiferroicity is at work, namely a charge-order driven mechanism. It was speculated that the charge order within the dimer reduces the frustration of the triangular lattice and thereby allows magnetic order to form.

However, the ferroelectric nature of the ground state is discussed controversially in literature. The electronic mechanism proposed in Ref. [5] clearly requires a charge disproportionation $\delta$ within the dimer. Experimentally, a charge disproportionation $\delta$ can be determined by infrared spectroscopy [168]. Such experiments showed no charge disproportionation within their experimental resolution of $\delta < 0.005\,e$ in $\kappa$-Cl and $\kappa$-CuCN [138], which led the authors of Ref. [138] to the claim that no charge order is present in $\kappa$-$(\mathrm{ET})_2X$ salts. Instead, it was argued that the dielectric response in $\kappa$-Cl arises from a relaxation of charged domain walls in the magnetic state [139]. The relaxor type of ferroelectric response

in $\kappa$-CuCN (and similarly observed for the related compound $\kappa$-(ET)$_2$Ag$_2$(CN)$_3$ [169]) was attributed to domain formation due to a broken symmetry on a local scale in the cyanide groups in the anion layer [170].

## 6.2. Study of the multiferroic ground state in $\kappa$-(BEDT-TTF)$_2$Cu[N(CN)$_2$]Cl

In order to gain more insight into the coupling of spin and charge degrees of freedom at the multiferroic phase transition, we studied the dielectric response $\varepsilon'(T)$ and the magnetic susceptibility $\chi(T)$ on the same single crystals[1]. In one crystal, both of these measurements were complemented by measurements of the thermal expansion coefficient $\alpha(T)$ as a probe to detect lattice degrees of freedom at the proposed multiferroic transition.

Figure 6.3 shows the result of these measurements on two crystal $\kappa$-Cl#AF063 (left) and $\kappa$-Cl#mp1065 (right), which represent characteristic results of the in total 8 different crystals studied. These two crystals were grown by slightly different routines (see Ref. [171] for more details). The dielectric constant $\varepsilon'(T)$ (top panels), which was measured in an out-of-plane direction due to the lower conductance, exhibits for both crystals a pronounced peak at low temperatures, the height of which decreases upon increasing frequency. The dielectric constant at a frequency of 20 Hz reaches values up to 3000 (800) for #AF063 (#mp1065), which is slightly larger than the value obtained for $\kappa$-Cl in Ref. [5]. However, the frequency dependence of the peak position is distinctly different. In the case of crystal #AF063, the peak position is to a good approximation frequency-independent. This response is characteristic for an order-disorder-type ferroelectric order and was revealed for in total 5 out of 8 crystals. In contrast, crystal #mp1065 shows the characteristic frequency dependence of a relaxor ferroelectric. Similar behavior was revealed in two other crystals. Interestingly, it was found that the resistance (not shown) shows a much more pronounced anomaly at $T_{MF}$ in those crystals which reveal an order-disorder type ferroelectric response. Irrespective of the different frequency response, the magnetic susceptibility $\chi$ shows a very similar response (middle panel). Both crystals show an increase of the susceptibility, measured with field oriented along the *ac* plane, at $T \approx 25\,\mathrm{K}$. The increase of $\chi$ is consistent with the signatures, reported in literature [133], which were attributed to the transition into a canted antiferromagnetic state. The transition temperature $T_N$ into the antiferromagnetic state can be estimated from the peak position in the derivative of $\chi(T) \cdot T$ (right axis, middle panels). We find $T_N \approx 23\,\mathrm{K}$ for #AF063 and $T_N \approx 25\,\mathrm{K}$ for #mp1065, which

[1] The results shown here were published as "*Multiferroicity in the Mott insulating charge-transfer salt $\kappa$-(BEDT-TTF)$_2$Cu[N(CN)$_2$]Cl*, M. Lang *et al.*, IEEE Trans. Magn. **6**, 2700107 (2014) [171]". Measurements of the dielectric constant $\varepsilon'(T)$ were performed by Dr. Peter Lunkenheimer, University of Augsburg. Susceptibility measurements $\chi(T)$ by using a SQUID magnetometer were performed together with Nguyen Hieu Hoang (AG Lang) [172].

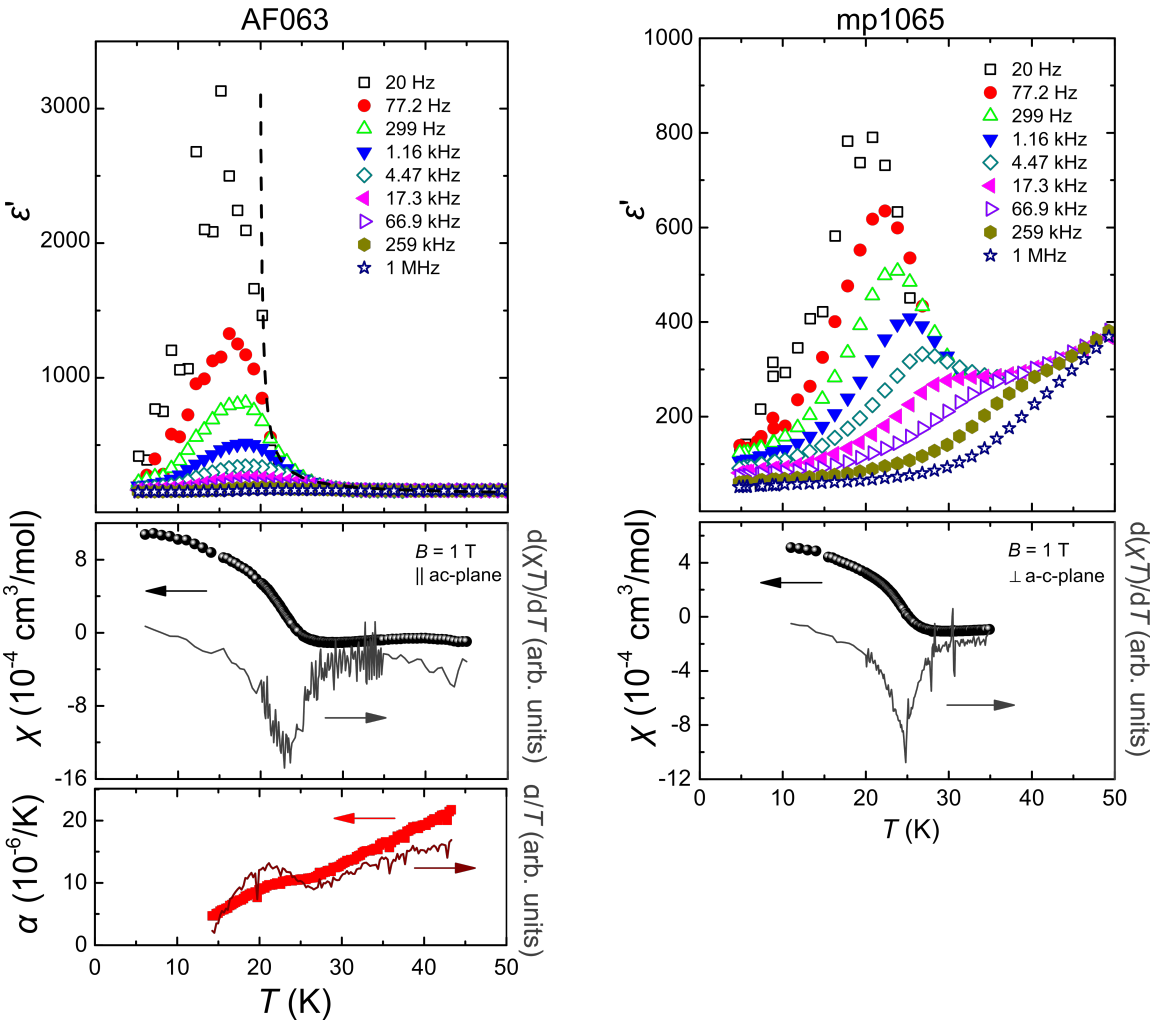


Figure 6.3.: The dielectric constant $\varepsilon'(T)$ at various frequencies (top panel), the magnetic susceptibility $\chi(T)$ (middle panel) and the thermal expansion coefficient $\alpha(T)$ (bottom panel) as a function of temperature of two κ-(BEDT-TTF)$_2$Cu[N(CN)$_2$]Cl crystals #AF063 (left) and #mp1065 (right). Top panel: Dashed line corresponds to a Curie-Weiss fit with $T_{CW} = 20\,\mathrm{K}$. Middle panel: Left axis shows the susceptibility $\chi(T)$ in a field of 1 T parallel to the $ac$ plane and right axis the derivative of $\chi \cdot T$ with respect to temperature. Bottom panel: Left axis shows the thermal expansion coefficient $\alpha$ along the in-plane $a$ axis, the right axis a plot of $\alpha(T)/T$ vs. $T$.

are slightly higher than the peak position of $\varepsilon'(T)$ at low frequencies. In order to investigate the coupling of spin and charge degrees of freedom, the transition temperature into the magnetic state has to be compared to the transition temperature into the ferroelectric state $T_{FE}$. By performing a Curie-Weiss fit to the experimental data (broken line in the top panel) in case of the order-disorder type ferroelectric order, a Curie-Weiss temperature of $T_{CW} = 20\,\mathrm{K} \approx T_{FE}$ can be inferred. The ferroelectric transition temperature is thus slightly smaller than the magnetic transition temperature, but nevertheless comparable in magnitude. The present study seems to indicate that the magnetic transition is the driving

phase transition, however, this is by far not conclusive, as the signatures in both $\varepsilon'(T)$ and $\chi(T)$ are rather broad. In addition, thermal expansion measurements on crystal #AF063 along the in-plane $a$ axis (lower panel) demonstrate that the lattice shows an anomalous behavior in the range $22\,\mathrm{K} \leq T \leq 27\,\mathrm{K}$, as already noted in Ref. [5] for the out-of-plane $b$ axis. This temperature range, which is highlighted in a representation of $\alpha/T$ vs. $T$ (right scale), includes $T_N$ ($\approx 23\,\mathrm{K}$), but not $T_{FE}$ ($\approx 20\,\mathrm{K}$).

## 6.3. Summary

This complementary study of the dielectric constant $\varepsilon'(T)$ and the magnetic susceptibility $\chi(T)$ revealed that all $\kappa$-Cl crystals show a dielectric anomaly at a temperature, which is very close to the magnetic-ordering temperature. The study also pointed out significant sample-to-sample variations in the frequency dependence of the dielectric response, which might explain the conflicting interpretations of experimental results in literature. However, in the majority of crystals the characteristics of a long-range ordered ferroelectric transition could be confirmed. Despite these discrepancies in the dielectric behavior, all crystals showed a similar transition into the canted antiferromagnetic state. Clearly, more efforts are needed to identify the detailed coupling mechanism for multiferroicity in this material, especially whether charge order with a small charge disproportionation can really trigger long-range magnetic order in such a frustrated system.

# 7. Thermodynamic properties of $\kappa$-(BEDT-TTF)$_2$Hg(SCN)$_2$Cl

In this chapter we will present a detailed thermodynamic and transport investigation of the organic charge-transfer salt $\kappa$-(BEDT-TTF)$_2$Hg(SCN)$_2$Cl. This material was first synthesized about 20 years ago [173]. However, the ground-state properties have not been investigated until now in great detail. In light of the controversial discussion of charge order within the ET dimer in the $\kappa$-(ET)$_2X$ phases, as presented in the previous chapter 6, this material plays a special role, as there is clear experimental evidence for a sizeable charge disproportionation within the dimer [34] below $T \approx 30\,\mathrm{K}$. It thus may serve as a reference system to study the role of intra-dimer charge degrees of freedom for the ferroelectric behavior of these salts[1]. To this end, we will discuss the low-temperature ground state properties of this material in detail by using thermodynamic as well as transport probes which aim at unraveling the interplay of charge, spin and lattice degrees of freedom. In addition, structural degrees of freedom of the ethylene end groups at higher temperatures will be discussed.

## 7.1. Literature results

The system $\kappa$-(ET)$_2$Hg(SCN)$_2$Cl, abbreviated as $\kappa$-HgCl hereafter, is a member of the series $\kappa$-(ET)$_n$Hg(SCN)$_{3-n}X$ with $X =$ Cl, Br ($n = 2$) and $X =$ Cl ($n = 1$) [173, 175] with monoclinic crystal structure. All of these compounds exhibit a metallic behavior at room temperature and undergo a metal-insulator transition at lower temperatures [173,175]. The compound of interest here, $\kappa$-HgCl, undergoes this transition at $T_{MI} \approx 30\,\mathrm{K}$ [174], accompanied by an increase of the resistance of about 6 orders of magnitude from $T_{MI}$ to low temperatures (see Fig. 7.1 (left)). In contrast, the Br-analogue with $X =$ Br and $n = 2$ undergoes this transition at much higher temperatures of $T_{MI} \approx 140\,\mathrm{K}$ [173].

The metallic and insulating state of $\kappa$-HgCl were studied intensively by optical spectroscopy [34]. The authors claimed that the high-temperature spectra in the metallic state are in accordance with the properties of a half-filled metallic compound in the presence of

[1] This work is a collaborative work between groups at the University of Frankfurt and the University of Augsburg. The individual contributions are indicated whenever the respective result will be presented.

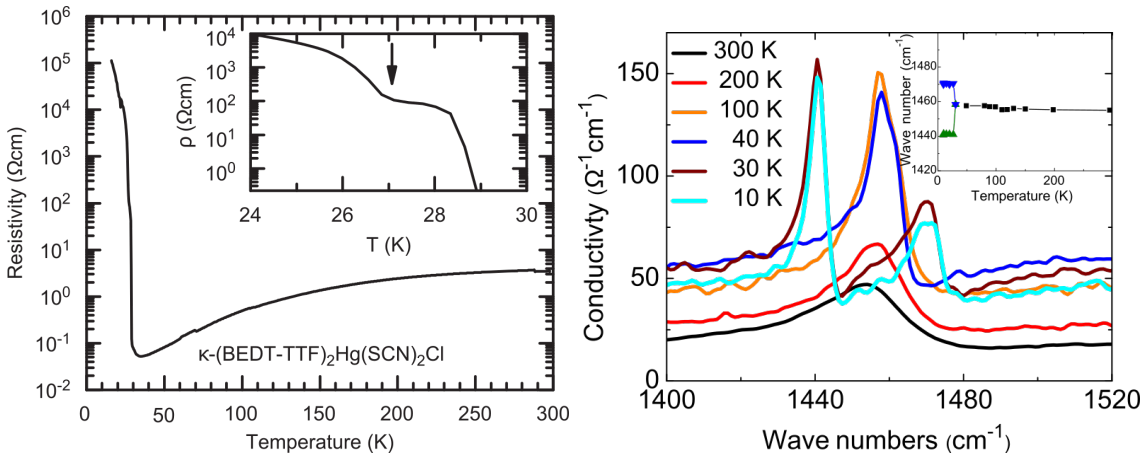


Figure 7.1.: Resistivity of κ-(BEDT-TTF)$_2$Hg(SCN)$_2$Cl indicating a metal-insulator transition at $T_{MI} \approx 30\,\mathrm{K}$ [174] (left) and optical conductivity spectra at different temperatures around $T_{MI}$ demonstrating the charge order at $T_{MI}$ [34] (right). Content reprinted from Ref. [174] with permission of Elsevier and from Ref. [34] with permission of the American Physical Society.

strong electron correlations close to a Mott transition, described by the Hubbard model with an on-site Coulomb repulsion $U$. However, the observed metal-insulator transition as a function of $T$ appeared to be not compatible with this picture. A study of the charge-sensitive C=C bond of the inner ring of the ET molecule by vibrational spectroscopy [34] (see Fig. 7.1 (right)) identified this transition as a charge-ordering transition. In the spectrum, at higher temperatures $T > 30\,\mathrm{K}$ one peak is present at around $1450\,\mathrm{cm}^{-1}$, which splits into two peaks at $T \approx 30\,\mathrm{K}$, clearly implying the presence of two inequivalent ET molecules with different charges. The charge disproportionation $\delta$ can be estimated to be $\delta = 0.2\,e$. The occurrence of charge order here presents a breakdown of the simple dimer picture with a Mott-insulating ground sate, which was commonly used for the description of the properties of the κ-(ET)$_2X$ family. It was proposed that the present material κ-HgCl is better described in terms of a so-called *paired electron crystal* (PEC) [176,177] which describes a possible charge-ordered ground state in strongly dimerized quarter-filled systems in the presence of strong frustration.

The properties of the present materials are obviously better described in terms of a quarter-filled model with on-site Coulomb interaction $U$ and intra-dimer interaction $\tilde{V}$, in contrast to the other κ-(ET)$_2X$ salts, which are located much closer to the situation of an effectively half-filled conduction band. DFT calculations can provide further insight, why a quarter-filled scenario appears more appropriate for κ-HgCl. To this end, DFT calculations were performed within an individual molecule basis[2] [178] at different temperatures

[2]DFT calculations were performed by Dr. H. Jeschke and Prof. Dr. R. Valentí, Institut für Theoretische Physik, University of Frankfurt.

$\kappa$-(ET)$_2$Hg(SCN)$_2$Cl

| $T$ (K) | $t_1$ (meV) | $t_2$ (meV) | $t_3$ (meV) | $t_4$ (meV) | $t'/t$ | $U/t$ |
|---|---|---|---|---|---|---|
| 10 | 116.7 | 62.1 | 86.9 | 40.9 | 0.836 | 4.5 |
| 50 | 113.9 | 63.4 | 88.3 | 39.1 | 0.861 | 4.4 |
| 100 | 119.1 | 64.7 | 88.6 | 40.5 | 0.842 | 4.5 |
| 300 | 125.3 | 60.0 | 79.8 | 40.4 | 0.796 | 5.0 |

$\kappa$-(ET)$_2$Cu[N(CN)$_2$]Br

| $T$ (K) | $t_1$ (meV) | $t_2$ (meV) | $t_3$ (meV) | $t_4$ (meV) | $t'/t$ | $U/t$ |
|---|---|---|---|---|---|---|
| 100 | 177.0 | 95.6 | 60.0 | 36.2 | 0.455 | 5.4 |

Table 7.1.: DFT calculations on the hopping parameters $t_1$ to $t_4$ between the ET molecules in $\kappa$-(BEDT-TTF)$_2$Hg(SCN)$_2$Cl at different temperatures [178] in comparison to the corresponding parameters in $\kappa$-(BEDT-TTF)$_2$Cu[N(CN)$_2$]Br [123]. The hopping parameters between the individual molecules $t_2$ to $t_4$ (depicted in Fig. 7.2) can be mapped onto the hopping parameters $t$ and $t'$ in the effective-dimer model via $t = (|t_2| + |t_4|)/2$ and $t' = |t_3|/2$. The frustration ratio $t'/t$ and correlation strength $U/t$ are determined in the effective-dimer model with $U \approx 2t_1$.

between 10 K and 300 K, at all of which structural data is available from literature [34]. The parameters of relevance here are in total four hopping parameters $t_1$ to $t_4$ (see Fig. 7.2 bottom left for a definition of the hopping terms). In the effective-dimer model, the intra-dimer hopping $t_1$ is assumed to be much larger than the other three hopping terms $t_2$ to $t_4$. The latter three can be mapped on the hopping parameters $t = (|t_2| + |t_4|)/2$ and $t' = |t_3|/2$ of the triangular lattice in the effective-dimer model [111].

Table 7.1 shows the four relevant hopping terms $t_1$ to $t_4$ determined for $\kappa$-HgCl in comparison to those parameters for $\kappa$-(ET)$_2$Cu[N(CN)$_2$]Br. The latter material is a metallic compound, representing those $\kappa$-(ET)$_2X$ materials with effectively half-filled conduction band. It is obvious that the intra-dimer hopping $t_1$ is distinctly smaller for $\kappa$-HgCl than for the other $\kappa$-phase materials. Rather, the intra-dimer hopping $t_1$ in $\kappa$-HgCl is comparable in size to the other hopping terms between different dimers $t_2$ to $t_4$, highlighting the relevance of intra-dimer charge degrees of freedom in the present material. This peculiarity is inherent to structural details of $\kappa$-HgCl (see Fig. 7.2). In contrast to the well-examined $\kappa$-salts with planar polymeric chain-like anions (right), as, e.g., (Cu[N(CN)$_2$]Cl)$^-$ or (Cu[N(CN)$_2$]Br)$^-$, $\kappa$-HgCl contains non-planar anions (left). The coupling of the anions via the ethylene end groups causes the ET molecules within a dimer to be slightly rearranged. In $\kappa$-HgCl the ET molecules do not show a perfect face-to-face alignment, but are slightly shifted with respect to each other along the $a$ axis. This, in turn, reduces the overlap of the $\pi$ orbitals of the adjacent ET molecules, giving rise to a weaker dimerization $\propto t_1$.

Comparing the hopping parameters to the ET molecules of neighboring dimers $t_2$-$t_4$ indicates that $\kappa$-HgCl shows a much more isotropic behavior between $t_2$ and $t_4$. Within the

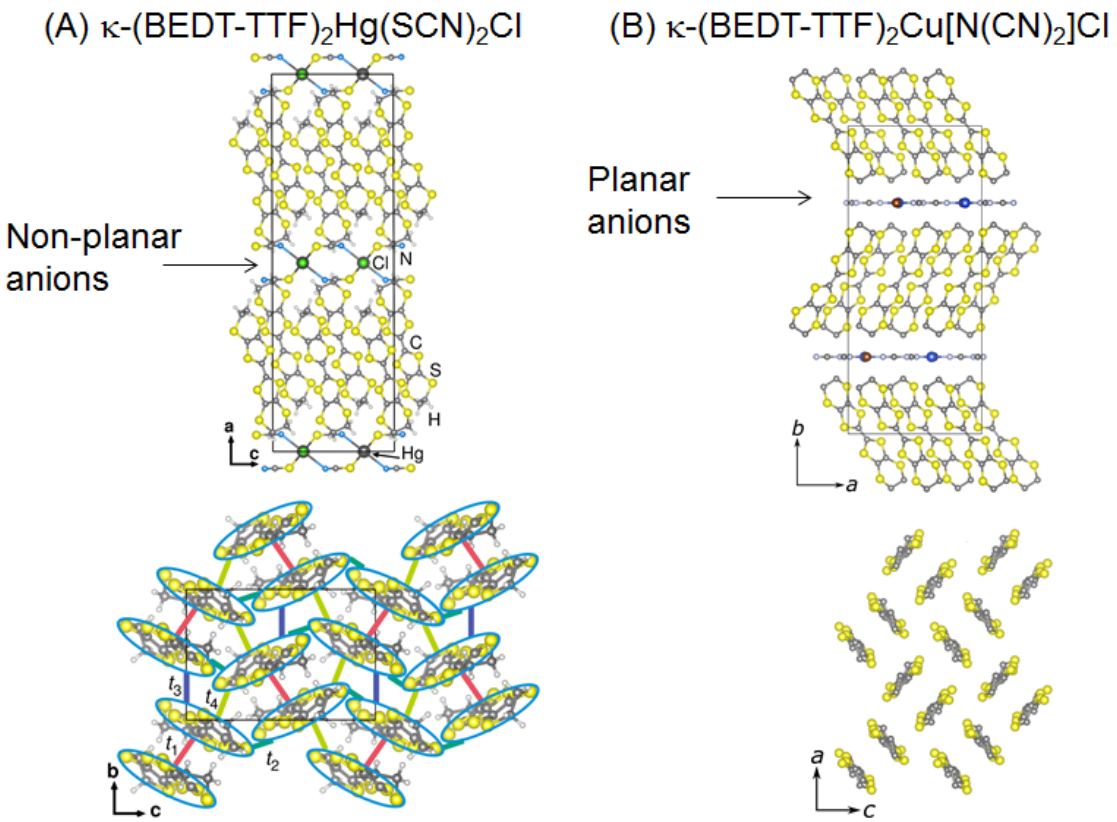


Figure 7.2.: Comparison between the structure of κ-(BEDT-TTF)$_2$Hg(SCN)$_2$Cl (A) [34] and κ-(BEDT-TTF)$_2$Cu[N(CN)$_2$]Cl (B) [112]. Top panel of the figure shows a view along the out-of-plane axis ($a$ axis for κ-(BEDT-TTF)$_2$Hg(SCN)$_2$Cl and $b$ axis for κ-(BEDT-TTF)$_2$Cu[N(CN)$_2$]Cl). The bottom panel shows a view on the ET plane. The cyan ellipses surround one ET molecule. The hopping parameters $t_1$ (pink), $t_2$ (dark green), $t_3$ (blue) and $t_4$ (light green) between the individual ET molecules are shown by solid lines.

effective-dimer model, the present material is rather highly frustrated with $t'/t \approx 0.86$ at 50 K, displaying a frustration value similar to that of the spin-liquid candidate compound κ-CuCN (see Tab. 4.2). In addition, the estimate of the correlation strength $U/t$ shows that this material is less strongly correlated than the other κ-phase materials. In summary, the calculations on the individual molecule basis support the notion that κ-HgCl is more appropriately described in terms of a quarter-filled conduction band with less strong dimerization.

In this respect, the present material may serve as a reference system to investigate the role of intra-dimer charge degrees of freedom for the physical properties of the κ-(ET)$_2X$ material class. Especially, the proposed charge order within the ET dimer allows to investigate whether such a state is sufficient to form an electronically-driven ferroelectric ground state in the quasi-2D κ-(ET)$_2X$ salts, the occurrence of which is controversially discussed in

| crystal | $R(P,T)$ | $\varepsilon'(T,\nu)$ | $C(T)$ | $\alpha(T)$ |
|---|---|---|---|---|
| #JAS1721 | x | x | | |
| #AF087-2 | x | | | |
| #AF087-2 | | | x | |
| #AF087-4 | | | | x |
| #AF093-1 | | x | | |

Table 7.2.: List of investigated $\kappa$-(BEDT-TTF)$_2$Hg(SCN)$_2$Cl samples. $R(P,T)$ stands for resistance measurements under pressure, $\varepsilon'(T,\nu)$ for measurements of the dielectric constant, $C(T)$ for specific heat measurements and $\alpha(T)$ for thermal expansion measurements.

literature (see chapter 6). Of similar importance for the theoretical modeling of the role of intra-dimer charge degrees of freedom is the behavior of this system under pressure, as revealed for other $\kappa$-(ET)$_2X$ systems.

Notwithstanding, most of the phase transitions in the organic charge-transfer salts involve not only a single degree of freedom, as, e.g., charge, but are rather a consequence of the mutual interaction of several degrees of freedom. By using thermodynamic probes, such as measurements of the thermal expansion and the specific heat, we will try to identify the role of other degrees of freedom, such as spin and lattice, at the charge-order metal-insulator transition. It will be of special interest to identify whether a distinct coupling of spin- and charge degrees of freedom is present in this material, as in $\kappa$-Cl this coupling was suggested to give rise to interesting multiferroic properties. Indeed, in literature indications for a magnetic ordering in $\kappa$-HgCl at the metal-insulator transition $T_{MI} \approx 30\,\mathrm{K}$ were reported from ESR-measurements [174]. However, until now, no other technique was able to provide a proof for the magnetic ordering in this material.

## 7.2. Properties of the metal-insulator transition

At first, we address the question of the role of the intra-dimer charge degrees of freedom on the phase diagram by measuring the resistance of two different crystals under $^4$He-gas pressure[3] (see Tab. 7.2 for an overview of all $\kappa$-HgCl samples investigated). Figure 7.3 shows the result of these measurements in the temperature range $2\,\mathrm{K} \leq T \leq 60\,\mathrm{K}$ at various constant pressures, ranging from ambient pressure up to high pressures of $P \approx 300\,\mathrm{MPa}$. At ambient pressure both crystals, depicted in Fig. 7.3 (A) and (B), show a metallic behavior at high temperatures down to $T \approx 30\,\mathrm{K}$ with absolute resistance values [179] similar to the ones reported in literature [174]. At $T \approx 30\,\mathrm{K}$ both crystals undergo a transition from the metallic to the insulating state. Crystal #JAS1721 (A) changes its resistance by only one to two orders of magnitude, whereas crystal #AF086-2 shows a resistance

[3] Measurements of the resistance under pressure were performed by David Zielke and Sebastian Köhler (AG Lang).

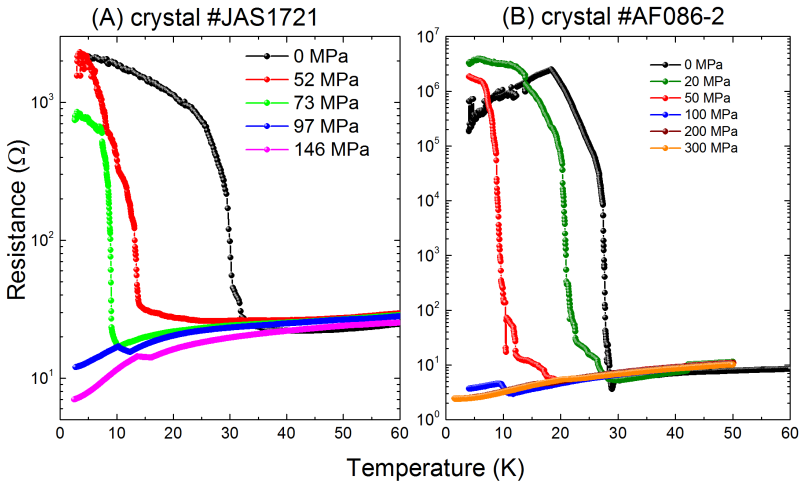


Figure 7.3.: Resistance $R$ as a function of temperature $T$ of $\kappa$-(BEDT-TTF)$_2$Hg(SCN)$_2$Cl under various external pressures $P$ ranging from ambient pressure up to about 300 MPa for two different crystals, #JAS1721 (A) and #AF086-2 (B). Pressure values are given at high temperatures. Note that the pressure medium helium solidifies at low temperatures accompanied by a pressure loss, which is responsible for the kink in the resistance curves at low temperatures at $P$ = 97 MPa and 146 MPa (A) and $P$ = 100 MPa, 200 MPa and 300 MPa (B).

change up to 4-5 orders of magnitude at the transition. Notably, at lower temperatures the temperature dependence of the insulating state is rather weak. Upon pressurizing, the transition temperature decreases rapidly with an initial rate of $\mathrm{d}T_{MI}/\mathrm{d}P \approx -(0.33 \pm 0.03)\,\mathrm{K/MPa}$, as clearly demonstrated by the data sets taken at $P = 52$ and 73 MPa (Fig. 7.3 A) and $P$ = 20 and 50 MPa (Fig. 7.3 B). We stress that the pressure dependence, determined here, is similar for both crystals. At higher pressures, above which the metal-insulator transition is completely suppressed, only metallic behavior can be detected down to lowest temperatures $T \geq 2\,\mathrm{K}$. Note that the small kinks observed in the measurements at $P = 97$ and 146 MPa (Fig. 7.3 A) and at $P = 100$ MPa (Fig. 7.3 B) result from the solidification of the pressure medium $^4$He at low temperatures, which is accompanied by a pressure loss. Surprisingly, there are no indications for superconductivity in this material under pressure, in contrast to other $\kappa$-(ET)$_2X$ salts, which turn superconducting as soon as the Mott type metal-insulator transition is suppressed (see Fig. 4.6). We can only speculate about the reasons of the absence of superconductivity in this particular material. Possible explanations include the rather weak correlation in this system, as demonstrated by DFT calculations, or that intra-dimer charge degrees of freedom drastically alter the conditions for superconductivity to form. Nevertheless, more efforts are needed in future to explain the absence of superconductivity in this material.

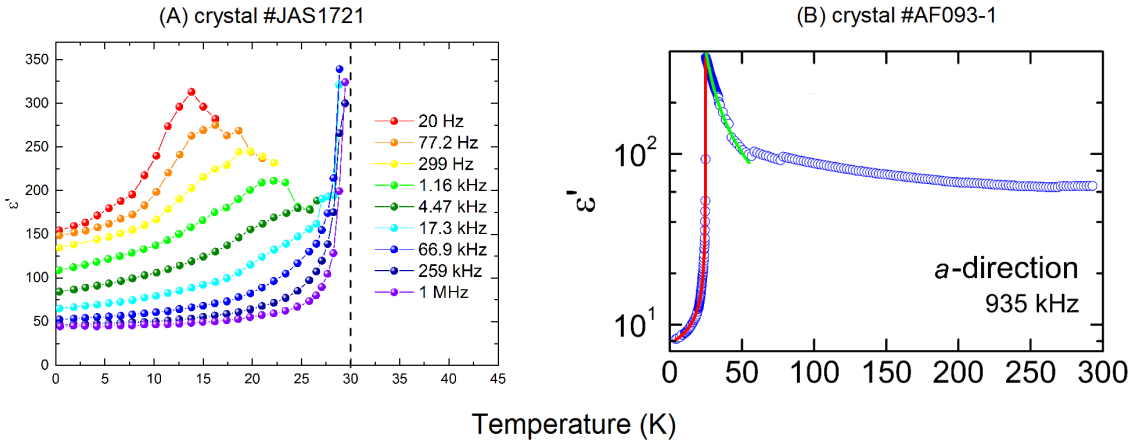


Figure 7.4.: Measurements of the dielectric constant $\varepsilon'$ as a function of temperature $T$ at various constant frequencies on two different single crystals of $\kappa$-(BEDT-TTF)$_2$Hg(SCN)$_2$Cl, #JAS1721 (A) and #AF093-1 (B).

We will now investigate the dielectric properties of these crystals in more detail in order to look for a possible electronically-driven ferroelectric ordering[4]. Figure 7.4 shows the dielectric constant $\varepsilon'(T)$ for two different crystals of $\kappa$-HgCl, one of which was already characterized by $R(P,T)$ measurements, in the temperature range $2\,\mathrm{K} \leq T \leq 45\mathrm{K}$ (A) and $2\,\mathrm{K} \leq T \leq 300\mathrm{K}$ (B). Both crystals show a dielectric response around 30 K, coinciding with the charge-order metal-insulator transition, with a maximum of $\varepsilon' \approx 300$ at low frequencies. This observation speaks clearly in favor of the presence of a polarization as a result of charge order which breaks inversion symmetry. Interestingly, the dielectric constant revealed for this material is rather similar in size as for $\kappa$-Cl, which demonstrably exhibits a smaller charge disproportionation within the dimer, if present [138,171]. The reason for the similar values of $\varepsilon'$ might be related to the different tilting angles of the ET molecules with respect to the out-of-plane axis. Measurements of the dielectric constant in the organic charge-transfer salts are often performed along an out-of-plane direction, which ensures low-enough conductivity and thus low charge-transport contributions. The dominant polarization occurs within the plane, but nevertheless a small out-of-plane component should be present due to the tilting of the ET molecules with respect to the out-of-plane axis. The tilting angle (see Fig. 7.2) is much smaller for $\kappa$-HgCl than for $\kappa$-Cl, which might in turn cause a similar out-of-plane polarization despite the distinctly different charge disproportionation $\delta$ and dipole sizes for both systems. A closer look on the dielectric properties reveals that the peak position of the dielectric constant of crystal #JAS1721 (A) shows a frequency dependence, characteristic for a relaxor-type ferroelectric state. This crystal showed only a rather small change of the resistance at $T_{MI}$, which might indicate that this particular

[4] Dielectric measurements presented in this subsection were performed by Jonas Fischer and PD Dr. Peter Lunkenheimer, University of Augsburg.

sample is of somewhat lower quality as the crystals from batches #AF087 and #AF093, and thus long-range ferroelectric order is prevented to form. Similar correlations between the anomaly in the resistance and the dielectric response were also observed for $\kappa$-Cl (see chapter 6). In contrast, crystal #AF093-1 shows a clear ferroelectric-like anomaly which is reminiscent of textbook examples of ferroelectric order, as, e.g., observed in $BaTiO_3$ [180]. These results support the notion that ferroelectricity can arise in the $\kappa$-$(ET)_2X$ salts as a result of bond- and site-centered charge order. Nevertheless, for a clear proof of long-range ferroelectric ordering, frequency-dependent measurements of the dielectric constant on crystal #AF093-1, as well as PUND measurements (see chapter 6) are inevitable.

After the discussion of the results from transport quantities, namely resistance and dielectric properties, which mainly couple to charge degrees of freedom, we now turn to the thermodynamic properties, i.e., the thermal expansion $\Delta L/L$ and specific heat[5] $C(T)$. Measurements of the relative length change provide a sensitive tool to investigate the role of lattice degrees of freedom at a phase transition. Evidence for a decisive role of lattice degrees of freedom at the charge-order transition were provided for the quasi-1D organic charge-transfer salts [181]. This idea was supported by theoretical investigations [182–184]. The quasi-2D salt $\kappa$-Cl also shows lattice effects at the proposed multiferroic, i.e., coupled magnetic and ferroelectric, transition (see chapter 6).

Figure 7.5 shows the relative length change $\Delta L_i/L_i = \frac{L_i(T)-L_i(T_0)}{L_i(300\,\mathrm{K})}$ ($T_0$ is a reference temperature) of one single crystal of $\kappa$-HgCl along the two in-plane axes $i = b, c$ and the out-of-plane $i = a$ axis in the temperature range $20\,\mathrm{K} \leq T \leq 40\,\mathrm{K}$, i.e., around $T_{MI} \approx 30\,\mathrm{K}$. We observe pronounced, slightly broadened jumps of the length along all crystallographic axes around $T_{MI} \approx 30\,\mathrm{K}$. The two in-plane axes $b$ and $c$ show a decrease of the length on going from the low-temperature insulating, charge-ordered state to the high-temperature metallic state. This observation of the in-plane expansivities is consistent with the notion that the delocalized electrons contribute to the cohesion of the solid, thus reducing the lengths in the metallic state within the ET layer. It is remarkable that the out-of-plane $a$ axis demonstrates sizeable lattice effects of the same order of magnitude as the two in-plane axes, however with a different sign. The observed lattice effect corresponds to an expansion of the crystal in the $a$ direction upon entering the metallic phase. This result might indicate that the coupling of the ET molecules to the anion layers is relevant in forming the charge-ordered state. The displacement of charges within the ET layer can in principle induce a shift of the negatively-charged anion layer in order to reduce the electrostatic Coulomb energy. A similar contraction along the out-of-plane axis upon entering the charge-ordered state was already observed in the quasi-1D organic charge-transfer salts [181]. In general, lattice effects are expected at a ferroelectric transition reflecting the break of inversion symmetry. Thus, the strong and anisotropic length changes observed here are fully consistent with the

[5] Measurements of the specific heat were performed by David Zielke (AG Lang).

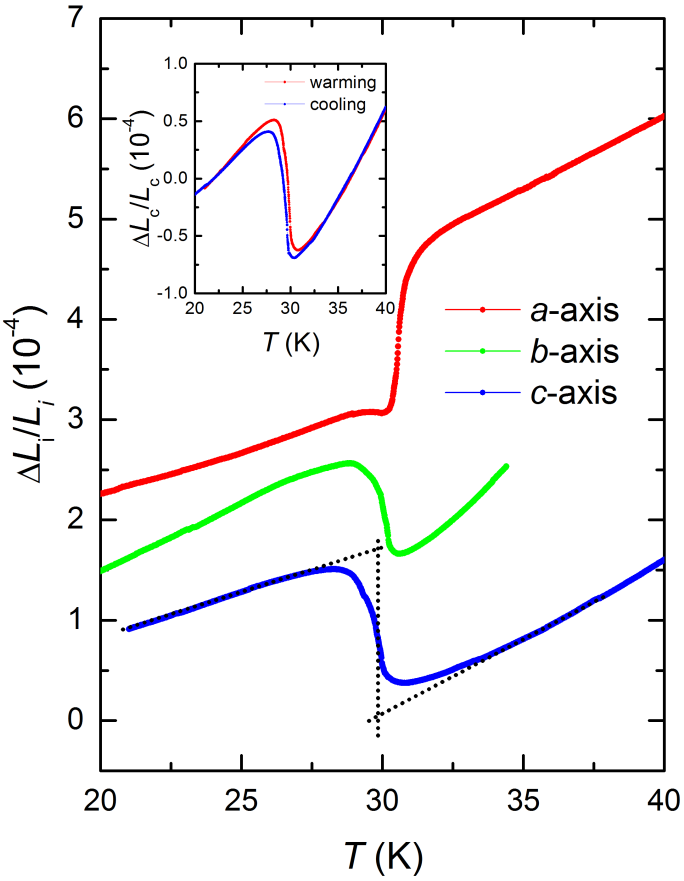


Figure 7.5.: Relative length change $\Delta L_i/L_i$ along all crystallographic directions $i = a, b, c$ as a function of temperature $T$ across the metal-insulator transition in $\kappa$-(BEDT-TTF)$_2$Hg(SCN)$_2$Cl, taken upon warming. The data sets are offset for clarity. Dotted lines indicate the construction for the determination of the jump size in the relative length at the metal-insulator transition. Inset: Relative length change along the $c$ axis, $\Delta L_c/L_c$, upon warming (red) and cooling (blue).

scenario of bond- and site-centered charge order as the origin for ferroelectricity in these materials.

In order to analyze the phase transition in more detail, we first determine the transition temperature $T_{MI}$, which we assign to the inflection point of $\Delta L_i(T)/L_i$. We find three slightly different values for the data along the different crystallographic axes, as already apparent from the bare data in Fig. 7.5, namely $T_{MI,a} = (30.5 \pm 0.1)\,\mathrm{K}$, $T_{MI,b} = (30.0 \pm 0.1)\,\mathrm{K}$ and $T_{MI,c} = (29.8 \pm 0.1)\,\mathrm{K}$. We assign this slight discrepancy to the influence of the small uniaxial force exerted by the dilatometer (see Appendix A.3) due to the high pressure sensitivity of this particular transition, as discussed above. The uniaxial pressures determined for this measurements on a crystal of dimensions $0.25 \times 1.1 \times 0.9\,\mathrm{mm}^3$ amount to $P_a \approx 0.6\,\mathrm{MPa}$ and $P_c \approx P_b \approx 2\,\mathrm{MPa}$. The uniaxial pressure dependencies are positive for the out-of-plane $a$ axis and negative for the in-plane $b$ and $c$ axis, as suggested by the

relative length changes across the transition. Thus, the transition temperature, determined from a measurement along the $a$ axis, $T_{MI,a}$ is slightly higher than $T_{MI,b}$ and $T_{MI,c}$.

The precise determination of the transition temperatures helps to clarify the nature of the phase transition: The jump-like signatures in $\Delta L_i(T)/L_i$ are accompanied by a distinct hysteresis between warming and cooling of $\Delta T_{MI} = (0.3 \pm 0.1)\,\mathrm{K}$, as exemplarily shown in the inset of Fig. 7.5 for measurements along the $c$ axis. These two observations are strong indications that this transition is a first-order transition, in contrast to previous reports [174] that could not resolve any hysteresis. For a precise determination of the volume change at the first-order transition, we have to overcome the obstacle that the signatures at the transition are slightly broadened due to a small amount of disorder, present in any real system. To this end, we replace the broadened jumps by infinitely sharp jumps by extrapolating the normal background from both sides of the transition up to $T_{MI,i}$ with $i = a, b, c$. We assume that the background expansion can be approximated by straight lines close to the transition. This procedure is exemplarily indicated for the measurement of the $c$ axis in Fig. 7.5. The resulting relative length changes across the metal-insulator transition amount to $(\Delta L_a/L_a)_{T_{MI}} = (1.45 \pm 0.05) \cdot 10^{-4}$, $(\Delta L_b/L_b)_{T_{MI}} = -(1.60 \pm 0.05) \cdot 10^{-4}$ and $(\Delta L_c/L_c)_{T_{MI}} = -(1.65 \pm 0.05) \cdot 10^{-4}$. All these values correspond to data taken upon warming, i.e., $(\Delta L_i/L_i)_{T_{MI}} = \lim_{T \to T_{MI}} [(\Delta L_i/L_i)_{T > T_{MI}} - (\Delta L_i/L_i)_{T < T_{MI}}]$. To determine the volume change, we assume a 90° angle between all crystallographic axes and neglect a small correction arising from the monoclinic $\beta = 91°$ angle (at 10 K [34]). With this in mind, the volume change is given by $\Delta V/V \simeq (\Delta L_a/L_a) + (\Delta L_b/L_b) + (\Delta L_c/L_c) = -(1.80 \pm 0.15) \cdot 10^{-4}$. The overall volume change is negative while going from the insulating to the metallic side and supports the notion, as mentioned above, that delocalized electrons contribute to the cohesion of the solid. This volume change $\Delta V/V$ with a molar volume of $V_{mol} = 5.36 \cdot 10^{-4}\mathrm{m}^3/\mathrm{mol}$ can be related to the entropy change $\Delta S$ by the use of the Clausius-Clapeyron equation 2.16, valid for first-order transitions, with the help of the pressure dependence of the transition temperature. The latter quantity was determined previously from resistance measurements under pressure. We thus estimate the entropy change to be $\Delta S = (290 \pm 30)\,\mathrm{mJ\,mol^{-1}\,K^{-1}}$.

Before interpreting the entropy change associated with the metal-insulator transition, we provide a more direct approach to this property via specific heat measurements using a high-resolution home-built *ac* calorimeter [105]. Figure 7.6 (A) shows the data of the specific heat $C(T)$ on a single crystal of $\kappa$-HgCl with mass of $m = (76 \pm 19)\,\mu\mathrm{g}$ in the temperature range $1.8\,\mathrm{K} \leq T \leq 35\,\mathrm{K}$. The data reveal an increase of the specific heat as a function of temperature with a small hump around $T \approx 28.5\,\mathrm{K}$, which is shown on an enlarged scale in Fig. 7.6 (B). The hump can be clearly assigned to the occurrence of the phase transition. In case of a first-order transition, a divergent or discontinuous specific heat at the phase transition is expected. However, disorder effects as well as the finite oscillation amplitude

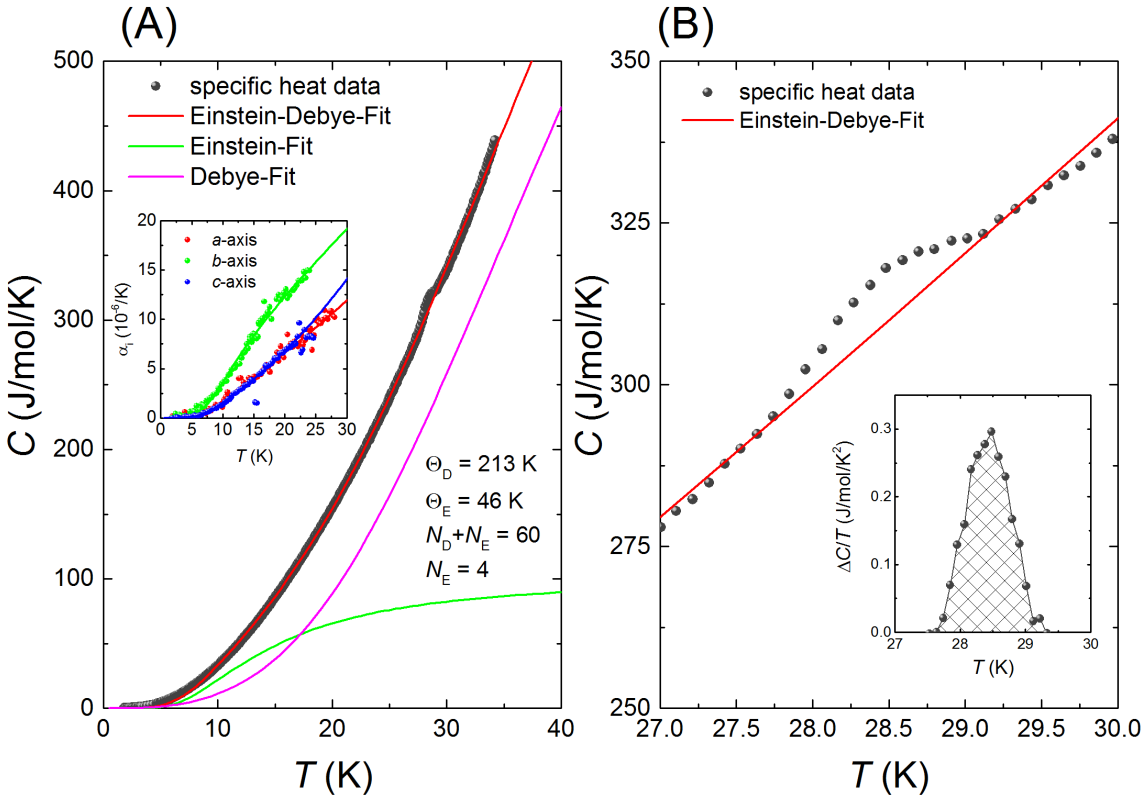


Figure 7.6.: (A) Experimentally determined specific heat $C$ of a single crystal of $\kappa$-(BEDT-TTF)$_2$Hg(SCN)$_2$Cl as a function of temperature $T$ in the temperature range $1.8\,\mathrm{K} \leq T \leq 35\,\mathrm{K}$ (grey symbols). Red line corresponds to a fit of the phononic background contribution $C_{Ph}$, which is described by a sum of an Einstein (green line) and a Debye contribution (pink line). Inset: Experimentally determined thermal expansion coefficient $\alpha_i = L_i^{-1}\mathrm{d}L_i/\mathrm{d}T$ for $i = a, b, c$ (symbols) and the modeling of the background expansion (solid lines) by a combined Einstein and Debye fit (for details, see text). (B) Detailed view on the experimental data (grey symbols) near the phase transition region around 28.5 K, together with the background fit $C_{Ph}$ (red solid line). Inset: Plot of $\Delta C/T = (C_{measured} - C_{Ph})/T$ vs. $T$, with $\Delta C$ being the specific heat associated with the phase transition. Shaded area corresponds to the entropy change at the phase transition.

of the *ac* calorimetry may contribute to a broadening of the signatures in the present case. The data are clearly dominated by a large background contribution. In order to assess the specific heat associated with the phase transition, the background contributions have to be subtracted. As the material is insulating for $T < 30\,\mathrm{K}$, electronic contributions to the specific heat can be neglected in this temperature regime. The background is most likely dominated by phononic contributions arising from the large number of oscillators per unit cell in these organic charge-transfer salts. The phononic specific heat $C_{Ph}$ can be modeled by Debye oscillators of number $N_D$ with Debye temperature $\Theta_D$ and Einstein oscillators of number $N_E$ with Einstein temperature $\Theta_E$ with a fixed number of oscillators $N_D$+$N_E$ =60, i.e., the number of molecules per formula unit,

$$C_{Ph}(T) = 9N_D R\left(\frac{T}{\Theta_D}\right)^3 \int_0^{\Theta_D/T} x^4 \frac{e^x}{(e^x-1)^2}\,\mathrm{d}x + 3N_E R\left(\frac{\Theta_E}{T}\right)^2 \frac{e^{\Theta_E/T}}{(e^{\Theta_E/T}-1)^2}. \quad (7.1)$$

Whereas the former ones account well for the contribution of acoustic phonons with an, in first approximation, linear dispersion close to the Brillouin zone center, the latter ones describe optical phonons with only a small dispersion [37]. The relevance of optical phonons for modeling the background specific heat can be inferred from plotting $C/T^3$ vs. $T$. In this representation, Debye contributions, which follow $C \propto T^3$ at low temperatures, are constant, whereas Einstein contributions show a pronounced maximum. For the present data, such a maximum appears in this representation at $T \approx 6.6\,\mathrm{K}$, which can thus be related to the presence of low-lying optical phonons. Similar contributions to the specific heat at low temperatures were also identified for other organic charge-transfer salts, such as κ-(ET)$_2$I$_3$ [185]. These low-lying optical phonon modes of wavenumber $\approx 32\,\mathrm{cm}^{-1}$ were often assigned to librational modes [185], associated with the anion molecules [186, 187].

By employing an Einstein-Debye-Fit (red line in Fig. 7.6), as represented by eq. 7.1 with a fixed number of oscillators, we find a very good agreement to the experimental data for $T < 27.5\,\mathrm{K}$, yielding a Debye temperature $\Theta_D = (210 \pm 20)\,\mathrm{K}$, an Einstein temperature of $\Theta_E = (46 \pm 5)\,\mathrm{K}$ and a number of Einstein oscillators of $N_E = 4$ per formula unit. The error bars given here mainly arise due to the uncertainty in the sample mass. The Debye temperature (see pink line for the Debye contribution to $C_{Ph}$) extracted from the present fit is in good agreement with values revealed for other organic charge-transfer salts ranging typically from 180 K to 220 K (see, e.g., [185, 188–190]), which reflect the softness of the crystal lattice. In addition, the Einstein temperature (see green line for the Einstein contribution to $C_{Ph}$) determined here of $\Theta_E \approx 46\,\mathrm{K}$ is similar to the value reported for κ-(ET)$_2$I$_3$ [185], the specific heat of which was modeled with $N_E = 2$ oscillators. Both of these parameters thus represent reasonable values and confirm the reliability of the fit. In general, the thermal expansion coefficient $\alpha_i = L_i^{-1}\mathrm{d}L_i/\mathrm{d}T$ with $i = a, b, c$, corresponding to the derivative of the data shown in Fig. 7.5, can also be described by a sum of Einstein and Debye contributions. In this case, the individual contributions to the thermal expansions $\alpha_{Einstein} = \Gamma_{Einstein} C_{Einstein}$ and $\alpha_{Debye} = \Gamma_{Debye} C_{Debye}$ are connected to the respective specific heat contribution via the Grüneisen parameters $\Gamma_{Einstein}$ and $\Gamma_{Debye}$. We note that the thermal expansion data along all three crystallographic axes can also be nicely modeled with an Einstein-Debye-model with the same Einstein and Debye temperatures $\Theta_E$ and $\Theta_D$ for $T < 25\,\mathrm{K}$ (see Fig. 7.6 (A), inset). In the fitting procedure, only the two Grüneisen parameters were used as free parameters.

After the determination of the background contribution, we can investigate the contribution of the phase transition to the specific heat by subtracting the background from the mea-

sured experimental data (see Fig. 7.6 (B), inset). The integration of $\Delta C/T = (C - C_{Ph})/T$ in the temperature range between 27.5 and 29.5 K (shaded area in the inset of Fig. 7.6 (B)) yields an entropy change of $\Delta S = (250 \pm 50)\,\mathrm{mJ\,mol^{-1}\,K^{-1}}$ associated with the phase transition[6]. This value of $\Delta S$ is, within the error bars, consistent with $\Delta S$ determined from the volume change by means of the Clausius-Clapeyron equation, discussed above. Given the fact that this transition is a metal-insulator transition, we would expect an entropy change associated with the charge degrees of freedom of $\Delta S = \gamma T_{MI}$ with $\gamma$ being the electronic Sommerfeld coefficient. Given that this entropy change is solely due to the delocalization of the charge carriers, our result of $\Delta S$ would indicate a Sommerfeld coefficient of $\gamma \approx 10\mathrm{mJ\,mol^{-1}\,K^{-2}}$. This value is at the lower bound of $\gamma$ values reported in literature for various organic charge-transfer salts ranging from $\gamma = 10\,\mathrm{mJ\,mol^{-1}\,K^{-2}}$ to $30\,\mathrm{mJ\,mol^{-1}\,K^{-2}}$ [185, 188–191]. This observation is in accordance with the distinctly weaker electronic correlations in $\kappa$-HgCl, as predicted by DFT, resulting in a smaller effective mass. Thus, the present result of the entropy change at the phase transition can be explained by invoking only charge degrees of freedom. However, whether the spins still contribute to the entropy at this temperature cannot be resolved from the present data. In fact, in case of a magnetic ordering, especially in strongly anisotropic systems, the change in spin entropy from a paramagnetic metal to ordered local moments in the insulating state can be very small. The question of magnetic ordering is particularly interesting for a deeper understanding of the coupling of intra-dimer charge degrees of freedom and spin in other $\kappa$-phase materials, especially for the proposed multiferroic transition in $\kappa$-Cl [5] and the mysterious 6 K anomaly in $\kappa$-CuCN, to which both spin and charge degrees of freedom contribute [135]. The issue of a possible magnetic ordering in the present material $\kappa$-HgCl attracts further attention due to the high frustration ratio $t'/t$ close to 1, as predicted by DFT calculations. Nevertheless, to unambiguously clarify the role of the spin degrees of freedom in this material, magnetization measurements would be helpful. However, all attempts to resolve magnetic signatures by SQUID magnetometry have been unsuccessful so far due to limitations in the available sample mass.

## 7.3. Glass-like freezing of the ethylene end groups

After the discussion of the low-temperature properties around the metal-insulator transition, we focus now on structural degrees of freedom at higher temperatures arising from the two possible ethylene end group conformations. The structural data, reported in literature [34], indicated that both ethylene end groups, i.e., the outer ethylene end groups, which make close contacts to the anion layers, and the inner ethylene end groups (see Fig. 7.2),

[6] Note that the specific heat values in the present work are normalized to one mole formula unit, i.e., normalized to one dimer carrying one spin 1/2 on average.

are disordered at room temperature. Thereby, the relative occupancies for the two different conformations are 55:45 for the inner ethylene end groups and 78:22 for the outer ones. Upon cooling down to 100 K, the authors claimed that the outer ethylene end group motion is frozen with 84% of the inner ethylene end groups being in the staggered conformation. However, it is still unknown whether in this material the different end groups freeze in a glassy manner or not. In general, not all of the $\kappa$-(ET)$_2X$ salts show a glass transition. Moreover, in some cases, even two consecutive glass transitions were observed [119]. Recently, by studying various examples of $\kappa$-(ET)$_2X$ by *ab initio* calculations [50], a possible origin of the glassy freezing was identified, based on the coupling of the ET molecules to the polymeric chain-like anion layer, the collective motion of which freezes out at the glass transition. In the following, we will use thermal expansion measurements, which provide a very sensitive probe to structural modifications, to identify a possible glassy freezing in the present material $\kappa$-HgCl. We will compare the results with *ab initio* calculations[7] to crosscheck the proposed model in Ref. [50] in this particular case with a non-planar anion layer.

Figure 7.7 (A) shows the relative length change $\Delta L_i(T)/L_i$ of $\kappa$-HgCl along all three crystallographic directions as a function of temperature in the range 5 K$\leq T \leq$200 K. The data sets were normalized to $T_0 = 200$ K, i.e., $\Delta L_i(T)/L_i = (L_i(T) - L_i(200\,\mathrm{K}))/L_i(300\,\mathrm{K})$. Upon cooling from 200 K, we observe a strongly anisotropic response along the different crystallographic directions. The out-of-plane $a$ axis and the in-plane $b$ axis show a monotonous decrease with decreasing temperature. In contrast, the $c$ axis length shows a remarkable and unusual behavior: The length first shrinks upon cooling until $T \approx 140$ K and then expands upon further cooling. At around 63 K the $a$ and $b$ axis expansion show a kink, whereas the $c$ axis expansion changes its sign again, implying a contraction upon cooling below $\approx$63 K. The step-like feature at about 30 K is related to the metal-insulator transition, as discussed above in detail. Similar anomalies in $\Delta L_i/L_i$, as in this case observed at around 63 K, and the so-called NTE (*negative thermal expansion*) effect above that temperature along the $c$ axis were observed in other organic charge-transfer salts [119, 132]. They were interpreted in literature in terms of the glass-like freezing of the ethylene end groups motions, which are coupled to anion degrees of freedom, as we will discuss below in more detail.

In order to illustrate the detailed behavior around $T_g$, we consider the derivative of the relative length change data with respect to temperature, the thermal expansion coefficient $\alpha_i(T)$ with $i = a, b, c$ (see Fig. 7.7 (B)). The data reveal step-like anomalies with characteristic over- and undershoots at the low- and high-temperature flank of the anomaly for all directions upon warming at around $T_g \approx$63 K. The directional anisotropy is similar to the one observed at the glass transition in $\kappa$-(ET)$_2$Cu[N(CN)$_2$]Br [119]. In addition, a

[7] *Ab initio* calculations on the ethylene end group confirmations were performed by Dr. Stephen M. Winter, University of Frankfurt.

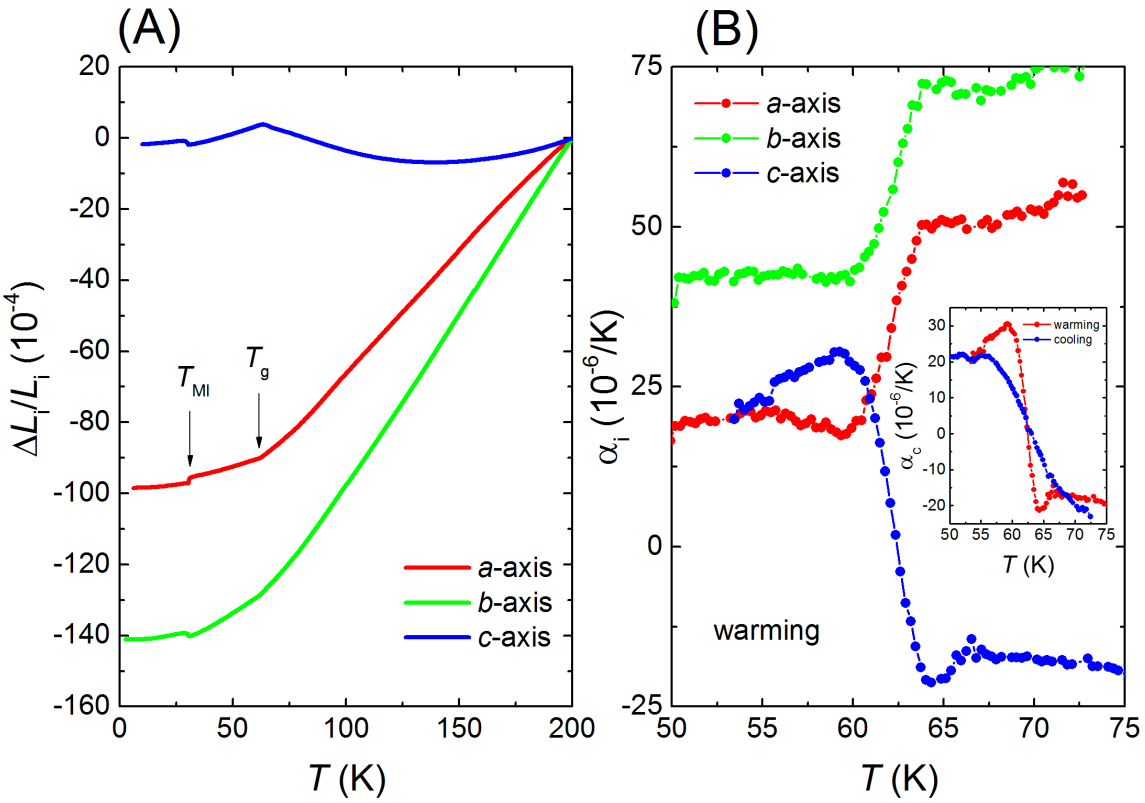


Figure 7.7.: (A) Relative length changes $\Delta L_i/L_i$ along all crystallographic directions $i = a, b, c$ of $\kappa$-(BEDT-TTF)$_2$Hg(SCN)$_2$Cl up to high temperatures $T \approx 200\,\mathrm{K}$. The step-like anomaly at $T \approx 30\,\mathrm{K}$ can be assigned to the metal-insulator transition at $T_{MI}$, the kink at $T \approx 63\,\mathrm{K}$ to a glass-like freezing of the ethylene end groups at $T_g$. (B) Thermal expansion coefficient $\alpha_i = L_i^{-1}\mathrm{d}L_i/\mathrm{d}T$ with $i = a, b, c$ around the glass transition at $T_g \approx 63\,\mathrm{K}$. Inset: Thermal expansion coefficient $\alpha_c$ for a slow cooldown (blue) with a rate of $q = -3\mathrm{K/h}$ and for the subsequent warmup (red) with a slow rate of $q = 1.5\,\mathrm{K/h}$.

pronounced hysteresis between warming and cooling (see Fig. 7.7 (B), inset) is observed with no over- and undershoots upon cooling. All of these signatures are characteristic for a glass-forming system [48] and incompatible with those of a thermodynamic phase transition.

Besides these signatures, a glass transition is also accompanied by a pronounced cooling-rate dependence. As outlined in detail in Sec. 2.3, the experimental observation time $t$, which depends on the cooling rate $q \propto 1/t$, has to be contrasted with the relaxation time $\tau$ of the system, which dramatically slows down close to the glass transition, giving rise to a cooling-rate dependence [48]. Figure 7.8 (A) shows the thermal expansion coefficient $\alpha_c(T)$ along the in-plane $c$ axis for different cooling speeds ranging from $q = -1.2\,\mathrm{K/h}$ to $-20.7\,\mathrm{K/h}$. The anomaly in $\alpha_c(T)$ shifts rapidly to higher temperatures upon increasing the cooling speed, as expected for a glass-forming system. Altogether, the observed features provide strong evidence for a glass transition in the present compound. We note that

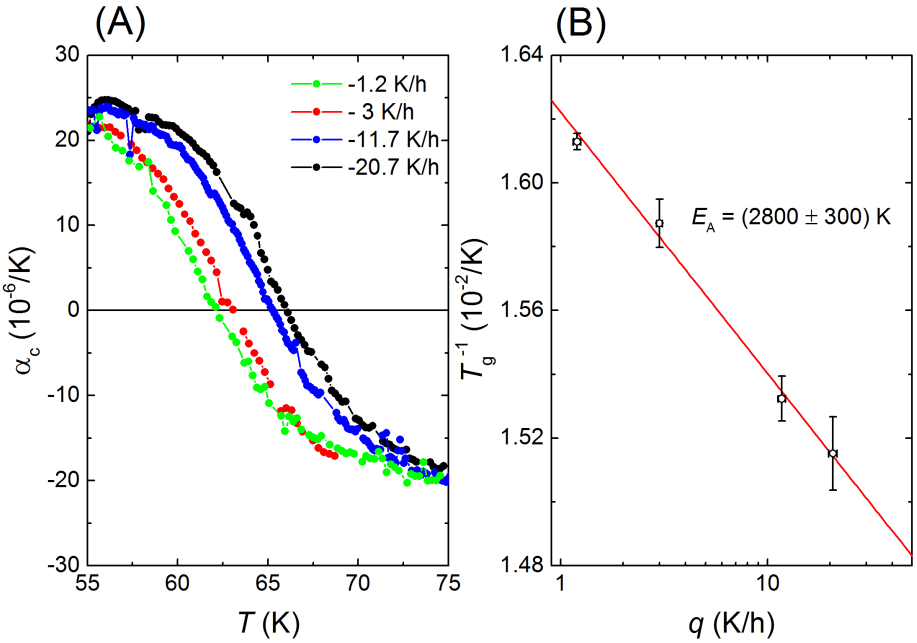


Figure 7.8.: (A) Cooling-rate dependence of the glass transition in κ-(BEDT-TTF)$_2$Hg(SCN)$_2$Cl, resolved in measurements of the thermal expansion coefficient $\alpha_c = L_c^{-1}\mathrm{d}L_c/\mathrm{d}T$. Cooling speeds ranging from $q$ =-1.2 K/h to -20.7 K/h were used. (B) Estimation of the activation energy $E_A$ from a plot of the inverse glass transition temperature $T_g^{-1}$ vs. the cooling rate in a logarithmic representation $\log q$ (after eq. 2.34).

the NTE effect observed here along the $c$ direction, along which the non-planar anions have chain-like character (see Fig. 7.2), is in accordance with previous observations of the NTE in κ-(ET)$_2$Cu[N(CN)$_2$]Br [192] and its deuterated variant [193], both of which contain planar anion chains. In the former work, it was argued that the structural changes cannot solely be understood by taking only the ethylene end group conformational degrees of freedom into account. Instead, they proposed that structural degrees of freedom in the anion layer contribute to the observed NTE, in which transversal displacement of the C and the N atoms in a chain-like structure can cause an overall shrinkage of the length in chain direction [193, 194].

For the determination of the activation energy, we analyze the cooling-rate dependence in more detail. According to eq. 2.34, the activation energy can be estimated in a thermally-activated process from the slope of a straight line in a representation of the inverse glass transition temperature $T_g^{-1}$ vs. the logarithm of the cooling speed $\log q$. To this end, we define the glass transition temperature $T_g$ as the temperature at which $\alpha_c(T)$ reaches the maximal slope. The so-derived data follow to a good approximation a straight line in the above-mentioned representation (see Fig. 7.8 (B)). From the slope an activation energy of $E_A = (2800 \pm 300)$ K can be determined. This activation energy $E_A$ is in the same range

as the previously determined activation energies ranging from $E_A = 2000\,\mathrm{K}$ to $3100\,\mathrm{K}$ (see Ref. [50] for a list of probes and corresponding $E_A$ values).

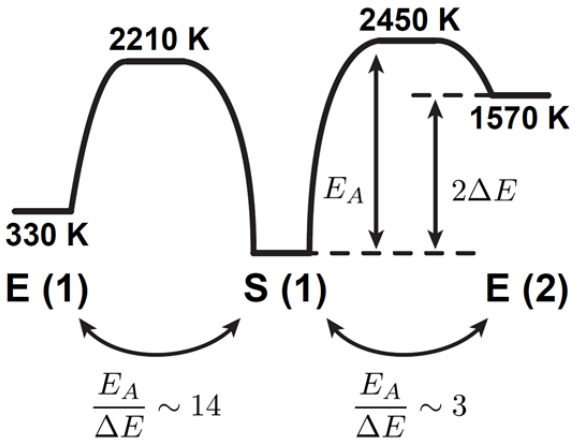


Figure 7.9.: Computed energies of the various ethylene end group confirmations in $\kappa$-(BEDT-TTF)$_2$Hg(SCN)$_2$Cl by *ab initio* calculations [195]. S(1) refers to the most stable configuration which is a staggered confirmation. E(1) is the eclipsed confirmation when flipping the inner ethylene end group, E(2) when flipping the outer ethylene end group. $E_A$ is the activation energy of the respective flipping process, $2\,\Delta E$ the energy difference between the two conformations.

The *ab initio* calculations, which aim at an understanding of the experimental findings, were performed using the same procedure, as described in Ref. [50]. Importantly, the interaction between the ethylene end groups and the anions are covered in this approach. The computed energy scheme is shown in Fig. 7.9. The computed ground state is a staggered conformation, labeled with S(1), in agreement with the experimentally determined structural data [34]. Closest in energy to the ground state with energy difference $2\Delta E = 330\,\mathrm{K}$ is an eclipsed (E (1)) conformation, which is obtained by flipping the inner ethylene end group. The second possible eclipsed conformation E(2) results from the ground state staggered conformation by flipping the outer ethylene end groups. However this process comes along with a distinctly higher energy difference of $2\Delta E = 1570\,\mathrm{K}$. The highest energy with an energy difference of $2\Delta E = 1920\,\mathrm{K}$ is obtained for the staggered conformation S(2) by a flipping of both ethylene end groups. This energy scheme is consistent with the notion that the outer ethylene end groups interact strongly with the anion layer and thus, a flipping of these ethylene end groups is energetically unfavorable. The activation energy $E_A$ for the different processes were calculated, as follows:

$$E_{A,S(1)\rightarrow E(1)} = 2210\,\mathrm{K} \tag{7.2}$$

$$E_{A,S(1)\rightarrow E(2)} = 2450\,\mathrm{K}. \tag{7.3}$$

In Ref. [50], it was found empirically that only conformations with $E_A/\Delta E \gtrsim 5$ show a glassy freezing. Following this suggestion, only the inner ethylene end groups are expected to show a glass transition in $\kappa$-HgCl with a high value of $E_A/\Delta E \approx 14$ in contrast to the outer ethylene end groups. The latter ones, which show only a small ratio $E_A/\Delta E \approx 3$, are coupled too strongly to the anion layer to allow for a flipping. Thus, the *ab initio* calculations suggest the existence of only one glass transition in $\kappa$-HgCl with an activation energy of $E_A = 2210\,\mathrm{K}$. This result is consistent with the presented experimental evidence for one glass transition with an activation energy $E_A = (2800 \pm 300)\,\mathrm{K}$ in a similar range.

## 7.4. Summary

In this chapter, we presented a detailed investigation of the ground-state properties of the quasi-2D organic charge-transfer salt $\kappa$-(ET)$_2$Hg(SCN)$_2$Cl, which undergoes a charge-order metal-insulator transition at $T_{MI} \approx 30\,\mathrm{K}$. We demonstrated experimentally that the responsible intra-dimer charge degrees of freedom lead to a purely electronically-driven ferroelectric state, as previously proposed, but which is controversially discussed for other $\kappa$-(ET)$_2X$ salts. In accordance with this picture, in which an inversion symmetry is broken to obtain an overall polarization, we observed strong and anisotropic lattice effects along all crystallographic directions. From a thermodynamic analysis of the lattice effects as well as of the specific heat, we obtained the entropy change associated with the phase transition. This entropy change can be solely attributed to the localization of charge carriers. However, the role of spin degrees of freedom at the phase transition could not be identified unambiguously with the help of the present data. In addition, measurements under pressure indicated a high pressure sensitivity of the metal-insulator transition. Surprisingly, no indications for superconductivity were found at pressures high enough to stabilize the metallic state down to low temperatures. This contrasts with other $\kappa$-(ET)$_2X$ salts, which show the highest superconducting transition temperature among the organic charge-transfer salts. Further we could demonstrate that the observed glass transition at higher temperatures is consistent with the predictions of recent calculations. This material shows a variety of intriguing properties, which are worth being studied in more detail: The absence of superconductivity clearly asks for more research into this direction. Another aspect of interest for future research are the magnetic properties of this system, especially in light of the high degree of frustration present in this material, as predicted by DFT calculations. All of these aspects will contribute to a better understanding of the properties of strongly correlated materials with a quarter-filled conduction band in the presence of strong frustration.

# 8. Conclusion and Outlook

This thesis aimed at identifying and understanding the interplay of charge and lattice degrees of freedom at metal-insulator transitions that are driven by strong electron correlations, i.e., the Mott and charge-order metal-insulator transitions. To this end, measurements of the thermal expansion were performed, which have proven to be particularly suited to deliver insight into the role of lattice degrees of freedom in strongly correlated electron systems. Prime examples of such systems are the studied organic charge-transfer salts, which stand out by a high tuneability of the interaction strength.

The main topic of this thesis was the investigation of the universal behavior of the pressure-induced finite-temperature Mott critical endpoint in the organic charge-transfer salt $\kappa$-(BEDT-TTF)$_2$Cu[N(CN)$_2$]Cl. The identification of the underlying universality class is of central importance for the understanding of the mechanisms, which drive the collective behavior at a given phase transition. Despite intensive research on different materials, the universality class of the Mott transition remained illusive. Until now, the Mott transition was viewed within a simplified purely electronic picture, represented by the Hubbard model with on-site Coulomb repulsion $U$. In the present work, it was proven experimentally that lattice effects play a crucial role for the universal behavior, in contrast to the assumptions made in previous works. The smoking gun criterion here was the observation of a breakdown of Hooke's law of elasticity upon approaching the critical endpoint, reflected in a strongly non-linear variation of the length as a function of pressure. This observation clearly demonstrates a non-perturbative coupling of the critical electronic subsystem to the lattice degrees of freedom, resulting in a substantial softening of the lattice. In this particular organic charge-transfer salt, these non-linearities were observed in wide ranges of temperature and pressure, exceeding the critical point by $\Delta T/T_c \approx 20\%$ in temperature and by $\Delta P/P_c \approx 10\%$ in pressure. The further analysis of the data in terms of the critical behavior was performed on the basis of a theoretical prediction [21, 22] of the influence of the lattice on the electronic system. Therein, it was claimed that due to the long-ranged shear forces of the crystal lattice the coupling of the critical electronic system to a compressible lattice with finite shear moduli causes a crossover to mean-field critical behavior close to the critical endpoint, corresponding to the universal properties of a solid-solid endpoint. It could be demonstrated that the obtained data set on the relative length change is fully consistent with this scenario. This was possible by employing a mean-field model,

extended by the effects of weak disorder, which provides an excellent description of the full data set on a quantitative level. This case study on the organic charge-transfer salt $\kappa$-(BEDT-TTF)$_2$Cu[N(CN)$_2$]Cl thus allows to draw important conclusions about the Mott transition in any real material in the presence of a compressible lattice. The significance of electron-lattice coupling can be inferred from the fact that the Mott transition is amenable to pressure tuning, as pressure affects directly the lattice spacing. This, in turn, modifies the overlap of orbitals of adjacent molecules and thus changes the electronic correlation strength, i.e., the ratio of Coulomb repulsion $U$ to the kinetic energy $W$. As a consequence, every pressure-tuneable Mott transition is governed by the electron-lattice coupling, which, sufficiently close to the endpoint, will eventually induce mean-field critical behavior. Correspondingly, even though this transition is driven by electronic degrees of freedom, it will show the universal properties of an isostructural solid-solid endpoint.

The result of this work has a strong impact on the previously proposed description of the Mott transition in terms of a Hubbard model that only takes electronic degrees of freedom into account. It clearly calls for an extended description of the effects of correlated electrons by involving elastic degrees of freedom. In the course of the present study two aspects appeared, which could be of interest for further research from both theoretical, but also experimental side: First, it would be enlightening to study transport properties, which directly couple to the charge degrees of freedom, in the presence of a compressible lattice theoretically on a microscopic level. Such a study, even though it is a very challenging task, might help to understand in more detail previous investigations on the conductance [17,18], which aimed to resolve the critical behavior. This issue is also fascinating in light of the idea that $\kappa$-(BEDT-TTF)$_2$Cu[N(CN)$_2$]Cl reveals quantum-critical behavior [148] at higher temperatures as a consequence of the large competing interaction strengths $U$ and $W$ in the system. The second important aspect, which became evident during this work, was that the analysis of the universal behavior very close to the endpoint can be plagued by disorder effects, that are present in any real system. To include these effects, a phenomenological approach was applied, which however does not provide any insight into the microscopic effects of disorder close to a critical endpoint that is governed by electron-lattice coupling. Thus, the results here clearly ask for more research in the direction of including disorder effects in the theoretical modeling. From the experimental side, x-ray irradiation of organic charge-transfer salts can provide a systematic access to the role of disorder for strongly correlated electrons [143].

The above-studied organic charge-transfer salt $\kappa$-(BEDT-TTF)$_2$Cu[N(CN)$_2$]Cl is situated so close to the Mott transition due to the strong structural dimerization, which allows to treat these materials in an effective-dimer model with half-filled conduction band. Nevertheless, in recent years intra-dimer effects, i.e., effects beyond the effective-dimer model, attracted attention, mainly by the proposal of charge-order driven multiferroicity in $\kappa$-

(BEDT-TTF)$_2$Cu[N(CN)$_2$]Cl [5]. However, this issue is controversially discussed in literature as no charge ordering could be detected up to now in this material. Within this work, the multiferroic properties were investigated in more detail by performing measurements of the dielectric constant as well as the magnetization on the same single crystal. The former quantity is sensitive to the ferroelectric order, whereas the latter one is suited to detect magnetic ordering. This study confirmed that despite some sample-to-sample variations most of the crystals showed a simultaneous homogeneous ferroelectric and magnetic order. This observation is in accordance with the previously proposed scenario that intra-dimer charge degrees of freedom are responsible for the ferroelectric ground state.

To investigate intra-dimer effects in the family of $\kappa$-phase organic charge-transfer salts in more detail, the salt $\kappa$-(BEDT-TTF)$_2$Hg(SCN)$_2$Cl turned out to be a very good reference system. This material shows, according to DFT calculations [178], by far the weakest dimerization of all $\kappa$-(BEDT-TTF)$_2X$ salts investigated yet, which implies that the intra-dimer interactions can become comparable to the inter-dimer interactions. Thus, this material should show in a more pronounced manner the properties of electron correlations in a quarter-filled band. This theoretical prediction was complemented by previous experiments, which identified a charge-order metal insulator transition at $T_{MI} \approx 30\,\mathrm{K}$ [34]. In the present work, a further characterization of this material, about which only little is known in literature, was performed by the means of transport and thermodynamic measurements. Importantly, this study showed that intra-dimer charge degrees of freedom can lead to a purely electronically-driven ferroelectricity. As demonstrated by thermal expansion measurements, the ferroelectric transition here is accompanied by strong and anisotropic lattice effects along all crystallographic directions. In fact, lattice effects are expected at any ferroelectric transition, as the inversion symmetry must be broken in order to create a finite polarization. Together with specific heat results, the entropy change at the transition was estimated and found to be fully consistent with the expectation for a metal-insulator transition. This metal-insulator transition could be rapidly suppressed with pressure, and surprisingly, no indications for superconductivity were found in the pressure-induced metallic state in contrast to other $\kappa$-(ET)$_2X$ salts. In addition, a glass-like freezing of the ethylene end groups at higher temperatures, similar to other $\kappa$-phase ET salts, was detected the properties of which are in accordance with recent theoretical models [50]. These models emphasize the importance of the coupling of the ethylene end groups to the anions as a source for this glassy behavior.

Even though the investigation of $\kappa$-(BEDT-TTF)$_2$Hg(SCN)$_2$Cl demonstrated convincingly that intra-dimer charge degrees of freedom have to be taken into account for the description of phenomena, such as ferroelectricity, a number of questions still remain puzzling. Among them is the question whether spin degrees of freedom are also involved in this phase transition and whether this material even undergoes a multiferroic transition.

An answer to this question will shed more light onto the coupling between charge and spin in forming the ground state not only in $\kappa$-(BEDT-TTF)$_2$Hg(SCN)$_2$Cl, but also in $\kappa$-(BEDT-TTF)$_2$Cu[N(CN)$_2$]Cl. This, in turn, will help to identify the driving mechanism of multiferroic ground states in strongly frustrated systems. Thus, a more detailed magnetic characterization by means of SQUID measurements, magnetic torque measurements, NMR or ESR measurements is highly desired. Besides that, a further study of the absence of superconductivity in this material will provide more insights on the mechanisms which are important in forming superconductivity in the organic charge-transfer salts.

All together, this work contributed to a further understanding how phase transitions between metallic and insulating states occur in the presence of strong electron correlations. It emphasized the need to take into account lattice effects in the description of the Mott metal-insulator transition, but also in charge-order transitions. Thus, it provides the important basis for a more advanced modeling of these phenomena in strongly correlated electron systems. Such a description is essential for a still-missing understanding of the emergence of exotic phases, such as high-temperature superconductivity or spin-liquid states, or even for being able to predict these states in novel materials.

# A. Appendix

## A.1. Calculations of the dielectric constant of helium under pressure

As shown in chapter 3.1.2, a very precise knowledge of the dielectric constant of helium under gas pressure is vital for a high-resolution determination of length changes under pressure. This section describes in detail a theoretical approach to calculate the dielectric constant of helium $\varepsilon_r(T,P)$ as a function of pressure $P$ and temperature $T$ for a system with constant volume $V$, but changing particle number $N$. As suggested by the Clausius-Mosotti equation A.1, the changes in the dielectric constant can be related to changes in the particle density $n = N/V$. First efforts to calculate the particle density by the van-der-Waals equation were performed by Dr. Rudra S. Manna [26] and have been continued by Dr. Ulrich Tutsch at the beginning of this work. The basics of these calculations will be presented here. In chapter 3 these results have been compared to a detailed experimental investigation of the dielectric constant in a large $T$-$P$-range, which has been obtained in the course of the present thesis and the Bachelor work of Phillip Ross [196].

$$\frac{\epsilon_r - 1}{\epsilon_r + 2} = \frac{n\alpha}{3\epsilon_0} \text{ with } \alpha = 22.47 \cdot 10^{-42} \frac{\mathrm{Cm}^2}{\mathrm{V}} \tag{A.1}$$

The van-der-Waals equation is an extension of the ideal gas law [39]. The latter describes the equation of state of a gas of non-interacting particles as a function of pressure $P$, temperature $T$ and volume $V$ while neglecting the volume of the particle itself. This approximation is not valid in real gases, since the molecules have a volume and interact with each other. To take these factors into account, the pressure is replaced by an effective pressure $P_{eff} = P + an^2/V^2$ and the volume is replaced by an effective volume $V_{eff} = V - nb$. These effective formulas contain two new variables $a$ and $b$: $a$ measures the attraction between the particles and $b$ the volume of the molecules. Obviously, these parameters are material-specific. The resulting van-der-Waals equation is given in equation A.2 [39].

$$Nk_BT = \left(P + \frac{N^2 a}{V^2}\right)(V - Nb) \tag{A.2}$$

This is a cubic equation which can be solved using Cardano's method. The solution of this equation is already described in Ref. [26]. The curves shown in chapter 3.1.2 have been calculated by assuming that the volume of the particles changes as a function of pressure, resulting in a pressure dependence of the parameter $b$. This pressure dependence can be calculated from literature data for the pressure dependence of the mass density of helium $\rho$ [197–201], which is available up to pressures of about 100 MPa (see equation A.3).

$$b = \frac{m_{He-atom}}{\rho} \text{ and } m_{He-atom} = 4u \tag{A.3}$$

The parameter $a$ has a literature value of $9.513 \cdot 10^{-51}\,\mathrm{Pa\,m^6}$. It was found that changing this parameter to $1.6 \cdot 10^{-50}\,\mathrm{Pa\,m^6}$ provides the best description of the obtained data.

## A.2. Verification of the determination of the dielectric constant of helium under pressure

In order to verify our procedure to evaluate the experimentally obtained capacitance $C(P,T)$ data and to calculate the thermal expansion coefficient, involving a precise determination of the dielectric constant as well as the cell effect (see chapter 3), we performed the following sets of experiment: First of all, we precisely determined the cell effect by measuring an aluminum (Al) sample at ambient pressure, the expansion of which is well known [90], and calculated the cell effect. In order to verify that this calibration is precise, we performed the same measurement with a copper (Cu) sample and checked that we can reproduce the literature results for Cu [90] with very high precision. Afterwards, we concentrated on measurements under pressure to verify our determination of the dielectric constant. To this end, we measured the dielectric constant of $^4$He with an Al sample at $P = 4\,\mathrm{MPa}$ and $P = 10.2\,\mathrm{MPa}$ (see Fig. 3.5) and the Cu sample at $P = 9.6\,\mathrm{MPa}$ (see Fig. A.1). The dielectric constant $\varepsilon_r(T,P)$ at a certain pressure is given by $\varepsilon_r(T,P) = C(P,T)/C(P = 0\,\mathrm{MPa})$, abbreviated as $C/C_0$. In order to compare the data sets taken with the Al sample and the Cu sample, we interpolated the two Al data sets at $P = 4\,\mathrm{MPa}$ and $10.2\,\mathrm{MPa}$ linearly and determined in that way a data set for $P = 9.6\,\mathrm{MPa}$ based on Al measurements. This interpolated data set is shown in Fig. A.1 by the red line compared to one measurement on the Cu sample at exactly this pressure value (black line). We find a very good agreement of these data sets with deviations in the range of $(\epsilon_{r,Al} - \epsilon_{r,Cu})/\epsilon_{r,Al} < 0.1\%$. In a next step, we used the dielectric constant, derived from the Al data, to evaluate the thermal expansion of Cu. The inset of Fig. A.1 shows a comparison of the measured thermal expansion of Cu and the literature values. We find an excellent agreement between our data set and the literature values. It thus confirms that we determined the cell effect correctly and that an interpolation of the dielectric constant between given data sets is precise enough

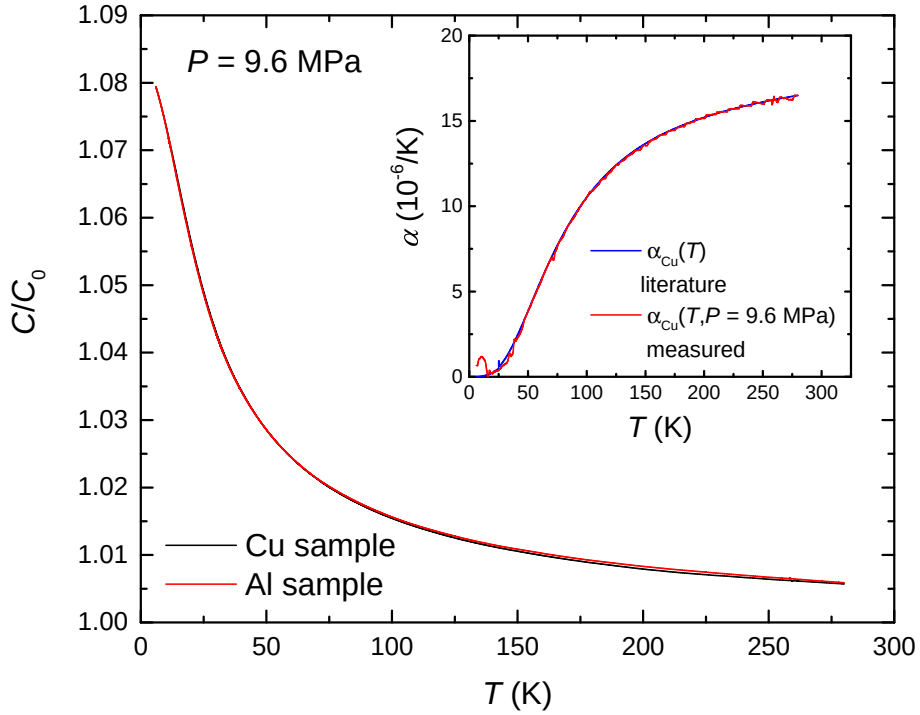


Figure A.1.: Experimental verification of the determination of the dielectric constant of helium under pressure. The black line shows data of the dielectric constant $\epsilon_r = C/C_0$ at $P = 9.6\,\mathrm{MPa}$, obtained with a copper (Cu) sample. The red line shows the linear interpolation of $C/C_0$ data, taken at $P = 4\,\mathrm{MPa}$ and $P = 10.2\,\mathrm{MPa}$ on an aluminum (Al) sample, to obtain data for $P = 9.6\,\mathrm{MPa}$. Inset: Blue line shows the thermal expansion coefficient $\alpha$ of Cu as known from literature [90]. The red line corresponds to the measured thermal expansion coefficient of a Cu sample at 9.6 MPa. For the analysis the dielectric constant, determined from the interpolation of the Al data, has been used.

as long as the pressure distance between these data sets is not too high. In the analysis of the measurements on $\kappa$-Cl, we recorded the dielectric constant in a much more narrow temperature window with only a small step size in pressure of about 1 MPa (see Fig. 3.5), which is supposed to increase the accuracy even further.

## A.3. Determination of the uniaxial pressure exerted by the capacitive dilatometer

While mounting a crystal in a capacitive dilatometer, a small uniaxial pressure is applied to the crystal when the starting capacitance for a measurement is adjusted. Organic charge-transfer salts are usually highly pressure-sensitive so that a knowledge of the applied force $F$ is important for understanding the obtained measurement results. It can easily be determined experimentally for each dilatometer cell by putting different weights on the upper

capacitor plate and measuring the resulting capacitance change $\Delta C$. For the ambient pressure cell such kind of experiment has been performed by Dr. M. de Souza [193] and yielded

$$\frac{\Delta F}{\Delta C} \approx 0.12 \frac{\mathrm{N}}{\mathrm{pF}}. \tag{A.4}$$

By estimating a surface area of $A \approx 1\,\mathrm{mm}^2$ and an initial capacitance change of 2 pF, a uniaxial pressure of $\approx$0.2 MPa = 2 bar is exerted by the dilatometer.

The capacitance changes of one particular dilatometer for a given force is clearly cell-dependent because of the different strengths of springs used. Therefore the same experiment was performed for the dilatometer cell used for measurements under pressure. Cylinders, made out of brass with different weights between 260 mg and 730 mg, resulted in capacitance changes up to 0.005 pF. It has been found that

$$\frac{\Delta F}{\Delta C} \approx 1.1 \frac{\mathrm{N}}{\mathrm{pF}}, \tag{A.5}$$

which is a factor of 10 higher than for the ambient pressure dilatometer. Therefore in general, experiments on organic charge-transfer salts under pressure have been performed with a starting capacitance of 5.1 pF at the finite-pressure setup, which is only 0.2 pF higher than the empty cell capacitance.

# Bibliography


[1] M.-S. Nam, A. Ardavan, S. Blundell, J. Schlueter, *Fluctuating superconductivity in organic molecular metals close to the Mott transition*, Nature **449**, 584-587 (2007). Cited on pages 3 and 28.

[2] P. A. Lee, N. Nagaosa, X.-G. Wen, *Doping a Mott insulator: Physics of high-temperature superconductivity*, Rev. Mod. Phys. **78**, 17–85 (2006). Cited on pages 3, 11 and 28.

[3] B. Keimer, S. Kivelson, M. Norman, S. Uchida, J. Zaanen, *From quantum matter to high-temperature superconductivity in copper oxides*, Nature **518**, 179-186 (2015). Cited on pages 3, 11 and 28.

[4] T. Kimura, T. Goto, H. Shintani, K. Ishizaka, T. Arima, Y. Tokura, *Magnetic control of ferroelectric polarization*, Nature **426**, 55-58 (2003). Cited on pages 3, 11 and 28.

[5] P. Lunkenheimer, J. Müller, S. Krohns, F. Schrettle, A. Loidl, B. Hartmann, R. Rommel, M. de Souza, C. Hotta, J. Schlueter, M. Lang, *Multiferroicity in an organic charge-transfer salt that is suggestive of electric-dipole-driven magnetism*, Nat. Mater. **11**, 755-758 (2012). Cited on pages 3, 11, 28, 34, 66, 115, 116, 117, 118, 120, 133, 141 and 165.

[6] N. F. Mott, R. Peierls, *Discussion of the paper by de Boer and Verwey*, Proceedings of the Physical Society **49**, 72 (1937). Cited on pages 3 and 29.

[7] N. F. Mott, *Metal-insulator transition*, vol. 26 (WILEY-VCH Verlag, 1990). Cited on pages 3, 11, 28 and 29.

[8] J. H. de Boer, E. J. W. Verwey, *Semi-conductors with partially and with completely filled 3 d -lattice bands*, Proc. Phys. Soc. **49**, 59 (1937). Cited on pages 3 and 29.

[9] M. Imada, A. Fujimori, Y. Tokura, *Metal-insulator transitions*, Rev. Mod. Phys. **70**, 1039-1263 (1998). Cited on pages 3, 11, 29, 30 and 35.

[10] L. Kadanoff, *Scaling Laws for Ising Models near $T_c$*, Physics **2**, 263-272 (1966). Cited on pages 3 and 23.

[11] B. Widom, *Equation of State in the Neighborhood of the Critical Point*, The Journal of Chemical Physics **43**, 3898-3905 (1965). Cited on pages 3 and 23.

[12] K. Kanoda, *Recent progress in NMR studies on organic conductors*, Hyperfine Interact. **104**, 235–249 (1997). Cited on pages 4, 7, 12, 27, 31, 63 and 64.

[13] N. Toyota, M. Lang, J. Müller, *Low-Dimensional Molecular Metals* (Springer, 2007). Cited on pages 4, 11, 12, 27, 31, 37, 55, 57 and 60.

[14] M. Greiner, O. Mandel, T. Esslinger, T. Hänsch, I. Bloch, *Quantum phase transition from a superfluid to a Mott insulator in a gas of ultracold atoms*, Nature **415**, 39-44 (2002). Cited on page 4.

[15] C. Castellani, C. D. Castro, D. Feinberg, J. Ranninger, *New Model Hamiltonian for the Metal-Insulator Transition*, Phys. Rev. Lett. **43**, 1957–1960 (1979). Cited on pages 4 and 70.

[16] G. Kotliar, E. Lange, M. J. Rozenberg, *Landau Theory of the Finite Temperature Mott Transition*, Phys. Rev. Lett. **84**, 5180–5183 (2000). Cited on pages 4, 70 and 71.

[17] P. Limelette, A. Georges, D. Jérome, P. Wzietek, P. Metcalf, J. M. Honig, *Universality and Critical Behavior at the Mott Transition*, Science **302**, 89–92 (2003). Cited on pages 4, 7, 31, 70, 71, 86, 106, 107 and 140.

[18] F. Kagawa, K. Miyagawa, K. Kanoda, *Unconventional critical behaviour in a quasi-two-dimensional organic conductor*, Nature **436**, 534-537 (2005). Cited on pages 4, 22, 23, 64, 71, 72, 81, 86, 105, 108, 110, 113 and 140.

[19] M. Abdel-Jawad, R. Kato, I. Watanabe, N. Tajima, Y. Ishii, *Universality Class of the Mott Transition*, Phys. Rev. Lett. **114**, 106401 (2015). Cited on page 4.

[20] L. Bartosch, M. de Souza, M. Lang, *Scaling Theory of the Mott Transition and Breakdown of the Grüneisen Scaling Near a Finite-Temperature Critical End Point*, Phys. Rev. Lett. **104**, 245701 (2010). Cited on pages 4, 17, 26, 65, 72, 73, 83, 84, 98, 105, 108 and 112.

[21] M. Zacharias, L. Bartosch, M. Garst, *Mott Metal-Insulator Transition on Compressible Lattices*, Phys. Rev. Lett. **109**, 176401 (2012). Cited on pages 5, 40, 73, 74, 75, 86, 87, 88, 104 and 139.

[22] M. Zacharias, A. Rosch, M. Garst, *Critical elasticity at zero and finite temperature*, The European Physical Journal Special Topics **224**, 1021-1040 (2015). Cited on pages 5, 74, 104, 105 and 139.

[23] P. Majumdar, H. R. Krishnamurthy, *Lattice Contraction Driven Insulator-Metal Transition in the $d = \infty$ Local Approximation*, Phys. Rev. Lett. **73**, 1525–1528 (1994). Cited on pages 5 and 74.

[24] S. R. Hassan, A. Georges, H. R. Krishnamurthy, *Sound Velocity Anomaly at the Mott Transition: Application to Organic Conductors and $V_2O_3$*, Phys. Rev. Lett. **94**, 036402 (2005). Cited on pages 5 and 74.

[25] R. S. Manna, B. Wolf, M. de Souza, M. Lang, *High-resolution thermal expansion measurements under helium-gas pressure*, Rev. Sci. Instrum. **83** (2012). Cited on pages 5, 11, 41 and 47.

[26] R. S. Manna, *Thermal expansion studies on low-dimensional frustrated quantum magnets: the case of $\kappa$-(BEDT-TTF)$_2$Cu$_2$(CN)$_3$ and azurite*, Ph.D. thesis, Goethe-Universität Frankfurt am Main (2012). Cited on pages 5, 41, 47, 143 and 144.

[27] R. Küchler, T. Bauer, M. Brando, F. Steglich, *A compact and miniaturized high resolution capacitance dilatometer for measuring thermal expansion and magnetostriction*, Rev. Sci. Instrum. **83**, 095102 (2012). Cited on pages 5 and 48.

[28] R. Pott, R. Schefzyk, *Apparatus for measuring the thermal expansion of solids between 1.5 and 380K*, J. Phys. E: Sci. Instrum. **16**, 444 (1983). Cited on pages 5, 11, 41 and 43.

[29] A. Jayaraman, D. B. McWhan, J. P. Remeika, P. D. Dernier, *Critical Behavior of the Mott Transition in Cr-Doped $V_2O_3$*, Phys. Rev. B **2**, 3751–3756 (1970). Cited on pages 7, 73 and 106.

[30] A. G. Gavriliuk, I. A. Trojan, V. V. Struzhkin, *Insulator-Metal Transition in Highly Compressed NiO*, Phys. Rev. Lett. **109**, 086402 (2012). Cited on pages 7 and 106.

[31] S. Wang, J. Zhu, Y. Zhang, X. Yu, J. Zhang, W. Wang, L. Bai, J. Qian, L. Yin, N. S. Sullivan, C. Jin, D. He, J. Xu, Y. Zhao, *Unusual Mott transition in multiferroic $PbCrO_3$*, PNAS **112**, 15320-15325 (2015). Cited on pages 7 and 106.

[32] Y. Kurosaki, Y. Shimizu, K. Miyagawa, K. Kanoda, G. Saito, *Mott Transition from a Spin Liquid to a Fermi Liquid in the Spin-Frustrated Organic Conductor $\kappa$-(ET)$_2$Cu$_2$(CN)$_3$*, Phys. Rev. Lett. **95**, 177001 (2005). Cited on pages 7 and 106.

[33] Y. Shimizu, H. Akimoto, H. Tsujii, A. Tajima, R. Kato, *Mott Transition in a Valence-Bond Solid Insulator with a Triangular Lattice*, Phys. Rev. Lett. **99**, 256403 (2007). Cited on pages 7 and 106.

[34] N. Drichko, R. Beyer, E. Rose, M. Dressel, J. A. Schlueter, S. A. Turunova, E. I. Zhilyaeva, R. N. Lyubovskaya, *Metallic state and charge-order metal-insulator transition in the quasi-two-dimensional conductor $\kappa$-(BEDT-TTF)$_2$Hg(SCN)$_2$Cl*, Phys. Rev. B **89**, 075133 (2014). Cited on pages 7, 13, 61, 121, 122, 123, 124, 130, 133, 137, 141 and 165.

[35] Y. Shimizu, K. Miyagawa, K. Kanoda, M. Maesato, G. Saito, *Spin Liquid State in an Organic Mott Insulator with a Triangular Lattice*, Phys. Rev. Lett. **91**, 107001 (2003). Cited on pages 11, 28 and 65.

[36] L. Balents, *Spin liquids in frustrated magnets*, Nature **464**, 199-208 (2010). Cited on pages 11, 28 and 36.

[37] H. Ibach, H. Lüth, *Festkörperphysik* (Springer, 2002). Cited on pages 15, 17, 28, 29, 37 and 132.

[38] L. Zhu, M. Garst, A. Rosch, Q. Si, *Universally Diverging Grüneisen Parameter and the Magnetocaloric Effect Close to Quantum Critical Points*, Phys. Rev. Lett. **91**, 066404 (2003). Cited on pages 17 and 73.

[39] W. Nolting, *Grundkurs Theoretische Physik 4* (Springer, 2005). Cited on pages 18, 19 and 143.

[40] W. Nolting, *Grundkurs Theoretische Physik 6 - Statistische Physik* (Springer, 2007). Cited on pages 18, 19, 20, 21, 22, 23, 25 and 26.

[41] F. Schwabl, *Statistische Mechanik* (Springer, 2006). Cited on pages 19, 20, 21, 22 and 23.

[42] M. Vojta, *Quantum Phase Transitions*, Rep. Prog. Phys. **66**, 2069 (2003). Cited on page 19.

[43] M. Vojta, Thermal and Quantum Phase Transitions, Lecture Notes given at the Les Houches Doctoral Traning School in Statistical Physics (2015). Cited on pages 19, 23 and 25.

[44] N. Goldenfeld, *Lectures on Phase Transitions and the Renormalization Group* (Perseus Book, 1992). Cited on pages 20, 21, 22 and 23.

[45] P. Kopietz, L. Bartosch, F. Schütz, *Introduction to the Functional Renormalization Group* (Springer-Verlag Berlin Heidelberg, 2010). Cited on page 23.

[46] L. Landau, *On the theory of phase transitions. I.*, Zh. Eksp. Teor. Fiz. **11**, 26 (1937). Cited on page 24.

[47] P. Fonseca, A. Zamolodchikov, *Ising Field Theory in a Magnetic Field: Analytic Properties of the Free Energy*, J. Stat. Phys. **110**, 527-590 (2003). Cited on page 26.

[48] J. Müller, *Thermodynamische Untersuchungen an quasi-zweidimensionalen organischen Supraleitern*, Ph.D. thesis, Technische Universität Dresden (2001). Cited on pages 27 and 135.

[49] B. Hartmann, J. Müller, T. Sasaki, *Mott metal-insulator transition induced by utilizing a glasslike structural ordering in low-dimensional molecular conductors*, Phys. Rev. B **90**, 195150 (2014). Cited on pages 27, 62 and 66.

[50] J. Müller, B. Hartmann, R. Rommel, J. Brandenburg, S. M. Winter, J. A. Schlueter, *Origin of the glass-like dynamics in molecular metals $\kappa$-(BEDT-TTF)$_2$X:Implications from fluctuation spectroscopy and ab initio calculations*, New J. Phys. **17**, 083057 (2015). Cited on pages 27, 66, 67, 134, 137, 138 and 141.

[51] G. Czycholl, *Theoretische Festkörperphysik* (Springer, 2008). Cited on pages 28, 32 and 33.

[52] A. Sommerfeld, *Zur Elektronentheorie der Metalle auf Grund der Fermischen Statistik*, Zeitschrift für Physik **47**, 1–32 (1928). Cited on page 28.

[53] F. Bloch, *Bemerkung zur Elektronentheorie des Ferromagnetismus und der elektrischen Leitfähigkeit*, Z. Phys. **57**, 545–555 (1929). Cited on page 28.

[54] G. Kotliar, D. Vollhardt, *Strongly correlated materials: Insights from dynamical mean-field Theory*, Physics Today **57**, 53 (2004). Cited on pages 29, 31 and 32.

[55] N. F. Mott, *The Basis of the Electron Theory of Metals, with Special Reference to the Transition Metals*, Proc. Phys. Soc. London, Sect. A **62**, 416 (1949). Cited on page 29.

[56] N. F. Mott, *On the Transition to Metallic Conduction in Seminconductors*, Can. J. Phys. **34**, 1356-1368 (1956). Cited on page 29.

[57] N. F. Mott, *The transition to the metallic state*, Philos. Mag. **6**, 287-309 (1961). Cited on page 29.

[58] K. Kanoda, R. Kato, *Mott Physics in Organic Conductors with Triangular Lattices*, Annual Review of Condensed Matter Physics **2**, 167-188 (2011). Cited on page 30.

[59] A. Georges, G. Kotliar, W. Krauth, M. J. Rozenberg, *Dynamical mean-field theory of strongly correlated fermion systems and the limit of infinite dimensions*, Rev. Mod. Phys. **68**, 13-125 (1996). Cited on pages 30, 31, 32 and 71.

[60] A. Georges, L. de' Medici, J. Mravlje, *Strong Correlations from Hund's Coupling*, Annu. Rev. of Condens. Matter Phys. **4**, 137-178 (2013). Cited on page 30.

[61] P. W. Anderson, *Ordering and Antiferromagnetism in Ferrites*, Phys. Rev. **102**, 1008–1013 (1956). Cited on page 30.

[62] J. Hubbard, *Electron Correlations in Narrow Energy Bands*, Proc. R. Soc. A: Math. Phys. Eng. Sci. **276**, 238–257 (1963). Cited on page 30.

[63] J. Hubbard, *Electron Correlations in Narrow Energy Bands. II. The Degenerate Band Case*, Proc. R. Soc. A: Math. Phys. Eng. Sci. **277**, 237–259 (1964). Cited on page 30.

[64] J. Hubbard, *Electron Correlations in Narrow Energy Bands. III. An Improved Solution*, Proc. R. Soc. A: Math. Phys. Eng. Sci. **281**, 401–419 (1964). Cited on page 30.

[65] J. Kanamori, *Electron Correlation and Ferromagnetism of Transition Metals*, Progr. Theoret. Phys. **30**, 275-289 (1963). Cited on page 30.

[66] P. Limelette, P. Wzietek, S. Florens, A. Georges, T. A. Costi, C. Pasquier, D. Jérome, C. Mézière, P. Batail, *Mott Transition and Transport Crossovers in the Organic Compound $\kappa$-(BEDT-TTF)$_2$Cu[N(CN)$_2$]Cl*, Phys. Rev. Lett. **91**, 016401 (2003). Cited on

pages 31, 63, 64, 70, 71 and 106.

[67] W. Metzner, D. Vollhardt, *Correlated Lattice Fermions in $d = \infty$ Dimensions*, Phys. Rev. Lett. **62**, 324–327 (1989). Cited on page 31.

[68] M. J. Rozenberg, X. Y. Zhang, G. Kotliar, *Mott-Hubbard transition in infinite dimensions*, Phys. Rev. Lett. **69**, 1236–1239 (1992). Cited on page 31.

[69] A. Georges, W. Krauth, *Numerical solution of the $d = \infty$ Hubbard model: Evidence for a Mott transition*, Phys. Rev. Lett. **69**, 1240–1243 (1992). Cited on page 31.

[70] F. Lechermann, A. Georges, A. Poteryaev, S. Biermann, M. Posternak, A. Yamasaki, O. K. Andersen, *Dynamical mean-field theory using Wannier functions: A flexible route to electronic structure calculations of strongly correlated materials*, Phys. Rev. B **74**, 125120 (2006). Cited on page 33.

[71] H. Seo, C. Hotta, H. Fukuyama, *Toward Systematic Understanding of Diversity of Electronic Properties in Low-Dimensional Molecular Solids*, Chem. Rev. **104**, 5005-5036 (2004). Cited on page 33.

[72] C. Hotta, *Theories on Frustrated Electrons in Two-Dimensional Organic Solids*, Crystals **2**, 1155 (2012). Cited on page 33.

[73] J. van den Brink, D. I. Khomskii, *Multiferroicity due to charge ordering*, J. Phys.: Condens. Matter **20**, 434217 (2008). Cited on pages 34, 115 and 117.

[74] M. Dressel, *Ordering phenomena in quasi-one-dimensional organic conductors*, Naturwissenschaften **94**, 527–541 (2007). Cited on page 34.

[75] P. Lunkenheimer, A. Loidl, *Dielectric spectroscopy on organic charge-transfer salts*, J. Phys.: Condens. Matter **27**, 373001 (2015). Cited on pages 34, 115 and 117.

[76] M. Abdel-Jawad, I. Terasaki, T. Sasaki, N. Yoneyama, N. Kobayashi, Y. Uesu, C. Hotta, *Anomalous dielectric response in the dimer Mott insulator $\kappa$-(BEDT-TTF)$_2$Cu$_2$(CN)$_3$*, Phys. Rev. B **82**, 125119 (2010). Cited on pages 34, 66, 115, 116 and 165.

[77] P. Lunkenheimer, B. Hartmann, M. Lang, J. Müller, D. Schweitzer, S. Krohns, A. Loidl, *Ferroelectric properties of charge-ordered $\alpha$-(BEDT-TTF)$_2I_3$*, Phys. Rev. B **91**, 245132 (2015). Cited on page 34.

[78] R. Gross, A. Marx, *Festkörperphysik* (Walter de Gruyter GmbH & Co KG, 2014). Cited on pages 34 and 35.

[79] P. W. Anderson, *Absence of Diffusion in Certain Random Lattices*, Phys. Rev. **109**, 1492–1505 (1958). Cited on page 35.

[80] F. Gebhard, *The Mott Metal-Insulator Transition* (Springer, 1997). Cited on page 35.

[81] V. Dobrosavljević, G. Kotliar, *Mean Field Theory of the Mott-Anderson Transition*, Phys. Rev. Lett. **78**, 3943–3946 (1997). Cited on page 35.

[82] S. H. Simon, *The Oxford Solid State Basiscs* (OUP Oxford, 2013). Cited on page 35.

[83] B. J. Powell, R. H. McKenzie, *Quantum frustration in organic Mott insulators: from spin liquids to unconventional superconductors*, Rep. Prog. Phys. **74**, 056501 (2011). Cited on page 36.

[84] A. P. Ramirez, *Strongly geometrically frustrated magnets*, Annu. Rev. Mater. Sci. **24**, 453-480 (1994). Cited on page 36.

[85] M. Born, K. Huang, *Dynamics Theory of Crystal Lattices* (Oxford University Press, Oxford, UK, 1954). Cited on page 37.

[86] L. D. Landau, E. M. Lifshitz, *Theory of Elasticity* (Pergamon Press, 1959). Cited on page 37.

[87] M. Zacharias, *Mott Transition and Quantum Critical Metamagnetism on Compressible Lattices*, Ph.D. thesis, Universität zu Köln (2013). Cited on page 37.

[88] F. Mouhat, F.-X. Coudert, *Necessary and sufficient elastic stability conditions in various crystal systems*, Phys. Rev. B **90**, 224104 (2014). Cited on page 39.

[89] C. Balz, *Thermische Ausdehnung des Multiferroikums $FeTe_2O_5Br$ und Bau einer hochauflösenden Dilatometerzelle*, Master's thesis, Goethe Universität Frankfurt am Main (2011). Cited on pages 42 and 46.

[90] F. R. Kroeger, C. A. Swenson, *Absolute linear thermal expansion measurements on copper and aluminum from 5 to 320 K*, J. Appl. Phys. **48**, 853-864 (1977). Cited on pages 43, 44, 144 and 145.

[91] *R. Modler*, Master's thesis, TH Darmstadt (1992). Cited on page 44.

[92] *M. Köppen*, Master's thesis, TH Darmstadt (1995). Cited on page 44.

[93] G. F. Strouse, *Standard Reference Material 1751: Gallium Melting-Point Standard*, National Institute of Standards and Technology (2004). Cited on page 45.

[94] C. Dietrich, *Thermische Ausdehnung niedrigdimensionaler organischer Ladungstransfersalze und Kalibration einer hochauflösenden Dilatometerzelle*, Master's thesis, Goethe Universität Frankfurt am Main (2014). Cited on page 46.

[95] J. W. Loram, K. A. Mirza, C. P. Joyce, A. J. Osborne, *Specific-Heat Evidence for Quasi-1D Magnetic Order in CuO*, Europhys. Lett. **8**, 263 (1989). Cited on page 46.

[96] J. Müller, M. Lang, F. Steglich, J. A. Schlueter, A. M. Kini, U. Geiser, J. Mohtasham, R. W. Winter, G. L. Gard, T. Sasaki, N. Toyota, *Comparative thermal-expansion study of $\beta''$-$(ET)_2SF_5CH_2CF_2SO_3$ and $\kappa$-$(ET)_2Cu(NCS)_2$: Uniaxial pressure coefficients of $T_c$ and upper critical fields*, Phys. Rev. B **61**, 11739–11744 (2000). Cited on page 48.

[97] F. Pobell, *Matter and Methods at Low Temperatures* (Springer-Verlag Berlin Heidelberg, 2007). Cited on pages 47 and 52.

[98] D. Langer, *Solidification of helium at 77°K*, J. Phys. Chem. Solids **21**, 122 - 123 (1961). Cited on page 47.

[99] Courtesy of S. Köhler, Uni Frankfurt. Cited on page 48.

[100] Institute of High Pressure Physics, Polish Academy of Sciences, Unipress Equipment Division, *High-Pressure Helium Gas Cell - serial number 1198/09* (2009). Cited on page 48.

[101] Institute of High Pressure Physics, Polish Academy of Sciences, Unipress Equipment Division, *Helium Gas Compressor U11 300 MPa Type U11/MP5* (2011). Cited on page 48.

[102] C. Kittel, *Introduction to Solid State Physics* (NJ: John Wiley & Sons, Inc., 2005). Cited on pages 50 and 54.

[103] D. Chasseau, J. Gaultier, M. Rahal, L. Ducasse, M. Kurmoo, P. Day, *Pressure dependence of the structural and electronic properties of the molecular superconductor, (BEDT-TTF)$_2$Cu(NCS)$_2$*, Synth. Met. **42**, 2039 - 2042 (1991). Cited on pages 54 and 93.

[104] W. Buckel, R. Kleiner, *Supraleitung: Grundlagen und Anwendungen* (Wiley-VCH, 2012). Cited on page 54.

[105] J. Müller, M. Lang, R. Helfrich, F. Steglich, T. Sasaki, *High-resolution ac-calorimetry studies of the quasi-two-dimensional organic superconductor κ-(bedt-ttf)$_2$cu[n(cn)$_2$]br*, Phys. Rev. B **65**, 140509 (2002). Cited on pages 55 and 130.

[106] H. H. Wang, A. M. Kini, L. K. Montgomery, U. Geiser, K. D. Carlson, J. M. Williams, J. E. Thompson, D. M. Watkins, W. K. Kwok, *Synthesis of the new highest $T_c$ ambient-pressure organic superconductor, κ-(BEDT-TTF)$_2$Cu[N(CN)$_2$]Br, by five different routes*, Chem. Mater. **2**, 482-484 (1990). Cited on page 56.

[107] J. Ferraris, D. O. Cowan, V. Walatka, J. H. Perlstein, *Electron transfer in a new highly conducting donor-acceptor complex*, J. Am. Chem. Soc. **95**, 948-949 (1973). Cited on page 57.

[108] Jérome, D., Mazaud, A., Ribault, M., Bechgaard, K., *Superconductivity in a synthetic organic conductor (TMTSF)$_2$PF$_6$*, J. Physique Lett. **41**, 95-98 (1980). Cited on page 57.

[109] J. Wosnitza, *Festkörperphysik: Organische Supraleiter: Auf der Suche nach der Natur des supraleitenden Zustands*, Phys. J. **56**, 41–45 (2000). Cited on page 58.

[110] T. Komatsu, N. Matsukawa, T. Inoue, G. Saito, *Realization of Superconductivity at Ambient Pressure by Band-Filling Control in κ-(BEDT-TTF)$_2$Cu$_2$(CN)$_3$*, J. Phys. Soc. Jpn. **65**, 1340-1354 (1996). Cited on page 61.

[111] H. Kino, H. Fukuyama, *Electronic States of Conducting Organic κ-(BEDT-TTF)$_2$X*, J. Phys. Soc. Jpn. **64**, 2726-2729 (1995). Cited on pages 61 and 123.

[112] J. Williams, A. Kini, H. Wang, K. Carlson, U. Geiser, L. Montgomery, G. Pyrka, D. Watkins, J. Kommers, *From semiconductor-semiconductor transition (42 K) to the highest-$T_c$ organic superconductor, κ-(ET)$_2$Cu[N(CN)$_2$]Cl ($T_c$ = 12.5 K)*, Inorg. Chem. **29**, 3272-3274 (1990). Cited on pages 61 and 124.

[113] Y. Watanabe, H. Sato, T. Sasaki, N. Toyota, *Lattice Parameters of κ-(BEDT-TTF)$_2$Cu[N(CN)$_2$]Br*, J. Phys. Soc. Jpn. **60**, 3608-3611 (1991). Cited on pages 61 and 75.

[114] J. Müller, *Fluctuation Spectroscopy: A New Approach for Studying Low-Dimensional Molecular Metals*, ChemPhysChem **12**, 1222–1245 (2011). Cited on pages 62 and 63.

[115] D. Guterding, R. Valentí, H. O. Jeschke, *Influence of molecular conformations on the electronic structure of organic charge transfer salts*, Phys. Rev. B **92**, 081109 (2015). Cited on pages 62 and 66.

[116] S. Lefebvre, P. Wzietek, S. Brown, C. Bourbonnais, D. Jérome, C. Mézière, M. Fourmigué, P. Batail, *Mott Transition, Antiferromagnetism, and Unconventional Superconductivity in Layered Organic Superconductors*, Phys. Rev. Lett. **85**, 5420–5423 (2000). Cited on pages 63, 64, 65, 70, 71 and 106.

[117] D. Fournier, M. Poirier, M. Castonguay, K. D. Truong, *Mott Transition, Compressibility Divergence, and the P-T Phase Diagram of Layered Organic Superconductors: An Ultrasonic Investigation*, Phys. Rev. Lett. **90**, 127002 (2003). Cited on pages 63, 64, 65, 70, 71 and 79.

[118] F. Kagawa, T. Itou, K. Miyagawa, K. Kanoda, *Transport criticality of the first-order Mott transition in the quasi-two-dimensional organic conductor* $\kappa - (\mathrm{BEDT-TTF})_2\mathrm{Cu[N(CN)_2]Cl}$, Phys. Rev. B **69**, 064511 (2004). Cited on pages 63, 64, 70, 71 and 108.

[119] J. Müller, M. Lang, F. Steglich, J. A. Schlueter, A. M. Kini, T. Sasaki, *Evidence for structural and electronic instabilities at intermediate temperatures in κ-(BEDT-TTF)$_2$X for X = Cu[N(CN)$_2$]Cl, Cu[N(CN)$_2$]Br and Cu(NCS)$_2$: Implications for the phase diagram of these quasi-two-dimensional organic superconductors*, Phys. Rev. B **65**, 144521 (2002). Cited on pages 63, 64, 66, 75 and 134.

[120] R. H. McKenzie, *Similarities Between Organic and Cuprate Superconductors*, Science **278**, 820–821 (1997). Cited on page 64.

[121] M. Lang, J. Müller, *Quasi-Twodimensional Organic Superconductors*, Superconductivity Review (1996). Cited on page 64.

[122] J. Wosnitza, *Quasi-Two-Dimensional Organic Superconductors*, J. Low Temp. Phys. **146**, 641–667 (2007). Cited on page 64.

[123] D. Guterding, S. Diehl, M. Altmeyer, T. Methfessel, U. Tutsch, H. Schubert, M. Lang, J. Müller, M. Huth, H. O. Jeschke, R. Valentí, M. Jourdan, H.-J. Elmers, *Evidence for Eight-Node Mixed-Symmetry Superconductivity in a Correlated Organic Metal*, Phys. Rev. Lett. **116**, 237001 (2016). Cited on pages 64 and 123.

[124] Y. Nakazawa, H. Taniguchi, A. Kawamoto, K. Kanoda, *Electronic specific heat at the boundary region of the metal-insulator transition in the two-dimensional electronic system of $\kappa$-(BEDT-TTF)$_2$Cu[N(CN)$_2$]Br*, Phys. Rev. B **61**, R16295–R16298 (2000). Cited on page 64.

[125] V. Kataev, G. Winkel, D. Khomskii, D. Wohlleben, W. Crump, K. Tebbe, J. Hahn, *ESR of single crystals of $\kappa$-(BEDT-TTF)$_2$Cu[N(CN)$_2$]X (X = Br and I)*, Solid State Commun. **83**, 435 - 439 (1992). Cited on page 64.

[126] H. Mayaffre, P. Wzietek, C. Lenoir, D. Jérome, P. Batail, *$^{13}$C NMR Study of a Quasi-Two-Dimensional Organic Superconductor $\kappa$-(ET)$_2$Cu[N(CN)$_2$]Br*, Europhys. Lett. **28**, 205 (1994). Cited on page 64.

[127] A. Kawamoto, K. Miyagawa, Y. Nakazawa, K. Kanoda, *$^{13}$C NMR Study of Layered Organic Superconductors Based on BEDT-TTF Molecules*, Phys. Rev. Lett. **74**, 3455–3458 (1995). Cited on page 64.

[128] S. M. De Soto, C. P. Slichter, A. M. Kini, H. H. Wang, U. Geiser, J. M. Williams, $^{13}$C *NMR studies of the normal and superconducting states of the organic superconductor $\kappa$-(ET)$_2$Cu[N(CN)$_2$]Br*, Phys. Rev. B **52**, 10364–10368 (1995). Cited on page 64.

[129] T. Sasaki, N. Yoneyama, A. Matsuyama, N. Kobayashi, *Magnetic and electronic phase diagram and superconductivity in the organic superconductors $\kappa$-(ET)$_2$X*, Phys. Rev. B **65**, 060505 (2002). Cited on page 64.

[130] J. Merino, R. H. McKenzie, *Transport properties of strongly correlated metals: A dynamical mean-field approach*, Phys. Rev. B **61**, 7996–8008 (2000). Cited on page 65.

[131] G. Kotliar, S. Murthy, M. J. Rozenberg, *Compressibility Divergence and the Finite Temperature Mott Transition*, Phys. Rev. Lett. **89**, 046401 (2002). Cited on page 65.

[132] M. de Souza, A. Brühl, C. Strack, B. Wolf, D. Schweitzer, M. Lang, *Anomalous Lattice Response at the Mott Transition in a Quasi-2D Organic Conductor*, Phys. Rev. Lett. **99**, 037003 (2007). Cited on pages 65, 73, 84, 105 and 134.

[133] K. Miyagawa, A. Kawamoto, Y. Nakazawa, K. Kanoda, *Antiferromagnetic Ordering and Spin Structure in the Organic Conductor, $\kappa$-(BEDT-TTF)$_2$Cu[N(CN)$_2$]Cl*, Phys.

Rev. Lett. **75**, 1174–1177 (1995). Cited on pages 65, 117 and 118.

[134] D. F. Smith, S. M. De Soto, C. P. Slichter, J. A. Schlueter, A. M. Kini, R. G. Daugherty, *Dzialoshinskii-Moriya interaction in the organic superconductor κ-(BEDT-TTF)$_2$Cu[N(CN)$_2$]Cl*, Phys. Rev. B **68**, 024512 (2003). Cited on page 65.

[135] R. S. Manna, M. de Souza, A. Brühl, J. A. Schlueter, M. Lang, *Lattice Effects and Entropy Release at the Low-Temperature Phase Transition in the Spin-Liquid Candidate κ-(BEDT-TTF)$_2$Cu$_2$(CN)$_3$*, Phys. Rev. Lett. **104**, 016403 (2010). Cited on pages 65 and 133.

[136] H. C. Kandpal, I. Opahle, Y.-Z. Zhang, H. O. Jeschke, R. Valentí, *Revision of Model Parameters for κ-Type Charge Transfer Salts: An Ab Initio Study*, Phys. Rev. Lett. **103**, 067004 (2009). Cited on page 65.

[137] K. Nakamura, Y. Yoshimoto, T. Kosugi, R. Arita, M. Imada, *Ab initio Derivation of Low-Energy Model for κ-ET Type Organic Conductors*, J. Phys. Soc. Jpn. **78**, 083710 (2009). Cited on page 65.

[138] K. Sedlmeier, S. Elsässer, D. Neubauer, R. Beyer, D. Wu, T. Ivek, S. Tomić, J. A. Schlueter, M. Dressel, *Absence of charge order in the dimerized κ-phase BEDT-TTF salts*, Phys. Rev. B **86**, 245103 (2012). Cited on pages 66, 117 and 127.

[139] S. Tomić, M. Pinterić, T. Ivek, K. Sedlmeier, R. Beyer, D. Wu, J. A. Schlueter, D. Schweitzer, M. Dressel, *Magnetic ordering and charge dynamics in κ-(BEDT-TTF)$_2$Cu[N(CN)$_2$]Cl*, J. Phys.: Condens. Matter **25**, 436004 (2013). Cited on pages 66 and 117.

[140] H. Akutsu, K. Saito, M. Sorai, *Phase behavior of the organic superconductors κ-(BEDT-TTF)$_2$Cu[N(CN)$_2$]X (X = Br and Cl) studied by ac calorimetry*, Phys. Rev. B **61**, 4346–4352 (2000). Cited on page 66.

[141] B. Hartmann, D. Zielke, J. Polzin, T. Sasaki, J. Müller, *Critical Slowing Down of the Charge Carrier Dynamics at the Mott Metal-Insulator Transition*, Phys. Rev. Lett. **114**, 216403 (2015). Cited on pages 66 and 105.

[142] J. Wosnitza, *Fermi Surfaces of Low-Dimensional Organic Metals and Superconductors* (Springer-Verlag Berlin Heidelberg, 1996). Cited on page 67.

[143] T. Sasaki, *Mott-Anderson Transition in Molecular Conductors: Influence of Randomness on Strongly Correlated Electrons in the κ-(BEDT-TTF)$_2$X System*, Crystals **2**, 374-392 (2012). Cited on pages 67, 111 and 140.

[144] T. Furukawa, K. Miyagawa, T. Itou, M. Ito, H. Taniguchi, M. Saito, S. Iguchi, T. Sasaki, K. Kanoda, *Quantum Spin Liquid Emerging from Antiferromagnetic Order by Introducing Disorder*, Phys. Rev. Lett. **115**, 077001 (2015). Cited on page 67.

[145] E. Gati, M. Garst, R. Manna, U. Tutsch, B. Wolf, L. Bartosch, H. Schubert, T. Sasaki, J. Schlueter, M. Lang, *Breakdown of Hooke's law of elasticity at the Mott critical endpoint in an organic conductor*, Science Advances **2**, e160146 (2016). Cited on page 69.

[146] D. B. McWhan, A. Menth, J. P. Remeika, W. F. Brinkman, T. M. Rice, *Metal-Insulator Transitions in Pure and Doped* $V_2O_3$, Phys. Rev. B **7**, 1920–1931 (1973). Cited on pages 70 and 73.

[147] M. Imada, *Universality classes of metal-insulator transitions in strongly correlated electron systems and mechanism of high-temperature superconductivity*, Phys. Rev. B **72**, 075113 (2005). Cited on page 72.

[148] T. Furukawa, M. K., H. Taniguchi, R. Kato, K. Kanoda, *Quantum criticality of Mott transition in organic materials*, Nature Physics **11**, 221-224 (2015). Cited on pages 72, 105 and 140.

[149] F. Kagawa, K. Miyagawa, K. Kanoda, *Magnetic Mott criticality in a $\kappa$-type organic salt probed by NMR*, Nature Phys. **5**, 880-884 (2009). Cited on page 72.

[150] S. Papanikolaou, R. M. Fernandes, E. Fradkin, P. W. Phillips, J. Schmalian, R. Sknepnek, *Universality of Liquid-Gas Mott Transitions at Finite Temperatures*, Phys. Rev. Lett. **100**, 026408 (2008). Cited on pages 72 and 110.

[151] Courtesy of M. Garst, U Köln. Cited on page 74.

[152] A. Levanyuk, A. Sobyanin, *Second-order phase transitions without divergences in the second order derivatives of the thermodynamic potential*, Zh. Eksp. Teor. Fiz. Pis. Red. **11**, 540-543 (1970). Cited on page 74.

[153] T. Hiramatsu, Y. Yoshida, G. Saito, A. Otsuka, H. Yamochi, M. Maesato, Y. Shimizu, H. Ito, H. Kishida, *Quantum spin liquid: Design of a quantum spin liquid next to a superconducting state based on a dimer-type ET Mott insulator*, J. Mater. Chem. C **3**, 1378-1388 (2015). Cited on page 75.

[154] R. A. Cowley, *Acoustic phonon instabilities and structural phase transitions*, Phys. Rev. B **13**, 4877–4885 (1976). Cited on pages 86, 87 and 105.

[155] T. Nattermann, *Instabilities in Ising systems with short- and long-range-correlated quenched random fields*, J. Phys. C: Solid State Physics **16**, 6407-6413 (1983). Cited on page 90.

[156] J. Burgy, A. Moreo, E. Dagotto, *Relevance of Cooperative Lattice Effects and Stress Fields in Phase-Separation Theories for CMR Manganites*, Phys. Rev. Lett. **92**, 097202 (2004). Cited on page 90.

[157] D. N. Nichols, R. J. Sladek, H. R. Harrison, *Elastic constants of $V_2O_3$ between 300 and 640 K: Anomalies near the high-temperature electrical transition*, Phys. Rev. B

**24**, 3025–3030 (1981). Cited on page 104.

[158] H. Terletska, J. Vučičević, D. Tanasković, V. Dobrosavljević, *Quantum Critical Transport near the Mott Transition*, Phys. Rev. Lett. **107**, 026401 (2011). Cited on page 105.

[159] V. Dobrosavljevic, *Wigner-Mott quantum criticality: From 2D-MIT to $^3$He and Mott organics, Contribution to: "Strong Correlation Phenomena around 2D Conductor-Insulator Transitions"* (Pan Stanford Publishing, 2016). Cited on page 105.

[160] I. Leonov, V. I. Anisimov, D. Vollhardt, *Metal-insulator transition and lattice instability of paramagnetic $V_2O_3$*, Phys. Rev. B **91**, 195115 (2015). Cited on page 106.

[161] S. Liu, B. Phillabaum, E. W. Carlson, K. A. Dahmen, N. S. Vidhyadhiraja, M. M. Qazilbash, D. N. Basov, *Random Field Driven Spatial Complexity at the Mott Transition in $VO_2$*, Phys. Rev. Lett. **116**, 036401 (2016). Cited on page 106.

[162] S. Köhler, U. Tutsch, Resistance measurements on x-ray irradiated $\kappa$-(BEDT-TTF)$_2$Cu[N(CN)$_2$]Cl under $^4$He gas pressure. Private communication. Cited on page 112.

[163] K. Byczuk, W. Hofstetter, D. Vollhardt, *Mott-Hubbard Transition versus Anderson Localization in Correlated Electron Systems with Disorder*, Phys. Rev. Lett. **94**, 056404 (2005). Cited on page 113.

[164] F. Nad, P. Monceau, *Dielectric Response of the Charge Ordered State in Quasi-One-Dimensional Organic Conductors*, J. Phys. Soc. Jpn. **75**, 051005 (2006). Cited on page 115.

[165] C. Hotta, *Quantum electric dipoles in spin-liquid dimer Mott insulator $\kappa$-$ET_2Cu_2(CN)_3$*, Phys. Rev. B **82**, 241104 (2010). Cited on page 116.

[166] B. Hartmann, *Fluktuationsspektroskopie an dem organischen Ladungstransfersalz $\kappa$-(BEDT-TTF)$_2$Cu[N(CN)$_2$]Cl*, Master's thesis, Goethe-Universität Frankfurt (2012). Cited on page 116.

[167] L. E. Cross, *Relaxor Ferroelectrics* (Springer Berlin Heidelberg, Berlin, Heidelberg, 2008), pp. 131–155. Cited on page 117.

[168] M. Dressel, N. Drichko, *Optical Properties of Two-Dimensional Organic Conductors: Signatures of Charge Ordering and Correlation Effects*, Chem. Rev. **104**, 5689-5716 (2004). Cited on page 117.

[169] M. Pinterić, P. Lazić, A. Pustogow, T. Ivek, M. Kuveždić, O. Milat, B. Gumhalter, M. Basletić, M. Čulo, B. Korin-Hamzić, A. Löhle, R. Hübner, M. Sanz Alonso, T. Hiramatsu, Y. Yoshida, G. Saito, M. Dressel, S. Tomić, *Anion effects on electronic structure and electrodynamic properties of the Mott insulator $\kappa$-(BEDT-TTF)$_2$Ag$_2$(CN)$_3$*, Phys. Rev. B **94**, 161105 (2016). Cited on page 118.

[170] M. Dressel, P. Lazić, A. Pustogow, E. Zhukova, B. Gorshunov, J. A. Schlueter, O. Milat, B. Gumhalter, S. Tomić, *Lattice vibrations of the charge-transfer salt κ-(BEDT-TTF)$_2$Cu$_2$(CN)$_3$: Comprehensive explanation of the electrodynamic response in a spin-liquid compound*, Phys. Rev. B **93**, 081201 (2016). Cited on page 118.

[171] M. Lang, P. Lunkenheimer, J. Müller, A. Loidl, B. Hartmann, N. H. Hoang, E. Gati, H. Schubert, J. A. Schlueter, *Multiferroicity in the Mott Insulating Charge-Transfer Salt κ -(BEDT-TTF)$_2$Cu[N(CN)$_2$]Cl*, IEEE Trans. Magn. **50**, 1-7 (2014). Cited on pages 118 and 127.

[172] N. H. Hoang, *Susceptibility measurements on strongly correlated electron systems under He gas pressure*, Master's thesis, Goethe Universität Frankfurt am Main (2014). Cited on page 118.

[173] S. V. Konovalikhin, G. V. Shilov, O. A. D'yachenko, M. Z. Aldoshina, R. N. Lyubovskaya, R. B. Lyubovskii, *Crystal structures of the organic metals (ET)$_2$[Hg(SCN)Cl$_2$] and (ET)$_2$[Hg(SCN)$_2$Br]*, Russ. Acad. Sci., Division of chemical science **41**, 1819-1826 (1992). Cited on page 121.

[174] S. Yasin, E. Rose, M. Dumm, N. Drichko, M. Dressel, J. Schlueter, E. Zhilyaeva, S. Torunova, R. Lyubovskaya, *Electronic and magnetic studies of κ-(BEDT-TTF)$_2$Hg(SCN)$_2$Cl*, Physica B: Condensed Matter **407**, 1689 - 1691 (2012). Cited on pages 121, 122, 125, 130 and 165.

[175] M. Z. Aldoshina, R. N. Lyubovskaya, S. V. Konovalikhin, O. A. Dyachenko, M. K. Makova, R. B. Lyubovskii, *New Organic Metals ET$_2$[Hg(SCN)Cl$_2$] and ET$_2$[Hg(SCN)$_2$Cl]*, Mol. Cryst. Liq. Cryst. **230**, 185-189 (1993). Cited on page 121.

[176] S. Dayal, R. T. Clay, H. Li, S. Mazumdar, *Paired electron crystal: Order from frustration in the quarter-filled band*, Phys. Rev. B **83**, 245106 (2011). Cited on page 122.

[177] H. Li, R. T. Clay, S. Mazumdar, *The paired-electron crystal in the two-dimensional frustrated quarter-filled band*, J. Phys.: Condens. Matter **22**, 272201 (2010). Cited on page 122.

[178] H. Jeschke. Private communication. Cited on pages 122, 123, 141 and 167.

[179] C. Delleske, Charakterisierung der Leitfähigkeit von neuartigen organischen Ladungstransfersalzen. Bachelor's thesis, Goethe-Universität Frankfurt am Main (2016). Cited on page 125.

[180] S. Roberts, *Dielectric and piezoelectric properties of barium titanate*, Phys. Rev. **71**, 890–895 (1947). Cited on page 128.

[181] M. de Souza, P. Foury-Leylekian, A. Moradpour, J.-P. Pouget, M. Lang, *Evidence for Lattice Effects at the Charge-Ordering Transition in TMTTF$_2$X*, Phys. Rev. Lett. **101**, 216403 (2008). Cited on page 128.

[182] J. Riera, D. Poilblanc, *Influence of the anion potential on the charge ordering in quasi-one-dimensional charge-transfer salts*, Phys. Rev. B **63**, 241102 (2001). Cited on page 128.

[183] R. T. Clay, S. Mazumdar, D. K. Campbell, *Pattern of charge ordering in quasi-one-dimensional organic charge-transfer solids*, Phys. Rev. B **67**, 115121 (2003). Cited on page 128.

[184] S. Brazovskii, P. Monceau, F. Nad, *The ferroelectric Mott-Hubbard phase in organic conductors*, Synth. Met. **137**, 1331 - 1333 (2003). Cited on page 128.

[185] J. Wosnitza, X. Liu, D. Schweitzer, H. J. Keller, *Specific heat of the organic superconductor $\kappa$-(BEDT-TTF)$_2I_3$*, vol. 50 (American Physical Society, 1994). Cited on pages 132 and 133.

[186] P. Foury-Leylekian, S. Petit, I. Mirebeau, G. André, M. de Souza, M. Lang, E. Ressouche, A. Moradpour, J.-P. Pouget, *Low-temperature structural effects in the (TMTSF)$_2PF_6$ and $AsF_6$ Bechgaard salts*, Phys. Rev. B **88**, 024105 (2013). Cited on page 132.

[187] R. Świetlik, H. Grimm, D. Schweitzer, H. J. Keller, *Raman-Studies of the Organic Superconductor $\beta$-(BEDT-TTF)$_2IAuI$*, Z. Naturforsch. A **42**, 603-605 (1987). Cited on page 132.

[188] B. Andraka, G. R. Stewart, K. D. Carlson, H. H. Wang, M. D. Vashon, J. M. Williams, *Specific heat in zero and applied magnetic fields of the organic superconductor $\alpha$-di[bis(ethylenedithio)tetrathiafulvalene]-ammonium- tetra(thiocyanato)mercurate [$\alpha$-(ET)$_2$($NH_4$)Hg(SCN)$_4$]*, Phys. Rev. B **42**, 9963–9966 (1990). Cited on pages 132 and 133.

[189] S. Katsumoto, S. ichi Kobayashi, H. Urayama, H. Yamochi, G. Saito, *Low-Temperature Specific Heat of Organic Superconductor $\kappa$-(BEDT-TTF)$_2$Cu(NCS)$_2$*, J. Phys. Soc. Jpn. **57**, 3672-3673 (1988). Cited on pages 132 and 133.

[190] B. Andraka, J. S. Kim, G. R. Stewart, K. D. Carlson, H. H. Wang, J. M. Williams, *Specific heat in high magnetic field of $\kappa$-di[bis(ethylenedithio)tetrathiafulvalene]-di(thiocyano)cuprate [$\kappa$-(ET)$_2$Cu(NCS)$_2$]: Evidence for strong-coupling superconductivity*, Phys. Rev. B **40**, 11345–11347 (1989). Cited on pages 132 and 133.

[191] Garoche, P., Brusetti, R., Jérome, D., Bechgaard, K., *Specific heat measurements of organic superconductivity in (TMTSF)$_2ClO_4$*, J. Physique Lett. **43**, 147-152 (1982). Cited on page 133.

[192] A. U. B. Wolter, R. Feyerherm, E. Dudzik, S. Süllow, C. Strack, M. Lang, D. Schweitzer, *Determining ethylene group disorder levels in $\kappa$-(BEDT-TTF)$_2$Cu[N(CN)$_2$]Br*, Phys. Rev. B **75**, 104512 (2007). Cited on page 136.

[193] V. P. M. de Souza, *Thermal Expansion and Transport Properties of Low-Dimensional Organic Conductors*, Ph.D. thesis, Goethe-Universität Frankfurt am Main (2008). Cited on pages 136 and 146.

[194] A. L. Goodwin, C. J. Kepert, *Negative thermal expansion and low-frequency modes in cyanide-bridged framework materials*, Phys. Rev. B **71**, 140301 (2005). Cited on page 136.

[195] Courtesy of S. M. Winter, U Frankfurt. Cited on pages 137 and 166.

[196] P. Ross, Messung der dielektrischen Konstante von Helium unter Druck. Bachelor's thesis, Goethe-Universität Frankfurt am Main (2015). Cited on page 143.

[197] S. Van Sciver, *Helium Cryogenics*, International Cryogenics Monograph Series (Springer New York, 2012). Cited on page 144.

[198] O. V. Lounasmaa, *Pressure Coefficient and Compressibility of Liquid* $He^4$ *Very Close to the* $\lambda$ *Curve*, Phys. Rev. **130**, 847–851 (1963). Cited on page 144.

[199] W. Keesom, G. Macwood, *The viscosity of liquid helium*, Physica **5**, 737 - 744 (1938). Cited on page 144.

[200] D. G. Henshaw, *Structure of Solid Helium by Neutron Diffraction*, Phys. Rev. **109**, 328-330 (1958). Cited on page 144.

[201] J. S. Dugdale, J. P. Franck, *The Thermodynamic Properties of Solid and Fluid Helium-3 and Helium-4 above 3 degrees K at High Densities*, Proc. R. Soc. A: Math. Phys. Eng. Sci. **257**, 1–29 (1964). Cited on page 144.

# List of Figures

# List of Tables

# List of Abbreviations and Symbols

$(T_c, P_c/H_c)$ ..... critical endpoint

$\alpha$ ..... thermal expansion coefficient

$\alpha, \beta, \gamma, \delta, \nu$ ..... critical exponents

$\beta$ ..... volumetric expansion coefficient

$\chi$ ..... magnetic susceptibility

$\Delta L/L$ ..... relative length change

$\Delta V/V$ ..... relative volume change

$\delta$ ..... charge-transfer ratio

$\Gamma$ ..... Grüneisen parameter

$\kappa$ ..... compressibility

$\kappa$-Cl ..... $\kappa$-$(ET)_2Cu[N(CN)_2]Cl$

$\kappa$-CuCN ..... $\kappa$-$(ET)_2Cu_2(CN)_3$

$\kappa$-HgCl ..... $\kappa$-$(ET)_2Hg(SCN)_2Cl$

$\lambda_\alpha$ ..... eigenvalues of the elastic constant matrix

$\mathcal{F}$ ..... free energy

$\mathcal{G}$ ..... Gibbs free energy

$\mathcal{H}$ ..... Hamiltonian

$\phi$ ..... order parameter

$\rho$ ..... Density

$\sigma$ ..... stress

$\tau$ ..... relaxation time

$\tilde{V}$ ..... nearest-neighbor Coulomb interaction

$\varepsilon$ ..... strain

$\varepsilon'$ ..... real part of the dielectric consant

$\varepsilon_r$ ..... dielectric constant

$\vec{M}$ ..... Magnetization

$\vec{v_i}$ ..... eigenvectors of the elastic constant matrix

$\xi$ ..... correlation length

$a, b, c$ ..... crystallographic axes

$B$ ..... magnetic induction

$C$ ..... capacitance

$C$ ..... specific heat

$c^\dagger_{i,\sigma}$ $(c_{i,\sigma})$ ..... creation (annihilation) operator

$C_{ij}$ ..... elastic constant matrix in Voigt notation

$d$ ..... dimension

$E_A$ ..... activation barrier energy

$G$ ..... conductance

$H$ ..... magnetic field

$h$ ..... reduced field or pressure

$J$ ..... exchange energy

| | |
|---|---|
| $L$ | length |
| $n$ | band filling |
| $P$ | pressure |
| $q$ | cooling rate |
| $r$ | rigidity |
| $S$ | entropy |
| $S_i$ | Spin on lattice site $i$ |
| $T$ | temperature |
| $t$ | reduced temperature |
| $t, t'$ | hopping parameter in the effective dimer model |
| $t_1, t_2, t_3, t_4$ | hopping parameter in the molecule-based model |
| $T_g$ | glass transition temperature |
| $T_N$ | Néel temperature |
| $T_{CW}$ | Curie-Weiss temperature |
| $T_{FE}$ | ferroelectric transition temperature |
| $T_{MF}$ | multiferroic transition temperature |
| $T_{MI}$ | metal-insulator transition temperature |
| $U$ | Coulomb repulsion |
| $u$ | non-linearity in the mean-field potential |
| $V$ | volume |
| $W$ | bandwidth |
| $w$ | variance of the distribution function $P_w(s)$ |
| 1D, 2D, 3D | one-, two-, three-dimensional |
| BEDT-TTF/ET | bis(ethylenedithio)-tetrathiafulvalene |
| DFT | density functional theory |
| DMFT | dynamical mean-field theory |
| HOMO | highest occupied molecular orbital |
| LUMO | lowest occupied molecular orbital |
| MF | Mean field |
| MIT | metal-insulator transition |
| NTE | negative thermal expansion |
| SQUID | Superconducting Quantum Interference Device |

# Acknowledgments

Diese Arbeit wäre ohne die vielfältige Unterstützung vieler Personen nicht möglich gewesen, bei denen ich mich im Folgenden gerne bedanken möchte.

An erster Stelle möchte ich mich bei Prof. Dr. Michael Lang dafür bedanken, dass ich in seiner Arbeitsgruppe dieses spannende, aber zeitgleich auch herausfordende Projekt durchführen durfte. Durch Ihren steten Einsatz für dieses Projekt - angefangen vom Probeneinbau bis hin zum Interpretieren der Ergebnisse - haben Sie es ermöglicht, dass das Projekt in dieser erfolgreichen Form abgeschlossen werden konnte.

Weiterhin bedanke ich mich bei Prof. Dr. Jens Müller für die Übernahme des Zweitgutachtens dieser Arbeit.

Die Interpretation der experimenteller Ergebnisse dieser Arbeit beruhte vor allem auch darauf, dass dieses Projekt von theoretischer Seite begleitet wurde. Dabei spielte PD Dr. Markus Garst eine entscheidende Rolle. Danke für Deine Ideen und Dein Interesse an dem Projekt. Durch die vielen Diskussionen konnten wir viel von Dir über kritische Phänomene lernen und so sind viele wichtige Ideen für unsere Experimente entstanden. Auch danke ich Dr. Lorenz Bartosch, der diese Arbeit am Anfang theoretisch begleitet hat.

Die erfolgreiche Durchführung eines Experimentes beruht oft auf Erfahrungen und Kenntnissen, die andere Personen einem übermitteln: First of all, I would like to thank Dr. Rudra Sekhar Manna who taught me a lot about the performance of thermal expansion measurements, especially on how to mount organic charge-transfer salts in the dilatometer cell which represents one of the most challenging tasks in performing such kind of experiments. Weiterhin bedanke ich mich bei Dr. Ulrich Tutsch dafür, dass er mich anfangs im Umgang mit dem Kryostaten für thermische Ausdehnungsmessungen unter Druck vertraut gemacht hat. Ebenso haben seine Rechnungen zur Dielektrizitätskonstante von Helium unter Druck in der Auswertung der Messdaten sehr geholfen. Auch PD Dr. Bernd Wolf konnte mir sehr viel von seinem Erfahrungsschatz sowohl in Tieftemperaturphysik als auch in den Hochdruckanlagen dieser Arbeitsgruppe weitergeben.

The experiments would have not been possible without the high-quality single crystals that have been provided by Dr. Harald Schubert, Dr. John A. Schlueter and Prof. Dr. Takahiko Sasaki. Thank you all very much for the successful collaboration.

It is always helpful to discuss your progress with colleagues that work in the same research field. Here, I always enjoyed inspiring discussions with Benedikt Hartmann and Dr. Stephen Winter. Steve, thank you very much for taking the time to carefully proofread this thesis.

Natürlich gehört ein großer Dank der gesamten Arbeitsgruppe, die zu einem angenehmen Arbeitsklima beigetragen hat und dadurch oft Arbeit und Spaß miteinander verschmolzen sind. Allen voran danke ich Lars Postulka, mit dem ich die letzten sechs Jahre ein Büro teilen durfte. Danke für alle wissenschaftlichen wie auch nicht-wissenschaftlichen Diskussionen. Weiterhin gilt auch ein großer Dank allen anderen, teilweise ehemaligen Kollegen, mit denen ich eine schöne Zeit hier verbringen durfte: Dr. Stephan Knöner (Ernst), David Zielke, Sebastian Köhler, Steffi Hartmann, Satya Krishna Thallapaka, Christian Thurn, Caroline Delleske, Stephan Dörschug, Sebastian Becker, Dr. Phan Tham Cong, Dr. Yeekin Tsui, Nguyen Hieu Hoang, Carola Dietrich, Phillip Ross und Fabian Schulze-Heine.

Die Arbeit hier im Physikalischen Institut wird jeden Tag aufs Neue vor allem durch die Unterstützung der technischen und administrativen Mitarbeiter erleichtert. Dazu zählen in erster Linie die Feinmechanikwerkstatt um Herrn Hohmann und Herrn Pfeiffer, die Elektronikwerkstatt um Herrn Holzmann und Herrn Gärtner und die stets sehr zuverlässige Versorgung mit Kühlflüssigkeiten durch Herrn Rapphahn, die alle einen wichtigen Anteil an der erfolgreichen Durchführung von Tieftemperaturexperimentan haben. Innerhalb der Arbeitsgruppe waren auch Herr Dübel sowie Herr Schubert stets sehr hilfsbereit, was technische Fragen im Laboralltag angeht. Außerdem danke ich Frau Scherff für die stets umkomplizierte Unterstützung in allen administrativen Fragen.

Zuletzt gilt natürlich ein sehr großer Dank meiner Familie und meinen Freunden, die das Leben außerhalb der Forschung zu jederzeit bereichern. Der größte Dank gehört aber meinen Eltern, die stets ein großes Vorbild für mich waren und ohne die ich diesen Weg nie verfolgt hätte. Danke, dass ihr mich zu jederzeit unterstützt habt! Papa, ich wünschte, ich könnte sehen, wie Du nun Dein Versprechen einlöst und den Rasierer in die Hand nimmst.

Diese Arbeit wurde innerhalb des Sonderforschungsbereich Transregio 49 *Condensed Matter Systems with Variable Many-Body Interactions* durchgeführt.

# Eigenständigkeitserklärung

Hiermit erkläre ich, dass ich die vorgelegte Dissertation selbständig angefertigt und mich anderer Hilfsmittel als der in ihr angegebenen nicht bedient habe, insbesondere, dass alle Entlehnungen aus anderen Schriften mit Angabe der betreffenden Schrift gekennzeichnet sind.

Ich versichere die Grundsätze der guten wissenschaftlichen Praxis beachtet, und nicht die Hilfe einer kommerziellen Promotionsvermittlung in Anspruch genommen habe.